Parylene MEMS Technology for Adaptive Flow Control of Flapping Flight

Thesis by

Teerachai Nicholas Pornsinsirirak

In Partial Fulfillment of the Requirements

for the Degree of

Doctor of Philosophy

California Institute of Technology

Pasadena, California

2002

(Defended January 7, 2002)

© 2002

Teerachai Nicholas Pornsinsirirak

All Rights Reserved

To my parents and my family whose embracement

in higher education helped push me here

Acknowledgments

There are countless people who have come into and have touched my life. I will not be able to thank them all. But first and foremost, I would like to thank my parents whose love for their children is unlimited and whose motivation for higher education is never wavered. I would never be here without them. I thank them for their unconditional love and support. Second, I would like to thank all my brothers and sisters: Yupa, Greechat, Vichet, Tanaporn, and Suwalee. They are my pioneers and supporters. They are my inspiration to be the best I can be. Without their support and motivation, the road here would have been much more difficult. Thank you for believing in me. Whoever said Ph.D. was easy?

I would also like to thank my advisor, Prof. Yu-Chong Tai, for his guidance and advice throughout these years. He is one of the most brilliant professors I have ever come across. Many thanks for giving me an opportunity to work closely with him and getting a chance to explore the field of MEMS. I have learned and have grown tremendously both inside and outside the classrooms under his guidance.

My thanks also go to both previous and current members of the Caltech Micromachining Group who provided me initial guidance to start in the right direction, helped me with equipment trainings, and answered questions I had. In particular, I would like to thank my mentee, Matthieu Liger, for his enthusiasm and hard work. It has been a great pleasure guiding and working with you.

Life in the lab would have been difficult and day-to-day operation would not have gone smoothly without the help of our supporting staff members. Many thanks go to

Tanya Hefner and Trevor Roper (who seem to have all the answers of how to fix broken equipment). I also wish to thank my colleauges and friends with whom I had a chance to work from both UCLA and AeroVironment, Inc. These include Dr. Chih-Ming Ho, Dr. Hany Nassef, Steve Ho, Matt Keennon, and Joel Grasmeyer.

I can truly say that life at Caltech would be much more stressful and less fun without my water polo and volleyball friends. They have made the Caltech life outside the research lab fun. I especially would like to thank my water polo and swim coach, Clinton Dodd, along with his wife, Suzy, for all the supports and encouragements they have provided me throughout the years here. They are my extended family. The same can be said to the McNeils family in Rochester, Massachusetts, since the days at Tabor Academy: Dad Richard, Mom Ingrid, Richie, Tommy, and Heidi. Thank you. I would also like to thank all friends who, during this long journey, have touched my life and provided the encouragement and support I needed. Thanks for always being there when I needed someone to hang out with or talk to.

Lastly, this trip would have been impossible without the initial assistance of the Royal Thai government scholarship. Whoever could imagine that a kid who once grew up in the rural area of Thailand would end up obtaining his education from one of the best schools in the world? It has been a long road, and I hope my education will continue.

Parylene MEMS Technology for Adaptive Flow Control of Flapping Flight

Thesis by

Teerachai Nicholas Pornsinsirirak

In Partial Fulfillment of the Requirements

for the Degree of

Doctor of Philosophy

Abstract

This thesis is the culmination of research work in developing a parylene MEMS technology to fabricate MEMS wings and large-area parylene actuator skins for real-time adaptive flow control for flapping flight applications.

In this thesis, the novel MEMS-based wing technology is presented using titanium-alloy metal (Ti-6Al-4V) as wingframe and parylene-C as wing membrane. With this technology, the ability to produce light, yet robust, 3-D wings can be achieved. The use of MEMS technology enables systematic research in terms of repeatability, size control, weight minimization, and mass production of the wings. By fabricating the wing with the photolithography and etching techniques, fast turnaround time of various wing designs can be easily obtained. The wings are optimized to utilize the flow separation to

achieve a high lift coefficient, C_L, as large as five times that of the fixed-wing aircraft. The aerodynamic tests are performed in a high quality low-speed wind tunnel with velocity uniformity of 0.5% and speeds range from 1 to 10 m/s. The wind-tunnel test results are presented and discussed.

As part of the investigation to integrate MEMS actuators onto the wings for real-time adaptive flow control, the MEMS technology is developed to fabricate the first large-area wafer-sized, flexible parylene MEMS electrostatic actuator skins. The technology is first developed to fabricate parylene actuator diaphragm on a silicon chip. The actuator diaphragm is made of two metallized layers of parylene membranes with offset vent holes. Without electrostatic actuation, air can move freely from one side of the skin to the other side through the vent holes. With actuation, these vent holes are sealed and the airflow is controlled. The membrane behaves as a complete diaphragm. This function is successfully demonstrated using a 2-mm x 2-mm parylene diaphragm electrostatic actuator valves.

Finally, this technology is applied to fabricate large area wafer-sized actuator skins. The skins contain only parylene and metalized electrodes and have no bulk silicon as a structural component. Plate and check-valved skin types are fabricated and both are integrated onto the MEMS wings for aerodynamic flow control. The integration of micro-valved actuators has shown significant effect on the aerodynamic performance of the flapping flight. The wind-tunnel test results are analyzed and discussed in detail in this thesis.

Table of Contents

Chapter 1 Introduction to MEMS 1

1.1 Background 1

1.2 Micro-Electro-Mechanical Systems (MEMS) 3

1.2.1 Introduction to MEMS 3

1.2.2 MEMS Processing Overview 4

1.2.2.1 Bulking Micromachining Technology 6

1.2.2.2 Surface Micromachining Technology 12

1.2.2.3 LIGA Fabrication Process Technology 14

1.3 Overview of Thesis Dissertation 18

1.4 Bibliography 21

Chapter 2 MEMS Wing Technology 30

2.1 Introduction 30

2.2 Non-MEMS Wings 31

2.3 MEMS Wings 33

2.3.1 Silicon MEMS Wings 33

2.3.2 Parylene 35

2.3.2.1 Background 35

2.3.2.2 Types of Parylenes 36

2.3.2.3 Parylene Deposition Process 39

2.3.2.4 Parylene Patterning Process....41
2.3.2.5 Properties of Parylenes....41
2.3.3 Titanium-Alloy MEMS Wings....43
2.3.3.1 Titanium-Alloy Metal (Ti-6Al-4V)....43
2.3.3.2 Titanium-alloy MEMS Wings Fabrication Process....44
2.4 Challenges and Solutions....47
2.5 Summary....49
2.6 Bibliography....50
Chapter 3 Test Results of MEMS Wings....53
3.1 Introduction....53
3.2 Mechanical Tests and Results....54
3.2.1 Stiffness Test.....54
3.2.2 Flapping Test....57
3.3 Aerodynamic Tests and Results....59
3.3.1 Flapping-Wing Aerodynamics....59
3.3.2 Wind-Tunnel Setup and Initial Test Results....63
3.3.3 Leading-Edge Stiffness-Enhanced MEMS Wings....69
3.3.4 Aerodynamic Performance of 3-D Wings....71
3.3.4.1 Non-MEMS Wings vs. MEMS Wings....71
3.3.4.2 CIT7x3S20 vs. Other Designs of MEMS Wings....74
3.3.4.3 Effect of the Inboard Region....78
3.4 Summary....80
3.5 Bibliography....81

Chapter 4 Low-Temperature Parylene MEMS Technology 84

4.1 Introduction 84

4.2 Low-Temperature Parylene MEMS Technology 87

4.2.1 Anti-Stiction Techniques 88

4.2.1.1 Parylene Surface Roughening 89

4.2.1.2 Anti-Stiction Posts 89

4.2.1.3 Self-Assembled Monolayers (SAM) 90

4.2.1.4 BrF_3 Dry Etching of Silicon 94

4.3 Parylene MEMS Electrostatic Actuator on a Silicon Chip 96

4.3.1 Design 96

4.3.2 Rectangular Diaphragm Theory 97

4.3.3 Fabrication Process 102

4.3.4 Processing Challenges 106

4.4 Test Results and Discussions 109

4.4.1 Electrostatic Actuation Test 109

4.4.2 Load Deflection Test 110

4.5 Summary 114

4.6 Bibliography 116

Chapter 5 Parylene MEMS Actuator Skins for Adaptive Flow Control

.... 122

5.1 Introduction 122

5.2 Review of MEMS Devices in Fluidic and Aerodynamic Applications 123

5.3 Parylene MEMS Actuator Skins 128
5.3.1 Actuator Skin Device Concept 128
5.3.2 Actuator Skin Fabrication Concept 129
5.3.3 Skin Releasing Technologies 132
5.4 Parylene MEMS Active Plate Electrostatic Actuator Skin 135
5.4.1 Design 135
5.4.2 Fabrication Process 136
5.4.3 Processing Challenges 140
5.4.4 Electrostatic Actuation Test 144
5.4.5 Aerodynamic Test Results of Plate-Actuator Skin 147
5.5 Flexible Parylene MEMS Check-Valve Actuator Skins 150
5.5.1 Passive Check-Valve Pneumatic Actuator Skin 151
5.5.1.1 Design 151
5.5.1.2 Fabrication Process 152
5.5.1.3 Processing Challenges 156
5.5.1.4 Aerodynamic Test Results for Passive-Valved Skin 157
5.5.2 Active Check-Valve Electrostatic Actuator Skin 161
5.5.2.1 Design 161
5.5.2.2 Fabrication Process 162
5.5.2.3 Processing Challenges 165
5.5.2.4 Electrostatic Actuation Test 168
5.5.2.5 Aerodynamic Test Results of Active-Valved Skin 169
5.6 Summary 181

5.7 Bibliography 183

Chapter 6 Conclusion 187

6.1 Summary of Research 187

6.2 Future Research Directions 191

Appendix A Development of Biomimetic Flight A-1

A.1 Introduction A-1

A.2 Biomimetic Flight A-2

A.2.1 Background A-2

A.2.2 Micro-Air-Vehicle (MAV) A-5

A.2.3 Biomimetic MAVs A-9

A.2.4 The Microbat Project A-14

A.3 Summary A-22

A.4 Bibliography A-23

Appendix B Description of Fabrication Processes B-1

B.1 Titanium-Alloy MEMS Wings B-1

B.2 Parylene MEMS Electrostatic Actuator on a Silicon Chip B-5

B.3 Parylene MEMS Active Plate Electrostatic Actuator Skin B-17

B.4 Parylene MEMS Check-Valved Pneumatic Actuator Skin B-24

B.5 Parylene MEMS Check-Valved Electrostatic Actuator Skin B-31

List of Figures

Chapter 1 Introduction to MEMS

Figure 1-1 Trend of IC complexity over time: Moore's Law 3

Figure 1-2 TI's MEMS-based digital micromirror device pixel array 6

Figure 1-3 Bulk micromachining technology: Isotropic etching 8

Figure 1-4 Bulk micromachining technology: Anisotropic etching 9

Figure 1-5 Bulk micromachining technology: Anisotropic etching (DRIE) 11

Figure 1-6 Surface micromaching technology 13

Figure 1-7 LIGA fabrication process 15

Chapter 2 MEMS Wing Technology

Figure 2-1 Non-MEMS wings 32

Figure 2-2 MEMS fabricated silicon wings 34

Figure 2-3 Fabrication process of silicon MEMS wings 34

Figure 2-4 Chemical structures of parylenes 38

Figure 2-5 Parylene deposition system 39

Figure 2-6 Titanium-alloy MEMS wings 45

Figure 2-7 Fabrication process of titanium-alloy MEMS wings 46

Chapter 3 Test Results of MEMS Wings

Figure 3-1 Spring constant test setup of MEMS wings 54

Figure 3-2 Spring constant test setup diagram 55

Figure 3-3 Spring constants of butterfly wings 56

Figure 3-4 Various transmission designs....57

Figure 3-5 Transmission system....58

Figure 3-6 Aerodynamic forces and wake vortex on a wing....60

Figure 3-7 Cross section of a vortex wake generated by a moving wing....61

Figure 3-8 Force components on the wing during flapping....62

Figure 3-9 Wind-tunnel test setup....63

Figure 3-10 Spanwise stiffness effect....65

Figure 3-11 Leading-edge vortex separation during downstroke....67

Figure 3-12 Leading-edge spiral spanwise vortex....68

Figure 3-13 Lift generated during downstroke and upstroke....69

Figure 3-14 Thrust generated during downstroke and upstroke....69

Figure 3-15 Fabrication process of stiffness-enhanced MEMS wings....70

Figure 3-16 Lift and thrust coefficients of various types of wings....73

Figure 3-17 Input power....74

Figure 3-18 Various titanium-alloy MEMS wingframes with 15-μm membrane thickness....75

Figure 3-19 Comparison of lift and thrust performance of CIT 7x3 wings shown in Figure 3-18....77

Figure 3-20 Comparison of lift and thrust of type-D (7x3) and type-F (10x3) wings....78

Figure 3-21 Effect of the inboard region....79

Chapter 4 Low-Temperature Parylene MEMS Technology

Figure 4-1 Aerodynamic thrust performance of wings with different membrane

rigidity 85

Figure 4-2 The concept of active wing with integrated MEMS actuator membrane 86

Figure 4-3 Schematic diagram of the microstructure drying process that leads to stiction 88

Figure 4-4 Schematic diagram of the anti-stiction method using posts 90

Figure 4-5 Water contact angle on oxide- and SAM-coated Si surfaces.........................93

Figure 4-6 SAM process sequence 94

Figure 4-7 Schematic diagram of the anti-stiction technique using BrF_3 dry etching of silicon; (a) Post structures; (b) Thin film amorphous silicon 95

Figure 4-8 Cross-sectional view of the actuator device 97

Figure 4-9: Rectangular diaphragm with fixed edges 98

Figure 4-10 Schematic view of a rectangular membrane sample....................................101

Figure 4-11 Fabrication process flow for the parylene MEMS electrostatic actuator diaphragm...103

Figure 4-12 Fabricated parylene MEMS electrostatic actuator diaphragm with anti-stiction posts and photoresist etching holes...105

Figure 4-13 Comparison of diaphragms without and with anti-stiction techniques;
(a) 400-μm x 400-μm parylene diaphragm;
(b) 2-mm x 2-mm parylene diaphragm 106

Figure 4-14 The effect of parylene surface roughening;
(a) Good adhesion of metal layer to roughened parylene;
(b) Poor adhesion of metal layer to the non-roughened parylene surface....107

Figure 4-15 Cracking of parylene film after a long oxygen plasma patterning 108

Figure 4-16 Breakdown of the device after applying high voltage 110

Figure 4-17 Load deflection test setup 112

Figure 4-18 Load deflection test; (a) Before applying back pressure (0 psi)

(b) After applying back pressure (2 psi) 112

Figure 4-19 Load deflection test result indicates the stiffness change after actuation 113

Figure 4-20 Model fit for after-actuation test data 113

Chapter 5 Parylene MEMS Actuator Skins for Adaptive Flow Control

Figure 5-1 Micro hot-wired anemometer 124

Figure 5-2 MEMS-fabricated shear stress sensors 125

Figure 5-3 Integrated shear stress sensor skin on polyimide 125

Figure 5-4 Integrated MEMS system for turbulent boundary layer control 126

Figure 5-5 Balloon attached to a leading-edge section of F-15 wing 127

Figure 5-6 Schematic diagram of parylene actuator skins;

(a) Plate type; (b) Check-valved type 128

Figure 5-7 MEMS integrated-actuator wing concept: first approach 130

Figure 5-8 MEMS integrated-actuator wing concept: second approach 131

Figure 5-9 Cross-sectional view of the “plate” type actuator skin 135

Figure 5-10 Summary of the fabrication process of the parylene MEMS active

plate electrostatic actuator skin 137

Figure 5-11 Fabricated parylene MEMS active plate electrostatic actuator

skin (version 1) 139

Figure 5-12 Version 2 of the parylene MEMS active plate electrostatic actuator

skin with titanium-alloy wingframes 140

Figure 5-13 Photoresist bubbles underneath the parylene layer.................................... 141

Figure 5-14 Parylene layer wrinkles on top of burnt photoresist 141

Figure 5-15 Buckling of sputtered silicon film on un-annealed parylene 142

Figure 5-16 Cracking of parylene skin during parylene etching................................... 143

Figure 5-17 Aluminum film is attacked by AZ351 developer 144

Figure 5-18 Integrated plate-type actuator MEMS wings 148

Figure 5-19 Wind-tunnel aerodynamic test... 149

Figure 5-20 Phase-average results of the plate-type integrated-actuator wings 149

Figure 5-21 Summary of the fabrication process of the parylene MEMS

passive check-valve pneumatic actuator skin 153

Figure 5-22 Parylene MEMS check-valve pneumatic actuator skin 154

Figure 5-23 Snap shots of various stages of the check-valve during the fabrication 155

Figure 5-24 Loading effect for the parylene etching... 156

Figure 5-25 Phase-average results of the reference and hole-integrated wings 158

Figure 5-26 Passive check-valve actuator-integrated MEMS wings.............................. 159

Figure 5-27 Phase-average results of the check-valve actuator-integrated wings........... 159

Figure 5-28 Summary of the fabrication process of the parylene MEMS

active check-valve electrostatic actuator skin.. 163

Figure 5-29 Parylene MEMS active check-valve electrostatic actuator skins 164

Figure 5-30 Poor adhesion of parylene to Au surface 165

Figure 5-31 Disconnection of top electrode 166

Figure 5-32 Curling of valve cap.. 167

Figure 5-33 Leveled valve cap (with metal layer) ... 168

Figure 5-34 Breakdown of the electrostatic actuators ... 168

Figure 5-35 Examples of skin fabricated and integrated wings ... 169

Figure 5-36 Active check-valve electrostatic actuator-integrated MEMS wings ... 170

Figure 5-37 Comparison of phase-average results of the MEMS wings integrated with "circular" active and passive actuator skins ... 171

Figure 5-38 Phase average results of the "cambered" wings integrated with with "square" active-valved actuator at $J = 0.95$ ... 175

Figure 5-39 Phase average results of the "cambered" wings integrated with with "square" active-valved actuator at $J = 0.61$ ... 176

Figure 5-40 Phase average results of the "cambered" wings integrated with with "square" active-valved actuator at $J = 0.48$ ... 177

Figure 5-41 Phase average results of the "flat" wings integrated with with "square" active-valved actuator at $J = 0.48$ ... 179

Appendix A Development of Biomimetic Flight

Figure A-1 Examples of man-made ornithopters in 19th century ... A-3

Figure A-2 Ornithopter built by George Trouvé ... A-4

Figure A-3 Black Widow MAV ... A-6

Figure A-4 Size of natural flyers ... A-7

Figure A-5 MAV flight regime compared to existing flight vehicles ... A-7

Figure A-6 DARPA-funded ornithopter MAV programs ... A-10

Figure A-7 Other MAV concepts and prototypes ... A-11

Figure A-8 Super-capacitor- and battery-powered Microbat prototypes A-15

Figure A-9 The new redesigned lightweight gearbox transmission A-16

Figure A-10 Radio-Controlled Microbat prototype; duration 42 seconds (Dec '00) A-16

Figure A-11 Lithium polymer battery in comparison to Sanyo N50-AAA battery A-19

Figure A-12 Wingbeat energy conservation spring system..A-19

Figure A-13 The latest radio-controlled Microbat with PLiON battery;

duration 2 min 6 secs (8/01) A-20

Figure A-14 The Microbat in flight mode A-21

Appendix B Description of Fabrication Processes

Figure B-1 Titanium-alloy MEMS wing:

(a) Butterfly; (b) Simple wing spar CIT7x3S20 ....B-4

Figure B-2 Parylene diaphragm actuator chip:

(a) 1 mm x 5 mm rectangular actuator;

(b) 2 mm x 2 mm square design B-16

Figure B-3 Flexible parylene plate-type electrostatic actuator skin B-23

Figure B-4 Flexible parylene check-valved pneumatic actuator skin B-30

Figure B-5 Flexible parylene check-valved electrostatic actuator skin.......................B-38

List of Tables

Chapter 1 Introduction to MEMS

Table 1-1 MEMS technology comparison.....16

Table 1-2 MEMS fabrication process.....17

Chapter 2 MEMS Wings Technology

Table 2-1 Properties of parylenes.....42

Table 2-2 Mechanical properties of Ti-6Al-4V and parylene-C.....45

Chapter 3 Test Results of MEMS Wings

Table 3-1 Flapping frequency of various fabricated MEMS wings.....58

Table 3-2 Properties of various wings designs.....72

Chapter 4 Low -Temperature Parylene MEMS Technology

Table 4-1 Measured contact angle before and after treating with SAM.....92

Table 4-2 Contact angle measurements on various-treated parylene surfaces.....92

Chapter 5 Parylene MEMS Actuator Skins for Adaptive Flow Control

Table 5-1 Phase-average results of plate-type wings.....150

Table 5-2 Phase-average results of passive-valved type wings.....160

Table 5-3 Phase-average results of "circular" active-valved type wings.....172

Table 5-4 On and off states of "circular" active-valved type wings.....172

Table 5-5 Lift of “square” active-valved wings at various J values.....174

Table 5-6 Thrust of “square” active-valved wings at various J values.....174

Table 5-7 Comparison of lift and thrust of flat and cambered wings 180

Appendix A Development of Biomimetic Flight

Table A-1 Weight summary of the radio-controlled Microbat prototype A-17

Table A-2 Summary of the Microbat prototypes A-21

Symbols

A	Area
C_L	Lift coefficient
C_T	Thrust coefficient
D	Drag
L	Length
E	Young's modulus
I	Moment of inertia
J	Advanced ratio
K	Spring constant
L	Lift
P	Pressure
T	Thrust
U	Wind Speed
a	Dimension of the shorter side of the rectangular membrane
b	Wing semi-span
f	Flapping frequency
h	Membrane thickness
m	Mass
n	Ratio of a short to a long side of a rectangular membrane
t	Thickness of the beam
w	Width of the beam

y	Deflection height of the membrane
Γ	Circulation
Φ	Stroke angle
α	Non-dimensional deflection coefficient
ρ	Air density
β	Body inclination
σ	Residual stress
ν	Poisson's ratio

Abbreviations & Acronyms

Al	Aluminum
AOA	Angle Of Attack
APCVD	Atmospheric-Pressure Chemical Vapor Deposition
Au	Gold
BrF_3	Bromine Trifluoride
Cr	Chrome
Cr/Au/Cr	Chrome/Gold/Chrome
CMOS	Complimentary Metal-Oxide Semiconductor
CVD	Chemical Vapor Deposition
DARPA	Defense Advanced Research Projects Agency
DC	Direct Current
DI H_20	De-ionized Water
DLP	Digital Light Processing
DMD	Digital Micromirror Device
DOD	Department of Defense
DRIE	Deep Reactive Ion Etching
EDM	Electric Discharge Machining
EDP	Ethylene Eiamine, Pyrocatechol, and Water
EPAM	Electrostrictive Polymer Actuated Muscle
F	Farad
$FeCl_3$	Ferric Chloride

GaAs	Gallium Arsenide
Ge	Germanium
GPS	Global Positioning System
GTRI	Georgia Tech Research Institute
HF	Hydrofluoric Acid
HMDS	Hexamethyldisilazane
HNA	Hydrofluoric Acid, Nitric Acid, Acetic Acid
Hz	Hertz
IC	Integrated Circuit
IPA	Isopropanol Alcohol
KfK	Kernforschungszentrum Karlsruhe
KOH	Potassium Hydroxide
LACE	Laser-Assisted Chemical Etching
LIGA	Lithographie, Galvanoformung, Abformung (Lithography, Electrodeposition, Molding)
LPCVD	Low-Pressure Chemical Vapor Deposition
LTO	Low-Temperature Oxidation
MAV	Micro-Air-Vehicle
MBE	Molecular Beam Epitaxy
MEMS	Micro-Electro-Mechanical Systems
MFI	Micromechanical Flying Insect
MST	Micro System Technology
MUMPS	Multiuser MEMS Processes

NH_4OH	Ammonium Hydroxide
NiMH	Nickel Metal-Hydride
OTS	Octadecyltrichlorosilane
PCB	Printed Circuit Board
PECVD	Plasma-Enhanced Chemical Vapor Deposition
PLiON	Plastic Lithium-Ion
PMMA	Polymethyl Methacrylate
PR	Photoresist
PSG	Phospho-Silicate Glass
R&D	Research & Development
RCM	Reciprocating Chemical Muscle
Re	Reynolds Number
RFM	Radio Frequency Monolithics
RIE	Reactive Ion Etching
RPL	Rapid Prototyping Laboratory
SAM	Self-Assembled Monolayers
Si	Silicon
SiC	Silicon Carbide
Si_3N_4	Silicon Nitride
SiO_2	Silicon Dioxide
SMA	Shape-Memory-Alloy
SNF	Stanford Nano-Fabrication Facility
T	Torr

UAV	Unmanned-Air-Vehicle
UTIAS	University of Toronto Institute of Aerospace Studies
UV	Ultraviolet
VLSI	Very-Large-Scale Integration
XeF_2	Xenon Difluoride

Chapter 1

Introduction to MEMS

1.1 Background

Over the past century, the semiconductor technology that ultimately led to the integrated circuit (IC) has vastly revolutionized the world and changed the way we live and communicate across the globe. It can be traced back to the beginning of the 20th century when radio waves were detected using a silicon diode in 1906 [1]. During the World War II, the study of silicon (Si) and germanium (Ge) as the materials for detector diodes was emphasized and several commercial sources of high-purity Si and Ge were developed [2]. It was not until December of 1947 when the first transistor from Bell Labs was unveiled and this work resulted its inventors, William Shockley, John Bardeen, and Walter Brattain, the Nobel Prize for Physics in 1956.

It was in the late 1950s when the first working IC device was reported. Jack Kilby from Texas Instruments filed a patent application in early 1959 describing the

concept that allowed the circuit miniaturization using only semiconductor materials for all circuit components and a limited number of processing steps for the production [3]. A few months later, Robert Noyce of Fairchild Semiconductor also filed a separate patent on an IC using planar technology and adherent leads [4]. While most of the early IC works were all about bipolar transistors, it was not until 1962 when metal-oxide-semiconductor field-effect transistor (MOSFET) IC of 16 silicon n-channel transistors were constructed [5]. Since then, the race of miniaturization and integration was on. It has immensely impacted and revolutionized the electronics industry. Within the period of fifty years from the first IC device to today's very large scale integration (VLSI) technology, the microelectronics industry has increased the number of transistors fabricated on a single piece of semiconductor crystal by a factor of 100 million.

The growth of the IC complexity has followed Gordon Moore's observation, now known as "Moore's Law" [6-8]. In 1965, Moore was preparing a speech and as he started to graph data about the growth in memory chip performance, he realized there was a striking trend. When each new chip was released within 18-24 months of the previous chip, it contained roughly twice as much capacity as its predecessor. If this trend continued, computing power would rise exponentially over relatively brief periods of time. Moore's Law describes a trend that has continued and is still remarkably accurate in today's world as illustrated in Figure 1-1. It is the basis for many planners' performance forecasts. In 26 years the number of transistors on a chip has increased several thousand times, from 2,300 on the 4004 in 1971 to 7.5 million on the Pentium II, to 28 million on the Pentium III, and to 42 million on the Pentium 4 processor.

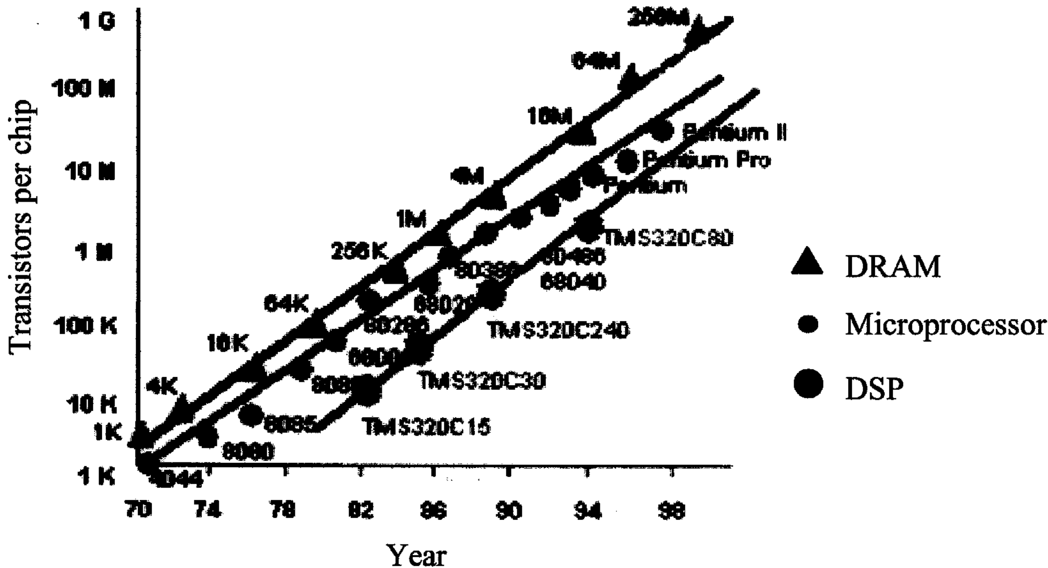

Figure 1-1: Trend of IC complexity over time: Moore's Law [6]

1.2 Micro-Electro-Mechanical Systems (MEMS)

1.2.1 Introduction to MEMS

Besides the reduction in physical size (volume and weight), the use of miniaturization technologies has provided advantages in cost reduction due to large volume production. As the need to miniaturize the IC component increases, the use of lithography and other micro fabrication technologies to create miniaturized devices has become popular in many areas of science and engineering. Micro-electro-mechanical systems, or MEMS, are integrated micro devices or systems combining both electrical and mechanical components with characteristic sizes ranging from nanometers to millimeters or sometimes even bigger. The devices are fabricated using IC batch processing techniques, such as etching, thin-film evaporation, and LPCVD, and materials, such as silicon, polysilicon, silicon oxide, silicon nitride, aluminum, and gold.

These systems can sense, control, and actuate on the micro scale, and function individually or in arrays to generate effects on the macro scale. MEMS technology has created new devices and systems solutions in diverse application areas, including high-density data storage, telecommunications switching, displays, inertial measurements, biomedical devices and instrumentation, flight control and wireless communication.

The name of MEMS was first started to be used by the Defense Advanced Research Projects Agency (DARPA), which is a central research and development organization for the Department of Defense (DOD). DARPA manages and directs selected basic and applied research and technology for traditional military applications. Soon the name was adopted among the U.S. researchers and worldwide. Other names, such as micro system technology (MST), microtechnology, microrobots, micromachines, and micromachining, are also often mentioned in other parts of the world. In this thesis, the names "MEMS" and "micromachining" will be used and are often interchangeable.

Over the past two decades, the MEMS research has flourished in both academic and commercial worlds. Numerous micro structures and devices were developed using the MEMS technology, for example, beams, sliders, cranks, pin-joints, gears [9,10], accelerometers [11-17], thermal sensors [18-21], pressure sensors [22-27], inkjet nozzles [28-30], electrostatic actuators [31-33], and digital mirror displays [34-36].

1.2.2 MEMS Processing Overview

Miniaturization of electrical and mechanical systems has led the progress of science and technology into a new direction. Micromachined devices and systems are inherently lighter, smaller, and usually more precise than conventional machined devices.

However, the development of these devices requires appropriate fabrication technologies which enable the definition of small geometry, precise dimensional control, design flexibility, and interfacing with control electronics. In addition, these technologies should also enable repeatability, reliability, high yield, and low-cost per device. In general, IC fabrication technology, which enables the miniaturization of electronics, meets all of the above criteria, especially the low-cost per device due to batch fabrication. Therefore, it is natural that it has been the primary enabling technology for the development of MEMS technology so far. What cannot be disputed is the fact that the IC fabrication technology is a powerful tool for batch processing and miniaturization of mechanical systems of the dimension domain that is not accessible by conventional machining techniques. However, there are still many differences between MEMS and IC fabrication technologies. For example, selective etching is applied in micromachining such that 3-D mechanical structures can be formed, while in IC fabrication planar processes are preferred in order to achieve smaller feature sizes for electronic devices on a wafer [37]. Thus, full flexibility for 3-D designs cannot be achieved. Because of its possibility to create 3-D and freestanding mechanical structures, MEMS technology is useful for many applications in various industries. For instance, in automotive industry, Analog Devices' MEMS-fabricated accelerometers are used to deploy airbags [11]. For projection display and hardcopy applications, Texas Instruments' digital light processing (DLP) technology features digital micromirror device (DMD) microchip that uses MEMS-based digital light switches to precisely control a light source [34]. This complicated 3-D micromirror device is shown in Figure 1-2.

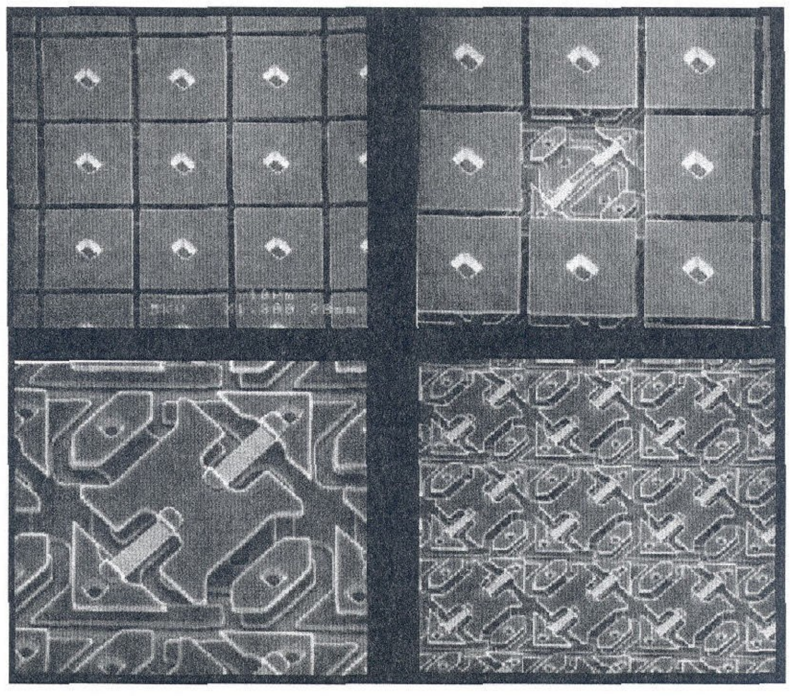

Figure 1-2: TI's MEMS-based digital micromirror device pixel array [34]

In most general form, MEMS devices would consist of the combination of mechanical microstructures, microsensors, microactuators, or integrated electronics. The MEMS technology to fabricate these structures and devices has been classified into three main categories: 1) bulk micromachining; 2) surface micromachining, and 3) LIGA technology. Each technology is briefly discussed in the following sections.

1.2.2.1 Bulk Micromachining Technology

Bulk micromachining refers to a fabrication technique to form 3-D structures by selectively etching into the substrate, removing the bulk of substrate away to leave behind desired micromechanical structures. The most common substrates are silicon. However, depending on the applications, materials such as glass, gallium arsenide (GaAs), silicon carbide (SiC), quartz, or other metals, such as copper and titanium alloy substrates, can

also be used. The fabrication technique uses wet (chemical) or dry (plasma) to etch the substrate, in combination with masking films or etching resistant layers, to form micro mechanical structures. The etching can be either isotropic (non-directional) or anisotropic (directional) depending on the mixtures and types of chemicals used as well as the crystal orientation of the substrate [38, 39].

For isotropic wet etching, HNA is often used. HNA is a combination of hydrofluoric, nitric, and acetic acids solution [40-42]. The etching rate of the silicon is independent of the crystal orientation. It is a complex etch system with highly variable etch rates. The etching characteristics depends on the silicon dopant concentration, the mix ratio of the three etch components, and even the degree of etchant agitation. The disadvantage of the HNA is that sometimes it can be difficult to mask since SiO_2 is etched for all mix ratios. Si_3N_4 or Au is desirable as masks because of longer etch times.

Recently, other new isotropic bulk micromachining techniques have been developed using gas phase dry etching. The fluorine-based interholagens in the vapor phase, such as xenon difluoride (XeF_2) [43-45] and bromine trifluoride (BrF_3) [46], can spontaneously etch silicon. The use of this type of etching in bulk micromachining has several advantages. For instance, the etching process is at room temperature and has little or no surface tension. This can prevent the damage of fragile structures during etching. Moreover, it gets rid of the stiction problem that is common in releasing structures such as beams, cantilevers, or diaphragms using wet etching. In addition, it also has high etch selectivity over most masking materials, such as silicon oxide (SiO_2) (>3000:1), silicon nitride (Si_3N_4) (>400:1), photoresist (>1000:1) and metal (Cr, Au) (>1000:1) [46]. The illustration and example of typical isotropic etchings are shown in Figure 1-3.

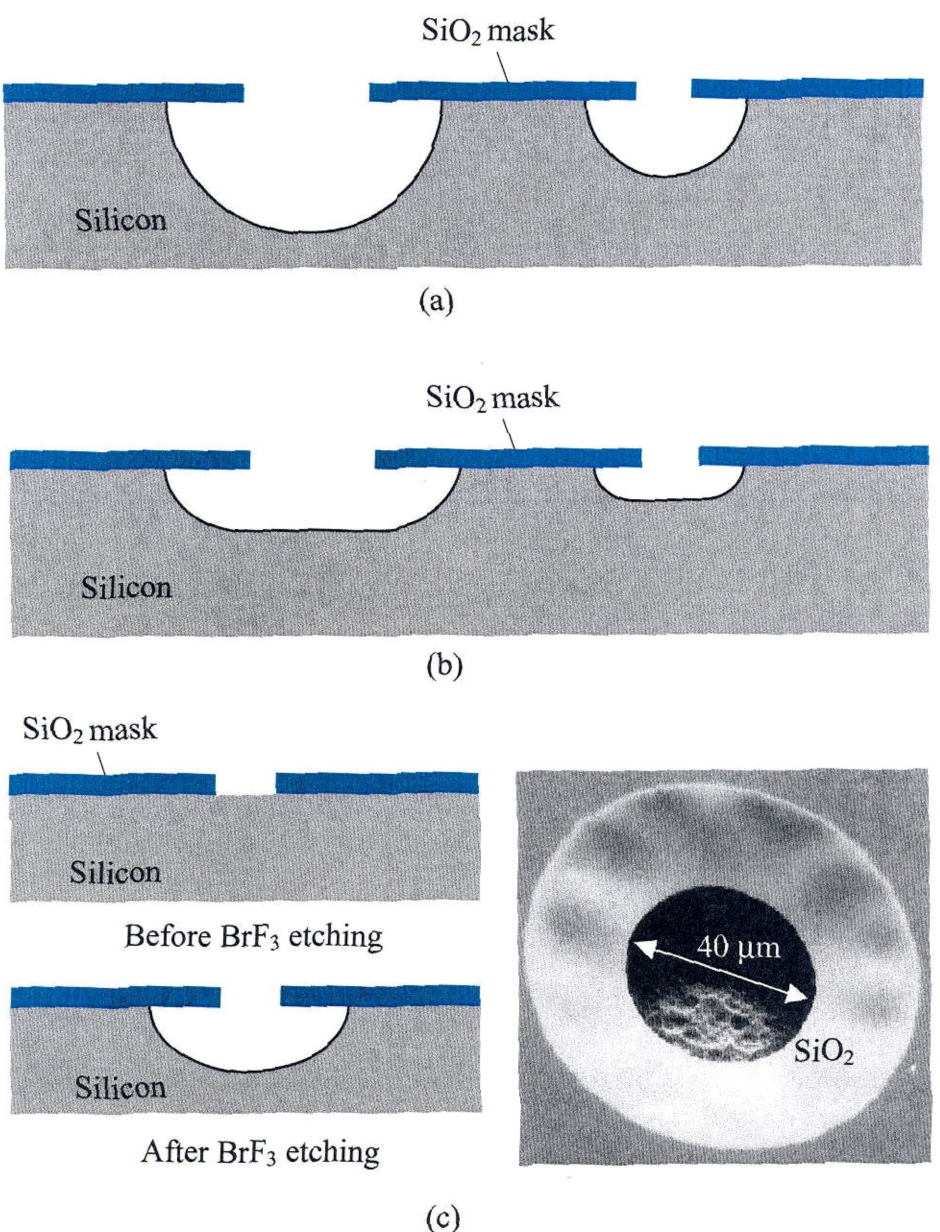

Figure 1-3: Bulk micromachining technology: Isotropic etching;

(a) Isotropic etching with agitation; (b) Isotropic etching without agitation; (c) Isotropic etching of gas phase BrF_3 bulk silicon etching [46]

For anisotropic or "orientation-dependent" etching, etching is much faster in one direction than in another. The etching rate is slowest in the <111> direction and fastest in the <100> and <110> directions. Thus the walls of <111> to <100> and <110> planes are formed at an angle of 54.74° and 90°, respectively, as illustrated in Figure 1-4. Some examples of anisotropic etchants are ethylene diamine, pyrocatechol, and water or EDP [47, 48], potassium hydroxide (KOH) [48, 49], ammonium hydroxide (NH_4OH) [50-52] and tetramethyl ammonium hydroxide or TMAH ($(CH_3)_4NOH$) [53].

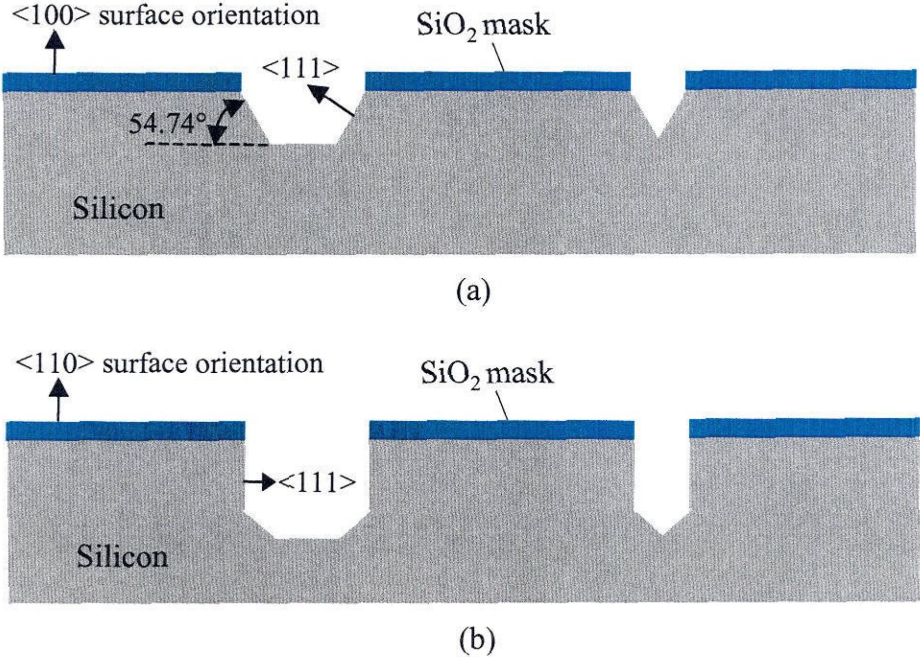

Figure 1-4: Bulk micromaching technology: Anisotropic etching;

(a) Anisotropic etching on <100> surface orientation; (b) Anisotropic etching on <110> surface orientation

EDP etchant is dopant dependent, exhibiting near zero etch-rate on silicon that has been highly doped with boron. It is also highly selective and can be masked by a variety of materials such as SiO_2, Si_3N_4, Cr, and Au. A wide range of etching rate (10 μm - 100 μm per min) can be achieved. However, EDP is very corrosive and potentially carcinogenic. Thus it is usually prohibited in most cleanrooms. NH_4OH can also be used as an anisotropic etchant for silicon etching. Nevertheless, it has not been popular due to its relatively slow etch rate, rough surface, and rapid evaporative losses of ammonia gas (noxious) when heated.

KOH and water is also orientation dependent and exhibits the highest <100>/<111> etch selectivity. For this reason, it is especially used for groove or trench etching with minimal undercut of the masks. The disadvantage of KOH is that SiO_2 is also etched. The etch-rate of SiO_2 in 58 °C KOH is about 5-600 A°/min. For structures that require long etching time, Si_3N_4 is the preferred masking materials for KOH.

TMAH solution is safer than EDP and is easy to handle. It is relatively low cost. It can be modified with additives so that it does not etch aluminum, hence compatible with IC fabrication and suitable for integrated MEMS/CMOS fabrication. The typical masking materials, i.e., SiO_2 or Si_3N_4, show excellent resistance to etching. The trade-off is that it has a smaller <100>/<111> etching ratio compared to that of KOH and has poorer boron etch-stop performance. The surface morphology tends to be rougher than that obtained with the other common etchants. For typical TMAH solutions, etching rate and surface roughness decrease as the concentration increases. Tabata, *et al.* [53] finds that at 5 wt %, the etched surface is quite rough due to longer H_2 bubble residence time. The surface becomes smooth at approximately 20 wt%.

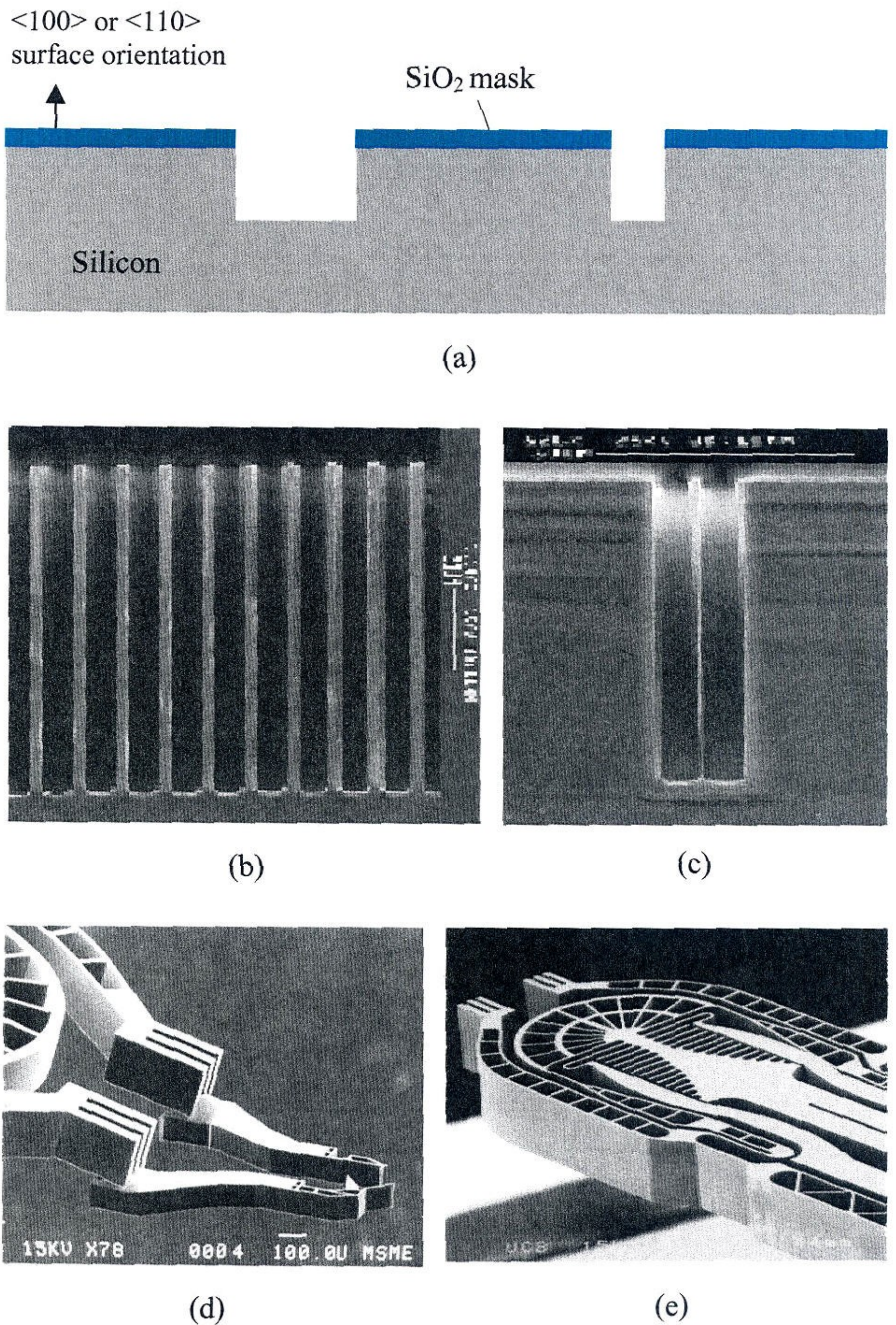

Figure 1-5: Bulk micromachining technology: Anisotropic etching;

(a) Deep reactive ion etching (DRIE); (b) Silicon trenches 80 μm deep, 2 μm linewidth, aspect ratio 40:1 [56]; (c) Twin trench in silicon with 5 μm openings [56]; (d) MEMSPI's microtweezer's tip [57]; (e) MEMSPI's microtweezer's body [57]

Another popular gas-phase technology for anisotropic etching is deep reactive-ion etching or DRIE [54-57]. DRIE can create very high aspect ratio structures (>20:1) into the silicon substrate with straight sidewall angle and arbitrary shapes based on various mask designs. DRIE etch-rate of silicon is in the order of 1 μm/min and it has an excellent selectivity to masking materials. For example, the selectivity over photoresist and SiO_2 can be greater than 50:1 and 100:1, respectively. The precise etch-depth can also be achieved by using the buried SiO_2 as an etch-stop layer. Some examples of cross-sectional profiles of micro structures fabricated by DRIE are shown in Figure 1-5.

1.2.2.2 Surface Micromachining Technology

Surface micromachining techniques use different layers of thin film materials deposited sequentially to build up the structures on the surface of a substrate. The substrate only provides a mechanical support and typically does not participate in the processing. Substrates can be silicon, quartz, glass, alumina, or even metal such as copper or titanium-alloy.

In general, surface micromachining uses films of two different materials: structural and sacrificial materials. The structural materials can be polysilicon, SiO_2, Si_3N_4, different types of polymers (parylene, PMMA, and Teflon) or even metals. The sacrificial layers can be polysilicon, phosphosilicate glass (PSG), SiO_2, polymers (photoresist and polyimide) or metals. The structural layers are patterned and etched into desirable forms. Then the sacrificial materials are etched away by wet or dry etching to release the desirable structures. With many different layers deposited on top of each other, interesting and complicated devices can be fabricated. It also adds more difficulty

and time into the fabrication process. The basic concept of surface micromachining is shown in Figure 1-6.

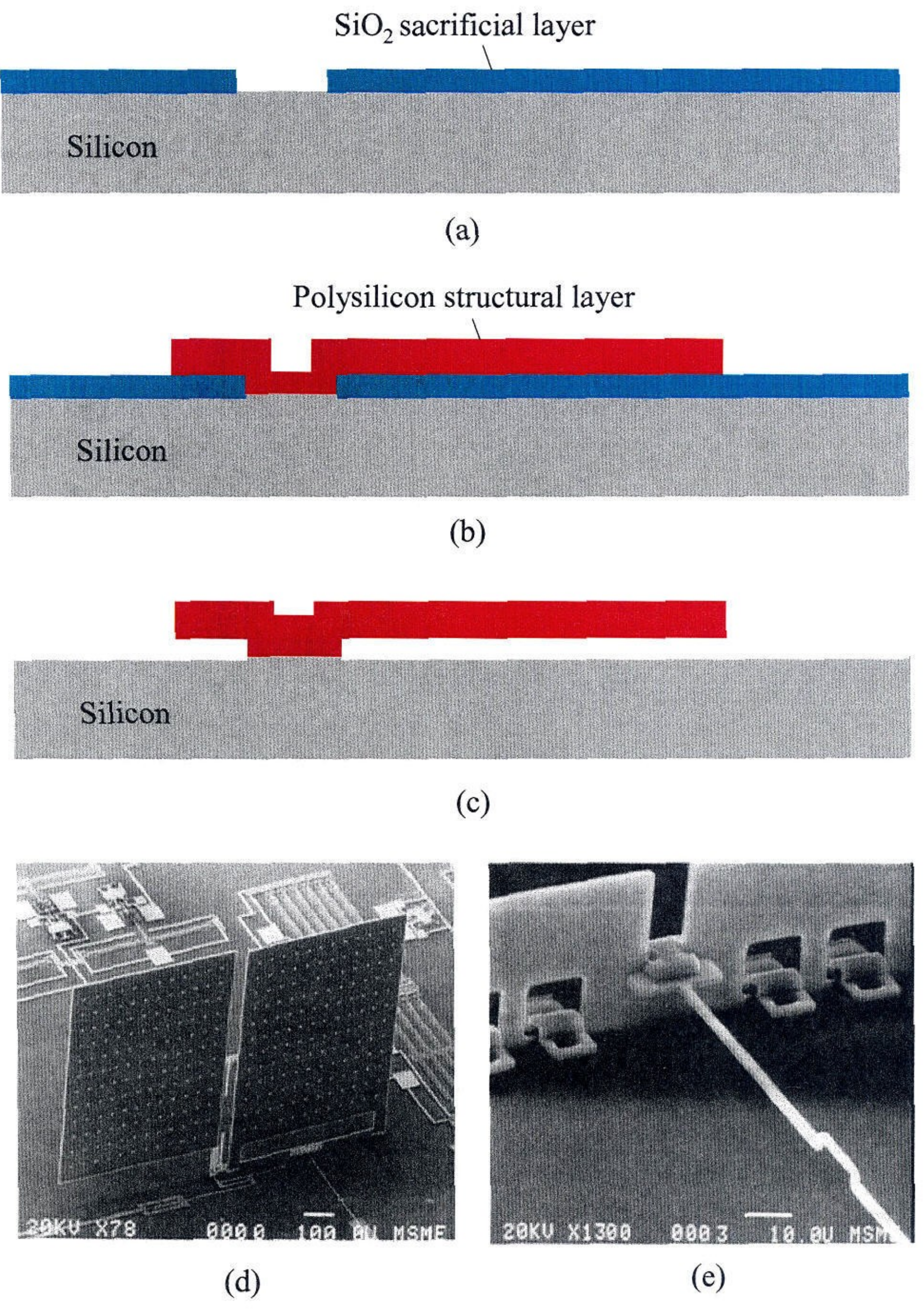

Figure 1-6: Surface micromachining technology: (a) Deposition and patterning of SiO_2 sacrificial layer; (b) Deposition and patterning of polysilicon structural layer; (c) Sacrificial layer releasing; (d)-(e) Examples of surface micromachining devices [58]

1.2.2.3 LIGA Fabrication Process Technology

LIGA combines the molding method with X-ray lithography and electroplating. It is the German acronym for X-ray lithography, electroplating and molding. It stands for Lithographie, Galvanoformung, Abformung (Lithography, Electrodeposition, Molding.) The combination usage of electroplating and X-ray lithography was first carried out at IBM in 1975 by Romankiw, *et al.* [59]. The high-aspect-ratio metal structures were made by electroplating gold in X-ray-defined resist patterns of height up to 20-μm thick. This work was first done without the abformtech (molding). The addition of molding to the lithography and electroplating process was developed by W. Ehrfeld, *et al.* [60-63] at the Karlsruhe Nuclear Research Center (Kernforschungszentrum Karlsruhe, or KfK) in Karlsruhe, Germany. The process is capable of yielding an extremely high aspect-ratio structure (at least 100:1) [64]. It involves a thick layer of X-ray resist, high-energy X-ray radiation exposure, and development to create a 3-D resist structure. Then the desired metal is filled into the resist mold by means of electroplating. After the removal of the resist, a free standing 3-D metal structure results. The metal shape may be a final product or serves as a mold insert for precision plastic injection molding. This fabrication process is shown in Figure 1-7.

The LIGA process serves as a "handshake-technology" between IC and classical manufacturing technologies. It borrows the lithography technology from the IC industry and electroplating and molding from the classical manufacturing industry. Although many interesting MEMS devices can be made through LIGA process, the cost of LIGA process is very expensive due to the need to access to a synchrotron source for high-energy X-ray radiation. The high construction cost for a typical synchrotron can be

several million dollars. These resources are very limited in the MEMS industry. Thus the LIGA process remains unpopular among many MEMS researchers.

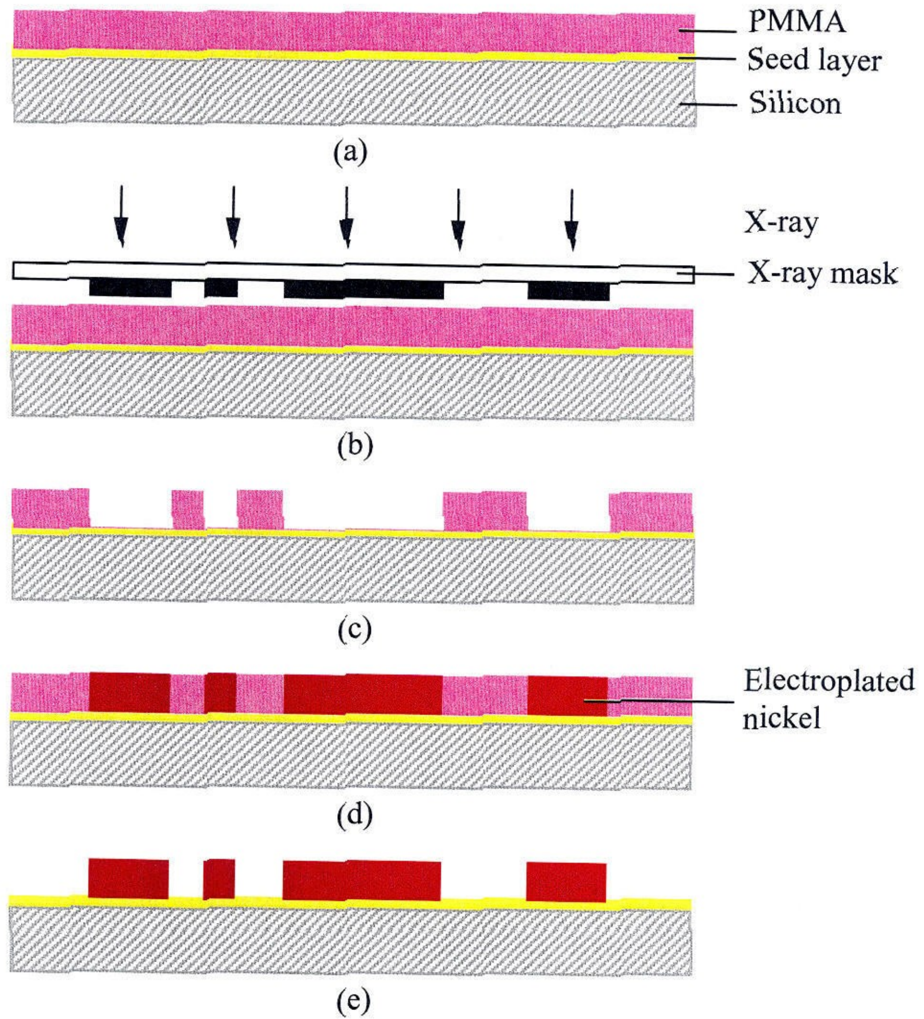

Figure 1-7: LIGA fabrication process: (a) Deposition of metal seed layer and spin-on PMMA; (b) Exposure to X-ray; (c) Development of PMMA; (d) Electrodeposition of nickel; (e) PMMA etch to release nickel

Table 1-1 shows the technological capability comparison among three MEMS technologies: bulk micromachining, surface micromachining and LIGA technologies. Table 1-2 includes a compilation of various process types used in MEMS fabrication steps that include photolithography, bulk and surface micromachinings, bonding, and LIGA process [65, 66].

Table 1-1: MEMS technology comparison [64]

Capability	**Bulk (Wet)**	**Surface**	**LIGA**
Maximum structural thickness	Wafer thickness	< 50 μm	500 μm
Planar geometry	Rectangular	Unrestricted	Unrestricted
Minimum planar feature size	√2 x depth	1 μm	3 μm
Side wall features	54.74° slope (100) 90° slope (110)	Limited by dry etch	0.2 μm runout over 400 μm
Surface and edge definitions	Excellent	Mostly adequate	Very good
Material properties	Very well controlled	Mostly adequate	Well controlled
Integration with electronics	Demonstrated	Demonstrated	Difficult
Capital investment & costs	Low	Moderate	High
Published knowledge	Very high	High	Moderate

Table 1-2: MEMS fabrication processes

Process Type	Examples
Annealing	Thermal annealing, laser annealing
Bonding	Eutectic bonding, anodic bonding, silicon fusion bonding, low temperature glass bonding, polyimide bonding, non-uniform press bonding, thermocompression metallic bonding, electrostatic bonding, epoxy bonding, adhesives, etc.
Doping	Diffusion (predeposition and drive on), ion implantation
Lithography	Photolithography, X-ray lithography, electron-beam lithography, screen printing
Thin-film deposition	Atmospheric-pressure chemical vapor deposition (APCVD), Plasma-enhanced chemical vapor deposition (PECVD), Low-pressure chemical vapor deposition (LPCVD), molecular beam epitaxy (MBE), thermal evaporation, sputtering, spin-on coating, plasma spraying, laser sputtering deposition, etc.
Directed deposition	Electroplating, stereolithography, laser-driven chemical vapor deposition, screen printing, transfer printing
Thin-film growth	Thermal oxidation, low-temperature oxidation (LTO)
Electroplating	Nickel electroplating, gold electroplating, copper electroplating
Etching	Wet chemical etching (isotropic and anisotropic), plasma etching,

	Reactive ion etching (RIE), Deep reactive ion etching (DRIE), physical sputtering, Xenon difluoride (XeF_2) dry etching, Bromine trifluoride (BrF_3) dry etching, electrochemical etching, etc.
Direct etching	Laser-assisted chemical etching (LACE)
Machining	Drilling, milling, electric discharge machining (EDM), diamond turning, sawing, etc.
Surface modification	Wet chemical modification, plasma modification, self-assembled monolayers (SAM)
Welding	Ultrasonic welding, seam welding, laser welding

1.3 Overview of Thesis Dissertation

This thesis dissertation presents the design, fabrication, and testing of parylene MEMS technology for micro adaptive flow control of flapping-wing flight applications. It is especially focused on the design and fabrication of titanium-alloy MEMS wings and the first flexible parylene MEMS actuator skins. The thesis is organized as follows:

Chapter 1 gives a background review of the IC technology that eventually leads to the branch of MEMS technology. Bulk micromachining, surface micromachining, and LIGA process are described.

Chapter 2 covers more in depth study of the novel design and fabrication of titanium-alloy wingspars and parylene wing membrane. It describes various designs of MEMS wings from bat-like wings to the current design wings CIT7x3. The properties of

titanium-alloy and parylene materials are also shown. Moreover, the discussions in this chapter include titanium-alloy, parylene, and new dry-film photoresist technologies. Challenges in fabrication of MEMS wings are also presented.

Chapter 3 shows the mechanical and aerodynamic test results of fabricated wings in the wind tunnel. The test results are interpreted and analyzed in this chapter. The aerodynamics of flapping-wing flight is presented. It also discusses the importance of the leading-edge stiffness and the inboard region in flapping-wing flight.

Chapter 4 shifts the focus to the low-temperature MEMS technology developed to fabricate parylene actuator diaphragm on a silicon chip. The actuator design, fabrication process, and challenges are presented. The anti-stiction technologies are also introduced in this chapter. These include the use of anti-stiction posts, BrF_3 gas-phase dry release, and self-assembled monolayers (SAM). Finally, the load deflection test results and the rectangular membrane model are studied.

Chapter 5 reviews the MEMS transducer devices in fluidic and aerodynamic applications starting from the late 1980s when a simple polysilicon bridge used to study the air flow [67] to the late 1990s when micro bubble actuators are used for aerodynamic control of a fighter jet [68]. This chapter also introduces the foundation of this thesis to use the novel parylene MEMS technology to fabricate actuator "skins" for adaptive flow control in flapping flight. It introduces the design and fabrication of parylene MEMS actuator "skins." This is where the concept of a single parylene actuator diaphragm discussed in chapter 4 is transformed from a silicon chip to a large area wafer-size skin with thousands of integrated actuators. These skins are later integrated onto the MEMS wings. The designs and fabrication of both plate- and check-valve-types are presented.

The challenges, such as wrinkle and cracking of thin films, and remedies are included in the discussion. Finally, the electrostatic actuation tests and wind-tunnel test results are analyzed and discussed in detail.

Chapter 6 concludes overall progress starting from creating the titanium-alloy wings to integration of parylene MEMS actuator skins onto the MEMS wings. The chapter summarizes the parylene actuator skin technologies developed in this thesis dissertation. The conclusion of the test results is discussed and future work is suggested.

Appendix A reviews the history and development of biomimetic flights. Various MAV programs are presented, especially the Caltech-led "Microbat" project.

Appendix B shows complete and detailed fabrication processing steps of titanium-alloy wing, parylene actuator diaphragm, and flexible parylene MEMS actuator skins. These steps, if followed closely, should enable the duplication of desired devices. They are merely a guide to successful fabrications of the devices tested in this thesis. Further improvement on the design and process step is encouraged to achieve a better device with superior performance.

1.4 Bibliography

[1] G. W. Pickard, "Thermo-Electric Wave Detectors," *Electrical World 4*, p. 1003, November 24, 1906.

[2] W. R. Runyan and K.E. Bean, *Semiconductor Integrated Processing Technology*, p. 1, Addison-Wesley Publishing Company, 1994.

[3] J. S. Kilby, "Miniaturized Electronic Circuits," *U.S. Patent 3,138,743*, June 23, 1964 (filed February 6, 1959).

[4] R. N. Noyce, "Semiconductor Device-and-Lead Structure," *U.S. Patent 2,918,877*, April 25, 1961 (filed July 30, 1959).

[5] S. R. Hofstein and F. P. Heiman, "The Silicon Insulated-Gate Field-Effect Transistor," *Proc. IEEE 51*, pp. 1190-1202, 1963.

[6] J. T. Clemens, "Silicon Microelectronics Technology," *Bell Labs Technical Journal*, Lucent Technologies, Inc., pp. 66-102, Autumn 1997.

[7] G. E. Moore, "Progress in Digital Integrated Electronics," *Tech. Digest of the 1975 International Electron Devices Meeting*, IEEE, Washington, D.C., pp. 1-13, Dec. 1-3, 1975.

[8] G. E. Moore, "VLSI: Some Fundamental Challenges," *IEEE Spectrum*, vol. 16, no. 4, pp. 30-37, Apr. 1979.

[9] L. S. Fan, Y. C. Tai, and R. S. Muller, "Integrated Movable Micromechanical Structures for Sensors and Actuators," *IEEE Transactions on Electron Devices*, vol. ED-35 (6), pp. 724-730, June 1988.

[10] M. Mehregany, K. J. Gabriel, and W. S. N. Trimmer, "Integrated Fabrication of Polysilicon Mechanisms," *IEEE Transactions on Electron Devices*, vol. ED-35 (6), pp. 719-723, June 1988.

[11] Analog Devices, Inc., http://www.analog.com.

[12] L. M. Roylance and J. B. Angell, "A batch-fabricated silicon accelerometer," *IEEE Trans. Electron Devices*, vol. ED-26, pp.1911-1917, 1979.

[13] W. D. Frobenius, S. A. Zeitman, M. H. White, D. D. O. Sullivan, and R. G. Hamel, "Microminiature gauged threshold accelerometer compatible with integrated circuit technology," *IEEE Trans. Electron Devices*, vol. ED-19, pp. 37, 1972.

[14] P. Chen, R. S. Muller, T. Shiosaki, and R. M. White, "Silicon cantilever beam accelerometer utilizing a PI-FET capacitive transducer," *IEEE Trans. Electron Devices*, vol. ED-26, pp.1857, 1979.

[15] K. E. Petersen, A. Shartel, and N. Ralay, "Micromachenical accelerometer integrated MOS detection circuitry," *IEEE Trans. Electron Devices*, vol. ED-29, pp. 23, Jan. 1982.

[16] M. Brandl and V. Kempe, "High Performance Accelerometer Based on CMOS Technologies with Low Cost Add-Ons," *Tech. Digest, The 14th IEEE Int. Conf. on Micro Electro Mechanical Systems (MEMS'01)*, Interlaken, Switzerland, pp. 6-9, Jan. 21-25, 2001.

[17] A. Partridge, A. E. Rice, and T. W. Kenny, "New Thin Film Epitaxial Polysilicon Encapsulation for Piezoresistive Accelerometers," *Tech Digest, The 14th IEEE Int. Conf. on Micro Electro Mechanical Systems (MEMS'01)*, Interlaken, Switzerland, pp. 54-58, Jan. 21-25, 2001.

[18] C. C. Williams and H. K. Wickramasinghe, "High Resolution Thermal Microscopy," *Proc. IEEE Ultrasonics Symposium*, Williamsburg, VA, vol. 1, pp. 393-397, Nov. 1986.

[19] A. W. Van Herwaarden and P. M. Sarro, "Thermal Sensors Based on the Seebeck Effect," *Sensor and Actuator*, vol. 10, pp. 321-346, 1986.

[20] Y.-C. Tai and R. S. Muller, "Lightly Doped Polysilicon Bridge as an Anemometer," *Tech. Digest, The 4th Int. Conf. On Solid-state Sensors and Actuators (Transducers '87)*, Tokyo, Japan, pp. 360-363, 1987.

[21] I. H. Choi and K. D. Wise, "A Silicon-Thermopile-Based Infrared Sensing Array for Use in Automated Manufacturing," *IEEE Trans. Electron Devices*, vol. ED-33, No.1, pp. 72-79, Jan. 1986.

[22] Lucas NovaSensor®, http://www.novasensor.com.

[23] Samaun, K. D. Wise, and J. B. Angell, "An IC Piezoresistive Pressure Sensor for Biomedical Instrumentation," *IEEE Trans. Biomed. Eng.*, vol. BME-20, pp. 101, 1973.

[24] A. C. M. Gieles and G. H. J. Somers, "Miniature Pressure Transducer with Silicon Diaphragm," *Phillips Tech. Rev.*, vol. 33, pp. 14, 1973.

[25] W. K. Ko, J. Hynecek, and S. F. Boettcher, "Development of a Miniature Pressure Transducer for Biomedical Applications," *IEEE Trans. Electron Devices*, vol. ED-26, pp.1896, 1979.

[26] H. Guckel and D. W. Burns, "Planner Processed Polysilicon Sealed Cavities for Pressure Transducer Arrays," *Tech. Digest, IEEE int. Electron Devices Meeting*, San Francisco, CA, pp. 223-225, Dec. 1984.

[27] P. Melvas, E. Kalvesten, and G. Stemme, "A Surface Micromachined Resonant Beam Pressure Sensor," *Tech Digest, The 14th IEEE Int. Conf. on Micro Electro Mechanical Systems (MEMS'01)*, Interlaken, Switzerland, pp. 38-41, Jan. 21-25, 2001.

[28] E. Bassous, H.H. Taub, and L. Kuhn, "Ink Jet Printing Nozzle Arrays Etched in Silicon," *Appl. Phys. Lett.*, vol. 31, pp.135-137, 1977.

[29] K. E. Petersen, "Fabrication of an Integrated Planar Silicon Ink-Jet Structure," *IEEE Trans. Electron Devices*, vol. ED-26, pp. 135-137, 1979.

[30] S.-W. Lee, H.-C. Kim, K. Kuk, and Y.-S, Oh, "A Monolithic Inkjet Print Heard: DomeJet," *Tech Digest, The 14th IEEE Int. Conf. on Micro Electro Mechanical Systems (MEMS'01)*, Interlaken, Switzerland, pp. 515-518, Jan. 21-25, 2001.

[31] L. S. Fan, Y. -C. Tai, and R. S. Muller, "IC-Processed Electrostatic Micromotor," *Tech.l Digest, IEDM*, pp. 666-669, 1988.

[32] W. C. Tang, T. C. H. Nguyen, and R. T. Howe, "Laterally Driven for Polysilicon Resonate Microstructures," *Sensor and Actuators*, vol. 20, pp. 25-32, 1989.

[33] M. Gel and I. Shimoyama, "High Aspect Ratio Micro Actuation Mechanism," *Tech Digest, The 14th IEEE Int. Conf. on Micro Electro Mechanical Systems (MEMS'01)*, Interlaken, Switzerland, pp. 582-585, Jan. 21-25, 2001.

[34] Texas Instruments, Inc., http://www.dlp.com/dlp

[35] M. A. Michalicek and V. Bright, "Flip-Chip of Advanced Micromirror Arrays," *Tech Digest, The 14th IEEE Int. Conf. on Micro Electro Mechanical Systems (MEMS'01)*, Interlaken, Switzerland, pp. 313-316, Jan. 21-25, 2001.

[36] H. Schenk, P. Dürr, D. Kunze, H. Laker, and H. Kück, "An Electrostatically Excited 2D-Micro-Sacnning-Mirror with an In-Plane Configuration of the Driving Electrodes," *Proc., The 13th IEEE Int. Conf. on Micro Electro Mechanical Systems (MEMS'00)*, Miyazaki, Japan, pp. 473-478, Jan. 23-27, 2000.

[37] S. Wu, *Integrated Polysilicon Thermistors for Microfluidic Sensing,* Ph.D. Thesis, California Institute of Technology, 2000.

[38] K. E. Petersen, "Silicon as a Mechanical Material," *Proceedings of the IEEE*, vol. 70, no. 5, pp. 420-457, May, 1982.

[39] G. T. A. Kovacs, N. I. Maluf, and K. E. Petersen, "Bulk Micromachining of Silicon," *Proc. of the IEEE* 86: (8) 1536-1551, Aug. 1998.

[40] H. Robbins and B. Schwartz, "Chemical Etching of Silicon, II. The System HF, HNO_3, H_2O and $HC_2H_3O_2$," *Journal of Electrochemical Society*, vol. 107, pp. 108-111, 1960.

[41] B. Schwartz and H. Robbins, "Chemical Etching of Silicon, VI. Etching Technology," *Journal of Electrochemical Society*, vol. 123, pp. 1903, 1976.

[42] K. R. Williams and R. S. Muller, "Etch Rate for Micromachining Process," *J. Microelectromech. Syst.*, vol. 5, no. 4, pp. 256-269, Dec. 1996.

[43] H. F. Winters and J. W. Coburn, "The etching of silicon with XeF_2 vapor," *Appl. Phys. Lett.*, vol. 34, no. 1, pp. 70-73, January 1979.

[44] P. B. Chu, J. T. Chen, R. Yeh, G. Lin, J. C. P. Huang, B. A. Warneke, and K. S. J. Pister, "Controlled Pulsed Etching with Xenon Difluoride," *Technical Digest,*

International Conference on Solid-State Sensors and Actuators (Transducers '97), vol. 1, pp. 665-668, Chicago, USA, June 1997.

[45] D. E. Lbbotson, J. A. Mucha, and D. L. Flamm, "Plasmaless Dry Etching of Silicon with Fluorine-Containing Compounds," *J. Appl. Phys.* vol 56, no. 10, pp. 2939-2942, Nov. 1984.

[46] X. Q. Wang, X. Yang, K. Walsh, and Y. -C. Tai, "Gas Phase Silicon Etching with Bromine Trifluoride," *Technical Digest, International Conference on Solid-State Sensors and Actuators (Transducers '97)*, vol. 2, pp. 1046-1415, Chicago, USA, June 1997.

[47] A. Reisman, M. Berkenblit, S. A. Chan, F. B. Kaufman, and D. C. Green, "The Controlled Etching of Silicon in Catalyzed Ethylenediamine-Pyrocatechol-Water Solutions," *Journal of Electrochemical Society*, Vol. 126 (8), pp. 1406-1415, 1979.

[48] H. Seidel, "The Mechanism of Anisotropic Silicon Etching and its Relevance for Micromachining," *Technical Digest, International Conference on Solid-State Sensors and Actuators (Transducers '87)*, pp. 120-125, Tokyo, Japan, June 1987.

[49] D. L. Kendall and G. R. de Guel, "Orientations of the Third Kind: the Coming of Age of (110) Silicon," *Micromachining and Micropackaging of Transducer*s, Elsevier Science Publishers B. V., Amsterdam, pp. 113-130, 1985.

[50] W. Kern, "Chemical Etching of Silicon, Germanium, Gallium Arsenide and Gallium Phosphide," *RCA Review*, vol. 39, pp. 278-308, June 1978.

[51] U. Schnakenberg, W. Benecke, and B. Lochel, "NH_4OH-Based Etchants for Silicon Micromachining," *Sensors and Actuators*, vol. A23, nos. 1-3, pp. 1031-1035, Apr. 1990.

[52] U. Schnakenberg, W. Benecke, B. Lochel, S. Ullerich, and P. Lange, "NH_4OH-Based Etchants for Silicon Micromachining: Influence of Additives and Stability of Passivation Layers," *Sensors and Actuators*, vol. A25, nos. 1-3, pp. 1-7, Oct. 1990 – Jan. 1991.

[53] O. Tabata, R. Asahi, H. Funabashi, K. Shimaoka, and S. Sugiyama, "Anisotropic Etching of Silicon in TMAH Solutions," *Sensors and Actuators (A: Physical)*, vol. 34, pp. 51-57, 1992.

[54] E. H. Klassen, K. Petersen, J. M. Noworolski, J. Logan, N. I. Maluf, J. Brown, C. Storment, W. McCulley, and G. T. A. Kovacs, "Silicon Fusion Bonding and Deep Reactive Ion Etching; A New Technology for Microstructures," *Digest of Tech. Papers, The 8th International Conference on Solid-State Sensors and Actuators (Transducers'95, Eurosensors IX)*, vol. 1, pp. 556-559, Stockholm, Sweden, June 25-29, 1995.

[55] J. Bhardwaj, H. Ashraf, and A. McQuarrie, "Dry Silicon Etching for MEMS," *Proc. Of the 191st Meeting of the Electrochemical Society, Mcirostructures and Microfabricated Systems III Symposium, vol. 97-5,* pp. 118-130, Montreal, Canada, May 4-9, 1997.

[56] Surface Technology Systems, http://www.stsystems.com.

[57] MEMS Precision Instruments, Inc., http://www.memspi.com

[58] M. Last, and K. Pister, "2DOF Actuated Micromirror Designed for Large DC Deflection," *Proc. of IEEE 3rd Intl. Conference on Micro Opto Electro Mechanical Systems (MOEMS '99)*, Mainz, Germany, Aug. 30 – Sept. 1, 1999.

[59] E. Spiller, R. Feder, J. Topalian, E. Castellani, L. Romankiw, and M. Heritage, "X-Ray Lithography for Bubble Devices," *Solod State Technol.*, pp. 62-68, Apr. 1976.

[60] E. W. Becker, W. Ehrfeld, D. Münchmeyer, H. Betz, A. Heuberger, S. Pongratz, W. Glashauser, H.J. Michel, and V. R. Siemens, "Production of Separation Nozzle Systems for Uranium Enrichement by a Combination of X-Ray Lithography and Galvanoplastics," *Naturwissenschaften*, vol. 69, pp. 520-523, 1982.

[61] E. W. Becker, W. Ehrfeld, P. Hagmann, A. Maner, and D. Münchmeyer, "Fabrication of Microstructures with High Aspect Ratios and Great Structural Heights by Synchrotron Radiation Lithography, Galvanoforming, and Plastic Moulding (LIGA Process)," *Microelectronic Engineering*, vol. 4, no. 1, pp. 35-36, May 1986.

[62] W. Ehrfeld, B. Bley, F. Götz, P. Hagmann, A. Maner, J. Mohr, H. O. Moser, D. Münchmeyer, W. Schelb, D. Schmidt, and E. W. Becker, "Fabrication of Microstructures using the LIGA Process," *1987 IEEE Micro Robots and Teleoperators Workshop*, Hyannis, MA, pp. 11/1-11/11, Nov. 9-11, 1987.

[63] W. Ehrfeld, B. Bley, F. Götz, D. Münchmeyer, W. Schelb, and D. Schmidt, "LIGA Process: Sensor Construction Techniques via X-Ray Lithography," *Tech. Digest, IEEE Solid-State Sensor and Actuators Workshop*, Hilton Head Island, SC, pp. 1-4, June 6-9, 1988.

[64] Y.-C. Tai, and W. C. Tang, "Overview and Practical Issues in MEMS Technologies," *MEMS Short Course Transducer '97*, Chicago, June 1997.

[65] G. T. A. Kovacs, *Micromachined Transducers Sourcebook*, p. 115, WCB/McGrall-Hill, 1998.

[66] MCNC Short Course, *Introduction to Microelectromechanical Systems and the Multiusers MEMS Processes (MUMPS),* Case Western Reserve University, Dec. 12-13, 1994.

[67] Y. -C. Tai and R. S. Muller, "Polysilicon Bridge as a Flow Meter," *Sensors and Actuators*, vol. 15, pp. 63-75, 1988.

[68] C. Grosjean and Y. -C. Tai. "Micro Balloon Actuators for Aerodynamic Control," *Proc. of the 11th Annual Intl. Workshop on Micro Electro Mechanical Systems (MEMS '98)*, pp. 166-171, Heidelberg, Germany, Jan. 25-29, 1998.

Chapter 2

MEMS Wing Technology

2.1 Introduction

Flapping flight is undoubtedly the most sophisticated realm of flights and has not been explored extensively compared to fixed-wing flight. Natural ornithopters (flapping-wing), such as birds, bats, and insects, have had millions of years to develop and adapt their wings to use in their flight controls efficiently. These wings utilize both quasi-steady- and unsteady-state aerodynamics to generate lift and thrust forces to help them fly. Duplication of such wings to achieve the same flight performance is impossible. However, we hope that we can adapt and use the existing technologies to create wings that aeroelastically can be used to study adaptive flow control of flapping flight.

Natural ornithopters have wings that are extremely lightweight, with very intricate skeletal structures, compared to their body weight. For such complicated structures, it would be possible but impractical to construct wings of this nature without MEMS

technology. It is possible that the wing design can evolve into a very sophisticated structure like that of a butterfly or dragonfly instead of the simpler structure of a bat wing. Hand or mechanical construction of such sophisticated wings becomes unrealistic and can be costly and time-consuming. Photolithographic technology is an alternative method to fabricate wings and can be much more efficient. The flexible thin films are deposited onto a substrate. Then lithographic patterning and etching back to define a skeletal structure will allow a systematic way to rapidly create prototypes of a wide variety of wing configurations. This method also allows mass-production and eventually leads to low cost batch-fabrication of an optimal wing design. The overall mass of these wings will be very small (~200 mg). It can be made lightweight by adjusting their thickness and width with existing thin film technology and optimal thinning of the skeletal structures.

This chapter discusses the fabrication of wings using MEMS technology. Based on the recent interest in micro-air-vehicle (MAV), the wings are palm-sized or smaller. The detailed fabrication process of titanium-alloy and parylene is described. Various properties of both materials as well as challenges and solutions are also presented.

2.2 Non-MEMS Wings

Given the size and weight limitation of MAV (see appendix A), it is important that every component of the overall system is light and minimal in weight, especially the wings. For non MEMS-based wings, the conventional and easiest way to construct the wings is to build the wingspars and membranes from light yet very strong materials by hands. Often, carbon fiber rods are used for skeleton structures because it is light and has

high stiffness. Thin mylar film is used as wing membrane. The first model wings are built using carbon fiber rods with 750-μm diameter as wingframes. The membrane is made from thin mylar film or thin waxed paper. The membrane is glued to the carbon rods as shown in Figure 2-1. This method of making wings can be cumbersome and tedious. There are also several disadvantages. For example, glue adds significant weight to the overall weight of the wings and they become too heavy. Furthermore, identical sets of wings are difficult to achieve unless molds are made for each fabrication. This process is costly, time-consuming, and very slow. This method cannot accommodate effectively and efficiently the study of the design's variable changes.

For many reasons we claim the new MEMS wing technology is necessary because MEMS wings enable systematic research in terms of repeatability, size control, weight minimization, mass production, and fast turn-around time. Moreover, complicated structures such as dragonfly, butterfly, and beetle wings can be easily fabricated using photolithographic technology [1].

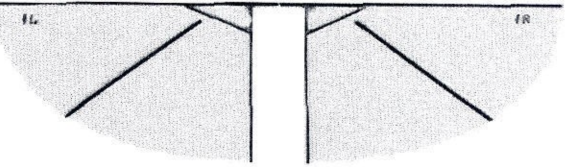

(a) Carbon fiber wings with mylar

(b) 3-D carbon fiber wings with paper

Figure 2-1: Non MEMS-based wings

2.3 MEMS Wings

2.3.1 Silicon MEMS Wings

In order to demonstrate that the proposed MEMS wings are possible, the prototype silicon MEMS-based wings are fabricated. The purpose of this prototype is to show the superiority of MEMS technology to create intricate and light structures. Initially, silicon is favorable as the frame material because it is used as a primary substrate material in the MEMS technology. Moreover, it is as strong as stainless steel and yet much lighter. Parylene technology enables the deposition of membrane material and it can be deposited at room temperature. It is extremely light and strong. A more in-depth discussion of parylene material will be presented in section 2.3.2. Furthermore, it is possible that silicon MEMS wings will allow for an integration of sensors and strain-gauges onto the wing to provide vital diagnostic information with regards to characterization and wing loading of air flow over the wings. This will allow for a methodical and directed approach to achieve an optimal wing configuration.

The first approach is to study the natural flyers and mimic their wings. The bat and dragonfly wing designs are chosen. Bat wings have simple bone structures while dragonfly wings have very complicated weblike bone structures. This is to demonstrate the capability of MEMS technology that can easily fabricate simple and complex structures. A sample of silicon MEMS wings are shown in Figure 2-2. The silicon wingframe is 50 μm thick and it is covered by 15-μm thin film parylene. The bone width of the bat wing is 350 μm wide.

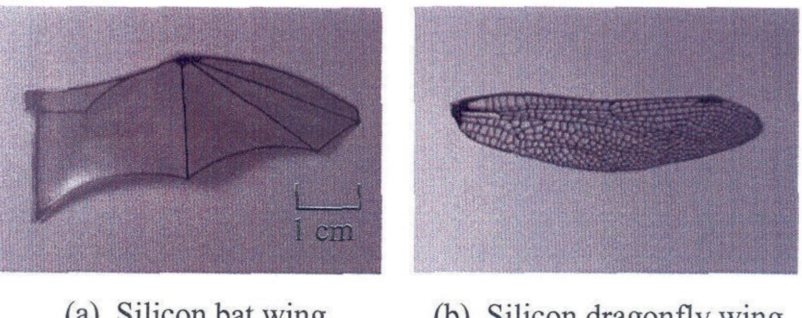

(a) Silicon bat wing (b) Silicon dragonfly wing

Figure 2-2: MEMS fabricated silicon wings [1]

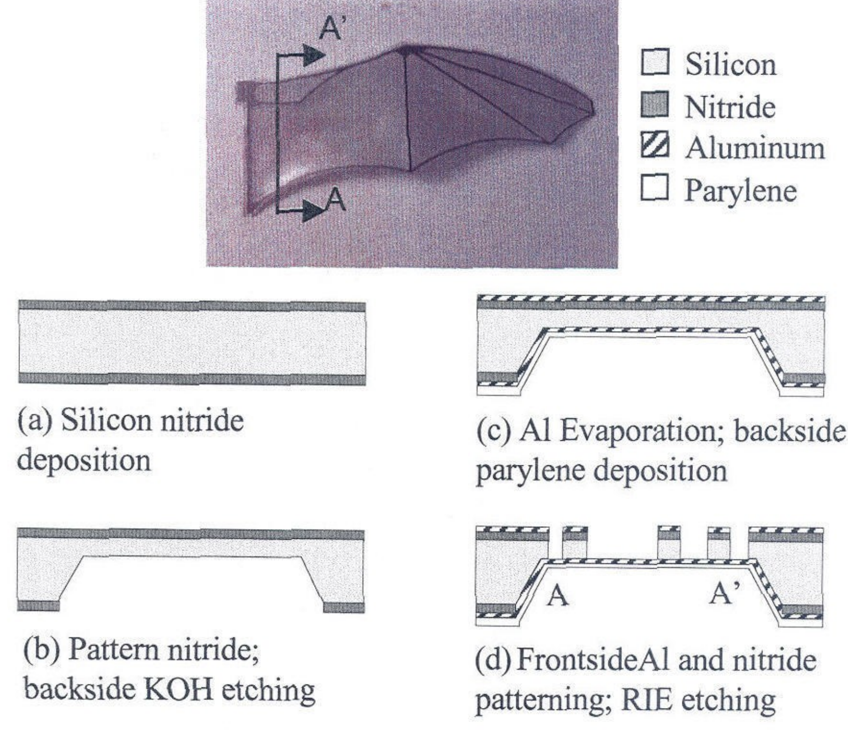

Figure 2-3: Fabrication process of silicon MEMS wings

The detailed silicon wing fabrication process is shown in Figure 2-3. First, silicon nitride thin film is deposited on both sides of a silicon wafer. It is used as a protecting mask during the KOH etching step. Next, the backside of silicon nitride is patterned and etched away. Then the silicon wafer is time-etched in KOH solution at 58 °C for

approximately 22 hours until about 50 μm of silicon diaphragm remained. Next, thin film aluminum is evaporated on both sides of the wafer and backside parylene deposition is performed. The frontside aluminum is used as a protection mask during RIE etching while the backside aluminum is used as an etch-stop to protect parylene membranes. Then, the frontside aluminum and nitride are patterned followed by an RIE etching to create wingframes. In order to strengthen the membrane further, the second parylene layer is deposited.

Silicon MEMS wings, however, are too fragile. They break too easily when simple flapping test is performed. Therefore, an entirely new process using titanium-alloy metal as wingframes is developed instead. Titanium-alloy metal is a light yet strong material. This novel process, using parylene as wing membrane, is thoroughly described in section 2.3.3.

2.3.2 Parylene

2.3.2.1 Background

In 1950's William F. Gorham developed the parylene coating process. Then in 1965, the process was commercialized by the Union Carbide Corporation which produced the dimers. Parylene coating is widely used to coat and protect electronic circuit components against corrosive gases or chemical agents in medical, electronic and automotive applications. Generally, it is pin-hole free. It has no cure catalyst residues and is therefore pure and chemically inert to most acids, alkalis, and organic solvents. These properties make this material very attractive as a passivation agent on top of devices [2].

Parylene is a thin, vacuum-deposited polymer. It differs from conventional coatings because it is deposited onto objects at room temperature as a film, and does not use solvents, catalysts, plasticizers, or other feature-enhancing additives. Parylene is the generic name for members of a unique thermoplastic polymer series [3]. It is based on a high-purity raw material called di-para-xylene, which is a white, crystalline dimer powder. A vacuum and thermal process converts the powder into a polymer film, which is formed on substrates at room temperature. It is colorless and transparent. It has low dielectric constant and high thermal stability [4].

Parylene's unique properties include precise conformity to substrate topography, pinhole-free coverage in very thin layers, and the ability to penetrate and coat complex surfaces. Parylene film resists chemical attack from organic solvents, inorganic reagents, and acids. It adheres well to many surfaces, and offers dielectric strength above 5000 V dc at 1 mil of film thickness [3]. It has a lubricious surface, with a coefficient of friction in the range of 0.25 to 0.33 (per ASTM D1894), which approaches that of PTFE (Teflon) [5]. Parylene can be coated on such diverse substrates as glass, metal, paper, resin, plastics, ceramic, ferrite, and silicon, and even on powdered and granular substances. The coating achieves conformal coverage, moisture protection, dielectric protection, and freedom from pinholes in layers as thin as 500 Å.

2.3.2.2 Types of Parylenes

There are currently four types of parylenes available commercially: parylene-N, parylene-C, parylene-D, and parylene-F [6]. Parylene-N, or poly-para-xylylene, is the basic member of the series and is synthesized from parylene dimer, or di-para-xylene, through vacuum pyrolysis and vapor deposition polymerization. The chemical structure

is completely linear and highly crystalline material as shown in Figure 2-4 (a). Parylene-N is a primary dielectric, exhibiting high dielectric strength and a very low dissipation factor. Its dielectric constant is independent of frequency. Because of its high molecular activity during deposition and low deposition rate, parylene-N has the highest penetrating power and is able to coat relatively deep recesses and blind holes. Its low dissipation factor and dielectric constant suit high-frequency substrates where the coating is in an electromagnetic field. It has a high melting point of 420 °C [3] thus making it an attractive polymer for high-temperature applications.

The second commercially available member of the series is called Parylene-C, or poly-monochloro-para-xylylene. Its structure is similar to that of parylene-N monomer except that one of the aromatic hydrogens on the benzene ring is substituted by a chlorine atom. The chemical structure is shown in Figure 2-4 (b). Parylene-C is synthesized from parylene-C dimer, or di-monochloro-para-xylene. Parylene-C polymer has excellent bulk properties, including its moisture barrier, toughness, and electrical insulation characteristics [7]. Along with its ability to provide a true pinhole-free conformal insulation, parylene-C is the material of choice for coating critical electronic assemblies. However, parylene-C has poor adhesion to most smooth or nonporous substrates. Thus surface roughening of the substrates or coating of silane A-174 primer adhesion promoter is usually performed before deposition of the parylene-C film. It also has the lowest melting point temperature at 290 °C among other types of parylenes. Parylene-C deposition is substantially faster than parylene-N, and therefore its crevice-penetrating ability is reduced compared to the more active parylene-N molecules. In this thesis, all processes use parylene-C and often will be referred as parylene.

The third member of the series is called parylene-D, or poly-dichloro-para-xylylene. Figure 2-4 (c) shows its chemical structure. It is produced from the same basic monomer of parylene-N except for the substitution of two aromatic hydrogens by two chlorine atoms on the benzene ring. Because of the added chlorine atoms, parylene-D has similar properties to parylene-C except that it can withstand higher temperatures. Its melting point is 380 °C which is much higher compared to that of parylene-C. Among these three types, parylene-D's crevice penetration ability is the least eminent.

The last member of the series is called parylene-F, or poly-tetrafluoro-para-xylylene. The chemical structure is shown in Figure 2-4 (d) with four outside hydrogen atoms replaced by fluorine atoms. The dimer used to deposit parylene-F has to be synthesized and cracked at 700 °C [6]. Parylene F has the lowest dielectric constant of 2.35 at 1 MHz and can stand a much higher temperature before decomposition occurs. Dissociation temperature up to 525 °C in N_2 environment has been reported [4].

$$\left[-CH_2-C_6H_4-CH_2- \right]_n \quad \text{(a)}$$

$$\left[-CH_2-C_6H_2Cl_2-CH_2- \right]_n \quad \text{(c)}$$

$$\left[-CH_2-C_6H_3Cl-CH_2- \right]_n \quad \text{(b)}$$

$$\left[-CF_2-C_6H_4-CF_2- \right]_n \quad \text{(d)}$$

Figure 2.4: Chemical structure of parylene: (a) parylene-N;

(b) parylene-C; (c) parylene-D; (d) parylene-F

2.3.2.3 Parylene Deposition Process

In order to achieve a successful parylene coating, proper preparation of the surface of the substrates is critical. To yield good adhesion, cleaning must be performed to remove all oils and contaminants from the surface. In addition, it may be necessary to promote adhesion with the use of a silane pretreatment. The complete parylene deposition system is shown in Figure 2-5.

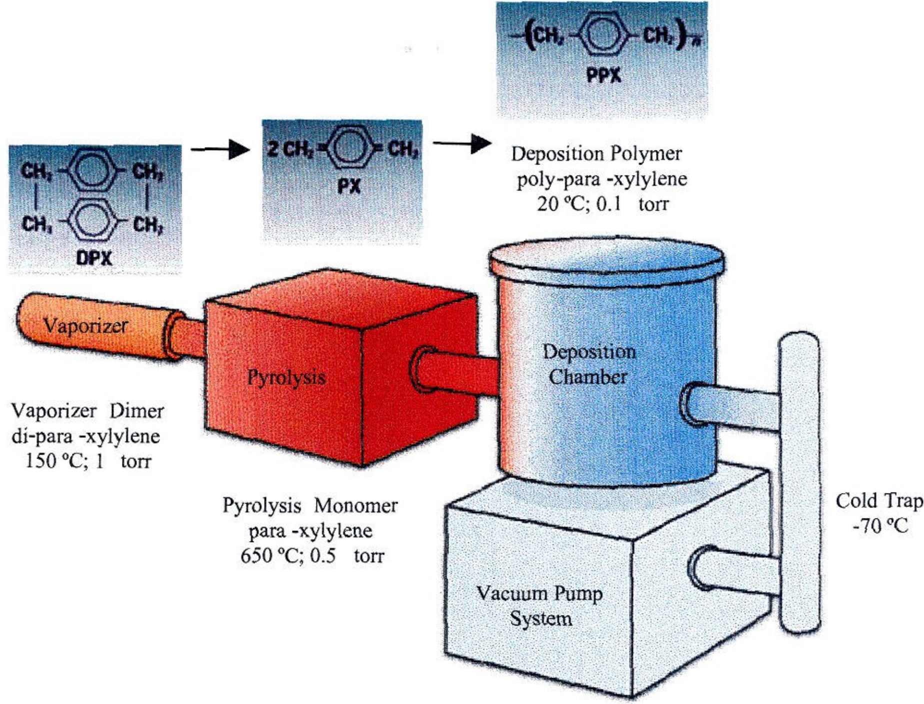

Figure 2-5: Parylene deposition system

The parylene deposition takes place in a parylene deposition system model PDS 2010 Labcoter 1 from Specialty Coating Systems, Inc. [3] Before deposition, surface treatment by A-174 silane is necessary to promote the adhesion if the surface of the substrate is hydrophilic, i.e., oxidized surface. First, the substrate is submerged for 15-30 minutes in 0.5% A-174/IPA/DI H_20 solution, i.e., 5 ml A-174 silane, 500 ml IPA, and

500 ml DI H_2O. It is recommended that the solution is mixed and stirred for at least 30 seconds and allowed to stand for a minimum of 2 hours before being applied to the surface. This solution should be changed after 24 hours. After the submerge stage, the substrate is air dried for another 15-30 minutes. Afterwards, IPA is used to rinse the substrate for 15 seconds and allow to air dry before parylene deposition.

The coating process begins with the sublimation of the raw material, di-para-xylylene - a solid white, crystalline dimer - at approximately 150 °C. This process takes place in a preliminary process zone called vaporizer. The vapor resulting from this preliminary heating is then molecularly cleaved, or pyrolyzed, in a second zone at 650-750 °C. This will decompose the dimer at the two methylene-methylene bonds to form monomers of para-xylylene, a highly reactive monomer gas.

In the deposition stage, the monomers enter the deposition chamber at room temperature and polymerize spontaneously onto the surface of substrates. Because there is no liquid phase, there is also no cure-related hydraulic or liquid surface-tension forces either initially or subsequently. The coating grows as a conformal film on all exposed substrate surfaces, edges, and in crevices, at a predictable rate. The film deposited at these conditions is transparent and smooth with good uniformity and pin-hole free. The pressure gradient across the three zones (from 1.0 to 0.5 to 0.1 torr) drives the parylene deposition while the substrate temperature remains near ambient. The excess parylene is condensed and trapped by a cold trap before exiting to the vacuum system. Due to the uniqueness of the vapor-phase deposition, the parylene film can be formed as structurally continuous films from as thin as a fraction of a micron to as thick as several mils.

Parylene's chemical structure, particularly its high molecular weight, crystallinity, and all-carbon backbone, is of significance to many applications, especially in medical and biology fields (bioMEMS). The absence of polar entities in the essential makeup of all the parylenes makes them hydrophobic, stable, and resistant to chemical attack. In contrast, other polymeric coating systems may have oxygen, nitrogen, or sulfur atom links in their backbone structures, and thus may require cross-linking to achieve desired properties. This makes them more vulnerable to solvents and chemical degradation.

2.3.2.4 Parylene Patterning Process

Parylene can be patterned by oxygen plasma, which is often used in removal of organic thin films. Photoresist and metals such as Al, Cr/Au, are often used as masks during patterning. The etching rate of the photoresist and parylene are found to be about the same. Therefore, metals are more favorable as masks for thick parylene etching. Other methods of patterning parylene have also been reported. For example, Loeb, *et al.* used laser micromachining to expose parylene at the tip of a fine needle [8]. Others have reported the creation of openings without conventional patterning and etching by using temperature-selective deposition of parylene [9, 10]. This can be achieved by localizing hot spots using heated resistors during parylene deposition. The deposition rate is very low if the temperature at the openings is held above 70 °C.

2.3.2.5 Properties of Parylenes

Some mechanical, thermal and electrical properties of the three most popular and commercially available parylenes (N, C, and D) are listed in Table 2-1 below.

Table 2-1: Properties of parylenes [3]

Properties	**Parylene-N**	**Parylene-C**	**Parylene-D**
Young's modulus (GPa)	2.4	2.8	2.6
Density (g/cm^3)	1.10-1.12	1.289	1.418
Index of refraction	1.661	1.639	1.418
Water absorbtion (% after 24 hrs)	< 0.1	< 0.1	< 0.1
Melting point (°C)	420	290	380
Linear coef. of expan. at 25 °C (x 10^{-5}, $(°C)^{-1}$)	6.9	3.5	3 – 8
Thermal conducivity at 25 °C (x 10^{-4} cal/cm.s.°C)	3.0	2.0	-
Specific heat at 20 °C (cal/g .°C)	0.20	0.17	-
Dielectric strength, (dc volts/μm)	276	221	217
Dielectric constant			
60 Hz	2.65	3.15	2.84
1 KHz	2.65	3.10	2.82
1 MHz	2.65	2.95	2.80
Moisture vapor transmission at 90% RH, (g .mil/100 in^2 .d)	1.5	0.21	0.25
N_2 permeability at 25 °C, (cm^3.mil/(100 in^2/d.atm))	7.7	1.0	4.5

2.3.3 Titanium-Alloy MEMS Wings

2.3.3.1 Titanium-Alloy Metal (Ti-6Al-4V)

In MEMS processing, metal processing has been an integral part of the fabrication process. Unless necessary, there is no need to develop a new technology to pattern and etch metals. Hence, metal can be a suitable choice to use as wingframe. Another advantage of using metal as wingframe is that it is ductile and can be bent into any shape desired. For the search of a suitable material for wingframe structures, various metals that are compatible with MEMS process are identified, i.e., aluminum, copper, stainless steel, and titanium-alloy. Although aluminum metal is light in weight and used extensively in MEMS process, it is too soft. So is bulk copper. Stainless steel is strong but its high mass density, twice as high as that of titanium-alloy metal, makes the wings become too heavy. Moreover, the etching of stainless steel can also be problematic. The etchant solution is ferric chloride ($FeCl_3$) and it is dark brown in color. Thus, it is impossible to monitor the etching progress because the solution is opaque. This makes it difficult to ascertain whether the etching is finished. Furthermore, the etching rate of stainless steel in $FeCl_3$ is very slow. The solution must be raised to a high temperature in order to achieve a reasonable etching rate.

Ti-6Al-4V is the most widely commercially used titanium-alloy. It is composed of 88% titanium, 6% aluminum, 4% vanadium, and 2% of other elements such as iron, carbon, hydrogen and oxygen [11]. It is commonly used for aircraft gas turbine disks and blades as well as airframe structural components that requires strength and high temperature tolerance. For this project, titanium-alloy metal (Ti-6Al-4V) is chosen for

several reasons. First, it is light and strong and can be easily tapered to vary the thickness of wingspars. Second, because titanium-alloy is ductile, it also can be bent to create wing camber to improve performance. Finally, the etching process of titanium-alloy can be conducted at room temperature and yields a reasonable etching rate (~2.5 μm/min). For wing membranes, the suitable material is parylene-C [12-15]. There are several advantages of using parylene-C as wing membrane: 1) it can be deposited directly onto titanium-alloy at any desired thickness; 2) its adhesion to titanium-alloy is excellent; 3) parylene film is light and strong, and can withstand high flapping frequency of more than 30 hertz without tearing; 4) its deposition rate is fast, much faster than parylene-N; and 5) parylene-C is deposited at room temperature. In addition, unlike vacuum metallization, parylene deposition is not line-of-sight. All sides of an object to be encapsulated are uniformly impinged by the gaseous monomers. This yields a truly conformal nature of the coating. Thus, if there are any step corners, they can be completely covered.

2.3.3.2 Titanium-Alloy MEMS Wings Fabrication Process

There has never been any report before regarding the titanium-alloy MEMS wing technology. For the first time, this technology is developed as a tool to systematically study the flapping-wing aerodynamics in the wind tunnel. For many reasons it is claimed that the new MEMS wing technology is necessary because MEMS wings enable systematic research in terms of precise size and weight controls, repeatability, batch fabrication, and fast production. Moreover, complicated wing structures can be easily fabricated by photolithographic technology. Figure 2-6 shows various fabricated titanium-alloy MEMS wings ranging from insect wings to simple-spar wings. Table 2-2 shows selected mechanical properties of both titanium-alloy metal and parylene-C.

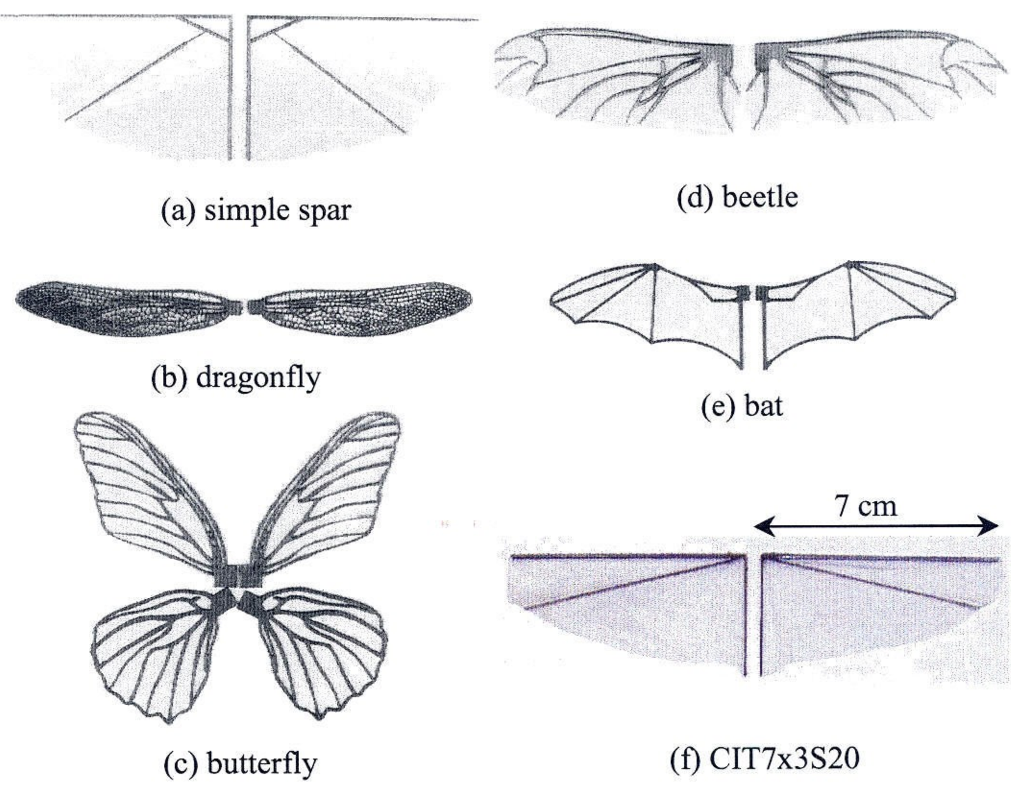

Figure 2-6: Titanium-alloy MEMS wings

Table 2-2: Mechanical properties of Ti-6Al-4V and parylene-C

Properties	**Ti-6Al-4V**	**Parylene-C**
Density, (g/cm^3)	4.5	1.3
Young's modulus, (GPa)	110	3
Tensile strength, (MPa)	100	70
Yield strength, (MPa)	97	56
Coefficient of thermal expansion, ($x10^{-5}$/°C)	0.9	3.5

The fabrication process of titanium-alloy MEMS wings is shown in Figure 2-7. The photoresist used in this process is dry-film resist (DFR-4713) obtained from Kepro Circuit System, Inc. [16] The lamination of dry-film resist technology is regularly used in the PCB manufacture industry but not in MEMS industry. This technology is particularly selected for this project because of several benefits. These benefits will be discussed in detail in section 2.4.

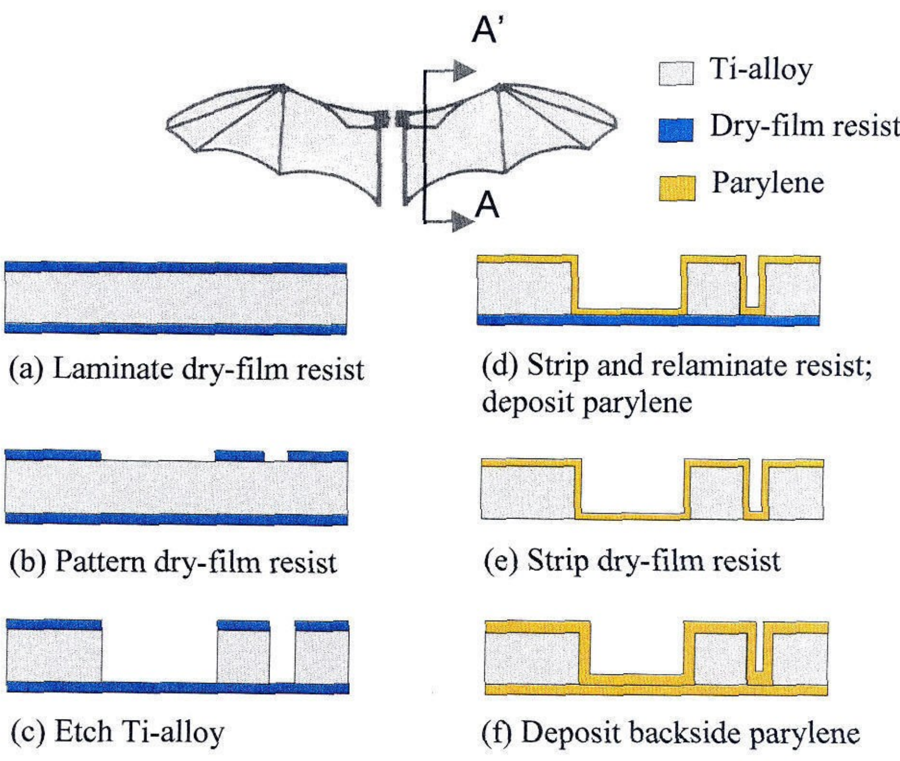

Figure 2-7: Fabrication process of titanium-alloy MEMS wings

First, a 250-μm-thick titanium-alloy substrate is cleaned in trichloro-ethylene (TCE) for 20 minutes. Then it is dipped in a diluted HF solution to roughen its surface to improve the adhesion to the dry-film resist. Next, the dry-film resist is laminated on both sides of the substrate. The resist is patterned for 45 seconds under UV light and is

developed in Na_2CO_3 solution for 5 minutes. Then it is hardbaked at 120 °C for 20 minutes to get rid of the excess water. This helps improve the adhesion of the resist to the substrate. Next, the substrate is etched in a mixed solution of 5% HF and 2% HNO_3. It is found that if the concentration of the acid is too strong, the dry-film resist would be attacked and peeled off before the etching is finished. At this concentration, the etching rate is approximately 2.5 μm/min. Because this is an isotropic etching, the undercut rate is the same as the etching rate. Therefore, undercut distance must be considered during the mask design.

After the etching process is finished and the wingframes are formed, the unexposed dry-film resist on the backside of the substrate is exposed to the UV light for at least 30 seconds. This makes it easy to strip off the dry-film. The resist is then stripped from both sides of the substrate in a diluted KOH solution. The typical mixture is 2 g of KOH in 100 ml of DI H_20. Next the dry-film resist is relaminated on the backside. It is used as a platform for parylene-C polymers to deposit on. For this process, 5-μm thickness of parylene is deposited. Generally, 7 g of parylene dimer yields approximately 5 μm. Afterwards, the dry-film resist is stripped in KOH. This leaves clear membranes of parylene attached to the titanium-alloy wingframes. Finally, the second layer of parylene is deposited to strengthen the wing membrane.

2.4 Challenges and Solutions

There are several technical challenges that have to be overcome in order to achieve a successful fabrication of MEMS wings. A good adhesion of the photoresist is important in the etching process. The typical spin-on photoresist could not be used in this

process because it is attacked and will peel off during the etching in HF. Therefore having a right protective mask during etching is very important. One of the crucial fabrication steps is the release of a large area of wing without damaging the membrane. The material chosen must be able to withstand HF and HNO_3 acids and can be stripped off easily without attacking titanium-alloy and the parylene. The negative dry-film resist is selected because it meets these requirements. In addition, its adhesion to titanium-alloy substrate is good during etching without any adhesion promoter. It is also stripped off easily in a diluted KOH solution after the film is exposed under the UV light beforehand. Moreover, its developer and the stripper solutions do not attack either titanium-alloy or parylene. This makes the dry-film resist a very attractive choice.

Non-uniformity of the titanium-alloy substrates can also present a difficulty during the etching because etching in a certain area is finished before others. Therefore over-etching is necessary. This can cause some spars to be etched too thin and break off while another spar is still attached to the substrate. The remedy of this problem is to measure and select the substrates that have uniform thickness before starting the process. If the non-uniformity still remains after the etching, localization of etching in the unfinished areas can be performed by carefully dipping in HF solution.

In addition to above mentioned problems, undercutting is also a challenge and can often cause the dry-film resist to peel off from the spars before the etching process is finished. Undercutting compensation must be considered during the mask layout to prevent this problem, i.e., the width of the spars should be increased to compensate the undercut distance.

2.5 Summary

The non-MEMS and MEMS-fabricated wings are designed and built. The non-MEMS wings are built using carbon fiber rods with mylar or paper as wing membrane. This method is cumbersome, time-consuming, and cannot create perfect matching wings. With MEMS fabrication technology, batch fabrication of identical wings can be fabricated. In addition, we can systematically study the aerodynamic performance of various wings with different design parameters such as number of spars, the membrane thickness, and the length and width of the spars both spanwise and chordwise directions. Detailed fabrication process is described along with properties of both titanium-alloy and parylene. The technical challenges encountered during the process and their solutions are discussed. The mechanical and wind-tunnel test results will be presented, analyzed, and discussed in detail in the chapter 3.

It is important that the fabrication of these MEMS wings is well-established because it is a foundation for the future direction of the research in this thesis where the goal is to integrate other types of passive or active MEMS devices onto these MEMS wings. These wings will be mounted in the test platform in the wind tunnel to perform various aerodynamic tests.

2.6 Bibliography

[1] T. N. Pornsin-Sirirak, S. W. Lee, H. Nassef, J. Grasmeyer, Y. -C. Tai, C. -M Ho, and M. Keennon, "MEMS Wing Technology for a Battery-Powered Ornithopter," *The 13th IEEE International Conference on Micro Electro Mechanical Systems (MEMS'00)*, Miyazaki, Japan, pp. 799-804, Jan. 23-27, 2000.

[2] J. T. C. Yeh, and K. R. Grebe, "Patterning of Poly-Para-Xylylenes by Reactive Ion Etching," *Journal of Vacuum Science & Technology A*, vol. 1, issue 2, pp. 604-608, 1983.

[3] Parylene Conformal Coatings Specifications and Properties, Specialty Coating Systems, Inc., 5707 West Minnesota Street, Indianapolis, IN 46241, Tel: (800) 356-8260, Fax: (317) 240-2073.

[4] P. K. Wu, G. -R. Yang, L. You, D. Mathur, A. Cocoziello, C. -I. Lang, J. A. Moore, and T. -M. Lu, "Deposition of High Purity Parylene-F Using Low Pressure Low Temperature Chemical Vapor Deposition," *Journal of Electronic Materials*, vol. 26, no. 8, pp. 949-953, 1997.

[5] L. Wolgemuth, "Assessing the Performance and Suitability of Parylene Coating," *Medical Device & Diagnostic Industry Magazine*, Aug. 2000.

[6] P. K. Wu, G. -R. Yang, J. F. McDonald, and T. -M. Lu, "Surface Reaction and Stability of Parylene N and F Thin Films at Elevated Temperatures," *Journal of Electronic Materials*, vol. 24, no. 1, pp. 53-58, Jan. 1995.

[7] H. Yasuda, B. H. Chun, D. L. Cho, T. J. Lin, D. J. Yang, and J. A. Antonelli, "Interface-Engineered Parylene C Coating for Corrosion Protection of Cold-Rolled Steel," *Corrosion Science*, vol. 52, no. 3, pp. 169-176, Mar. 1996.

[8] G. E. Loeb, R. A. Peck, and J. Martyniuk, "Toward the Ultimate Metal Microelectrode," *Journal of Neuroscience Methods*, vol. 63, pp. 175-183, 1995.

[9] R. Sabeti, E. M. Charlson, and E. J. Charlson, "Selective Deposition of Parylene," *Polymer Communications*, vol. 30, pp. 166-169, June 1989.

[10] E. M. Charlson, E. J. Charlson, and R. Sabeti, "Temperature Selective Deposition of Parylene-C," *Polymer Communications*, vol. 30, pp. 166-169, June 1989.

[11] American Society for Metals, *Metal Handbook*, 9th edition, vol. 3, pp. 388-391, 1980.

[12] P. F. Man, D. K. Jones, and C. H. Mastrangelo, "Microfluidic plastic capillaries on silicon substrates: A new inexpensive technology for bioanalysis chips," *Proc. IEEE, The 10th Annual International Workshop on Micro Electro Mechanical Systems (MEMS'97),* Nagoya, Japan, pp. 311-316, Jan. 26-30, 1997.

[13] X. Q. Wang, A. Desai, Y. -C. Tai, L. Licklider, and T. D. Lee, "Polymer-based Electrospray Chips for Mass Spectrometry," *The 12th IEEE International Conference on Micro Electro Mechanical Systems (MEMS '99),* Florida, U.S.A., pp. 523-528, Jan. 17-21, 1999.

[14] X. Q. Wang, Q. Lin, and Y. -C. Tai, "A Parylene Micro Check Valve," *The 12th IEEE International Conference on Micro Electro Mechanical Systems (MEMS '99),* Florida, U.S.A., pp. 177-182, Jan. 17-21, 1999.

[15] X. Yang, J. M. Yang, X. Q. Wang, E. Meng, Y. -C. Tai, and C. -M. Ho, "Micromachined Membrane Particle Filter," *The 11th Annual International Workshop on Micro Electro Mechanical Systems (MEMS '98),* Heidelberg, Germany, pp. 137-142, Jan. 25-29, 1998.

[16] Kepro Circuit Systems, Inc., 3640 Scarlet Oak Blvd., St. Louis, MO 63122, Tel: (800) 523-3878, Fax: (314) 861-9109.

Chapter 3

Test Results of MEMS Wings

3.1 Introduction

As described in the previous chapter, the MEMS technology enables an efficient way to batch fabricate identical and lightweight wings. Therefore, the fast turn-around time can be achieved without having to create several different molds for each wing design. Although the fabrication technique of MEMS silicon wings exists, the wings are found to be too fragile and can be broken easily. Hence, the novel titanium-alloy and parylene MEMS wings are developed. This chapter describes various tests of these MEMS wings, including mechanical test and aerodynamic test in the wind tunnel. Furthermore, various designs of MEMS wings and their aerodynamic test results are also discussed. In addition, the novel fabrication process of stiffness-enhanced titanium-alloy MEMS wing is introduced.

3.2 Mechanical Tests and Results

3.2.1 Stiffness Test

The wing stiffness test setup and its diagram are shown in Figure 3-1 and 3-2, respectively. This setup measures the spring constant of various types of wings. If the wing is stiff, it should yield a high spring constant value. First, the MEMS wing is clamped at its root by an adjustable vise. A square blade, connected to a force loadcell and an XYZ stage, is used to probe at various sections of the wings to measure its spring constant. This method of using a line-section probing is better than a point probing because it prevents the wing from twisting during the measurement. The force loadcell is connected to the force gauge that indicates how much the force is applied on top of the wing. The XYZ stage is connected to a displacement gauge that measures the deflection distance of the wing from equilibrium.

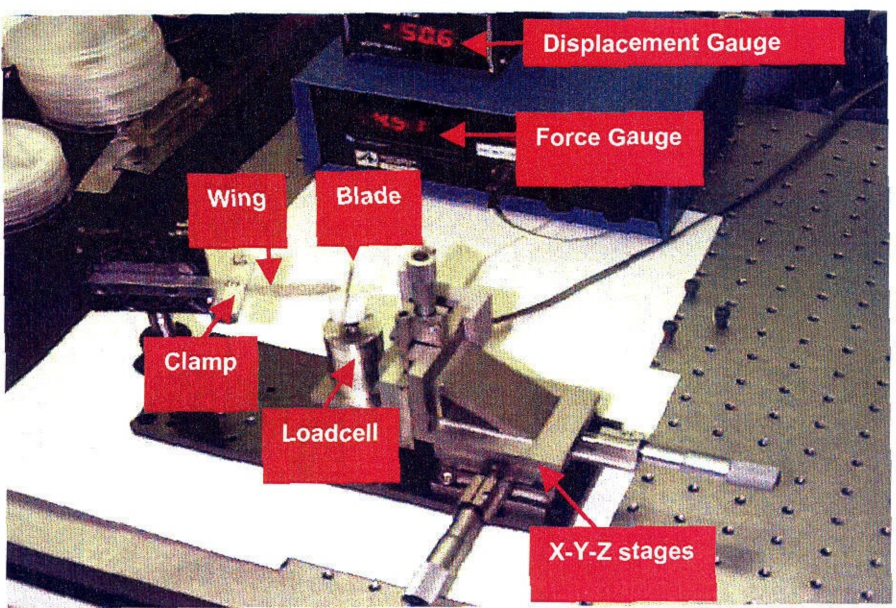

Figure 3-1: Spring constant test setup of MEMS wings

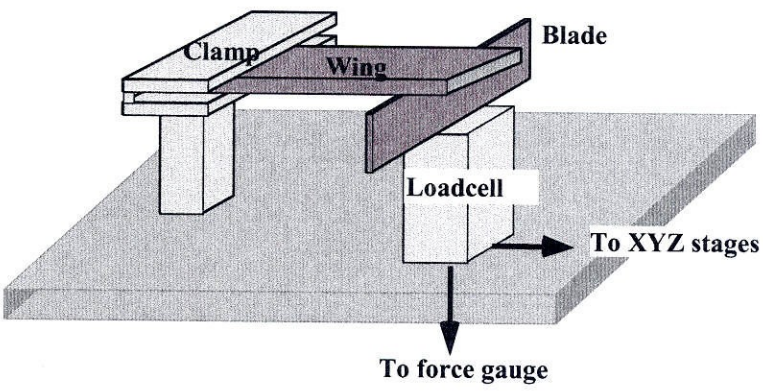

Figure 3-2: Spring constant test setup diagram

One advantage of MEMS metal wings is that they can be tapered to vary thickness to mimic the natural wing's stiffness distribution. At the same time, the wings can be become lighter as well. Tapering of MEMS wings can be achieved by selectively etching the wings in a diluted mixed solution of HF and HNO_3 acids. Three types of wings are tested by the spring constant setup: natural wings, tapered titanium-alloy wings, and non-tapered titanium-alloy wings. Figure 3-3 shows the plot of the wing's spring constant versus normalized distance from wing's root of all types of butterfly wings. It can be observed that without tapering the wings, metal wings are very stiff compared to natural wings. Tapered butterfly wings have stiffness characteristics closer to those of natural wings. From this plot, the relationship between the spring constant K of the butterfly wings, in N/m, to the normalized distance L from wings' roots can be obtained as follows:

$$K_{real\ butterfly} = 0.452L^{-2.663} \quad (3\text{-}1)$$

$$K_{tapered\ metal\ butterfly} = 7.73L^{-2.774} \quad (3\text{-}2)$$

$$K_{metal\ butterfly} = 2.775L^{-2.871} \quad (3\text{-}3)$$

Although these wings have various wing shapes, equations (3-1) to (3-3) show similar characteristics to the relationship between the spring constant K of a cantilever beam of length L shown in equation (3-4):

$$K = \frac{3EI}{L^3} \tag{3-4}$$

where E and I are the Young's modulus and inertia mass of the materials, respectively.

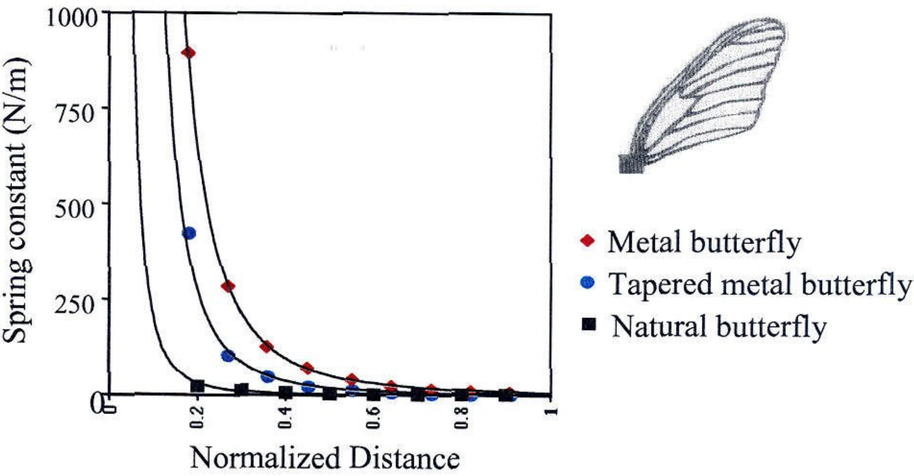

Figure 3-3: Spring constants of butterfly wings

Despite the fact that the natural wing does not have high spring constant compared to metal wings, its effective spring constant (normalized by weight) still has the highest value. At a normalized distance of 0.75, it can be calculated that the natural butterfly wing has an effective spring constant of 54 N/m/g compared to 50.7 and 39.9 N/m/g of tapered metal wings and metal wings, respectively. Tapered wings' stiffness, when normalized with weight, is comparable to that of the natural wing. This tapering method varies the thickness uniformity of the wing. Typically, the leading-edge and the

inboard area have the highest thickness while the trailing edge and the outboard area are thin and flexible. This is also similar to the observation of the natural wings.

3.2.2 Flapping Test

The flapping test is used to demonstrate the durability of the metal wings under various flapping frequencies. The wings are mounted on a small, lightweight, and low-friction transmission mechanism. This mechanism converts the rotary motion of the driving motor into the flapping motion of the wings [2]. Four transmission designs that yield such motion are shown in Figure 3-4. Based on simplicity, minimal weight, and flapping symmetry, transmission C was chosen and hand-built by the engineers at AeroVironment, Inc. [3].

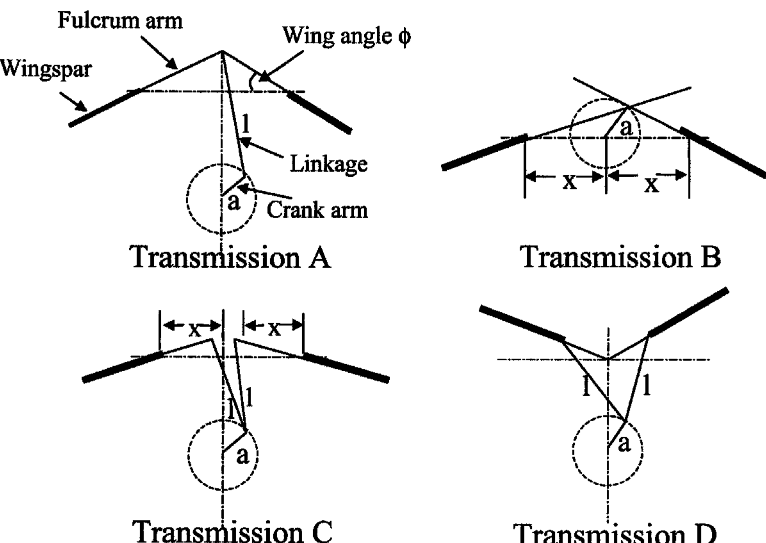

Figure 3-4: Various transmission designs

The design of transmission C restricts the flapping motion in a plane perpendicular to the motor shaft. A small electric DC motor with gearbox ratio of 22:1 is used to drive the rocking arms. The electric motor can handle input power of up to 2 watts. At this power with a no-load condition, i.e., with no wing attached, the

transmission arms can flap up to 42 Hz continuously without destroying the motor. The test transmission gearbox is shown in Figure 3-5. It weighs 2.8 grams and has 90% efficiency with the maximum power input of 2 watts. Various MEMS wings were mounted on the transmission system and several flapping tests were performed. The results are shown in Table 3-1.

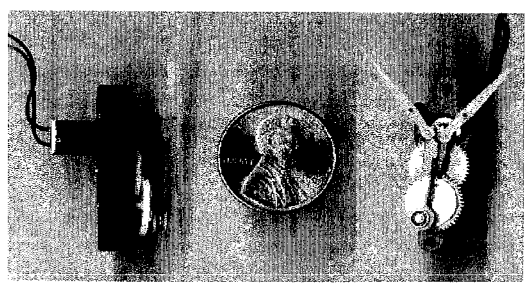

Figure 3-5: Transmission system

Table 3-1: Flapping frequency of various fabricated MEMS wings

Load Condition/Wing Types	**Wing Mass [mg]**	**Maximum Frequency [Hz]**
No load	-	42.5
Metal dragonfly wings	150	36.0
Metal bat wings	190	32.3
Natural dry beetle wings	670	25.7
Natural wet beetle wings	800	24.2
Metal butterfly wings	440	24.0
Carbon fiber simple-spar wings	370	16.2
Metal simple-spar wings	490	16.2
Metal beetle wings	500	14.6

Under the no-load condition, the maximum frequency produced by the motor is 42.5 Hz. Various MEMS wings are tested by this transmission system and flapping motions are performed. The light wings such as dragonfly wings could withstand more than 30 Hz. None of the MEMS wings experiences breaking or tearing of wingspars or membranes. This proves the robustness of the MEMS wings.

3.3 Aerodynamic Tests and Results

3.3.1 Flapping-Wing Aerodynamics

In general, flight by animals as well as by airplanes involves the transfer of momentum from flapping wings to the surrounding air. The physical characteristics of air determine the subsequent reaction forces on the bodies and wings that effect weight support and propulsion [4]. Most often in flapping flight, the lift and thrust productions are thought to have similar principles as conventional airplane wings. It is thought that "instantaneous" force on a flapping wing is the same as if the wing would experience in steady motion at the same instantaneous velocity and angle of attack. This assumption is called "quasi-steady" and is justifiable for fast forward flight, where the flight velocity dominates the flow over the wings and the flapping motion is considered just a small perturbation of this steady flow [5]. For low-speed and hovering flights with low Reynolds number ($<10^4$), unsteady aerodynamic effects may dominate over quasi-steady.

In flapping-wing aerodynamics, using the quasi-steady mechanism, the wings of birds or bats act as aerofoils as illustrated in Figure 3-6. For the wing to experience an upward lift force in air with density ρ, the average air pressure below the wing (P_1) must be greater than the pressure above it (P_2). This means that the average air velocity below

the wing (U_1) must therefore be lower than the air velocity above it (U_2) because of the inverse relationship between pressure and velocity according the Bernoulli's principle [7] which is given by

$$P_2 + \frac{\rho}{2}U_2^2 = P_1 + \frac{\rho}{2}U_1^2 = const. \tag{3-5}$$

This equation can also be written as

$$P_2 - P_1 = \frac{\rho}{2}(U_1^2 - U_2^2) \tag{3-6}$$

This velocity gradient can be represented by a vortex "bound" to the wing. The strength or *circulation* Γ of the bound vortex is a measure of the velocity difference. The lift L is directly proportional to the wind speed U and circulation Γ. The Kutta-Joukowski law [4] relates the magnitude of lift produced per unit wing span (L_{span}) as

$$L_{span} = \rho U \Gamma \tag{3-7}$$

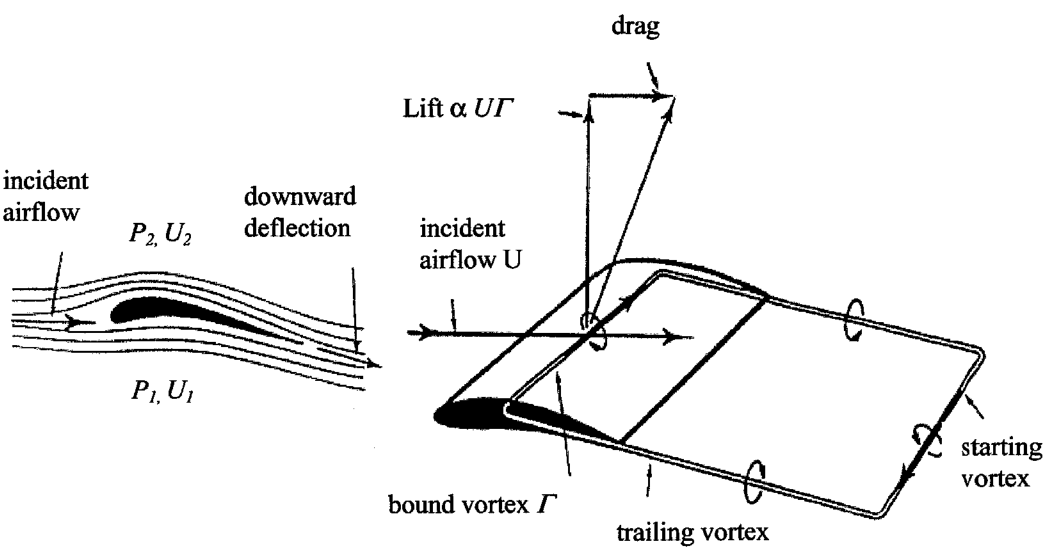

Figure 3-6: Aerodynamic forces and wake vortex on a wing [6]

As U increases, the area of the closed vortex loop also increases linearly with the velocity, i.e., bound vortex sweeps through space over a greater area at higher speed as seen in Figure 3.7. The instantaneous force that any vortex can produce is directly proportional to the rate at which it can move through space. The total lift L can be expressed as

$$L = C_L \frac{1}{2} \rho U^2 A \tag{3-8}$$

where C_L and A are the lift coefficient and wing planform area, respectively. The term $½\rho U^2$ is a very important quantity known as "dynamic pressure" and is an equivalent of the kinetic energy of a unit volume of air. Similarly, the thrust force T that pushes the flight body forward and the drag force that slows down the motion can be expressed as

$$T = C_T \frac{1}{2} \rho U^2 A \tag{3-9}$$

and

$$D = C_D \frac{1}{2} \rho U^2 A \tag{3-10}$$

where C_T and C_D are the thrust and drag coefficients, respectively.

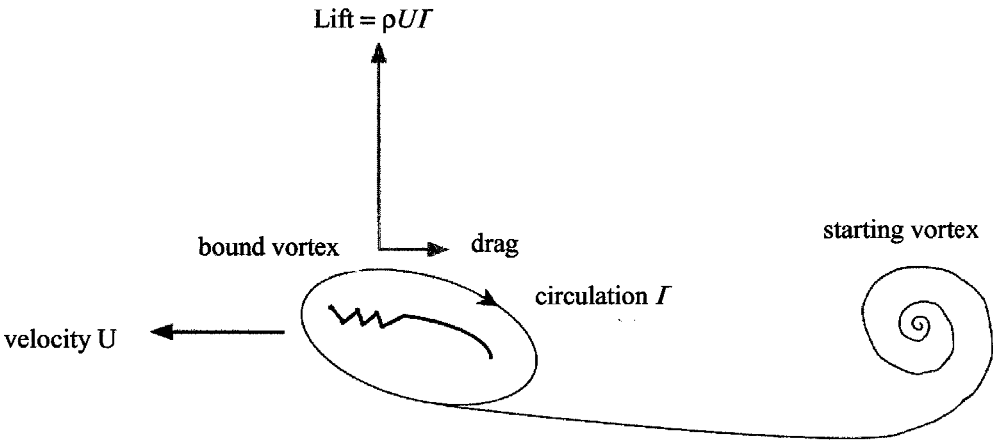

Figure 3-7: Cross section of a vortex wake generated by a moving wing [4]

Figure 3.8 shows the force components during flapping. In the downstroke, the wings generate both lift (vertical force component) and thrust (horizontal force compoment). However, in the upstroke the wings moved upward through the air and the horizontal force component acts as a negative thrust, i.e., drag. In order to obtain a mean positive thrust, it is essential that there be some asymmetry between downstroke and upstroke [6]. This can be achieved by modifying the configuration of the upstroke. The circulation can be reduced by means of changing the angle of incidence, altering the wing section profile, or decreasing the effective wingspan.

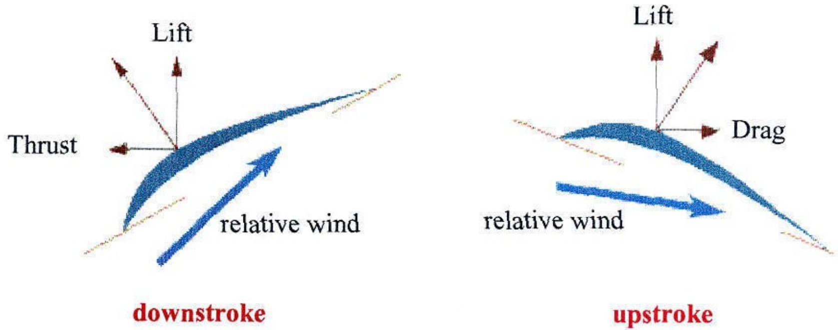

Figure 3-8: Force components on the wing during flapping

The amount of lift generated by the flow around the flapping wings depends on numerous parameters, such as flight speed, flapping frequency, angle of attack, orientation, wing deformations, and vortex shedding. Equation (3-7) shows that the lift production is directly proportional to the amount of vorticity produced over the wings. However, it is believed that the amount of thrust produced depends on how that vorticity is shed. This highly coupled nature of the unsteady flow proves to be difficult for the search to find an optimal wing design.

3.3.2 Wind-Tunnel Setup and Initial Test Results

The MAV aerodynamic study is conducted at UCLA in a high-quality low-speed wind tunnel with velocity uniformity of 0.5% and speeds from 1 to 10 m/s. The wind tunnel has a 30 x 30 x 60 cm test section with a 4:1 contraction. Most experiments are conducted at the wind speed U between 3-4 m/s because the minimum power required is believed to occur at this speed for small birds of this size [8]. Force measurements are taken using low capacity 2-D force loadcells capable of measuring lift and drag forces up to 150 and 100 grams, respectively. The data is processed by a 16-bit resolution ADC board (National Instrument PCI-6031E) with minimum force resolution of 33 and 24 mg for lift and drag, respectively. This test setup is shown in Figure 3-9.

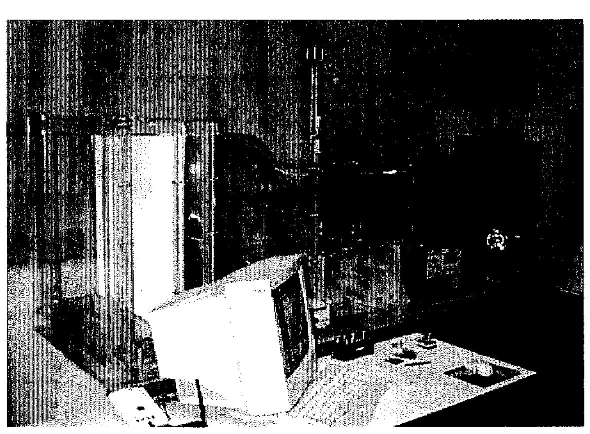

(a) Low-speed wind tunnel

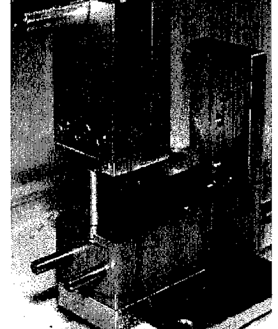

(b) Force loadcells

Figure 3-9: Wind-tunnel test setup

The aerodynamic performance of natural insect wings, carbon-fiber wings, and both flexible and stiffness-enhanced leading-edge MEMS wings are studied. It is important to study the effect of the flexibility of the wing to note how the lift is affected. This effect of the flexibility of the spanwise leading-edge is studied by using the

comparison of the natural wings and the metal bat wings. The natural cicada wings have very stiff leading-edge while the metal bat wings do not. The wind-tunnel test results of rigid cicada wings and the metal bat wings (without the support of carbon fiber rods at the leading-edge) are shown in Figure 3-10. The advance ratio J is the ratio of the flight speed to the speed of the wingtip which is directly proportional to the flapping frequency, f, and is given by

$$J = \frac{U}{2\Phi f b} \tag{3-11}$$

where Φ, f, and b are stroke angle, flapping frequency, and wing semi-span, respectively. Typically, unsteady-state flight has advance ratio J of less than 1. This can be observed from the natural flyers such as bumblebee, black fly, and fruit fly, whose advance ratios in free flight are 0.66, 0.50 and 0.33, respectively [10]. Low advance ratio J is an indication that these flyers must flap their wings at high speed compared to the speed of their flights in order to stay aloft. Therefore, the regime of $J < 1$ dominates by the unsteady-state flight. On the other hand, for $J >> 1$, the flight regime becomes quasi-steady and approaches steady-state. For example, a fixed-wing airplane operates in the regime of J near infinite because the wings' flapping frequency is zero. The aerodynamic lift and thrust coefficients can be expressed as [9]

$$C_L = \frac{2L}{\rho A U^2} \tag{3-12}$$

and

$$C_T = \frac{2T}{\rho A U^2} \tag{3-13}$$

These equations are simply the rearrangement of equation (3-8) and (3-9) in terms of C_L and C_T.

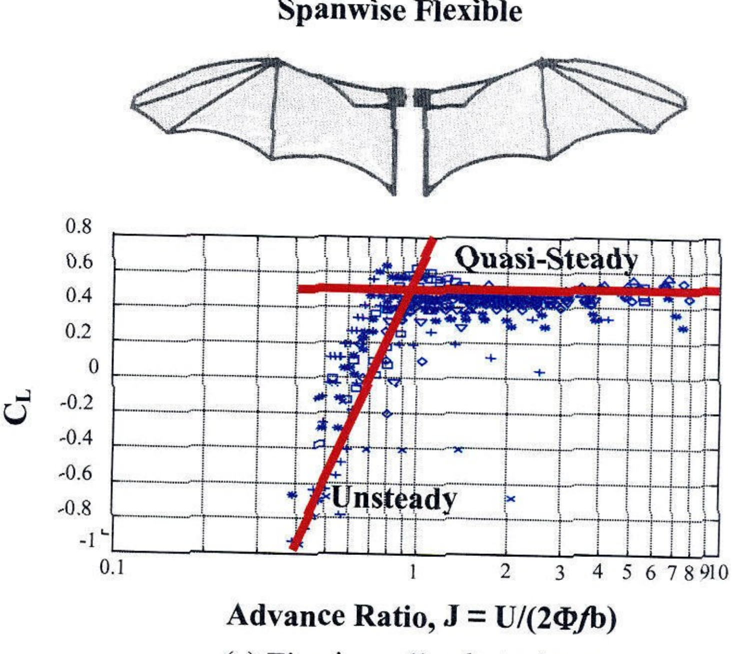

(a) Titanium-alloy bat wings

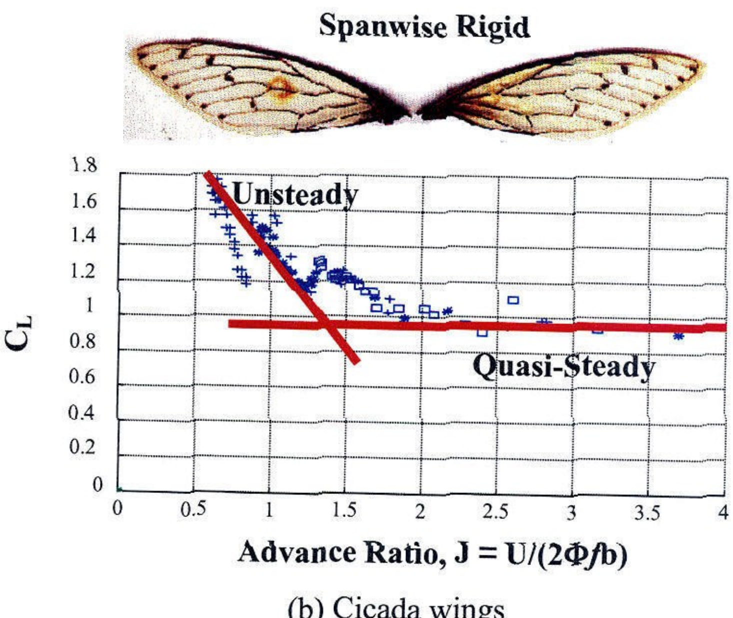

(b) Cicada wings

Figure 3-10: Spanwise stiffness effect

It can be seen from Figure 3-10 that spanwise stiffness is clearly an important factor in lift production in flapping flight. For the same size of wings, cicada wings with rigid leading-edge can produce larger lift coefficients, C_L, compared to wings that have flexible leading-edge. The lift coefficient is used as a factor to determine how much lift is produced. It is the number that aerodynamicists use to model all of the complex dependencies of shape, inclination, and flow condition on lift. In the regime of advance ratio J less than one (unsteady-state flow), the lift coefficients of wings with rigid leading-edge increase rapidly while those of flexible ones decrease to undesired negative values.

Vortex generation can be observed using flow visualization (smoke wire) in the wind tunnel. For large advance ratios ($J >> 1$), no vortex is generated and the flow is always attached (quasi-steady flow). However, as the advance ratio is reduced below unity ($J < 1$, unsteady flow), the dynamic stall vortex appeared regardless of the chord size of the wing. The diameter of the dynamic stall vortex is observed to be 3-4 cm near the midspan region. At the start of the downstroke, the flow stagnates at the leading-edge of the wing. The stagnation line progressively moves to the upper surface of the wing, thereby by forming a leading-edge vortex. This vortex continues to grow and attains its maximum size at about the middle of the downstroke. Then it is finally shed at the beginning of the upstroke [11]. This sequence is illustrated in Figure 3-11. This leading-edge vortex is accompanied by a strong outward spiral spanwise flow as seen in Figure 3-12. The vortex is very similar to the one observed by Van Den Berg, *et al.* [12-13] as well as Maxworthy [14] for their studies of hovering flight. This vortex accounts for the low pressure regime that produced the lift on the wings, increasing in size from wing base

to tip with a strong axial flow velocity. Between 25% and 75% of the wing length, its diameter increases approximately from 10% to 50% of the wing chord. The vortex separates from the wing at approximately 75% of the wing. If the circulation of the leading-edge vortex is fully used for lift generation, it can support up to two-thirds of the flyer's weight during the downstroke [13]. The growth of this circulation with time and spanwise position clearly identify dynamic stall as the unsteady aerodynamic mechanism responsible for high lift production.

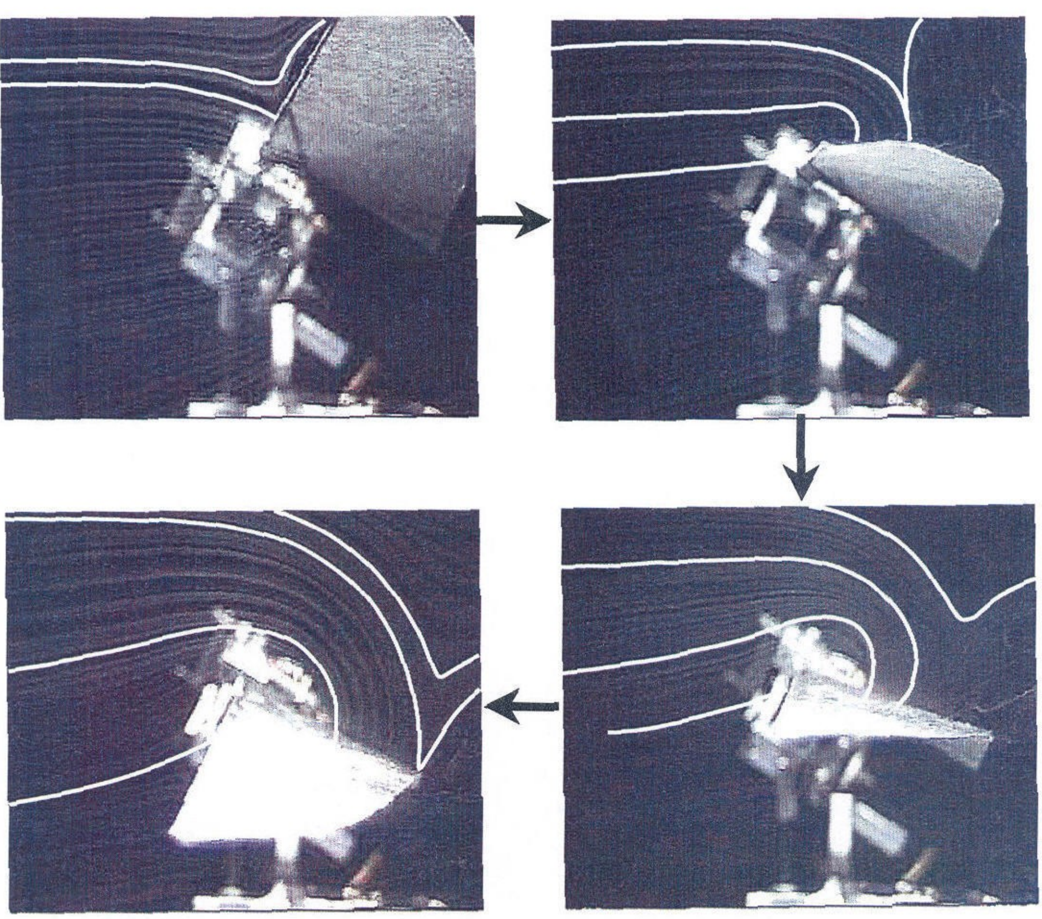

Figure 3-11: Leading-edge vortex separation during downstroke

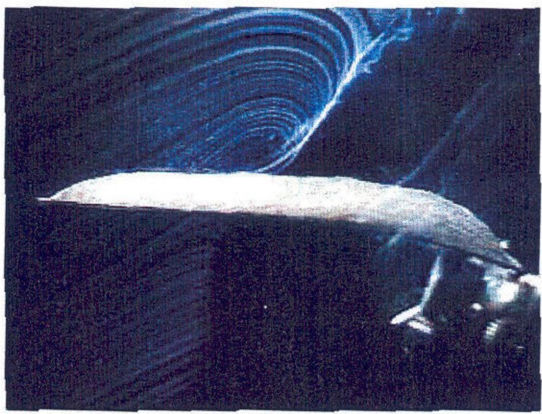

Figure 3-12: Leading-edge spiral spanwise vortex

Figure 3-13 shows the lift measurements correlate with the vortex formation. From the plot, the lift force is at a maximum value near the mid-downstroke region, which is when the separation vortex attains its maximum size. As the spanwise spiral vortex is shed, the lift force decreases and is negative during the upstroke. These results are similar to those of previous studies by Van Den Berg and Ellington [12-13], Weis-Fogh and Jensen [15], and Bennet *et al.* [16]. It confirms that the lift force is primarily produced during the downstroke with its maximum being located near mid-downstroke. The negative lift portion is attributed to a vortex that forms underneath the wing during the upstroke that is smaller than the separation vortex formed on the upper surface.

Figure 3-14 shows the thrust measurements correlate with the vortex formation. It is believed that the thrust production is intimately tied with the vortex shedding and the flexibility of the wings. Notice that thrust is not produced until the later part of the downstroke and well into the upstroke, which is the time when the flexible trailing edge starts to snap down. It is also the time when the separation vortex is being shed according to the flow visualization. Depending on the wing's flexibility and orientation, the vorticity could be shed differently which will affect the thrust.

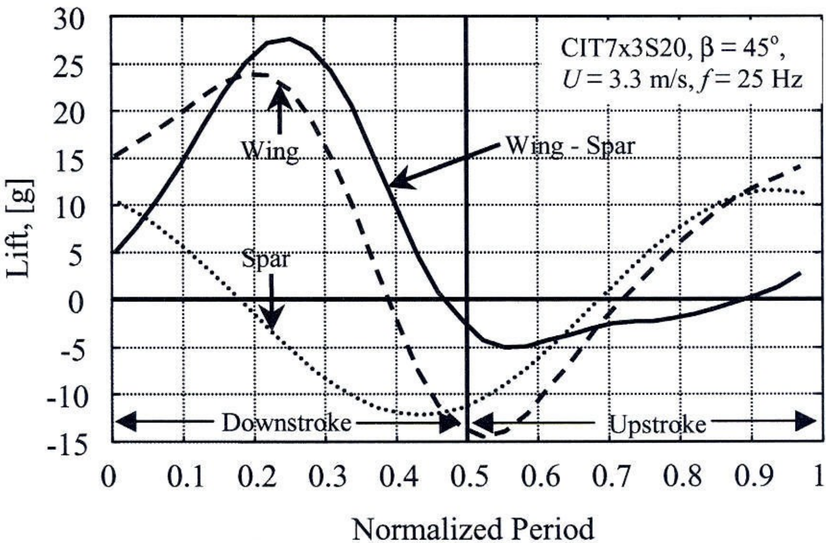

Figure 3-13: Lift generated during downstroke and upstroke

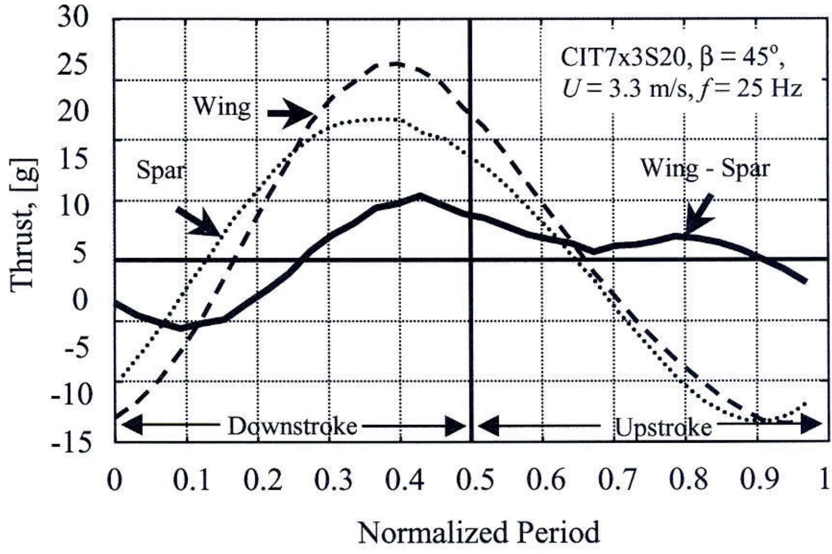

Figure 3-14: Thrust generated during downstroke and upstroke

3.3.3 Leading-Edge Stiffness-Enhanced MEMS 3-D Wings

The wind-tunnel test results shown in Figure 3-10 indicate that it is important for the leading-edge of the flapping wings to be stiff in order to take an advantage of the unsteady-state aerodynamics. The fabrication process of "stiffness-enhanced" titanium-

alloy MEMS wing is shown in Figure 3-15. It is a modification of the MEMS wing process described in Figure 2-7 in chapter 2. After the wingspars are formed, lightweight carbon fiber rods are attached to the leading-edge spars. Then they are sealed completely by parylene films following the next parylene deposition steps. This method has greatly enhanced the stiffness of the leading-edge. The wind-tunnel plot results of C_L and C_T versus advance ratio J show that these new wings have the same desirable aerodynamic characteristics compared to those of natural flapping flyers shown in Figure 3-10 (b). That is the lift coefficient C_L increases as the advance ratio J decreases.

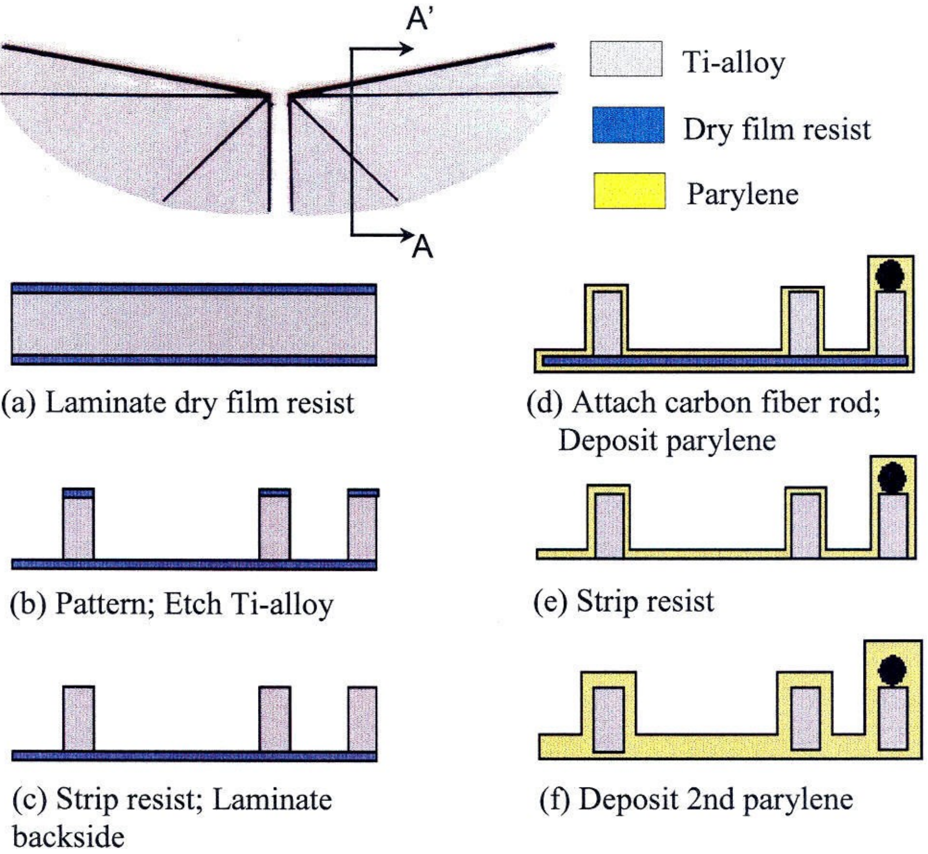

Figure 3-15: Fabrication process of stiffness-enhanced MEMS wings

3.3.4 Aerodynamic Performance of 3-D Wings

3.3.4.1 Non-MEMS Wings vs. MEMS Wings

The results of the wind-tunnel test have shown that nature-mimic MEMS wings with complicated structure, such as beetle and butterfly wings, perform poorly compared to the real wings. This is perhaps because the natural wings are much lighter and has more rigid leading-edge. Moreover, they also have three-dimensional (3-D) shapes. Therefore, instead of trying to mimic the natural wings, the effort is refocused on designing and fabricating simpler wings that can provide 3-D shapes to utilize the 3-D advantages and can generate high enough lift and thrust. Because MEMS wings are made from metal, these simpler wings can be bent to create a camber of the membrane to create 3-D wings.

We have fabricated and compared the aerodynamic performance of four types of wings. All of them have the span- and chord-length of 7 and 3 cm., respectively. The first two wings are non-MEMS wings and are constructed by using lightweight carbon-fiber rods as the wingframes. The wing membrane of type A is made from mylar and that of type B is made from paper. The last two designs are MEMS-based wings with titanium-alloy and parylene as wings' materials. Both of these wings feature one diagonal spar and 10° sweep-forward angle of leading-edge that enables the bending of the wings to create camber effect. The angles between the leading-edge and diagonal spar are 10° and 20° for type C and type D, respectively. Table 3-2 summarizes and lists the characteristics of these wings.

Table 3-2: Properties of various wing designs

Wing Types	**A**	**B**	**C**	**D**
Weight (each), [mg]	220	220	150	150
Frame material	C	C	Ti	Ti
Membrane material	Mylar	Paper	Parylene	Parylene
Angle of diagonal spa, °	45°	N/A	10°	20°
Planform LxW, [cm]	7x5	7x3	7x3	7x3

Note: C = carbon fiber rod; Ti = titanium-alloy
L = spanwise length; W = chordwise width

Lift and thrust coefficients resulted from the wind-tunnel tests are shown in Figure 3-16. The wings type A (carbon rod and mylar) yield the lowest lift coefficients for the given testing conditions (body inclination β = 45°, U = 3.3 m/s). The type-D MEMS wings (CIT7x3S20) with rigid leading-edge show the best results in terms of lift and thrust that are almost identical to the performance of the type-B paper wings. However, the type-D wings are much lighter than type-B (32% lighter). This is due to the advantage of using MEMS fabrication technology to fabricate the wing. Minimal glues are used. In addition, the power required to flap the type-D wings is also the lowest among the rest of the tested wings. Figure 3-17 shows the input power required to flap all four types of wings. Using the given electric test motor, flapping the wings type D at 25 Hz only requires 0.6 watt of power compared to 1 watt to flap type-A wings. Flapping at 30 Hz would require 1 watt while other wings would have needed more power.

Therefore, type-D MEMS wings (CIT7x3S20) will be used as reference wings for further studies in this thesis.

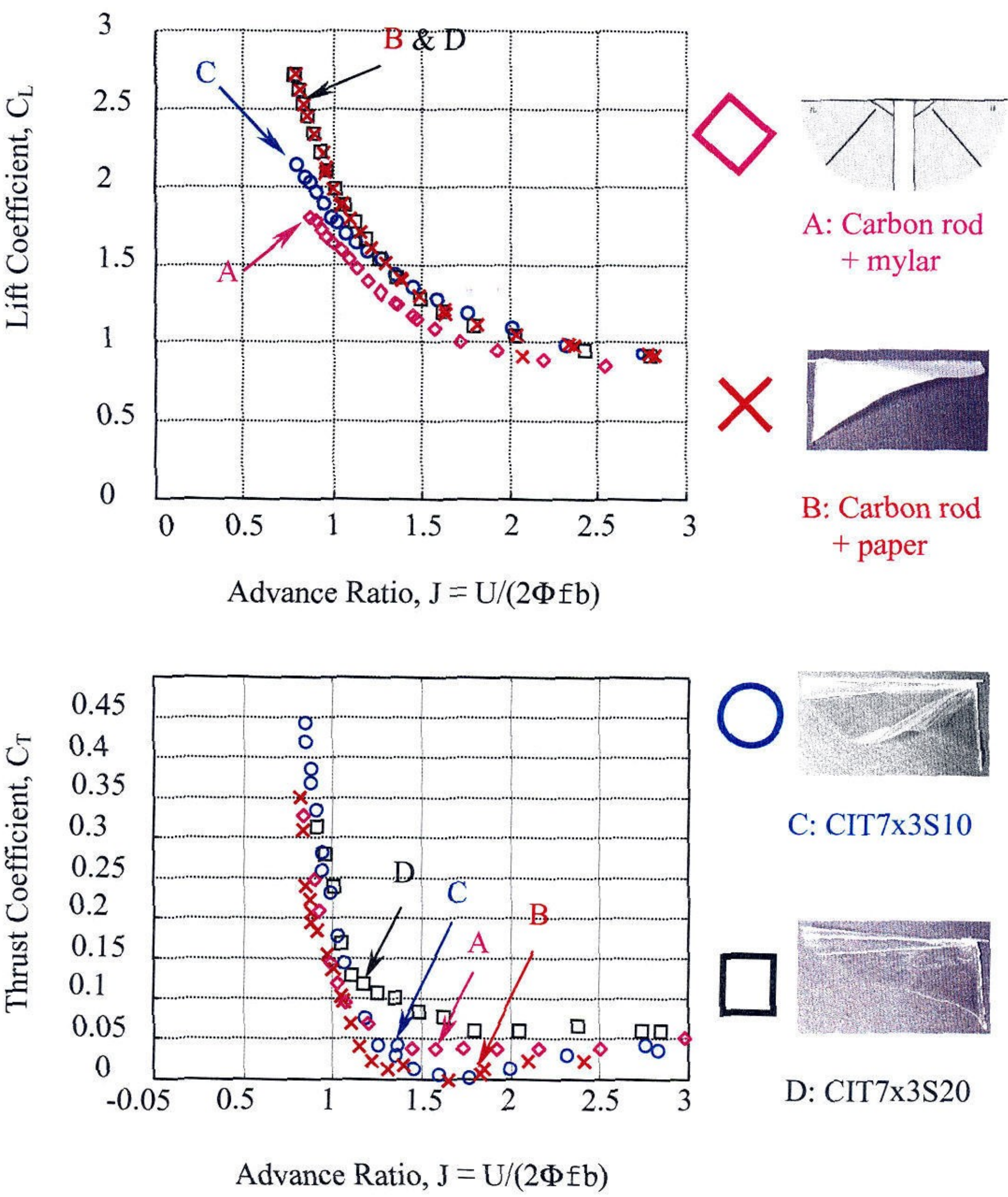

Figure 3-16: Lift and thrust coefficients of various types of wings

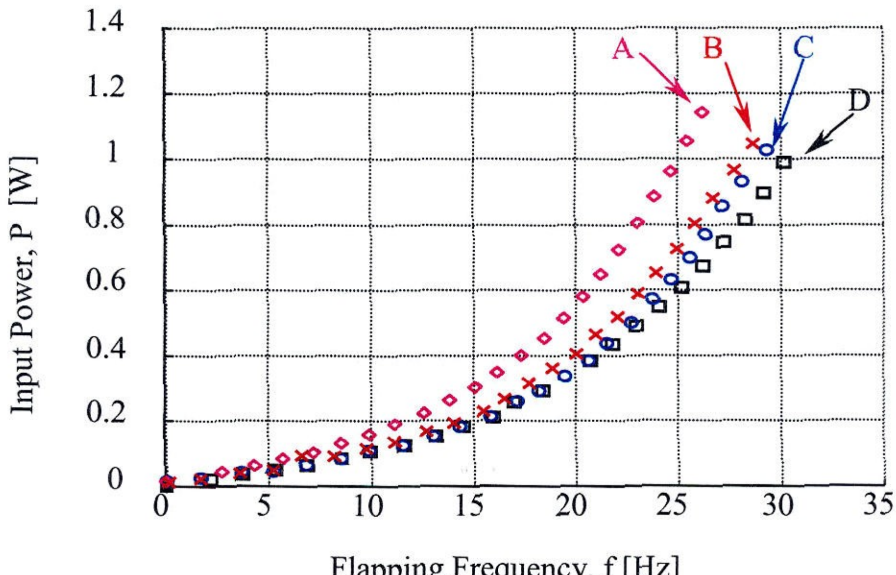

Figure 3-17: Input power

3.3.4.2 CIT7x3S20 vs. Other Designs of MEMS Wings

In addition to the two mentioned designs of MEMS wings (CIT7x3S10 and CIT7x3S20), other designs are also investigated with various variable values. This shows the advantage of the MEMS technology in which wings can be fabricated quickly when variables change. Various designs of MEMS wings are shown in Figure 3-18. In Figure 3-18 (a), the CIT7x3S10s2 has span- and chord-lengths of 7 cm. and 3 cm., respectively. Unless mentioned, all wings have a single diagonal spar and 10° forward-tilt angle of the leading-edge from the chord's normal. The code 'S10' denotes the 10° separation-angle between the leading-edge spar and the next diagonal spar. The number of diagonal spars between the leading-edge and the chord is denoted by 's2' while 'p' indicates different thickness of parylene membrane. In this study, different parameters are varied, i.e., span- and chord-lengths of the wings (Fig. 3-18 (a), (b), (d) & (f)), the angle of the supporting

diagonal spars (3-18 (a) & (c)), the number of the supporting diagonal spars (3-18 (c) & (d)), and membrane thickness (3-18 (d) & (e)).

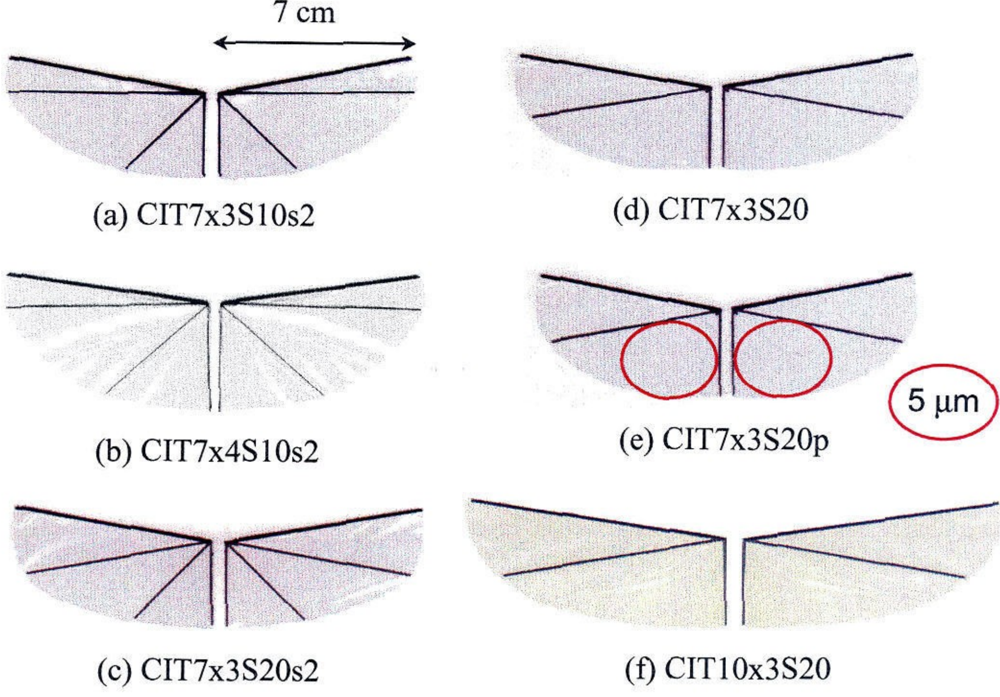

Figure 3-18: Various titanium-alloy MEMS wingframes with 15-µm membrane thickness

From the wind-tunnel test results, it is found that the 4-cm chord wings generate more lift when compared to the 3-cm wings. This is due to the fact that they have a larger wing area. However, they do not perform as well in terms of thrust performance. Varying the width of the diagonal spars generates little effect in terms of lift but the thrust performance can be improved up to 0.3 g when flapping at 25 Hz. This is because the spar with thinner width is more flexible. It is also found that the wings with two diagonal spars (s2) do not perform as well compared to those wings with only one diagonal spar. The reason is that there is less freedom for the movement of the membrane. Furthermore, varying the thickness of the membrane within the wing helps increase the performance of

the wings. By observing the insect wings, it is noticeable that the wing membrane is typically thicker at the leading-edge and is thinner at the trailing-edge. This provides distributive stiffness for each section of the wings and allows the wings to be flexible for aerodynamic advantages. Systematic distribution of the membrane thickness to control the membrane's shape has never been explored. This subject is worth it to investigate. By distributing integrated MEMS devices that can alter the thickness of the membrane onto the wings, aerodynamic performance can be altered as well. Such approach and device fabrication will be further discussed in chapters 5 and 6 where detailed fabrication and integration of MEMS device onto the MEMS wings are explored.

The comparisons of lift and thrust generated by all the CIT7x3 wing designs (shown in Figure 3-18 (a), (c), (d) & (e)) are presented in Figure 3-19. For the same size of wings, the lifts generated by type-D (CI7x3S20) and type-E (CIT7x3S20p) wings outperform those of type-A (CIT7x3S10s2) and type-C (CIT7x3S20s2) at the maximum achieved flapping frequency. This indicates that the number of diagonal spars is a factor. Having only one diagonal spar is better than having two because it allows the membrane to be more flexible. Except for type-A, the thrust meets the drag level requirement for cruising flight in all types of wings. The type-D wings (CIT7x3S20) show the best results in terms of lift, thrust, and power required when flapping at 30 Hz. Therefore, these wings are selected as a basic prototype model design for future wind-tunnel test.

The effect in aerodynamic performance of a larger wingspan is demonstrated in Figure 3-20. As expected, at the same flapping frequency, type-F wings (CIT10x3S20) with span-length of 10 cm. can generate much larger lift compared to the type-D wings (CIT7x3S20) with span-length of 7 cm. For instance, at 20 Hz, the type-D wings provide

about 5 g of lift while type-F generates almost 9 g of lift. However, for type-F wings, the maximum flapping frequency is only limited to about 23 Hz due to the loading limitation of the test motor. In terms of thrust, these wings barely make the drag requirement for this test. It also requires a much higher input power consumption of 1.5 watts in comparison to 1 watt of the type-D wings.

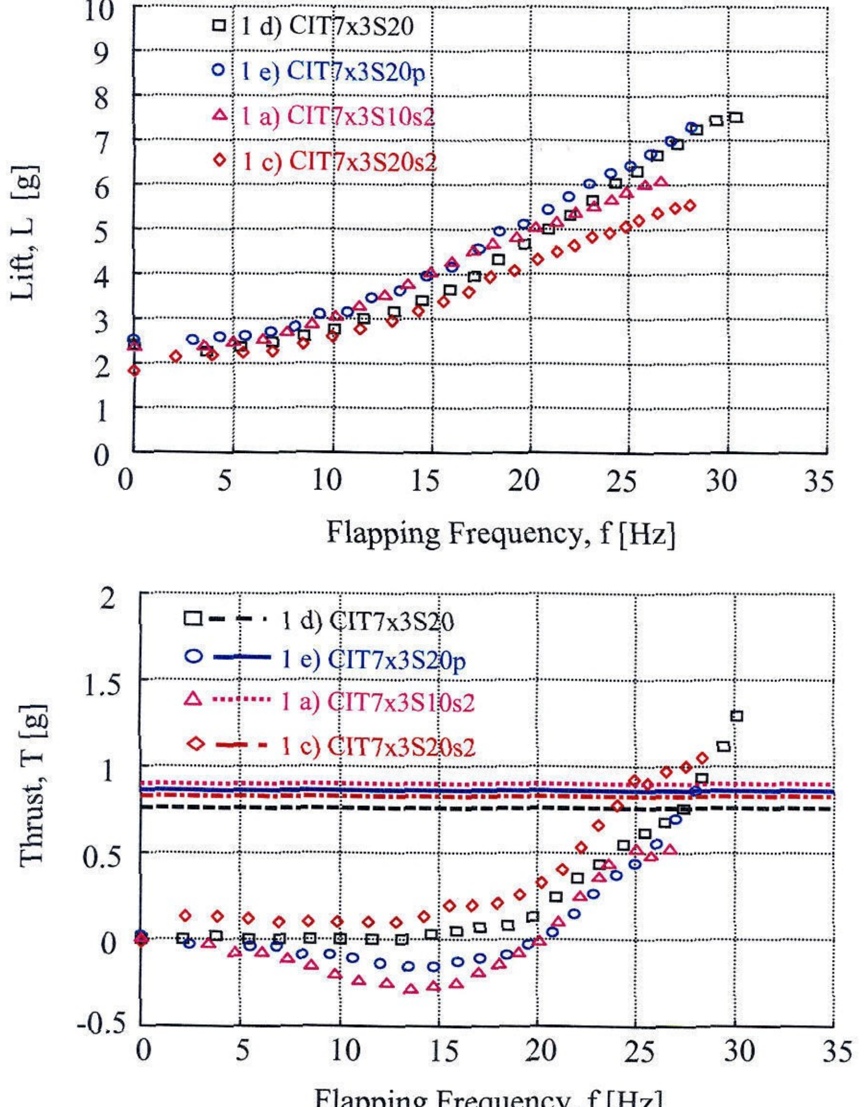

Figure 3-19: Comparison of lift and thrust performance of 7x3 wings in Figure 3-18

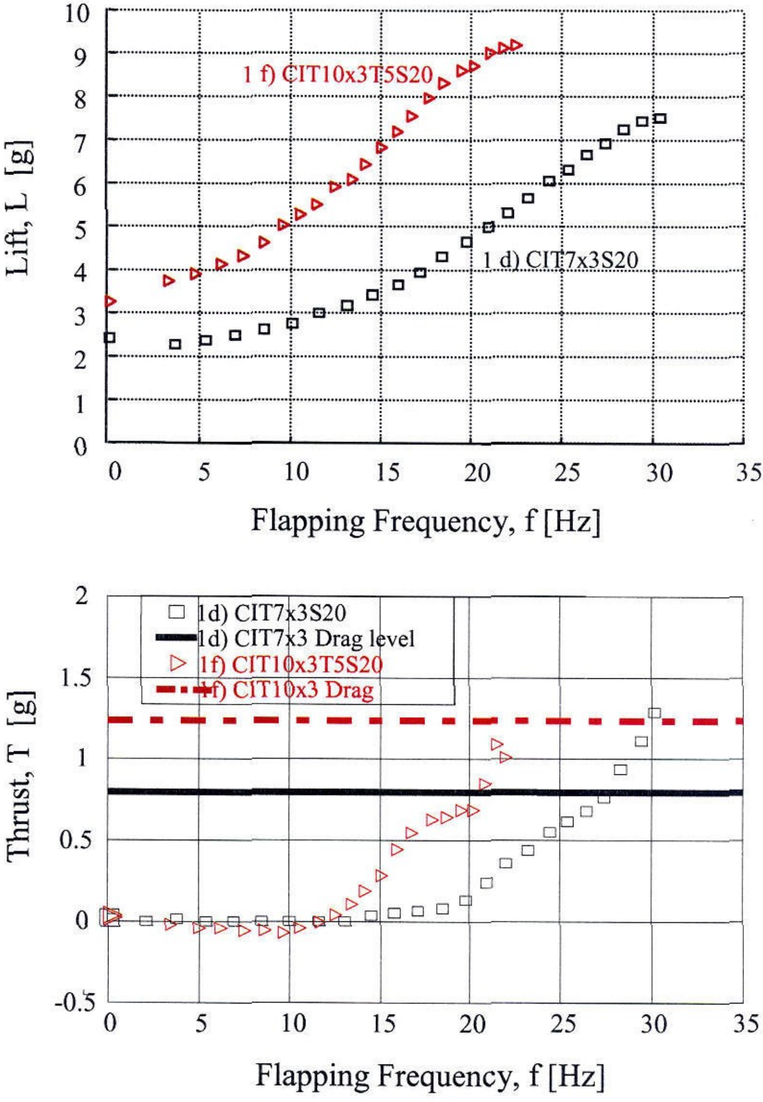

Figure 3-20: Comparison of lift and thrust of type-D (7x3) and type-F (10x3) wings

3.3.4.3 Effect of the Inboard Region

For the first time the effect of the inboard and outboard regions in relation to thrust and lift generations is identified. This effect is shown in Figure 3-21. Two sets of wings are compared where the inboard region of one set of wings is arbitrarily removed. Because the wingspeed varies along the span-length, the strength of the dynamic stall

vortex will also vary and thus the lift force. The angular flapping speed of the wings is higher towards the tips and leads to stronger amounts of vorticity in the outboard region of the wings. Therefore, it can be expected that the bulk of the lift is produced in the outboard region of the wings. Removal of the inboard region does not affect the lift coefficients as seen in Figure 3-21 because the vorticity in the outboard region is not affected. However, the thrust production is significantly influenced. The thrust performance of the wings without the inboard region deteriorates when compared to that of the wings with the inboard region, which is definitely an indication of the dependence of thrust on the inboard region.

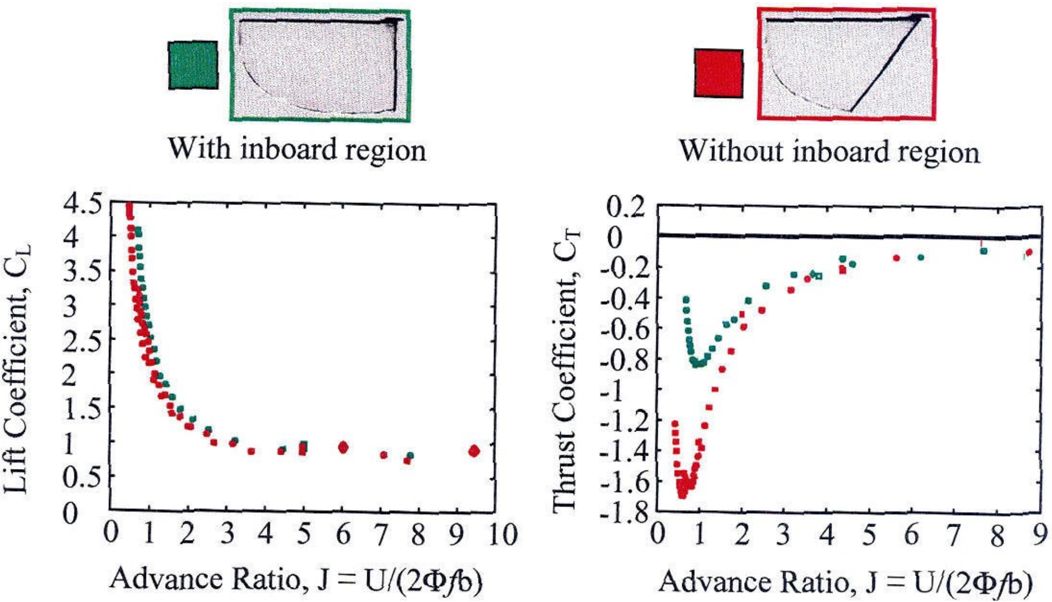

Figure 3-21: Effect of the inboard region

3.4 Summary

The mechanical and wind-tunnel tests performed on MEMS wings are analyzed and discussed as well as the aerodynamics of flapping flight. Wings with stiff leading-edge can produce higher lift coefficients for flapping flight. Flexible leading-edge wings generate negative lift coefficients for unsteady-state flows. A novel leading-edge stiffness-enhanced titanium-alloy wingframe technology has been developed using the existing MEMS technology. Several MEMS wings are fabricated with various parameters, such as chord- and spar-lengths, membrane thickness, number of spars, and sweep angles, differ. This ease of fabrication with several changes of variables also illustrates that only MEMS technology can quickly and systematically accommodate these types of studies.

Unsteady-state aerodynamic tests of these wings are performed in a low-speed wind tunnel. Among 7-cm. wings, the type-D wings (CIT7x3S20) show the best results in terms of lift, thrust, and the input power required. The type-F wings (CIT10x3S20) can generate much larger lift. However, their maximum flapping frequency is only limited to about 23 Hz and the wings require a high input power of 1.5 watts. We have also identified that the inboard region is primarily used to generate the thrust while the outboard region is used to generate the lift.

In order to further improve the aerodynamic performance of MEMS wings, the selective stiffness distribution control on the membrane is desired. It will help control the flexibility of the wings and how vortices are shed. This can be carried out by fabrication of MEMS actuator devices that can change the effective thickness of the parylene membrane. These actuators will be integrated onto the wings in the inboard and outboard

regions to help control the air flow as well as wing's stiffness. The novel technologies to fabricate the "actuator skins" will be developed and discussed extensively in chapters 4 and 5 in this thesis.

3.5 Bibliography

[1] S. Timoshenko and G. H. MacCullough, "Elements of Strength of Materials," 3rd edition, D. Van Nostrand Company, Inc., New York, 1949.

[2] T. N. Pornsin-Sirirak, Y. -C. Tai, H. Nassef, and C. -M. Ho, " Titanium-Alloy MEMS Wing Technology for A Micro Aerial Vehicle Application," *Sensors and Actuators, A: Physical*, vol. 89, Issue 1-2, pp. 95-103, Mar. 20, 2001.

[3] AeroVironment, Inc., Design Development Center, 4685-3H Industrial St., Simi Valley, CA 93063, (805) 581-2187, http://www.aerovironment.com.

[4] R. Dudley, "The Biomechanics of Insect Flight," Princeton University Press, New Jersey, 2000.

[5] C. P. Ellington and T. J. Pedley, "Biological Fluid Dynamics," *Proc. of Symposia of the Society for Experimental Biology number XLIX,* The Company of Biologists Limited, Cambridge, U.K., 1995.

[6] M. B. Fenton, P. Racey, and J. M. V. Rayner, "Recent Advances in the Study of Bats," Cambridge University Press, Cambridge, U.K., 1987.

[7] R. S. Shevell, "Fundamentals of Flight," 2nd edition, Prentice-Hall, Inc., New Jersey, 1989.

[8] J. M. V. Rayner, "A vortex theory of animal flight. Part 2. The forward flight of birds," *Journal of Fluid Mechanics*, vol. 91, pp. 731-763, 1979.

[9] M. Okamoto, K. Yasuda, and A Azuma, "Aerodynamic Characteristics of the Wings and Body of a Dragonfly," *J. of Experimental Biology*, vol. 199, pp. 281-294, 1996.

[10] S. Vogel, *Life in Moving Fluids*, 2nd edition., Princeton University Press, Princeton, 1994.

[11] T. N. Pornsin-Sirirak, Y. -C. Tai, H. Nassef, C. -M. Ho, "Unsteady-State Aerodynamic Performance of MEMS Wings," *Proc. International Symposium on Smart Structure and Microsystems 2000 (IS3M 2000)0*, The Jockey Club, Hong Kong, pp. G1-2, Oct. 19-21, 2000.

[12] C. Van Den Berg and C. P. Ellington, "The vortex wake of a 'hovering' model hawkmoth," *Philosophical Transactions of the Royal Society of London,* B 352, pp. 317-328, 1997.

[13] C. Van Den Berg and C. P. Ellington, "The three-dimensional leading-edge vortex of a 'hovering' model hawkmoth," *Philosophical Transactions of the Royal Society of London,* B 352, pp. 329-340, 1997.

[14] T. Maxworthy, "Experiments on the Weis-Fogh mechanism of lift generation by insects in hovering flight. Part 1. Dynamics of the 'fling'," *J. Fluid Mech.*, part 1, pp. 47-63, 1979.

[15] T. Weis-Fogh and M. Jensen, "Biology and physics of locust flight, I-IV," *Philosophical Transactions of the Royal Society of London,* B 239, pp. 415-584, 1956.

[16] A. G. Bennet, R. C. Obye, and P. M. Jeglum, "Ornithopter Aerodynamic Experiments," In: *Swimming and Flying in Nature* (ed. Wu, Brokaw, and Brennen), vol. 2, Plenum Press, New York, pp. 985-1000, 1975.

Chapter 4

Low-Temperature Parylene MEMS Technology

4.1 Introduction

In previous chapters, the detailed descriptions of the designs, fabrications, and test results of MEMS wing technology [1] using titanium-alloy [2] and parylene [3-14] as wingspars and membrane, respectively, have been discussed. It has been demonstrated that the stiffness of the leading-edge of the wings is important. The effect of the inboard and outboard regions of the wings in relation to thrust and lift generations is also discovered. It can be said that the bulk of the lift is produced in the outboard region of the wings where the vortex shedding occurs whereas the removal of the flexible inboard region affects the thrust. Hence, the conclusion is that providing distributive stiffness for each section of the wings and allowing the wings to be flexible in a certain section can certainly provide aerodynamic advantages. There has never been any report on the study of systematic distribution of the membrane thickness to control the membrane's shape.

This can be implemented by distributing the actuators in the area where the flexibility of the membrane can be affected after actuation of the devices. The shedding of the vortices can be controlled. Thus, the aerodynamic performance can be improved.

The further wind-tunnel experiments have indicated that aerodynamic thrust force produced by flapping is intimately related to the flexibility and the location of the wing membrane [15]. The comparison of the thrust performance of flexible wing membrane (mylar) to the rigid wing membrane (paper) is shown in Figure 4-1. The mylar wings, which are less rigid and have better flexibility than the paper wings, show higher thrust coefficients, hence higher thrust forces, compared to the more rigid paper wings. Therefore, in terms of thrust it is desirable to have wings with flexible membrane. Parylene is comparable to mylar and is a suitable choice.

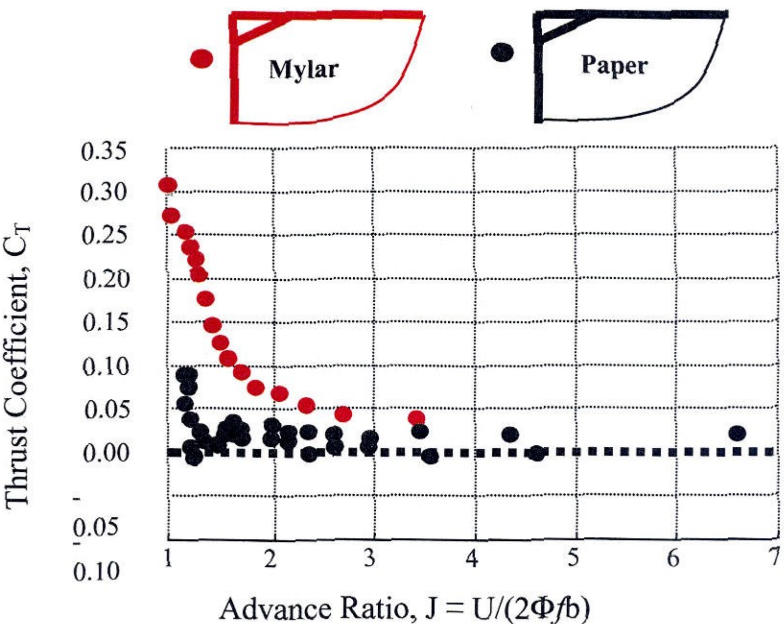

Figure 4-1: Aerodynamics thrust performance of wings with different membrane rigidity

This is a motivation to develop the low-temperature parylene MEMS technology and investigate the flexible parylene MEMS actuator membrane for micro adaptive flow control. By distributing actuators on the wing membrane, it is possible to have an active control of the flexibility of the wings to achieve optimal aerodynamic performance. This concept is illustrated in Figure 4-2. Before actuation, the offset vent holes on the diaphragm let the air move freely through the membrane; the membrane remains flexible. The pressures above and below the membrane are equal. Once actuated, the holes are sealed and the membrane behaves as a complete diaphragm. Pressure gradient exists. The thickness is also doubled. Therefore, the rigidity of the membrane increases; this will affect the aerodynamic performance. This kind of membrane will have important applications for adaptive airfoil because the wing loading can be controlled by simple electrostatic actuation.

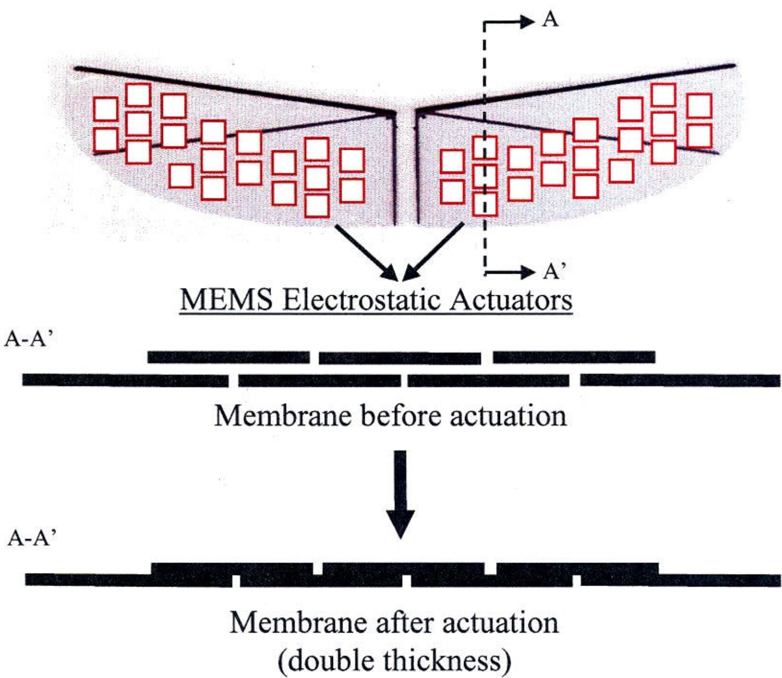

Figure 4-2: The concept of active wing with integrated MEMS actuator membrane

To demonstrate this feasibility, we first fabricate and test the flexible, large area parylene MEMS actuator membrane on a silicon chip. The load deflection test setup is built to collect data that will be fitted into the load deflection of composite rectangular membrane model [16]. It will be demonstrated that the effective thickness of the parylene composite membrane changes after the actuation is performed.

4.2 Low-Temperature Parylene MEMS Technology

The development goal of the low-temperature MEMS technology is to enable the large area, wafer-sized actuator "skins" fabrication of the both passive and active parylene MEMS devices. They are to be integrated onto the MEMS wings to control and study their aerodynamic effects. However, we must first demonstrate a successful fabrication and testing of the conceptual actuators on a silicon chip before translating the concept on to skins. The chip fabrication process is discussed in detail in section 4.3. The test results and discussions are presented in section 4.4. The fabrication of parylene skins will be discussed in full detail in chapter 5.

As mentioned before, in order to realize the concept of free-standing parylene electrostatic actuator devices as illustrated in Figure 4-2, the fabrication success of free-standing parylene diaphragm must first be demonstrated. The success in releasing the parylene structures from the photoresist sacrificial layers as well as the prevention of structure stiction are key elements. Various anti-stiction techniques, including the anti-stiction posts and BrF_3 dry etching, are used to release the free-standing diaphragm. These techniques are further discussed in detail in the next section.

4.2.1 Anti-Stiction Techniques

In surface micromachining, the adhesion of microstructures to adjacent surfaces is called "stiction." Stiction can occur after the device is packaged, or due to over-range input signals, or electromechanical instability (in-use adhesion) [17]. It can also occur during the release process when the surface tension of the draining rinse liquid draws the microstructures into contact with the underlying substrate (release-related adhesion). In this thesis, the latter type is the area of particular concern because the device and skin releasing method is primarily by wet etching, i.e., photoresist disassociation in acetone.

Figure 4-3 shows a schematic diagram of a microstructure drying process that leads to stiction. The parylene cantilever beam is patterned and rested on top of the photoresist sacrificial layer. After the acetone disassociation of photoresist, if the length of the beam is greater than the critical length [18-20], the meniscus force will pull down the microstructure, causing stiction problem. Strong adhesion is generally caused by capillary, electrostatic or Van der Waals forces, and in some cases by chemical forces such as hydrogen bonding and solid bridging [21].

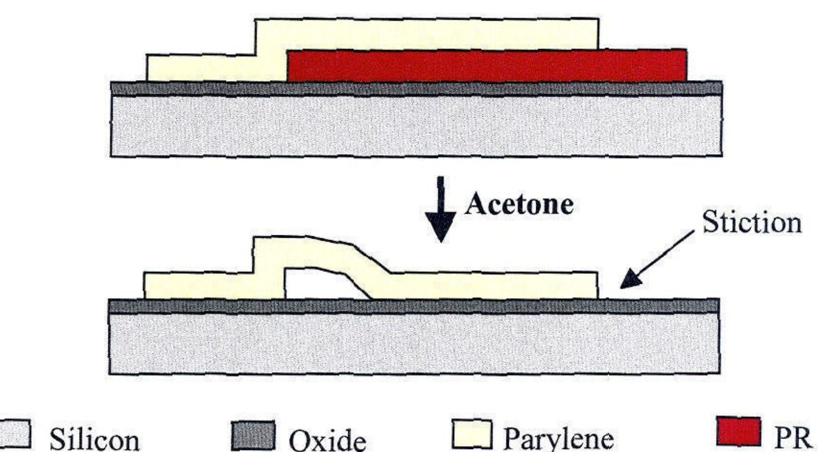

Figure 4-3: Schematic diagram of the microstructure drying process that leads to stiction

Because parylene is a soft material, after releasing the structures, stiction tends to occur. To alleviate the stiction problem, there are a few approaches to chemically or mechanically modify the surface of the substrate in order to reduce adhesion in microstructures. The following techniques are applied during the fabrication of the parylene MEMS electrostatic actuator diaphragm.

4.2.1.1 Parylene Surface Roughening

A surface roughening of parylene can be performed by briefly etching parylene in oxygen plasma environment. The roughening is performed in 200 mT of O_2 at 200 watts of power for 1 minute. Wang, *et al.* [22] used this technique to reduce the stiction between two parylene layers in the fabrication of parylene micro check-valve. In the case that the top layer of parylene collapses, by roughening the surface area of the bottom parylene layer, the contact area is reduced. Thus, the stiction can be minimized. This method is not an absolute prevention of stiction. It is, however, often used in combination with other techniques to ensure that all possible methods are considered in reduction of stiction.

4.2.1.2 Anti-Stiction Posts

Compared to polysilicon ($E \approx 130$ GPa), bulk parylene is soft and has a fairly low Young's modulus ($E \approx 4.5$ GPa) [23]. During the final release of parylene structures from the sacrificial photoresist, the surface tension can pull the structures down if the size of the released structures is greater than the critical length. Similar to the concept of micro dimples used to alleviate friction in rotating micromachines [24-25], an array of posts can be used to prevent the stiction after releasing to form a free-standing parylene

beam. Mastrangelo *et al.* [26] had successfully developed a two-step release process that uses an array of posts to prevent stiction. They fabricated parylene posts to prevent the stiction of polysilicon structures to the substrate during PSG etching. These posts act as "feet" to support the structures, preventing the collapse. Then later the structures can be released by etching away the parylene posts with oxygen plasma. In conjunction with the use of BrF_3 dry etching [27], this concept is adapted to fabricate a free-standing parylene actuator diaphragm on a silicon chip which will be explained in detail in section 4.3. The schematic diagram shown in Figure 4-4 illustrates the anti-stiction post concept.

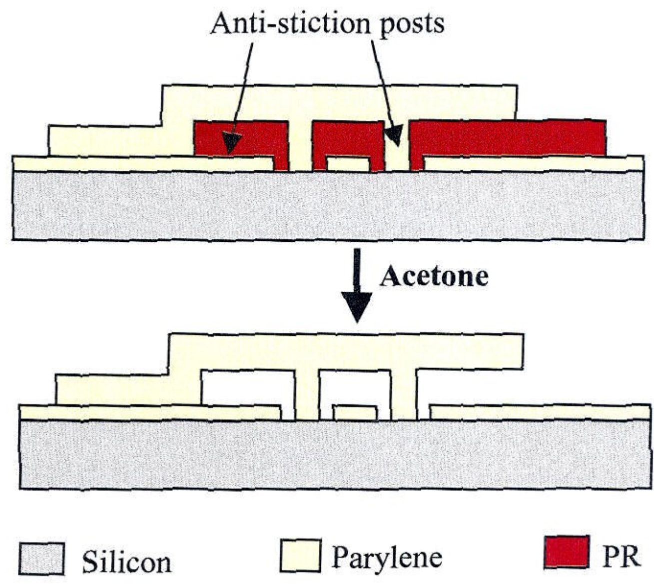

Figure 4-4: Schematic diagram of the anti-stiction method using posts

4.2.1.3 Self-Assembled Monolayers (SAM)

The SAM approach is to perform a surface treatment of the substrate by coating it with thin organic films called self-assembled monolayers (SAM) [28-32]. This process eliminates release stiction by effectively reversing the shape of the water meniscus which

forms underneath microstructures during the drying process. The SAM-coated surface is hydrophobic which repels water (water contact angle ≥ 90°) [28]. Depending on the type of the surface and whether the surface is treated with SAM, the contact angles will vary. The effect can be quantified by measuring the contact angle using the Ramé-Hart NRL contact angle goniometer. In this experiment, goniometer model 100-00 is used [33].

For hydrophilic SiO_2 surfaces, the water contact angle is < 30°. For the SAM-treated surface, the water contact angle increases to ≥ 110° [28]. The measurement of these contact angles on SiO_2 and SAM-treated silicon surfaces is shown in Figure 4-5.

Table 4-1 shows the measured contact angles on sample surfaces before and after treating with SAM agents (OTS). After the treatment of the gold and parylene surfaces with SAM, the contact angles increase from 60° to 91° and 78° to 120°, respectively. The values increase over 50% for the measured contact angles in both cases. The photoresist surface is not treated by SAM because IPA, a part of SAM surface treatment solution, can attack photoresist. Thus, such measurement would not be meaningful and therefore is not applicable.

Table 4-2 shows the contact angles measured on the parylene surfaces that are treated with various chemicals ranging from HMDS, IPA, and acetone, to developer and OTS. Some surface treatments have reduced the contact angles and make the surface more hydrophilic while others have increased the contact angles. It is clear that SAM-treated surface is hydrophobic with the contact angle much higher than 90° (about ~120°) while roughening of the parylene surface reduces the contact angle from 78° to less than 5° and the surface becomes hydrophilic.

Table 4-1: Measured contact angles before and after treating with SAM

Surface Type	**Before SAM**	**After SAM**
Gold	60°	91°
AZ Photoresist	68°	n/a
Parylene	78°	120°

Table 4-2: Contact angle measurements on various-treated parylene surfaces

Parylene Surface Treatment	**Measured Contact Angle**	**Comment**
None	78°	-
HMDS	78°	No effect
H_2O_2	78°	No effect
AZ developer (1 min)	78°	No effect
Piranha at 80° C	68°	Reduce contact angle
BrF3	67°	Reduce contact angle
IPA	63°	Reduce contact angle
Methanol	60°	Reduce contact angle
AZ 351 developer (1 min)	60°	Reduce contact angle
Roughen surface	<5°	Reduce contact angle
Acetone	83°	Increase contact angle
A-174	86°	Increase contact angle
OTS (SAM)	120°	Increase contact angle

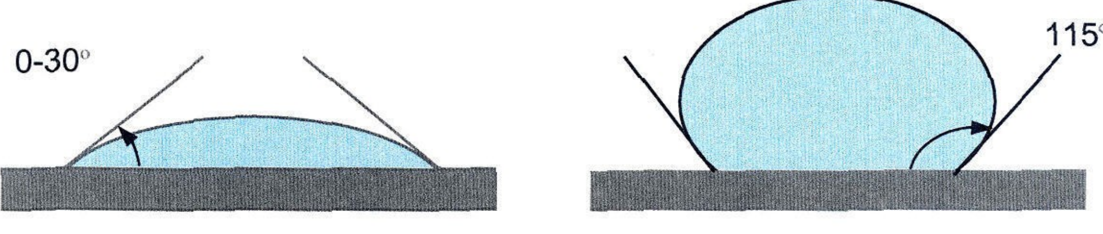

Oxide-coated surface Fluorinated SAM-coated surface

Figure 4-5: Water contact angle on oxide- and SAM-coated Si surface [28]

In the fabrication process of the parylene MEMS electrostatic actuator diaphragm, the SAM agent used is n-octadecyltriclorosilane, or OTS. The precursor molecules have a chemical formula of $C_{18}H_{37}SiCl_3$. The SAM coating, or silanization, of silicon with a R-$SiCl_3$ precursor, where R is the long chain $C_{18}H_{37}$ alkyl group, begins with the hydrolysis of the polar headgroup which converts the Si-Cl bonds to Si-OH (silanol) groups. Thus this process requires some amount of water to hydrolyze the Si-Cl headgroups (changing them to Si-OH). However, too much water will initiate bulk polymerization of the $SiCl_3$ and often manifests itself as particulates on the wafer. By selecting anhydrous solvents, such as iso-octane, this problem can be minimized.

Once the silanol groups are formed, they are strongly attracted to the hydrophilic surface of oxidized silicon. They condense and react with silanols on the other precursor molecules and silanols on the surface to produce covalent siloxane bonds, Si-O-Si. These monolayers are molecular thin. For OTS, the film is about 28 A° [28]. After the monolayer formation, the solid-vapor interface consists of long alkyl tail groups of the precursor molecule. These long alkyl tail groups make the surface hydrophobic. Therefore, after the surface of the device is coated with SAM agent, when the wafer is pulled out of the water, the surface should be dry.

Typically for the parylene MEMS electrostatic actuator diaphragm process, the SAM process sequence is introduced after the complete release of photoresist in acetone solvent. The wafer is then submerged in IPA for 10 minutes and moved into iso-octane bath for another 10 minutes. The solution of 1 mM of OTS in iso-octane is prepared. This roughly corresponds to a drop of OTS in 50 ml of iso-octane solution. Next, the wafer is submerged in the SAM bath for another 10 minutes. It is noticeable that the polarity of the solutions in this sequence decreases. After the SAM bath, the sequence is reversed. The wafer is placed in iso-octane and then IPA baths for additional 10 minutes each. Finally, the wafer is placed in a DI water bath before pulling out dry. This SAM process sequence is summarized in Figure 4-6.

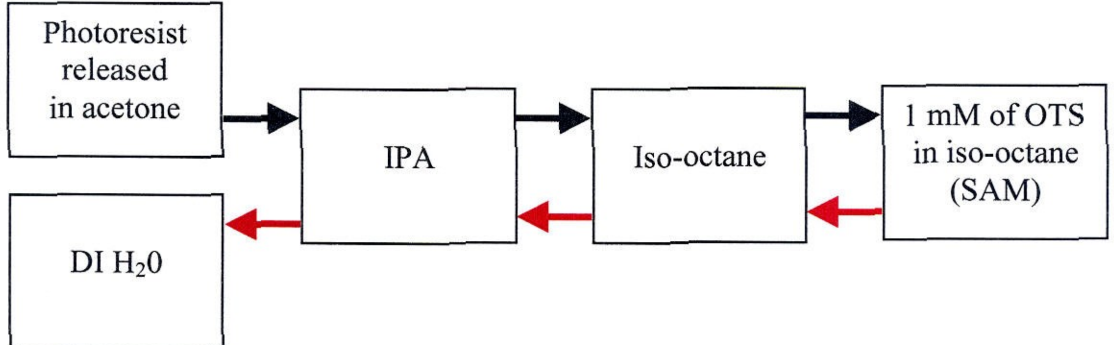

Figure 4-6: SAM process sequence

4.2.1.4 BrF_3 Dry Etching of Silicon

The pure gaseous BrF_3 etching process is isotropic [27]. It has a high vapor pressure at room temperature which implies ease of use and high etching rate. It also has a superb selectivity over SiO_2 (3000:1), Si_3N_4 (400-800:1) and photoresist (1000:1) [27]. Moreover, gaseous BrF_3 etching is also free of tension. Thus the stress of the membrane

is minimized. This silicon dry etching method is the last release step to free parylene posts that are rested on thin silicon membrane. Yao, *et al.* [20] has reported successful releases of parylene microstructures, such as cantilevers, bridges, and diaphragms, using composite sacrificial layers of photoresist and sputtered amorphous silicon. Stiction could occur in large structures after the releasing of photoresist in acetone. However, a subsequent etch of the sacrificial amorphous silicon in BrF_3 vapor can completely free the structures providing that the structures have restoring force larger than the gravitational force. The schematic diagram in Figure 4-7 presents the anti-stiction technique using BrF_3 dry etching of silicon to release structures.

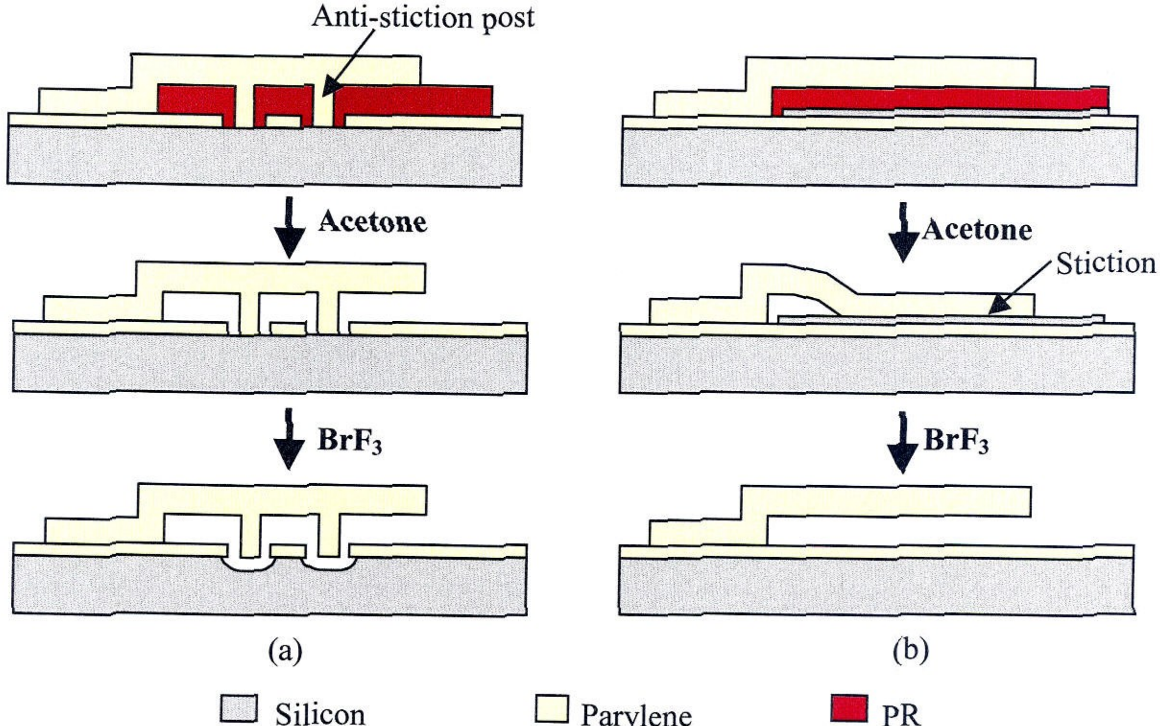

Figure 4-7: Schematic diagram of the anti-stiction technique using BrF_3 dry etching of silicon; (a) Post structures; (b) Thin film amorphous silicon

Each anti-stiction technique offers different advantages which may or may not prevent the occurrence of stiction if it is used alone. Therefore, the combination usage of these techniques is recommended in order to release large parylene structures successfully.

4.3 Parylene MEMS Electrostatic Actuator on a Silicon Chip

One advantage of using parylene as a MEMS material is that it can be deposited at a low temperature, i.e., room temperature. Because of parylene's flexibility, it has already proven to be a good material for MEMS wing membrane. It is useful to further investigate the fabrication of a MEMS device that can be used to alter the aerodynamic performance of MEMS wings. This work using parylene is novel and has never been reported before by any researchers. Therefore, it presents several challenges that must be overcome. For example, stiction, cracking, and wrinkle are some of the prominent problems. These issues will be further discussed in section 4.3.3.

4.3.1 Design

The design goals of the parylene MEMS electrostatic actuator on a silicon chip are to make the device with large diaphragm actuation area, reasonable actuation voltage, and vent-through holes with posts to minimize stiction. In addition, the chip must be able to fit into a chip holder for the load deflection test. The test is to verify the effective thickness of the composite membrane after actuation. Figure 4-8 illustrates the cross-sectional view of the actuator device.

The large area of 2-mm x 2-mm parylene electrostatic actuator diaphragm consists of two metallized electrodes sandwiched in between two parylene layers, each

with 2.8-μm thickness. There are nine rows and nine columns of posts. The diameter of each post is 20 μm and the spacing is 200 μm apart from each other. Photoresist is used as a sacrificial layer and is released by acetone to free the diaphragm. There are eight rows and eight columns of photoresist etching holes which also act as vent holes. Each hole has a 50-μm diameter and is spaced at 200 μm from each other. These vent holes allow air to flow through freely. Once the device is actuated, two layers of parylene form a single, thicker parylene membrane and seal the vent holes to prevent air flow.

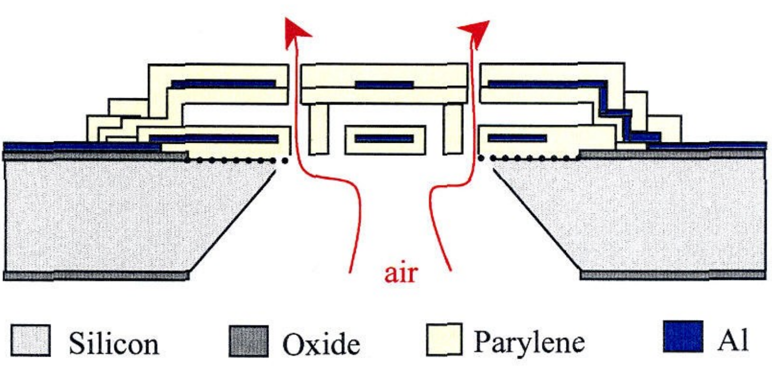

Figure 4-8: Cross-sectional view of the actuator device

4.3.2 Rectangular Diaphragm Theory

The performance characteristics of diaphragms are affected by their shapes, sizes, and boundary conditions. The deflection, linearity, and stress level caused by pressure loading depend a great deal on the shape of the diaphragm whether it is round, square, rectangular, or any other configuration. In addition to shape, the variation of thickness, rigid centers, and materials used all have a strong influence on characteristics of the diaphragm.

In general, the condition of rectangular plates with fixed edges, shown in Figure 4.9, involves rigorous mathematical analysis. However, by using coefficients α, the stress analysis and deflection of rectangular plates may be expressed simply as [34]:

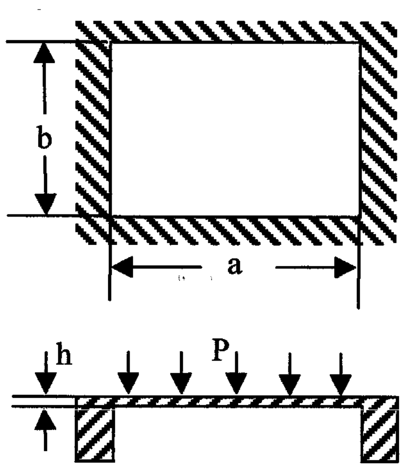

Figure 4-9: Rectangular diaphragm with fixed edges

$$y = \alpha\left(\frac{Pa^4}{Eh^3}\right)(1-v^2) \quad (4\text{-}1)$$

where

y = center membrane deflection,

P = pressure,

E = Young's modulus of membrane material,

h = membrane thickness,

a = the dimension of the shorter side of the rectangular membrane,

v = Poisson's ratio of membrane material,

α = a non-dimensional deflection coefficient which depends on the ratio (b/a).

For a square membrane, the ratio (b/a) is equal to 1. The deflection coefficient α is equal to 0.0151.

Equation (4.1) shows the deflection of a uniformly loaded rectangular diaphragm with rigidly clamped at outer edges and can be rearranged to be written in dimensionless form as

$$\left(\frac{Pa^4}{Eh^4}\right) = \frac{1}{\alpha(1-v^2)}\frac{y}{h} \tag{4-2}$$

For small deflections of flat plates, this equation is governed by a linear equation. If we plot $\left(\frac{Pa^4}{Eh^4}\right)$ vs. $\frac{y}{h}$, the slope is $\alpha(1-v^2)$. This only accounts for the bending load. The general characteristic equation for a flat diaphragm taking into account both the bending and tensile loads may be obtained by the method of superposition:

$$\left(\frac{Pa^4}{Eh^4}\right) = \left(\frac{Pa^4}{Eh^4}\right)_{bending} + \left(\frac{Pa^4}{Eh^4}\right)_{tension} \tag{4-3}$$

For a square diaphragm, the value of α is 0.0151. Rewriting equation (4-2) yields

$$\left(\frac{Pa^4}{Eh^4}\right) = \frac{66.225}{(1-v^2)}\frac{y}{h} \tag{4-4}$$

By the use of energy method which has been derived by Timoshenko and Woinowsky-Kreiger [35], the strain energy due solely to the stretching of the middle surface yields central deflection y to be

$$y = 0.318a\left(\frac{Pa}{Eh}\right)^{\frac{1}{3}} \tag{4-5}$$

which may also be written in the dimensionless form as

$$\left(\frac{Pa^4}{Eh^4}\right) = 31.1\left(\frac{y}{h}\right)^3 \tag{4-6}$$

By the method of superposition, the characteristic equation for the performance of a "square" diaphragm is the superposition of equations (4-5) and (4-6), hence

$$\left(\frac{Pa^4}{Eh^4}\right) = \frac{66.225}{(1-\nu^2)}\frac{y}{h} + 31.1\left(\frac{y}{h}\right)^3 \tag{4-7}$$

Equation (4-7) can be expressed in the characteristics form of pressure:

$$P = \frac{66.225}{(1-\nu^2)}\frac{Eh^3}{a^4}y + 31.1\frac{Eh}{a^4}y^3 \tag{4-8}$$

Equation (4-8) may also be written in the characteristic cubic equation form:

$$P = cy + dy^3 \tag{4-9}$$

where the coefficients c and d are $\frac{66.225}{(1-\nu^2)}\frac{Eh^3}{a^4}$ and $31.1\frac{Eh}{a^4}$, respectively.

The set up for the load-deflection test of the parylene MEMS actuator diaphragm operates in the large reflection range where the deflection is much greater than the thickness of the membrane. Large deflections of rectangular plates introduces nonlinear terms and are governed by two fourth-order, second-degree partial differential equations [34]. Theoretical performance calculations are lengthy and complex. An analysis of the load-deflection using energy minimization approach considering the contribution of internal tensile stress can be used instead [16, 35-36]. The total strain energy of the rectangular membrane can be obtained by superposition of the strain energy of deformation and the elastic strain energy due to internal tensile stress. The strain energy due to bending can be neglected in the case of very thin films with a deflection many times larger than their thickness. The Fourier expansion of the true solution with two undetermined constants is chosen for the functional form of the displacement of a point in

the membrane. Then the work input into the membrane is calculated to obtain the total potential energy of the membrane. Subsequently, the total potential energy is minimized with respect to the two constants in the displacement equations, making use of the principle of virtual displacements, resulting in a relationship between the load and the deflection. This method yields the load-deflection relationship of a large deflection rectangular membrane, shown in Figure 4-10, to be [16]

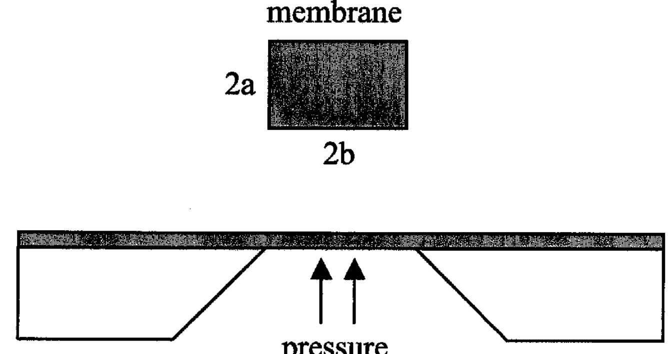

Figure 4-10: Schematic view of a rectangular membrane sample

$$P = \frac{C_1 \sigma h}{a^2} y + \frac{C_2 E h}{a^4} y^3 \tag{4-10}$$

where

C_1 and C_2 = numerical constants,

P = the applied pressure,

E = the Young's Modulus,

y = the height of the deflection,

σ = the internal stresss,

h = the membrane thickness,

a = the half-width of the short side of the membrane.

The constants C_1 and C_2 given in equations (4-11) and (4-12), respectively, are the values determined by the membrane shape ratio n, which is equal to (a/b), and Poisson's ratio v of the material. These constant can be written as

$$C_1 = \frac{\pi^4(1+n^2)}{64} \tag{4-11}$$

$$C_2 = \frac{\pi^6}{32(1-v^4)}\{\frac{9+2n^2+9n^4}{256} - [\frac{(4+n+n^2+4n^3-3nv(1+n))^2}{2\{81\pi^2(1+n^2)+128n+v[(128n-9\pi^2(1+n^2)]\}}]\} \tag{4-12}$$

For a square membrane, n is equal to 1. Assuming that the Poisson's ratio v is 0.25 for parylene material, C_1 and C_2 are calculated to be 3.04 and 1.83, respectively.

4.3.3 Fabrication Process

The fabrication process of the parylene MEMS electrostatic actuator diaphragm is shown in Figure 4-11. Double-sided alignment marks are etched onto both sides of the silicon wafers. The wafers are then cleaned in piranha solution. Next, 1.8-μm thermal oxide is grown at 1050 °C by wet oxidation. This layer is used as a mask during formation of the diaphragm by KOH etching. It is important to make sure that the thickness of oxide is enough to protect the wafer through the entire KOH etching. The oxide is patterned from the backside. Then the substrate is time-etched in KOH solution at 58 °C for 23 hours to form a thin 25-um-thick silicon diaphragm. This thin silicon diaphragm is used as a support for the parylene anti-stiction posts and will be released by BrF_3 dry etching during the last fabrication step. Care must be taken during the handling of wafers at this stage because the membranes are delicate and easy to be punctured.

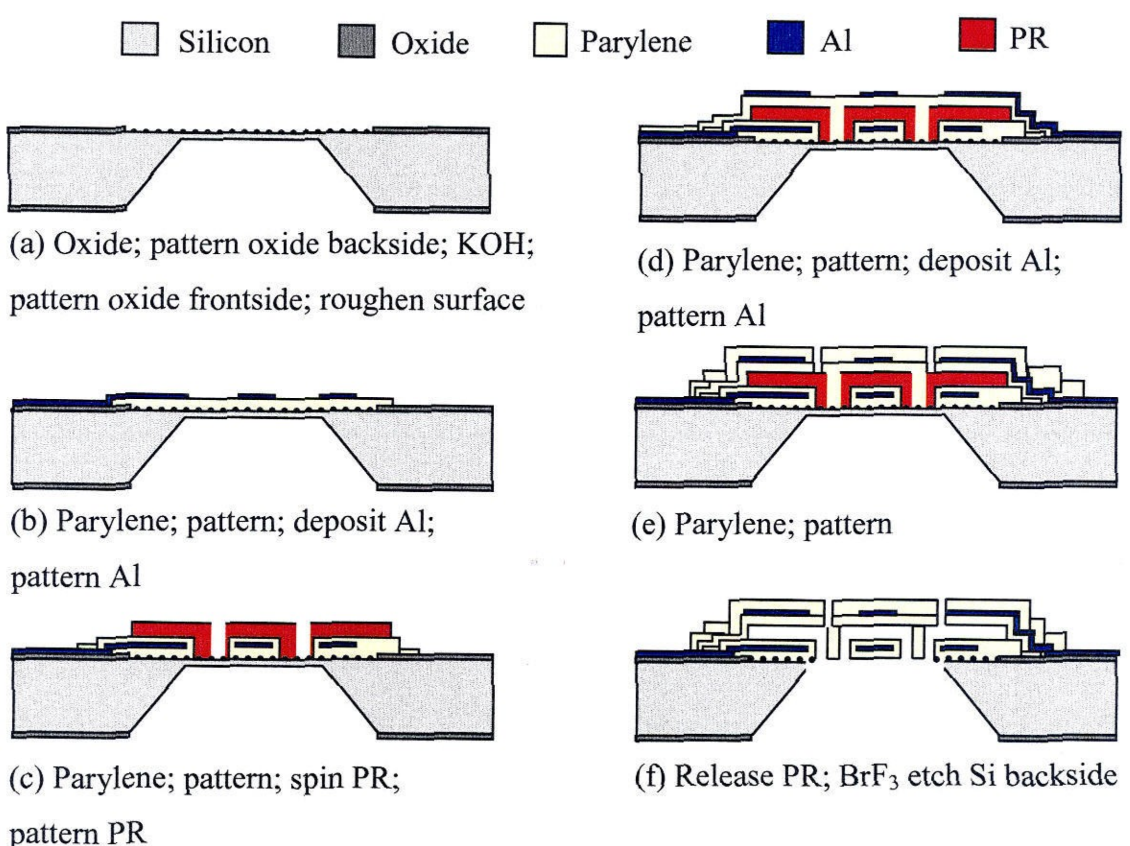

Figure 4-11: Fabrication process flow for the parylene MEMS electrostatic actuator diaphragm

Following the KOH etching, the remaining front-side oxide is patterned to create a membrane area of 2-mm x 2-mm. The surface is then roughened with a 3 mT pulse of BrF_3 for one minute. This helps improve the adhesion of parylene to the substrate surface. Otherwise, the parylene can peel off easily on a smooth surface of silicon. Next, the solution of 0.5% A-174 silane adhesion promotion (DI H_20: IPA: A-174 = 100:100:1 in volume) is used to further improve the adhesion. A-174 silane is commercially available and can be obtained from Specialty Coating Systems, Inc. [37]. The solution is stirred for at least 30 seconds and allowed to settle for a minimum of 2 hours. The wafers are then submerged in the prepared solution for 15 minutes and air-dried for another 15

minutes. Then they are rinsed with IPA for 15-30 seconds and dried in a convection oven for 30 minutes at 70 °C.

Next, the first thin film layer of parylene-C is deposited and patterned, followed by parylene surface roughening in O_2 plasma. Chrome, gold, and chrome (Cr/Au/Cr) composite layers are evaporated as ground electrodes and patterned. These layers have thickness of 100, 2800, and 100A°, respectively. The first layer of Cr is used to improve the adhesion to Au. The second layer of Cr improves the adhesion to the second parylene layer because A-174 silane adhesion promotion creates a good bonding strength between CrO_2 and parylene interface. The use of O_2 plasma to roughen the parylene surface before depositing Cr layer is also important because without roughening the surface, the delamination of metal layers sometimes occur due to poor adhesion. The next layer of parylene is then deposited to seal the ground electrodes. This will prevent short-circuiting the ground and the top electrodes.

After spinning on the 4-μm-thick sacrificial layer photoresist, the resist is patterned to form a mold for anti-stiction posts. The post size is 20 μm in diameter and its spacing is 200 μm apart. The third layer of parylene is then deposited and the surface is roughened in O_2 plasma. Top Cr/Au/Cr layers are evaporated and patterned, followed by the deposition of the last parylene layer. Finally, the top parylene membrane is etched to open up areas for electrode contacts and holes for acetone to release photoresist. These holes are 50 μm in diameter and 200 μm apart. The wafers are then submerged in acetone to release the diaphragm. After releasing the diaphragm, the wafer is submerged in SAM solution of octadecyltrichlorosilane (OTS) to make the surface hydrophobic.

Because parylene has a low Young's modulus, acetone surface tension can easily pull down the structures to the substrate to cause stiction. These challenges must be overcome. The anti-stiction technology developed is a combination of steps that use both wet photoresist dissolution and silicon dry etching in BrF_3. Photoresist dissolution allows large area parylene membrane to be released and BrF_3 dry etching prevents stiction. Also, surface of parylene is roughened in O_2 plasma to reduce the contact area of stiction. SAM coating of octadecyltrichlorosilane (OTS) is used to treat the parylene surface to become hydrophobic. Finally, anti-stiction posts are utilized to reduce the collapse of the top parylene membrane after wet releasing of photoresist.

A successfully-fabricated parylene MEMS electrostatic actuator is shown in Figure 4-12. Figure 4-13 shows the comparison of diaphragms with and without anti-stiction techniques. It is clear that stiction occurred on a 400-µm x 400-µm parylene diaphragm when no anti-stiction methods were used, whereas no stiction occurred for a much larger membrane of 2-mm x 2-mm parylene diaphragm in which posts and other stiction preventive methods were applied.

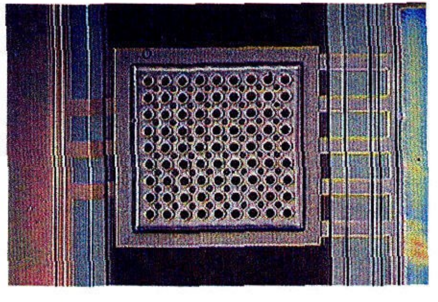

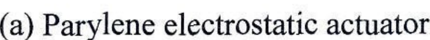

(a) Parylene electrostatic actuator

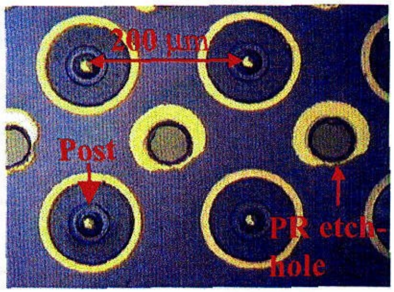

(b) Anti-stiction posts

Figure 4-12: Fabricated parylene MEMS electrostatic actuator diaphragm with anti-stiction posts and photoresist etching holes

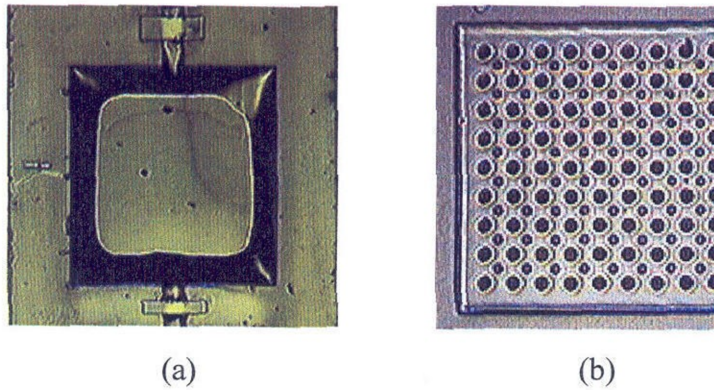

(a) (b)

Figure 4-13: Comparison of diaphragms without and with anti-stiction techniques; (a) 400-μm x 400-μm parylene diaphragm; (b) 2-mm x 2-mm parylene diaphragm

It is important to note that if there are no posts between the top and the bottom parylene membranes, freeing of large parylene membrane always causes stiction. As shown in Figure 4-13 (a), without anti-stiction posts, the top layer of parylene on a test structure is pulled down by meniscus force after releasing photoresist in acetone. The anti-stiction posts (Figure 4-13 (b)), which are rested on a thin silicon diaphragm, help prevent the stiction. This thin silicon diaphragm is then released by BrF_3 dry etching. The dry etching is performed at the last step because the membranes will no longer be in contact with any wet chemicals that can cause stiction to occur.

4.3.4 Processing Challenges

There are several issues worth mentioning regarding the processing of parylene. The first is related to the adhesion of the thin film metal layer to parylene. Figure 4-14 shows the adhesion effect of the metal layer to the roughened parylene surface. If the parylene is etched by oxygen plasma at 200 mT with 200-watts power for one minute (roughening), the adhesion of the metal layer is very good as seen in Figure 4-14 (a). By

roughening the surface of parylene, the contact surface area increases. On the other hand, without roughening, the metal layer peels off from the interface as seen in Figure 4-14 (b). It is also found that roughening the surface area not only improves the adhesion of the metal layer to parylene, but also improves the adhesion of any thin films that can be deposited by thermal evaporation or sputtering to parylene. If this step is not performed, the metal layer is likely to peel off during the fabrication process. This will destroy the device and the fabrication process will have to be started over again.

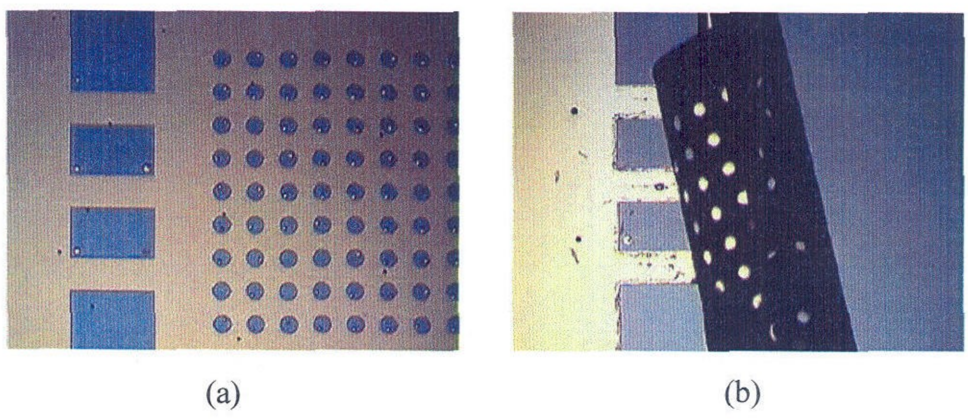

(a) (b)

Figure 4-14: The effect of parylene surface roughening; (a) Good adhesion of metal layer to the roughened parylene; (b) Poor adhesion of metal layer to the non-roughened parylene

The second issue is the cracking of parylene film during a long oxygen plasma patterning which is performed at 400 mT of O_2 at 400-watts power. The parylene etching rate at this setting is about 1 μm for every 6 minutes of etch time. The loading effect also contributes to the non-uniformity of the etching. Thus over-etching is typically performed. If the parylene layer is thick, longer time is needed to completely etch through the parylene layer. This contributes directly to the cracking and delaminating of the parylene film due to overheating. This effect is shown in Figure 4-15.

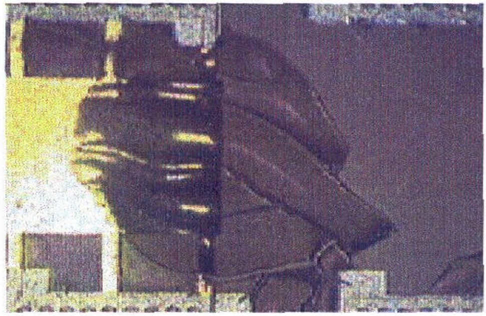

Figure 4-15: Cracking of parylene film after a long oxygen plasma patterning

One remedy is to rotate and cool the wafer down after each etch cycle. For example, the wafer is cooled down and rotated 180° in the chamber after each 6-10 minutes of etch cycle. This also improves the uniformity of the etching on the wafer. Another solution is to reduce the number of wafers in the chamber during etching. However, the wafers must still be cooled down and rotated in order to get rid of the cracking problem.

The third issue pertains to fusion of the top layer of parylene to the bottom layer. This problem happens during the deposition of the 3rd parylene layer after patterning the sacrificial photoresist. If the sacrificial photoresist is not thick enough to completely cover the corner steps of the bottom parylene layers, the corners are exposed during the next parylene deposition and can cause the top and bottom layers to be fused together. This fusion prevents the two parylene layers to separate after the release of photoresist, and actuation cannot be performed. Hence the device fails. Therefore, it is important that during this step the photoresist thickness must be carefully measured. If one coating of photoresist cannot cover the corner step, an additional spin coat is necessary. If all these problems are prevented, a great deal of time can be saved because the refabrication of the devices can be avoided.

4.4 Test Results and Discussions

4.4.1 Electrostatic Actuation Test

The use of electrostatic actuation for MEMS devices is attractive because of high energy density and large force [38]. Considering two parallel conductive plates with area A and are separated by a gap d, if a voltage V is applied across the plates, the attractive electrostatic force, F_e, is given by:

$$F_e = \frac{\varepsilon_0 A V^2}{2d^2} \tag{4-13}$$

where ε_o is the permittivity of the free space. The electrostatic force is non-linear because it depends on $(1/d^2)$. The design actuator area is 2 mm x 2 mm and the gap distance is 4 μm. If 50 volts of voltage is applied to the plates, the electrostatic force can be calculated to be about 28 mN. The pressure per unit area can also be calculated and yields 690 Pa, which is much larger than the calculated wing loading (~200 Pa).

The actuation test is performed using the probe station connected to a high voltage power supply model PS310/1250 – 25W from Stanford Research Systems, Inc. [39]. First, it is important to test for any shortages of the top and bottom electrodes. This can be performed by an ohmmeter. The measurement of the resistance between the ground and the high voltage pads should yield an infinite value. This implies an open circuit and indicates that there are no shortages between the two metal layers. Otherwise, the high voltage power supply would trip during the actuation test.

The test results show that the diaphragm without SAM coating requires a higher minimum voltage in order to move the membranes. The minimum actuation voltage is 30 volts. With SAM coating, the minimum actuation voltage is reduced to 13 volts. The

variation is perhaps because SAM coating helps reduce the stiction that may hinder the movement of the diaphragm during actuation. Hence lesser actuation voltage is required. Voltages between 30 to 150 volts are applied to actuate the device and the results are repeatable. Any higher voltages outside this range would not guarantee the performance of the device because the breakdown between the top and bottom metal layers is likely to occur. This breakdown is shown in Figure 4-16.

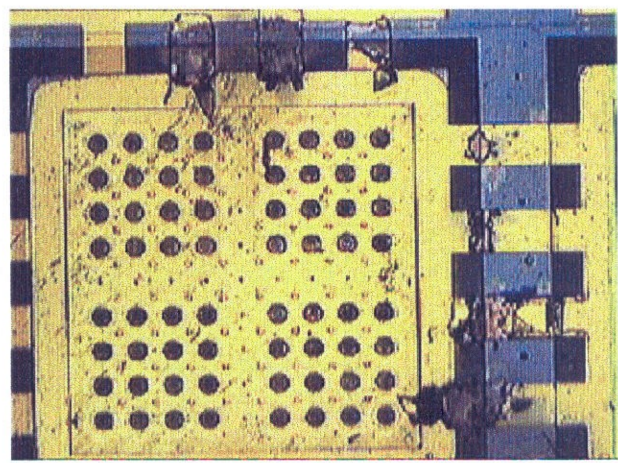

Figure 4-16: Breakdown of the device after applying high voltage

4.4.2 Load Deflection Test

The load-deflection method is used to determine the internal residual stress, σ, and Young's modulus, E, of the thin film membrane structure [16]. Theoretically, by measuring the relationship between the pressure and the center deflection of a rectangular membrane, σ and E values can be computed. For a square membrane with large deflection, the relationship between the applied pressure, P, and the deflection height, y, shown in equation (4-10), can be written as

$$P = 3.04\frac{\sigma h}{a^2}y + 1.83\frac{Eh}{a^4}y^3 \tag{4-14}$$

where

P = the applied pressure,

E = the Young's Modulus of the material,

y = the height of the central deflection,

σ = the internal stress,

h = the membrane thickness,

a = the half-width of the membrane.

The internal stress and Young's modulus appear in a linear and a cubic term of y, respectively.

The load deflection test setup is constructed as shown in Figure 4-17. The chip holder is connected to an air flow channel. By applying pressure to the backside of the membrane, the deflection distance can be measured by using a microscope to calibrate the deflection height. The measurements are performed both before and after actuation on the same die. The actuation voltage is set at 70 volts. Figure 4-18 shows the membranes before and after the back pressure is applied. Before actuation, the vent holes are open. After actuation, two layers of parylene membranes form a thicker membrane and the vent holes are closed. The membrane becomes more rigid. The deflection height decreases as seen in the plotted result in Figure 4-19. The actuation effect on the stiffness of the membrane can be noticed clearly.

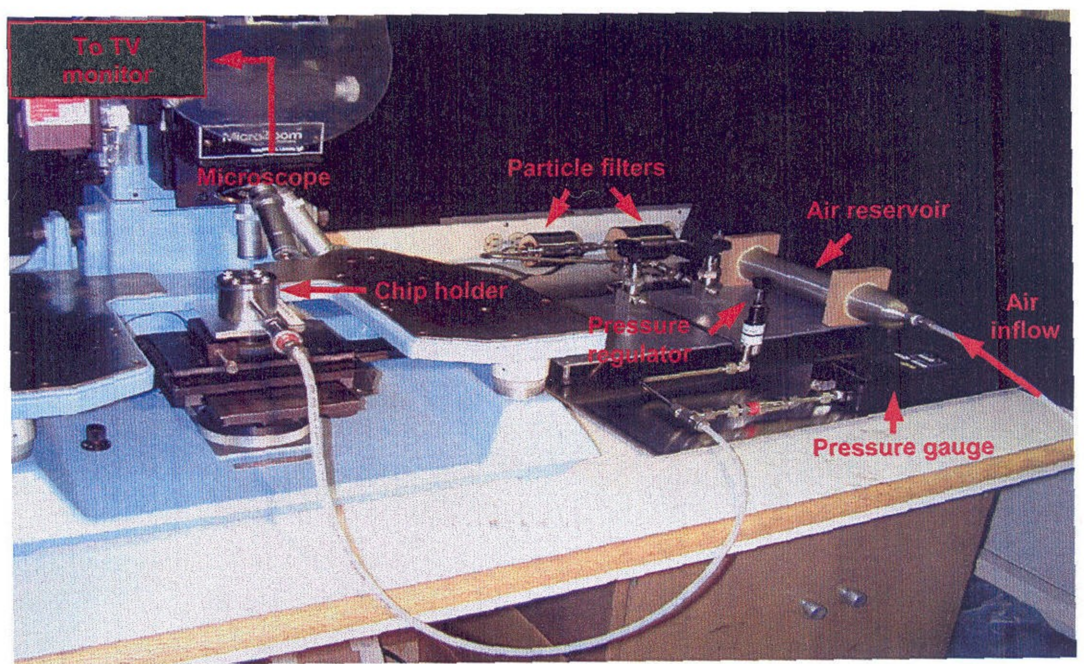

Figure 4-17: Load deflection test setup

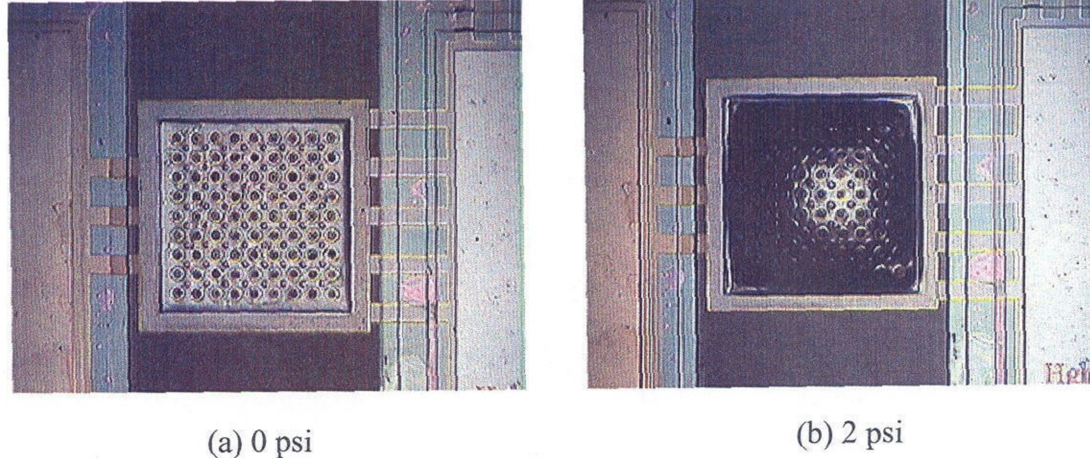

(a) 0 psi (b) 2 psi

Figure 4-18: Load deflection test; (a) Before applying back pressure (0 psi); (b) After applying back pressure (2 psi)

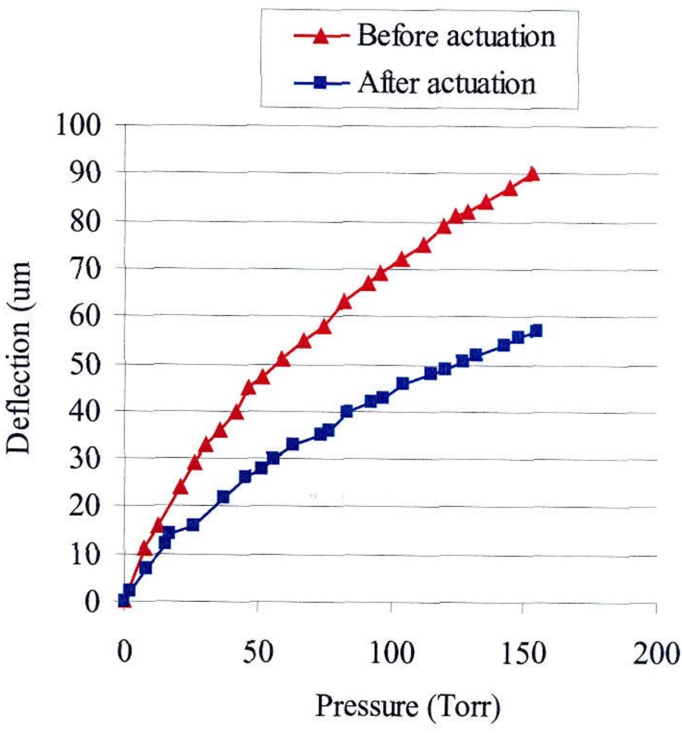

Figure 4-19: Load deflection test result indicates the stiffness change after actuation

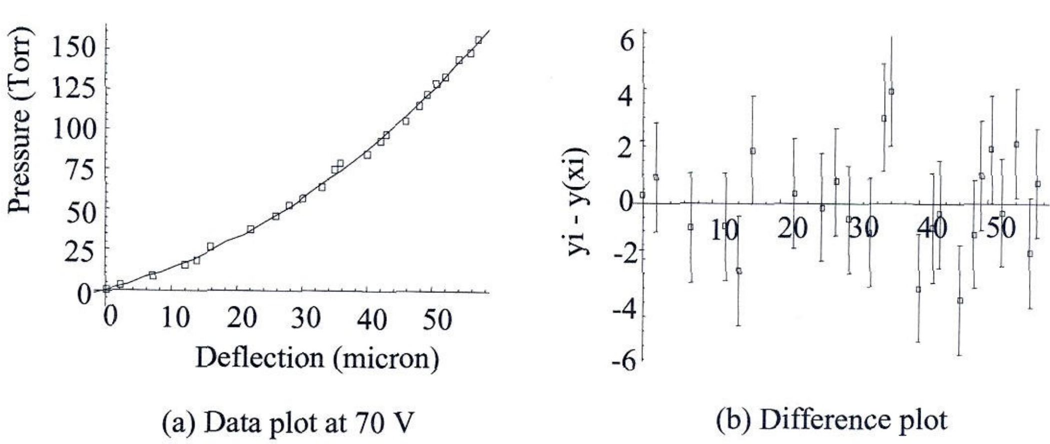

(a) Data plot at 70 V

(b) Difference plot

Figure 4-20: Model fit for after-actuation test data

Figure 4-20 shows the after-actuation data fitted by the load deflection for rectangular membrane model using equation (4-14). After the device is actuated, it is assumed that parylene MEMS electrostatic membrane behaves as a rectangular membrane. The model fit yields the relationship between the pressure, P, and the deflection height, y, as follows:

$$P = 1.561y + 0.000363y^3 \tag{4-15}$$

By comparing equation (4-15) to equation (4-14), the effective thickness after actuation can be determined. Using the coefficient of the cubic term in equation (4-15) with square dimension a = 1000 μm and Young's modulus of parylene E = 4.5 GPa ($3.36\text{x}10^7$ Torr), this results in the calculated effective thickness h to be 5.9 μm. The actual deposited diaphragm thickness is 5.6 μm, which is agreeable to the calculated effective thickness and within 5% difference. Therefore, the functionality of this flexible parylene MEMS electrostatic actuator diaphragm is proven. In addition, this method also yields the stress σ of parylene to be about 11.6 MPa.

4.5 Summary

The low-temperature parylene MEMS technology has been developed to fabricate parylene electrostatic actuator device for aerodynamic control. A large 2-mm x 2-mm parylene MEMS electrostatic actuator valve diaphragm is successfully designed and fabricated. The process includes the novel anti-stiction technologies that are crucial to successfully release large area parylene actuator membranes. The anti-stiction technologies include the combination usage of anti-stiction posts, SAM coating, surface roughening, and BrF_3 dry etching. The initial actuation voltage of this device is as low as

13 volts. However, a higher operational voltage, i.e., 70 volts, should be used to successfully actuate and hold down the membranes. The effective thickness of the composite diaphragm is calculated by fitting the load-deflection test data into a theoretical load deflection for rectangular membrane model. The result yields an effective thickness of 5.9 μm, which is very close with the actual measured thickness of 5.6 μm of the composite membranes.

The next step is to translate the low-temperature parylene MEMS technology from a diaphragm on a single silicon chip to a "skin" on the entire wafer. This skin is designed to be a totally free-standing and flexible parylene MEMS electrostatic actuator membrane. This novel technology is very challenging because the final released skin will have no structural support of bulk silicon at all. The skin releasing technology will be developed and described in the chapter 5. The chapter will also describe the integration of these flexible actuator membranes onto the membrane of MEMS wings. In addition, the wind-tunnel test results will be presented and discussed.

4.6 Bibliography

[1] T. N. Pornsin-Sirirak, S. W. Lee, H. Nassef, J. Grasmeyer, Y. -C. Tai, C. -M. Ho, and M. Keennon, "MEMS Wing Technology for a Battery-Powered Ornithopter," *Proceedings of the 13th IEEE Annual International Conference on MEMS 2000*, Miyazaki, Japan, pp. 799 – 804, Jan. 23-27, 2000.

[2] American Society for Metals, *Metal Handbook*, 9th edition, vol. 3, pp. 388-391, 1980.

[3] Parylene Conformal Coatings Specifications and Properties, Specialty Coating Systems, Inc., 5707 West Minnesota Street, Indianapolis, IN 46241, Tel: (800) 356-8260, Fax: (317) 240-2073.

[4] P. K. Wu, G. R. Yang, L. You, D. Mathur, A. Cocoziello, C. -I. Lang, J. A. Moore, and T. -M. Lu, "Deposition of High Purity Parylene-F Using Low Pressure Low Temperature Chemical Vapor Deposition," *Journal of Electronic Materials*, vol. 26, no. 8, pp. 949-953, 1997.

[5] L. Wolgemuth, "Assessing the Performance and Suitability of Parylene Coating," *Medical Device & Diagnostic Industry Magazine*, Aug. 2000.

[6] P. K. Wu, G. -R. Yang, J. F. McDonald, and T. -M. Lu, "Surface Reaction and Stability of Parylene N and F Thin Films at Elevated Temperatures," *Journal of Electronic Materials*, vol. 24, no. 1, pp. 53-58, Jan. 1995.

[7] H. Yasuda, B. H. Chun, D. L. Cho, T. J. Lin, D. J. Yang, and J. A. Antonelli, "Interface-Engineered Parylene C Coating for Corrosion Protecion of Cold-Rolled Steel," *Corrosion Science*, vol. 52, no. 3, pp. 169-176, Mar. 1996.

[8] G. E. Loeb, R. A. Peck, and J. Martyniuk, "Toward the Ultimate Metal Microelectrode," *Journal of Neuroscience Methods*, vol. 63, pp.175-183, 1995.

[9] R. Sabeti, E. M. Charlson, and E. J. Charlson, "Selective Deposition of Parylene," *Polymer Communications*, vol. 30, pp. 166-169, June 1989.

[10] E. M. Charlson, E. J. Charlson, and R. Sabeti, "Temperature Selective Deposition of Parylene-C," *Polymer Communications*, vol. 30, pp. 166-169, June 1989.

[11] P. F. Man, D. K. Jones, and C. H. Mastrangelo, "Microfluidic plastic capillaries on silicon substrates: A new inexpensive technology for bioanalysis chips." *Proc. IEEE, The 10th Annual International Workshop on Micro Electro Mechanical Systems (MEMS'97)*, Nagoya, Japan, pp. 311-316, Jan. 26-30, 1997.

[12] X. Q. Wang, A. Desai, Y. -C. Tai, L. Licklider, and T. D. Lee, "Polymer-based Electrospray Chips for Mass Spectrometry," The *12th IEEE International Conference on Micro Electro Mechanical Systems (MEMS '99)*, Florida, USA, pp. 523-528, Jan. 17-21, 1999.

[13] X. Q. Wang, Q. Lin, and Y. -C. Tai, "A Parylene Micro Check Valve," The *12th IEEE International Conference on Micro Electro Mechanical Systems (MEMS '99)*, Florida, USA, pp. 177-182, Jan. 17-21, 1999.

[14] X. Yang, J. M. Yang, X. Q. Wang, E. Meng, Y. -C. Tai, and C. -M. Ho, "Micromachined Membrane Particle Filter," *The 11th Annual International Workshop on Micro Electro Mechanical Systems (MEMS '98)*, Heidelberg, Germany, pp. 137-142, Jan. 25-29, 1998.

[15] T. N. Pornsin-Sirirak, Y. -C. Tai, H. Nassef, and C. -M. Ho, "Unsteady-State Aerodynamic Performance of MEMS Wings," *International Symposium on Smart*

Structures and Microsystems 2000 (IS^{3}M), The Jockey Club, Hong Kong, pp. G1-2, Oct. 19-21, 2000.

[16] O. Tabata, K. Kanahata, S. Sugiyama, and I. Igarashi, "Mechanical Property Measurements of Thin Films Using Load-Deflection of Composite Rectangular Membranes," *Sensors and Actuators, 20,* pp. 135 – 141, 1989.

[17] M.W. Judy and R. T. Howe, "Polysilicon Hollow Beam Lateral Resonators," *Digest of Technical Papers, The 7th International Conference on Solid-State Sensors and Actuators (Transducer'93)*, Yokohama, Japan, pp. 54-57, June 7-10, 1993.

[18] C. H. Mastrangelo and C. H. Hsu, "Mechanical Stability and Adhesion of Microstructures Under Capillary Forces: Part I: Basic Theory," *IEEE Journal of Microelectromechanical Systems*, vol. 2, pp. 33-43, 1993.

[19] N. Tas, T. Sonnenberg, H. Jansen, R. Legtenberg, and M. Elwenspoek, "Stiction in Surface Micromachining," *Journal of Micromechanics and Microengineering,* vol. 6, pp. 385-397, 1993.

[20] T. J. Yao, X. Yang, and Y. -C. Tai, "BrF_3 Dry Release Technology for Large Freestanding Parylene MEMS," *Digest of Technical Papers, The 11th International Conference on Solid-State Sensors and Actuators (Transducers '01),* Munich, Germany, pp. 652-655, June 10-14, 2001.

[21] R. Maboudian and R. T. Howe, "Critical Review: Adhesion in Surface Micromechanical Structures," *Journal of Vacuum Science and Technology B*, 15 (1), pp. 1-20, Jan/Feb 1997.

[22] X. Q. Wang, Q. Lin, and Y. -C. Tai, "A Parylene Micro Check Valve," *The 12th IEEE International Conference on Micro Electro Mechanical Systems (MEMS '99)*, Florida, U.S.A., pp. 177-182, Jan. 17-21, 1999.

[23] X. Yang, C. Grosjean, and Y. -C. Tai, "A Low Power MEMS Silicone/Parylene Valve," *Technical Digest, Proceedings of the 1998 Solid-State Sensor and Actuator Workshop (Hilton Head '98)*, pp. 316-319, June 8-11, 1998.

[24] L. S. Fan, Y. -C. Tai, and R. S. Muller, "IC-processed electrostatic micromotors," *Tech. Digest, IEEE INT. Electron Devices Meet.*, San Francisco, California, U.S.A., pp. 666-669, Dec. 11-14, 1988.

[25] W. C. Tang, T. C. H. Nguyen, and R. T. Howe, "Laterally Driven Polysilicon Resonant Microstructures," *Proceedings, IEEE Micro Electro Mechanical Systems Workshop (MEMS '89)*, Salt Lake City, Utah, U.S.A., Feb. 20-22, 1989, pp. 53-59.

[26] C. H. Mastrangelo and G. S. Saloka, "A Dry-Release Method Based on Polymer Columns for Microstructure Fabrication," *Proceedings, IEEE Micro Electro Mechanical Systems Workshop (MEMS '93)*, Fort Lauderdale, Florida, U.S.A., pp. 77-81, Feb. 7-10, 1993.

[27] X. Q. Wang, X. Yang, K. Walsh, and Y. -C. Tai, "Gas-Phase Silicon Etching with Bromine Trofluoride," *Digest of Technical Papers, The 9th International Conference on Solid-State Sensors and Actuators (Transducers '97)*, Chicago, IL, vol. 2, pp. 1505-1508, June 16-19, 1997.

[28] R. Maboudian, "Self-Assembled Monolayers as Anti-Stiction Coatings for Surface Microstructures," *Digest of Technical Papers, The 10th International Conference on*

Solid-State Sensors and Actuators (Transducer'99), vol. 1, Sendai, Japan, pp. 22-25, June 7-10, 1999.

[29] M. R. Houston, R. Maboudian, and R. T. Howe, "Self-Assembled Monolayer Film as Durable Anti-Stiction Coatings for Polysilicon Microstructures," *Solid-State Sensor and Actuator Workshop,* Hilton Head, South Carolina, pp. 42 – 47, June 2-6, 1996.

[30] U. Srinivasan, M. R. Houston, R. T. Howe, and R. Maboudian, "Alkylsiloxane-based Self-Assembled Monolayers for Stiction Reduction in Silicon Micromachines," *Journal of Micro-Electro-Mechanical Systems*, 7, pp. 252-260, 1998.

[31] U. Srinivasan, J. D. Foster, U. Habib, R. T. Howe, R. Maboudian, D. C. Senft, and M. T. Dugger, "Lubrication of Polysilicon Micromechanisms with Alkylsiloxane Self-Assembled Monolayers," *Technical Digest, Proceedings of the 1998 Solid-State Sensor and Actuator Workshop (Hilton Head '98)*, pp. 156-161, June 8-11, 1998.

[32] C. Cabuz, E. I. Cabuz, T. R. Ohnstein, J. Neus, and R. Maboudian, "High Reliability Touch-Mode Electrostatic Actuators (TMEA)," *Technical Digest, Proceedings of the 1998 Solid-State Sensor and Actuator Workshop (Hilton Head '98)*, pp. 296-299, June 8-11, 1998.

[33] Ramé-Hart, Inc., 8 Morris Avenue, Mountain Lakes, NJ 07046, Phone: (973) 335-0560 , http://www.ramehart.com.

[34] M. Di Giovanna, *Flat and Corrugated Diaphragm Design Handbook,* Marcel Dekker, Inc., New York, 1982.

[35] S. Timoshenko and S. Woinowsky-Krieger, *Theory of Plates and Shells,* McGraw-Hill, New York, 1959.

[36] M. G. Allen, M. Mehregany, R. T. Howe, and S. D. Senturia, "Microfabricated structures for the *in situ* measurement of residual stress, Young's modulus, and ultimate strain of thin films," *Appl. Phys. Lett.,* vol. 51, no. 4, pp. 241-243, 1987.

[37] Product Specifications, *A-174 Silane Promotion*, Specialty Coating Systems, Inc., Indianapolis, IN, Phone: (800) 356-8260.

[38] E. S. Hung and S. D. Senturia, "Leveraged Bending for Full-Gap Positioning with Electrostatic Actuation," *Technical Digest, Proceedings of the 1998 Solid-State Sensor and Actuator Workshop (Hilton Head '98)*, pp. 83-86, June 8-11, 1998.

[39] Stanford Research Systems, Inc., 1290-D Reamwood Avenue, Sunnyvale, CA 94089, Phone: (408) 744-9040 , http://www.srsys.com.

Chapter 5

Parylene MEMS Actuator Skins for Adaptive Flow Control

5.1 Introduction

From the study of the flapping flight, we have learned that the control of the wings' pressure distribution is very important in order to achieve an optimal aerodynamic performance. Therefore, it is logical to fabricate devices on the membrane, passive or active, that can regulate the wing loading. It is hoped that by distributing actuators on the wings, it is possible to actively control the air flow.

The concept of fabricating MEMS "skin" devices is still new. The advantages of the skin are its flexibility and lightweight. There have been only a few MEMS skin device research work that have been published and they were for "sensing" purposes. For example, Jiang, *et al.* developed the first flexible shear stress sensor skin for aerodynamic study using polyimide in 1997 [1]. There has never been any report

published on the work of any "actuator" device skin before, especially, on parylene. This is the first time that the large area parylene MEMS "actuator skin" has been developed for fluidic and aerodynamic applications. This work is very challenging.

This chapter presents a short review of the MEMS devices in fluidic and aerodynamic applications. It also describes in full detail the designs and fabrication processes of the various types of actuator skins. Finally, the wind-tunnel test results will be analyzed and discussed.

5.2 Review of MEMS Devices in Fluidic and Aerodynamic Applications

The miniaturization of micro transducers using MEMS technology offers several advantages in fluidic and aerodynamic applications. For example, spatial resolution is improved due to small physical size and temporal response can easily be increased due to low inertia of the transducers [2]. Further, MEMS technology enables the scientists and researchers to explore and study micro-flow, or even nano-flow, in the scale regime in which macro-scale devices would not be able to operate. Some of these applications include high-pressure flow studies by suspended microchannel and MEMS flow sensor for nano-fluidic applications [3-4].

There are several MEMS devices that are found in fluidic and aerodynamic applications. For instance, shown in Figure 5-1 is a MEMS-fabricated polysilicon micro hot-wire anemometer that is used to measure fluid flow velocity by measuring the variation of temperature of a heated resistive wire [5-7]. When the wire is electrically heated and is placed in the flow of fluid, the heat is taken away by the flow-induced

forced convection. The flow velocity can be measured through the change of resistance or the drop of output voltage across the wire.

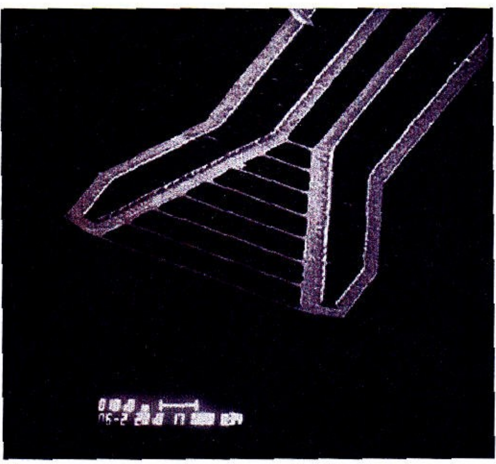

Figure 5-1: Micro hot-wired anemometer [7]

In turbulence control research, Jiang, *et al.* fabricated polysilicon micro surface shear stress sensors and studied their heat transfer characteristics, frequency and wind-tunnel responses. They integrated multi-rows of sensors together to create a high-resolution MEMS shear stress imager that, for the first time, mapped out the stress distribution along the wall so that the turbulence flow could be studied [9-10]. Soon after, the first flexible shear stress sensor skin using polyimide and silicon islands was developed and was tested on the leading-edge of a delta-wing aircraft to achieve real-time detection and profiling of the two-dimensional surface shear stress [1]. The shear stress sensors, imager, and flexible sensor skin are shown in Figure 5-2. Later, Jiang and Xu developed the newer version of the flexible shear stress sensor skin, shown in Figure 5.3, by integrating it with CMOS chip and testing it on an unmanned aerial vehicle.

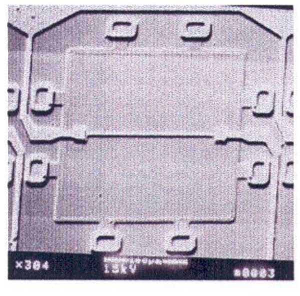

(a) Shear stress sensor

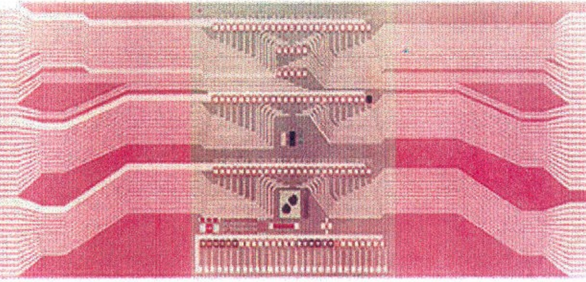

(b) Shear stress imager

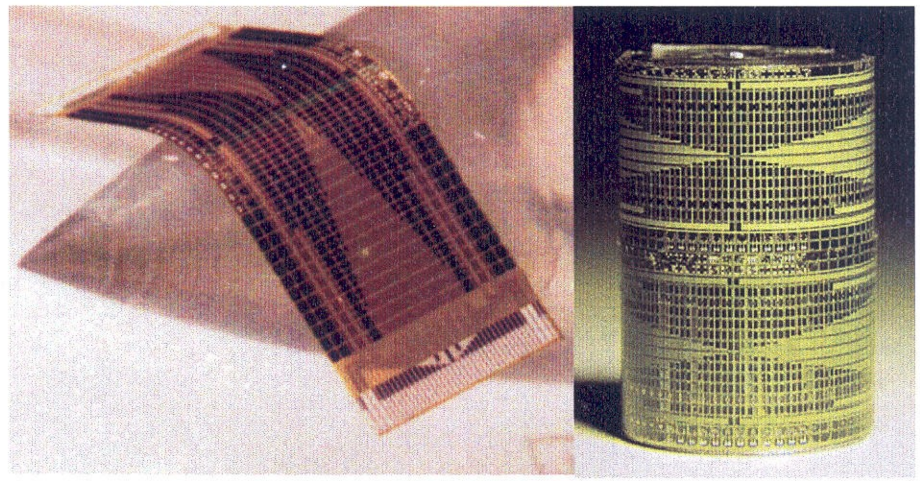

(c) Flexible shear stress sensor skin on polyimide

Figure 5-2: MEMS-fabricated shear stress sensors [1, 8, 9]

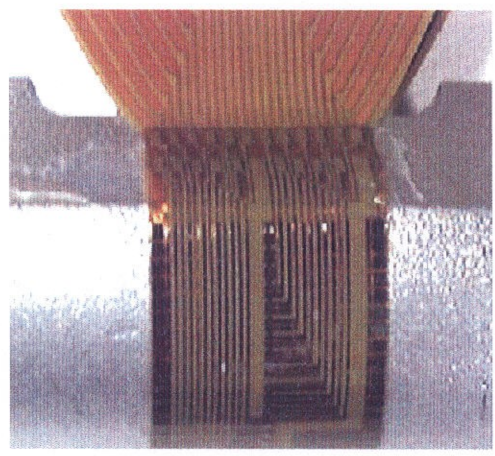

(a) Integrated shear stress sensor skin

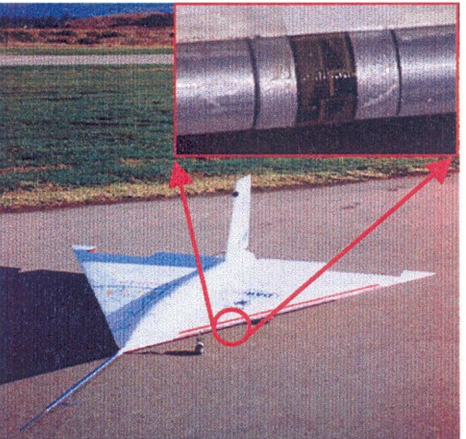

(b) Flight test on a delta-wing aircraft

Figure 5-3: Integrated shear stress sensor skin on polyimide [10]

The capability to profile 2-D shear stress by the shear stress imager allows the researcher to "see" the surface vortices of the fluid. In terms of aerodynamics, this detection is necessary to the study of turbulence flow because turbulence flow is directly related to drag force. The reduction of turbulence flow implies the decrease of drag. Tsao, *et al.* fabricated a large-scale integrated MEMS system to achieve active drag reduction [11]. As shown in Figure 5-4, the system consists of 18 shear stress sensors, 3 magnetic flap-type actuators, and control electronics for use in turbulent boundary layer control study. As turbulent fluid flows past the first row of sensors, the sensors detect the vortices. The electronic circuitry identifies regions of high shear stress and sends a signal to actuate the magnetic flap actuators to create counter-rotating vortices that reduces the drag. The second row of sensors, which locate after the actuators, are then used to determine the effect of the actuation on shear stress.

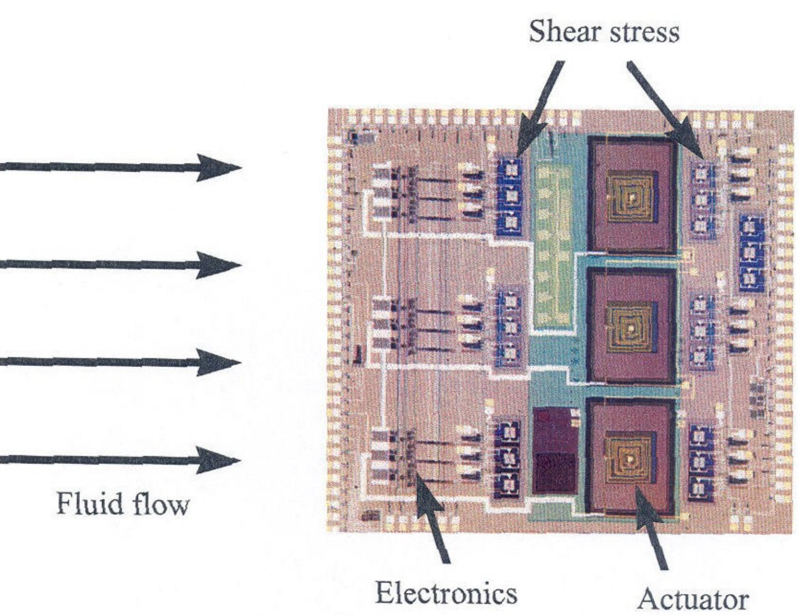

Figure 5-4: Integrated MEMS system for turbulent boundary layer control [11]

Another use of small surface perturbations by micro actuators to generate large aerodynamic control moments (pitch, yaw, and roll) can be seen by the research work of Charles, *et al.* The group has designed and developed a robust, large-force, large-deflection micro balloon actuators that can aerodynamically alter the maneuvering capability of a transonic aircraft [12]. These MEMS actuators are fabricated from silicone rubber and parylene, and can stand up to several psi of pressure as shown in Figure 5-5 (a). They are also robust enough for flight tests on a real aircraft or tests in a high-speed (>50 m/s) wind tunnel. Several strips of actuators have been flown successfully on an F-15 fighter jet with speed up to 0.9 Mach and temperatures fluctuated from -9 °F to 110 °F. It was found that all the MEMS devices survived the harsh flight test several times, which demonstrated the robustness of the devices. Figure 5-5 (b) shows the micro balloon, along with shear stress sensors, attached to a section of an F-15 wing.

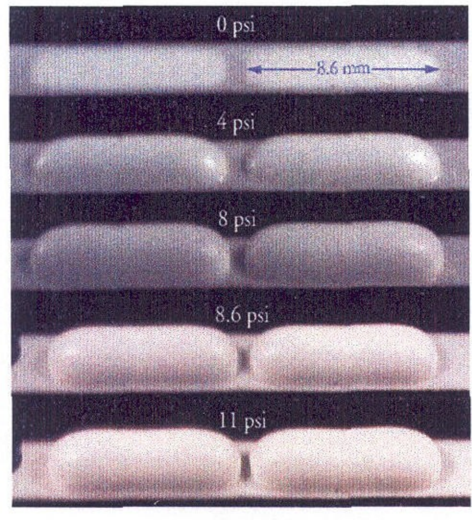

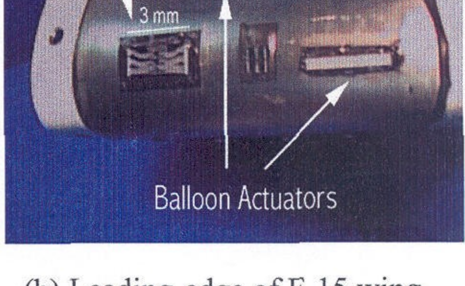

(a) Balloon actuators

(b) Leading-edge of F-15 wing

Figure 5-5: Balloon attached to a leading-edge section of F-15 wing [12]

These are just some examples of MEMS devices for the fluidic and aerodynamic applications. MEMS technology has enabled the fabrication of various sophisticated devices that traditional machining cannot offer. In addition to those devices, the novel parylene MEMS actuator skin technology for adaptive flow control will be introduced in the next section.

5.3 Parylene MEMS Actuator Skins

5.3.1 Actuator Skin Device Concept

There are two types of designs for the parylene actuator skins. The first design is the "plate" type and the other is the "check-valved" type. The schematic diagrams for these two types are illustrated in Figure 5-6.

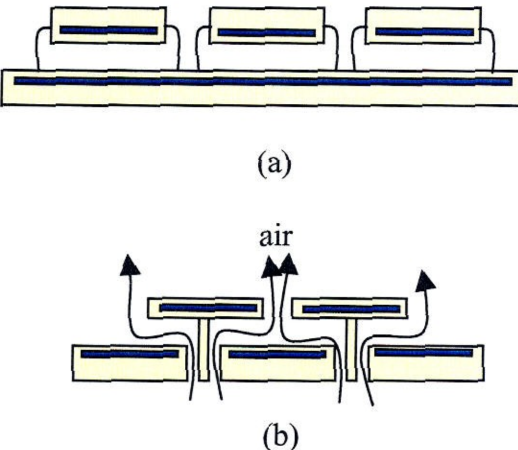

Figure 5-6: Schematic diagram of parylene actuator skins;

(a) Plate type; (b) Check-valved type

These two designs serve to study different purposes. The plate type features several large electrostatic actuation plates without any anti-stiction posts throughout the membrane. Once the actuation voltage is applied, the effective thickness of the

membrane is changed by doubling the thickness of each layer of parylene. Hence it affects the stiffness. We hope that the change in stiffness will be enough to impact the aerodynamic performance. The design and fabrication of this skin type is presented in section 5.4.

The check-valved type features vent-through holes with tethered valves throughout the membrane skin. When the valves are open, there is no pressure gradient between the top and the bottom of the membrane. Once the valves are closed, the difference in pressure gradient can affect the aerodynamic performance of the wings. There are two types of the check-valved actuators that have been fabricated: pneumatic check-valved and electrostatic check-valved actuators. For pneumatic check-valved actuator type, there are no metal layers on the skin. The actuation relies upon the wing loading during flapping cycle. For each cycle, the loading either pushes the valve caps to open or close, to control air movement through the vent holes. For electrostatic actuators type, two metal layers, the ground and high-voltage electrode pads, are sandwiched between two parylene layers. By applying voltages to regulate the actuators, the vent holes can be opened or closed by the electrostatic force. Hence the aerodynamic performance is affected.

5.3.2 Actuator Skin Fabrication Concept

The detailed descriptions of the designs, technological issues, and fabrication process of the freestanding parylene actuator diaphragm on a silicon chip have been described in the previous chapter. The electrostatic actuation test results have been successful and the load deflection test has proven that the effective thickness yields almost the same value to the actual thickness. The next step is to fabricate and release the

wafer-sized MEMS actuators parylene membranes or "skins." The goal is to integrate these free-standing parylene MEMS actuators skins onto the MEMS wings to form integrated actuator wings. By selectively distributing the actuators on the wings, the stiffness of the membrane can be controlled. Further improvement in terms of the aerodynamic performance of MEMS wings can be achieved.

There are two approaches to construct the MEMS integrated actuator wings. The first approach is to first fabricate the MEMS wings and then separately fabricate the MEMS actuator skin. The parylene skin is composed of MEMS actuator dice throughout the whole wafer with each individual die isolated from one another. Afterwards the MEMS actuators are integrated onto the MEMS wings at the desired locations by cut-and-paste method. This concept is illustrated in Figure 5-7.

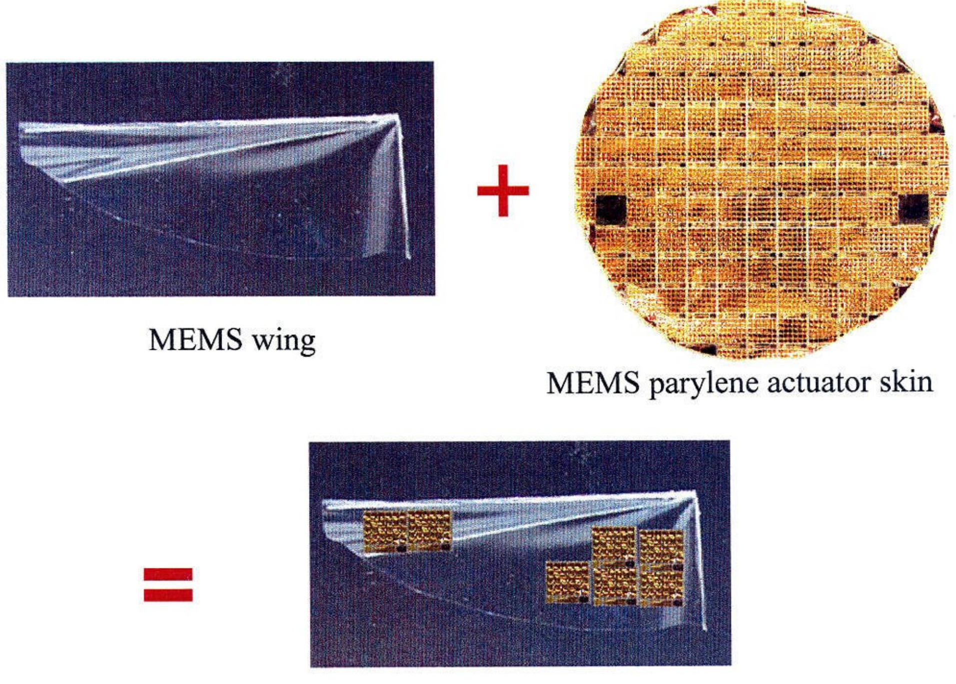

Figure 5-7: MEMS integrated actuator wing concept: first approach

The second approach is to first fabricate the titanium-alloy wingframe with no parylene membrane. Then the parylene actuator skin is separately fabricated by selectively placing the MEMS actuators at the desired locations on the skin. These actuators can be connected by electrode lines that run across the whole wafer. Then the skin is cut into a wing shape, with actuators at the desired locations, and pasted onto the titanium-alloy wingframe to complete the MEMS integrated actuator wing process. Figure 5-8 shows the concept of this approach. The advantage of this approach is that there is no glue involved. On the other hand, the locations of the actuators are fixed and cannot be changed. Hence the addition of actuators on the wings is impossible. In addition, fabrication of several skins is required for redundancy purpose and results in slower production time.

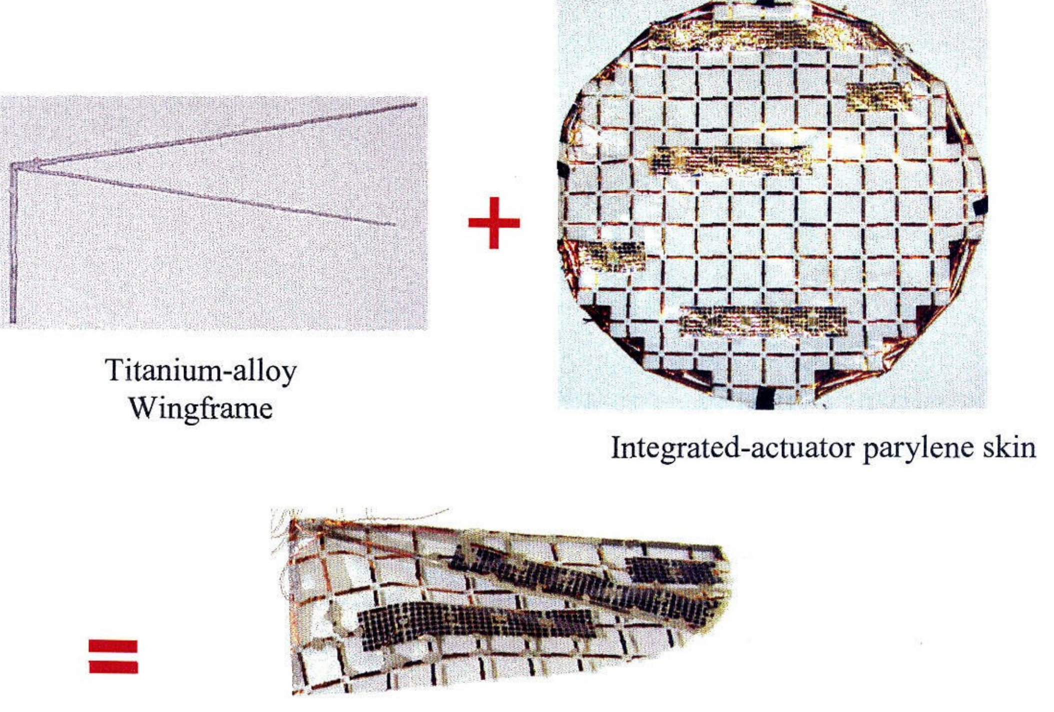

Figure 5-8: MEMS integrated-actuator wing concept: second approach

Moreover, the second approach is more complicated than the first one and requires the exact locations of where the actuators would be located on the wings. Although the first approach requires a separate fabrication of MEMS wings beforehand, it provides a better flexibility to integrate the actuator skin and requires less skin to construct the MEMS integrated actuator wings. Both approaches will be attempted and will be presented in detail in section 5.4. Section 5.3.3 discusses technologies to release the skin. The fact that the fabrication of parylene electrostatic actuator skin is a novel work and there has never been any report published before, several challenges that are present during the fabrication process, i.e., stiction, cracking, and wrinkles of thin films, will be discussed in details in this thesis.

5.3.3 Skin-Releasing Technologies

The realization of the parylene MEMS actuators from a diaphragm on a silicon chip to a membrane skin on an entire wafer also relies upon the success of the skin releasing technologies. There are two main technologies to release large area parylene skins. The first technology is to use photoresist as a sacrificial layer. Photoresist is laid down as the first fundamental film while other thin films are deposited and processed on top. At the end of the process, photoresist is disassociated in acetone solvent to release the final skin. This technology is easy to use and the skin is often released successfully. The drawback from this technology is that the photoresist cannot stand high temperature. Therefore, stress annealing temperature is rather limited. The second technology uses the dry etching of BrF_3 gas to etch a thin layer of sacrificial polysilicon to release the skin. The polysilicon layer can stand a much higher temperature than photoresist. However,

using BrF_3 gas to release the skin may cause parylene to be attacked by BrF_3 gas if the release time is too long.

Preliminary parylene test skins are fabricated to pre-test both technologies. For the first technology, the sacrificial layer is AZ4400 positive photoresist spun at 4 krpm for 40 seconds. The thickness is approximately 4 μm. The resist is softbaked for 15 minutes at 100 °C and later is hardbaked at 120 °C for an additional 20 minutes. A 5- μm parylene film is deposited and covered the entire wafer. Then the skin is cut open along the edges and is submerged in an acetone bath. Without agitation, it would take several days to completely release the skin off the entire wafer. Thus the use of ultrasonic agitation bath is recommended in this case. This way the skin can be easily released within a few hours.

The disadvantage of using photoresist as a sacrificial layer is that the processing temperature has to be kept lower than the hardbake temperature; otherwise, the photoresist can be burnt and will be hard to release. In addition, another problem often encountered is the generation of bubbles. If the photoresist is not hardbaked long enough to bake out the solvent completely, bubbles can be formed during parylene annealing at 120 °C. These bubbles are formed by the solvent that is evaporated during baking but is trapped by the parylene membrane. They can prevent proper processing of other thin film layers that form the actuators because the surface becomes non-planar.

The second technology is to use BrF_3 gas dry etching to etch a thin layer of polysilicon to release the skin. This technology is attractive because the release process is dry and there is no stiction problem due to the meniscus force. Also, the annealing of parylene can be performed at a temperature up to 250 °C because there is no photoresist

involved. However, the main concern for this technology is whether the BrF_3 gas can create enough undercut to release the entire skin. It may require a long etch-time for BrF_3 gas to release the entire skin. If that is the case, then this technology is not attractive because long exposure of parylene in BrF_3 gas may cause parylene to be attacked and its mechanical property is changed.

The fabricated test skin consists of a thin layer of 2-μm parylene on top of 4-μm polysilicon film. A thin film of SiO_2 is underneath the polysilicon film to protect the silicon substrate from being etched by BrF_3 gas. The parylene film is patterned throughout the film with etching holes of 50-μm diameter and 200 μm apart. The wafer is then placed into the BrF_3 etch-chamber. The chamber is pumped down to the base pressure of 40 mT before a 6-Torr pulse of BrF_3 gas is released to etch polysilicon. Each etch cycle lasts 6 minutes. The skin is finally released after 5 cycles. Through visual inspection, the color of the parylene film has changed from clear to milky white. The film is not as strong as before and can be torn easily. This confirms the fact that long exposure of parylene in BrF_3 gas should be avoided. Therefore polysilicon releasing technology may be not suitable in this case. Although the first technology using photoresist as a sacrificial layer has some disadvantages, it is more attractive because it does not change the property of the parylene film. In addition, the ease of the technology makes it more user-friendly. Thus, this releasing technology is selected and will be primarily used to release the parylene MEMS actuator skins for both plate and check-valved types.

5.4 Parylene MEMS Active Plate Electrostatic Actuator Skin

5.4.1 Design

The "plate" type design features four deposited layers of parylene. The first layer of parylene is about 4.5-µm thick and covers the entire wafer on top of the sacrificial photoresist, which must be hardbaked at 120 °C for at least 20 minutes to bake out the solvent. The ground composite metal electrode (Cr/Au/Cr) is evaporated on top of the first parylene layer and then followed by the second deposition of parylene film. The second parylene is used to protect any shortage of the ground metal electrode and the high-voltage metal electrode. The third and the forth parylene layers sandwich the high voltage metal electrode to form the plate actuators. The cross-sectional view of the skin design is shown in Figure 5-9.

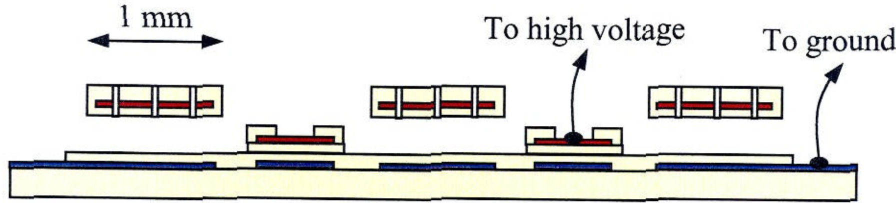

Figure 5-9: Cross-sectional view of the "plate" type actuator skin

On one wafer skin, there are a total of 107 dice. The distance between each die is 7.62 mm. On each die, there are 37 of 1-mm x 1-mm electrostatic actuator plates. There are two design versions of the skins. Both designs follow the first and second approach described in section 5.3, respectively.

5.4.2 Fabrication Process

The fabrication process of the parylene MEMS active plate electrostatic actuator skin is shown in Figure 5-10. This process has a total of six masks. First the sacrificial layer of 4-μm-thick AZ4400 photoresist is spun onto the wafer and patterned around the edges so that it can be completely encapsulated by the first deposition of parylene layer. The wafer is only used as a mechanical support structure and is not a part of the final skin device. The sacrificial photoresist is then hardbaked at 120 °C for 20 minutes to completely bake out the solvent before depositing the first layer of parylene. The failure to bake out the solvent will generate bubbles during the vacuum annealing of parylene and other subsequent bakings during the process. This problem will be discussed more in detail in section 5.4.3.

After depositing the first layer of parylene, the surface is roughened by oxygen plasma to improve the adhesion of the first ground metal electrode layer. Failure to perform this step may result in peeling of the metal layer during patterning. Next, the metal layer is evaporated. The ground electrode consists of 100 A° of Cr, 2800 A° of Au, and another 100 A° of Cr. The Cr layer helps improve the adhesion of the Au layer to the parylene. Then the second parylene layer of 1.5-μm thick is deposited. This layer of parylene is used to prevent any shortage between the ground and high-voltage electrodes during actuation. Then the wafer is annealed in a vacuum oven at 120 °C for 30 minutes to alter the stress in parylene film from compressive stress to tensile stress [13].

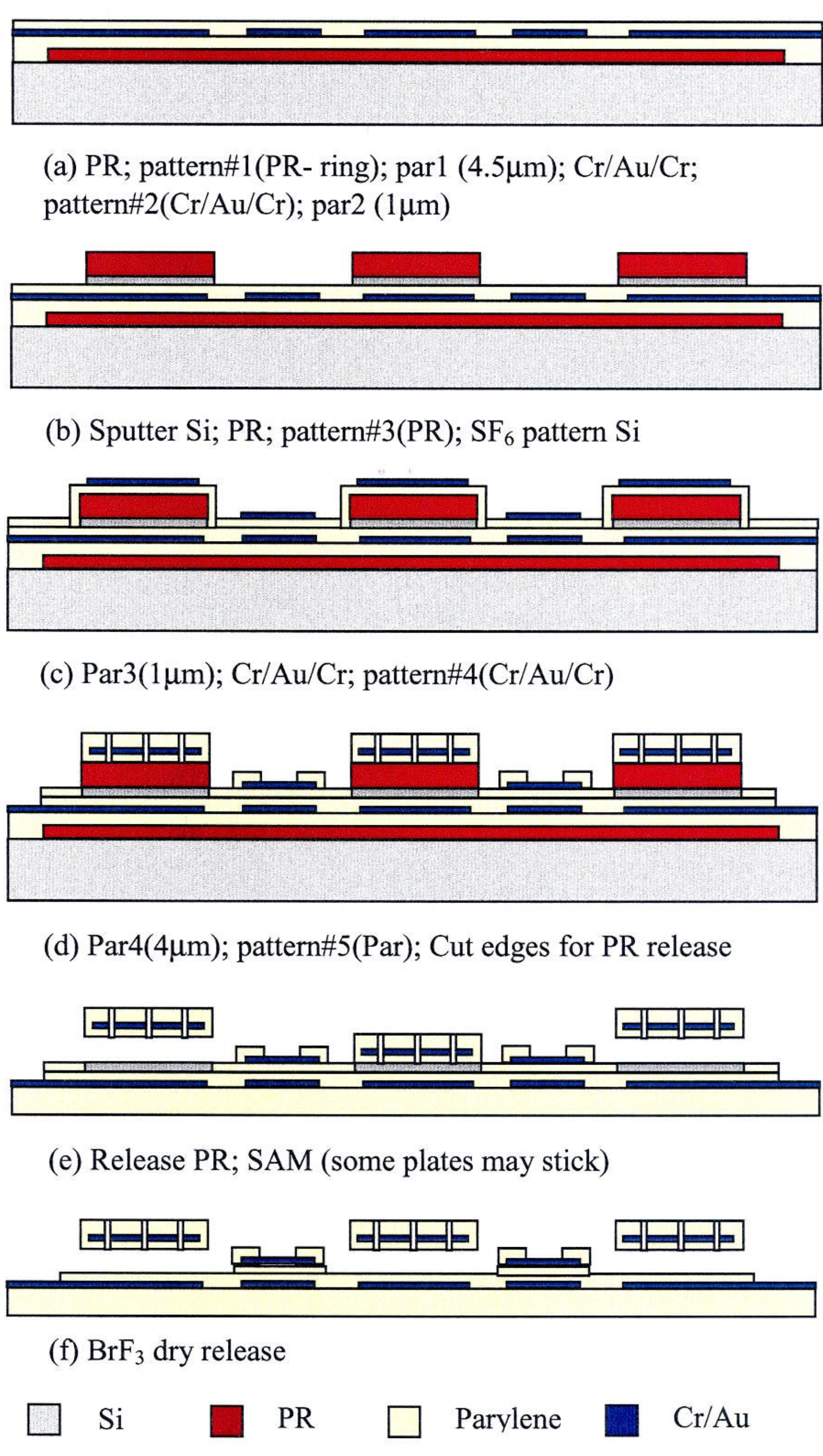

Figure 5-10: Summary of the fabrication process of the parylene MEMS active plate electrostatic actuator skin

Next, a thin layer (~4500 A°) of amorphous silicon is deposited and patterned. At the end of the fabrication process, this amorphous silicon will be etched by BrF_3 gas to prevent stiction between the top and bottom parylene membranes. This process takes place at the end because after the skin is completely released from the wafer, involvement of wet chemical is no longer desired. It is worth it to note that without the parylene annealing step, the mismatch stress in the amorphous silicon film will cause the thin film to buckle. These wrinkles will spread throughout the wafer during the process. This specific problem is discussed further in detail in section 5.4.3.

After the patterning of the amorphous silicon, 5-um thick of sacrificial AZ4400 photoresist is spun on and patterned. Then another thin parylene layer is deposited, followed by the thermal evaporation of Cr/Au/Cr composite layers as the top electrode. After the electrode is patterned, the last parylene is deposited and patterned. This completes the structure formation of the actuator plates. Then the wafer is submerged in an acetone dish to release the sacrificial layer photoresist. The dish is placed in an ultrasonic bath until the entire sacrificial layer photoresist is dissociated.

The next step is to treat the skin with the SAM coating. The process of SAM coating is well-described in the previous chapter. The skin is placed in an IPA bath for 10 minutes before transferring it to an iso-octane bath for another 10 minutes. The SAM bath is prepared by using one drop of OTS in 50 ml of iso-octane solvent. Then the skin is submerged in the SAM bath for an additional 10 minutes. Once the forward process is completed, the reverse process begins by re-submerging the skin for 10 minutes in the iso-octane bath, and then the IPA bath. Finally, it is dipped in a DI water bath. At this point, the OTS-coated skin is hydrophobic. When it is pulled out of the water, it should

be air-dried for at least 30 minutes. Once the skin is completely dry, the BrF_3 gas is used to release the amorphous silicon underneath the plate actuators. There are no stictions of the plate actuators. The first version of the flexible parylene MEMS active plate electrostatic skins is displayed in Figured 5-11. This version of skin features MEMS actuators everywhere on the parylene skin. Later they will be integrated onto the MEMS wings at the desired locations by cut-and-paste method.

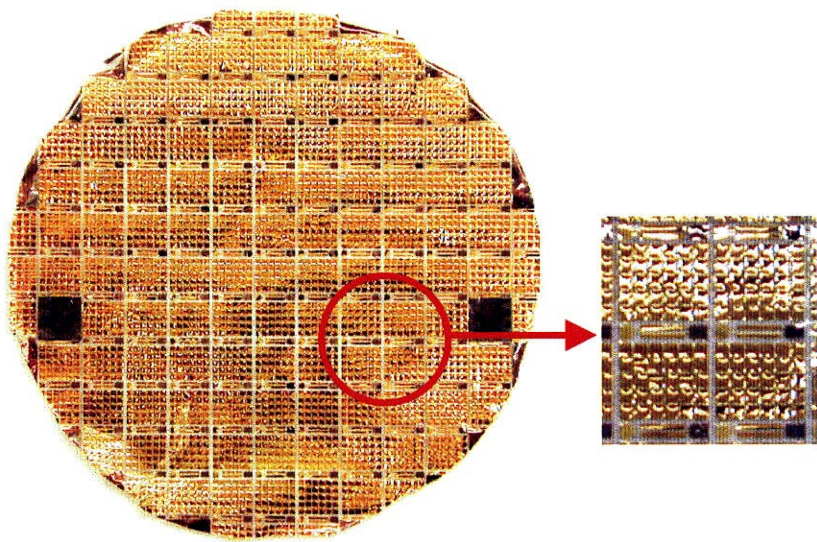

Figure 5-11: Fabricated parylene MEMS active plate electrostatic actuator skin (version 1)

The second version of the skin is shown in Figure 5-12. This version has actuators directly fabricated onto the parylene membrane skin at pre-determined locations. These actuators are connected by electrode lines. Then the skin is cut into a wing shape and pasted directly onto the pre-fabricated titanium-alloy wingframes. This design features five dice of actuators at the location of the trailing-edge and two dice of actuators at the outboard behind the leading-edge area. The goal is to alter the vortex

shedding and stiffness of these areas to show the aerodynamic effect of the actuators during flapping.

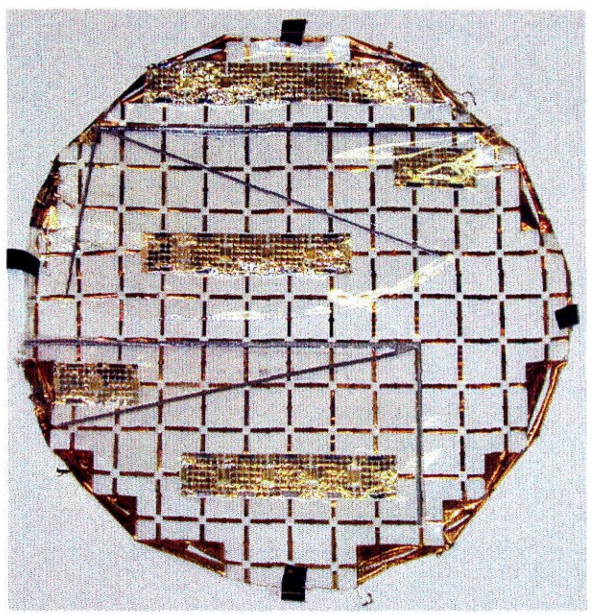

Figure 5-12: Version 2 of the parylene MEMS active plate electrostatic actuator skin with titanium-alloy wingframes

5.4.3 Processing Challenges

There are several processing issues that occur during the fabrication of parylene actuator skins that should be noted. First, bubbles in the first sacrificial photoresist layer are generated during the annealing of parylene film in a vacuum oven. This problem is shown in Figure 5-13. The cause of this problem is due to the fact that the sacrificial photoresist is not hardbaked long enough to get rid of the solvent. When the parylene layer is annealed in the vacuum oven at 120 °C, the solvent is evaporated and trapped by the parylene layer. The solution to this problem is to hardbake the photoresist at 120 °C for at least 20 minutes in the convection oven after spinning. When this procedure is

performed, there are no visible bubbles generated after the parylene annealing. The close-up of these bubbles can be seen in Figure 5-13 (b). It must be careful not to set the temperature in the vacuum oven too high beyond 120 °C because the sacrificial photoresist will burn. The wafer skin with burnt photoresist is shown in Figure 5-14.

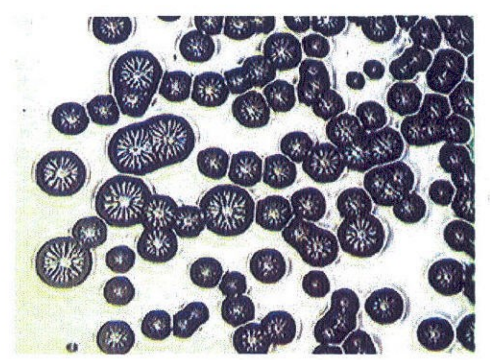

(a) Photoresist Bubbles

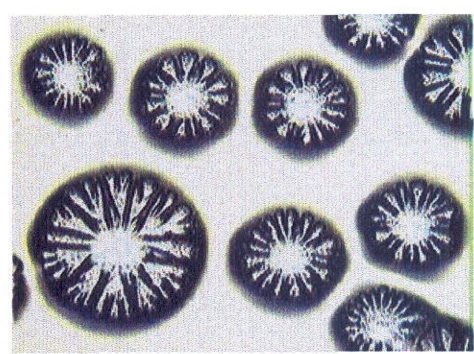

(b) Enlarged bubbles

Figure 5-13: Photoresist bubbles underneath the parylene layer

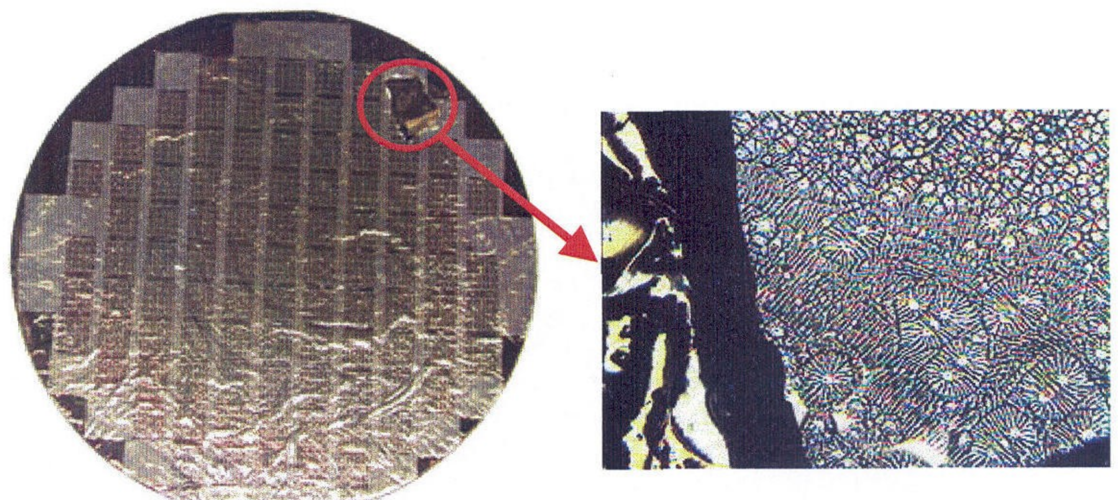

(a) Wafer with burnt photoresist

(b) Burnt resist underneath parylene

Figure 5-14: Parylene layer wrinkles on top of burnt photoresist

Second, the stress mismatch of the parylene and the amorphous silicon layers causes the thin amorphous silicon sputtered on top to wrinkle. This problem is shown in Figure 5-15. By annealing the parylene film, the stress in parylene becomes tensile. When the thin film of amorphous silicon is deposited, the buckling can be avoided. Decreasing the deposition power also helps reduce this problem.

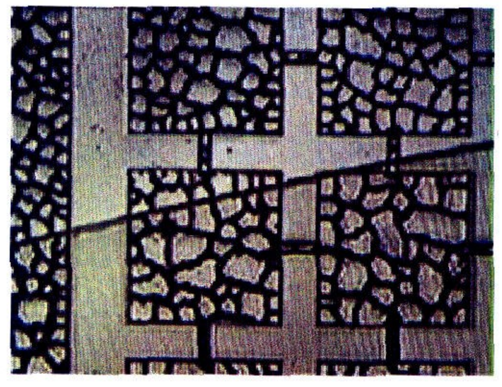

(a) Buckling of thin film

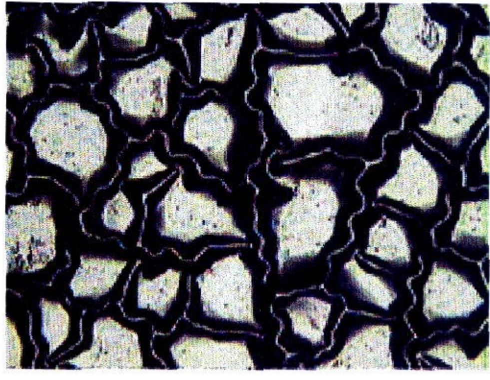

(b) Enlarged picture of wrinkles

Figure 5-15: Buckling of sputtered silicon film on un-annealed parylene

Third, parylene skin cracks during the parylene etching due to overheating. This problem is shown in Figure 5-16. Typically, the etching rate of the parylene in the oxygen plasma, set at 400-watts power and 400 mT of O_2, is about 1 μm per 6 minutes. If the parylene membrane is 6 μm, it requires over 30 minutes to etch through the layer. This can generate excessive heat and can cause the parylene to crack if the continuous etching time is too long. By rotating and cooling down the wafers in between short etching cycle, the cracking can be avoided and the etching uniformity can be improved. For example, each etch-cycle should be limited to 10 minutes and the wafers should be rotated and allowed to cool down.

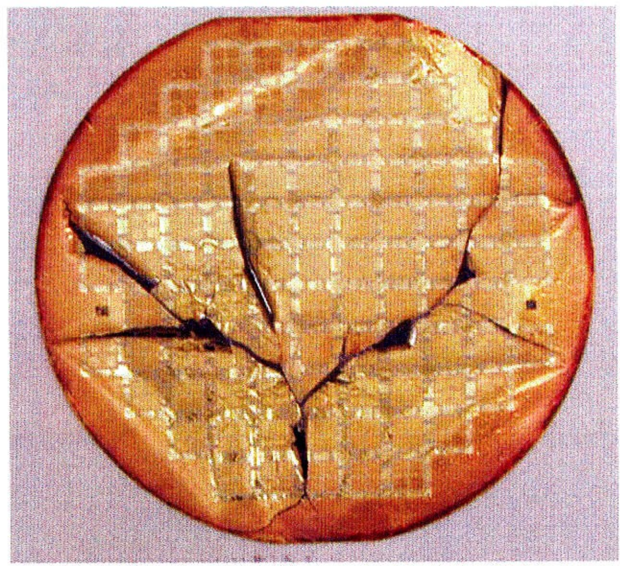

Figure 5-16: Cracking of parylene skin during parylene etching

Finally, the last issue is related to the use of an appropriate chemical during the process. For example, generally AZ developer is used in the fabrication process to develop photoresist after it is exposed by the UV light. However, a much stronger developer called AZ351 can be diluted by DI water (1:4 in volume) and used to develop exposed resist. Compared to AZ developer, AZ351 yields faster developing rate and better contrast. However, if AZ351 developer is used to develop photoresist that has a thin film aluminum underneath, the aluminum film will be attacked. AZ351 developer has an active component that can etch the aluminum film. This problem can be seen in Figure 5-12. Typically, aluminum thin film is used as a mask to protect parylene during the parylene etching and is etched by the aluminum etchant. AZ351 developer can etch aluminum, but it is slow and the surface is not as clean. To reduce this problem, it is recommended that during the developing step, AZ developer, 1:1 mixture with DI water, or AZ400K is used instead of AZ351 developer.

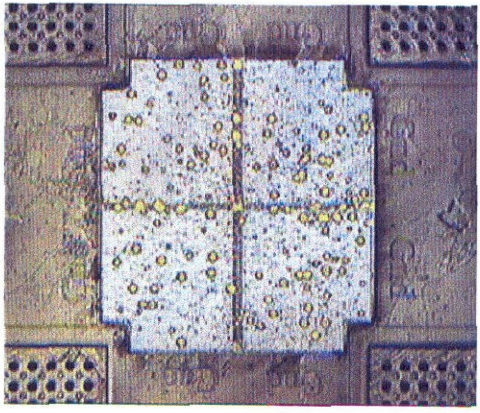

Figure 5-17: Aluminum film is attacked by AZ351 developer

5.4.4 Electrostatic Actuation Test

For two parallel conductive plates with area *A* and separated by a gap *z*, the non-linear electrostatic force F_e, generated by a voltage *V* is applied across the plates, is given by

$$F_e = \frac{\varepsilon_0 A V^2}{2z^2} \tag{5-1}$$

where ε_o is the permittivity of the free space and is equal to 8.85x10^{-12} F/m. Assuming that the device has a linear spring constant, the elastic restoring force of the spring is linear with distance *z* and can be expressed as

$$F_m = k_m(z_0 - z) \tag{5-2}$$

where z_o is the unactuated gap distance and k_m is the total spring constant of all the supporting arms of the plate. The design of the plate-type actuator has four arms. Given that each supporting arm has a spring constant *k*, the value of k_m and *k* can be written as

$$k_m = 4k \tag{5-3}$$

and $$k = \frac{3(EI_{beam})}{L^3} \tag{5-4}$$

where the quantity (EI_{beam}) is a superposition of product EI of parylene and gold materials and is given by

$$EI_{beam} = E_p I_p + E_g I_g = E_p(\frac{w_p t_p^3}{12}) + E_g(\frac{w_g t_g^3}{12}) \tag{5-5}$$

Because the thickness of gold layer is very thin (~1200 A°), the $E_g I_g$ value is negligible compared to $E_p I_p$ value. Thus EI_{beam} can be written as

$$EI_{beam} \approx E_p I_p \approx E_p(\frac{w_p t_p^3}{12}) \tag{5-6}$$

The equilibrium position of the plate may be found by equating the electrostatic force and spring force. As the voltage V increases, the gap distance decreases gradually at the beginning before the plate snaps to close the gap. The pull-in voltage V_{PI}, which corresponds to the last stable equilibrium point, is calculated to be

$$V_{PI} = \sqrt{\frac{8k_m z_0^3}{27\varepsilon_0 A}} = \frac{2z_0}{3}\sqrt{\frac{2k_m z_0}{3\varepsilon_0 A}} \tag{5-7}$$

This voltage is the minimum voltage applied to the parallel plates to pull in the plate to close the gap. The last stable equilibrium point of the plate before snapping down is calculated to be 1/3 of the unactuated gap distance.

The electrostatic actuation of the actuator on the skin uses the same principle. However, it is difficult to calculate the exact value of V_{PI} because the gap distance z_o can be changed after the skin is released from the wafer. Because the skin is made from flexible parylene film and is stretchable, the gap can be increased or decreased by how much the actuator skin is being stretched during testing. Moreover, after the integration

of actuator skin onto the MEMS wings, it is possible that the gap distance will not remain the same as before during actuation test. Therefore, in general high voltage, exceeding V_{PI}, is applied during testing to generate enough force to hold the plate down.

Similar to the electrostatic actuation test performed on the parylene MEMS electrostatic actuators on the silicon chip, the probe station - connected to a high-voltage power supply and an ohmmeter - is used. As mentioned before that after the skin is released, it is not entirely flat. Thus during testing, it must be slightly stretched out by adhesive tapes to ensure that the surface is as flat as possible. Also, it is important to make sure that the probe tips have good contacts with the electrode pads. A flat surface such as a silicon wafer is inserted underneath the skin during testing. Once the probes are in contact with the electrode pads, the skin is pressed down until it reaches the flat surface to secure the tips' positions. A small ball of silver paste is used as a buffered contact to make sure that the probe tips do not puncture through the skin. In addition, it is necessary to test for any shortages of top and bottom electrodes of each die. The measurement of the resistance by the ohmmeter between the ground and the high-voltage pads displays an infinite value. This indicates that there are no shortages between the two metal layers.

For each individual die test, voltages between 50 to 200 volts are applied to actuate the actuator plates. The electrostatic actuation test shows that voltages between 150 to 180 volts are good operational voltages. Breakdown tends to occur when the applied voltage is larger than 200 volts because the second layer of parylene is only 1.5 μm thick. The breakdown voltage is approximately in the same order of magnitude compared to the dielectric strength of parylene [14]. Several actuation tests are

performed and they are repeatable. The actuators continue to function even after several cycles.

Multiple dice are also connected for testing. Each die is connected through the electrode lines to both ground and high voltage pads using silver paste. Up to five connected dice configurations are tested and all plates can be actuated with voltages between 150 to 180 volts. The wind-tunnel test data will be discussed in section 5.4.5.

5.4.5 Aerodynamic Test Results of Plate-Actuator Skin

The low-speed wind tunnel test simulates the low Reynolds number flow of small birds and insects. Phase averaging is the method used to achieve instantaneous lift and thrust measurements by collecting the entire lift and thrust history of a complete downstroke and upstroke cycle. It also reduces the noise levels as many flapping cycles are averaged. The final data is the result of the integration of the lift and thrust values over the entire period of flapping cycle. Experimentally, a laser and a photodiode are used to form a reference signal. The laser is positioned so that the beam is interrupted by the tip of transmission arms at the start of the downstroke. Otherwise, the laser beam is directly detected by the photodiode. During testing, the signals for the photodiode and load cells are recorded. The data is sampled at 8192 points/sec, resulting in approximately 400 sample points for a single flapping period (assuming flapping at 20 Hz). Later, the data is post-processed by using the Matlab program to reconstruct the plot where the beam is interrupted from the photodiode signal, and hence when the downstroke starts. Then the data is folded back for each successive flapping period for the total average value of lift and thrust.

As mentioned earlier, the plate-type features large electrostatic actuation plates throughout the membrane. When the device is actuated, the effective thickness of the membrane is changed by doubling the thickness of each layer of parylene, hence the change in the membrane stiffness. We hope that the change in flexibility would be enough to impact the aerodynamic performance.

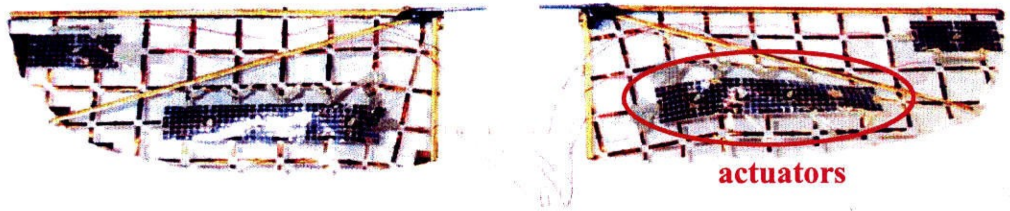

Figure 5-18: Integrated plate-type actuator MEMS wings

The MEMS wings integrated with plate-type actuators are shown in Figure 5-18. The actuators are placed behind the leading-edge areas where the vortex generation is to be altered. In addition, some actuators are located in the trailing-edge region to control the wing's flexibility. These are the locations where the actuators are hoped to create aerodynamic impacts. The wings are then mounted on the transmission connected to the loadcells that measure the lift and thrust forces in the wind tunnel. The wing mount is shown in Figure 5-19. The phase-average wind-tunnel test results of the plate electrostatic actuators are shown in Figure 5-20. The data is collected at 20-Hz flapping frequency, 30° AOA, and actuation voltage of 150 volts. The blue trace represents the wind-tunnel test data of the wings with actuators off, i.e., no voltage is applied. The red trace represents the data with actuators on. Table 5-1 shows the phase-average results of actuators both on and off states.

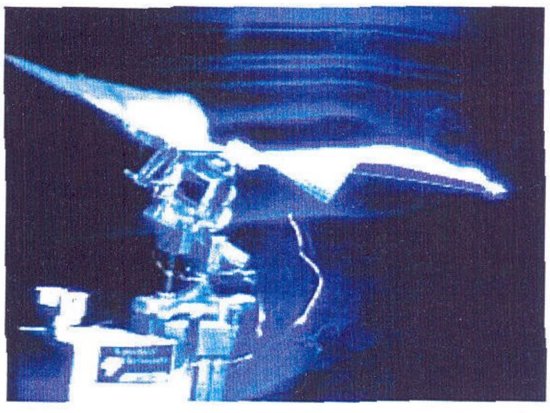

Figure 5-19: Wind-tunnel aerodynamic test

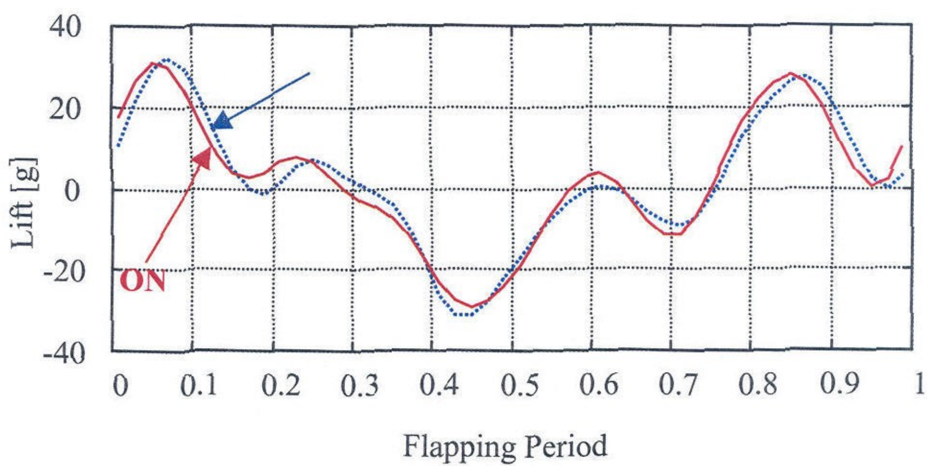

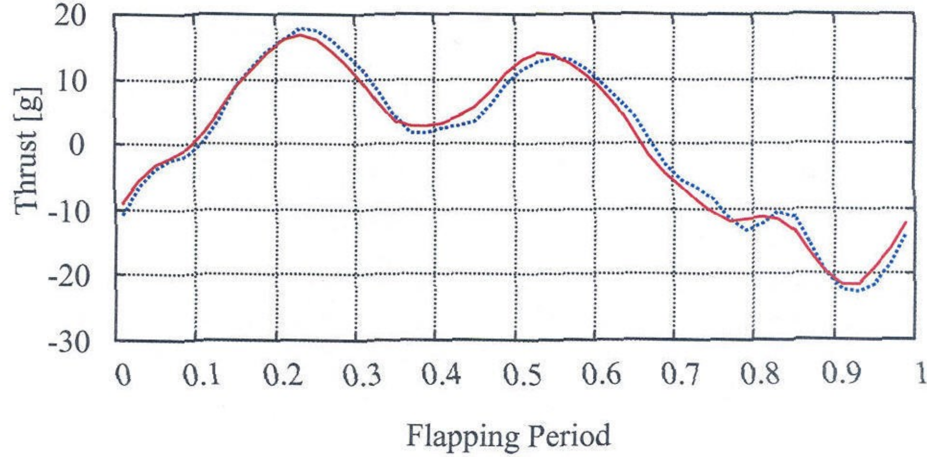

Figure 5-20: Phase-average results of the plate-type integrated-actuator wings

Table 5-1: Phase-average results of plate-type wings

Actuation	Lift [g]	Thrust [g]
Off	1.820	0.294
On	1.858 (+2%)	0.294 (0%)

The results show a small phase shift after the actuators are turned on. However, the improvement in aerodynamic performance is almost negligible - only 2% increase in the lift and no change in for thrust. This indicates that the actuation have little effect on the aerodynamic performance as we have previously expected for this type of design. Possible reasons for the poor results are perhaps because the placements of the actuators on the wings are not optimal and the parylene membrane is not thick enough to change the stiffness. In addition, the design of this type of actuator may not have been the best design to study this complicate problem. Thus, a new check-valved design is explored.

5.5 Flexible Parylene MEMS Check-Valved Actuator Skins

In a fluidic system, a check-valve is a device used to control liquid or gas flow in one direction. The valve is opened by a forward fluid flow and is closed by the reverse flow. It is analogous to a diode used to rectify the direction of current flow in an electric circuit [15]. Recently, various structures of MEMS micro check-valve such as cantilevers, float, gates, ring mesas, and membranes fabricated from silicon, metal, silicone, polyimide, and parylene have been developed [16-21]. However, they are mainly based on bulk micromachining of silicon or glass structure. There has been no previous work of check-valve presented using free-standing parylene skin before.

Two types of the check-valved actuator skins have been fabricated. The first type is passive check-valved pneumatic actuator skin. This type has no metal layer. The pneumatic actuation relies upon the wing loading during flapping. For each flapping cycle, the pressure loading either pushes the valve caps to open or close, controlling air movement through the vent holes. The opening of the valves equalizes the pressure between the upper and lower wing surfaces. Once the valves are close, the pressure difference can affect the aerodynamic performance. The second type is the active check-valved electrostatic actuator skin. This type contains two layers of metallization for the ground and high-voltage contacts similar to those of the plate-type electrostatic actuator skin. Electrostatic force is used to actuate the valves. Voltages can be applied to control the valves when to open or close, hence regulate the air flow.

5.5.1 Passive Check-Valved Pneumatic Actuator Skin

5.5.1.1 Design

The passive check-valved pneumatic actuator skin has two deposited layers of parylene. Each layer of parylene is approximately 8-μm thick. The valve area is separated by a 5-μm sacrificial photoresist layer. On a wafer skin, there are 13 rows and columns of dice with 107 dice in total. The distance between the center of each die is 7.62 mm. On each individual die, there are 5 rows and columns of parylene check-valves. Each check-valve consists of a circular vent hole and a valve cap. Each vent hole is 1.5 mm apart. The vent holes and valve caps have diameters of 500 and 900 μm, respectively. The valve cap is connected to the skin by four flexible reverse "S" arms which allow the valve cap to open or close depending on the direction of the air flow.

Once the check-valve is closed, the valve cap can cover the entire vent holes completely to minimize any air leakage.

5.5.1.2 Fabrication Process

The fabrication process of the parylene passive check-valved pneumatic actuator skin is shown in Figure 5-21. The skin is released by using thick photoresist as a sacrificial layer. This process has a total of four masks. The first mask patterns the amorphous silicon which is used for anti-stiction purpose. The second mask opens the vent hole through the bottom layer of parylene. The third mask defines the sacrificial layer photoresist. The final mask is used to pattern the top layer parylene to define the valve cap structure.

The process begins with spinning of the first sacrificial layer of AZ4400 photoresist at 3 krpm speed on the supported silicon wafer. The thickness is about 4 μm. The photoresist is then hardbaked at 120 °C for 30 minutes to completely bake out the solvent. The baking time and temperature will help reduce any problem with bubbles as previously discussed in section 5.4.3.

Next, the first layer of parylene is deposited. This layer is about 8-μm thick. The wafer is annealed in the vacuum oven at 120 °C for 20 minutes to help increase the tensile stress in the parylene film. This lessens the buckling and cracking of amorphous silicon which is the next thin film layer to be deposited. The ideal annealing temperature should have been 250 °C if possible. However, 120 °C should not be exceeded due to the fact that sacrificial photoresist cannot stand high temperature without getting burnt. Next, the parylene surface is roughened in the oxygen plasma at 200 mT and 200 watts of

power for two minutes. This helps improve the adhesion of amorphous silicon film to parylene.

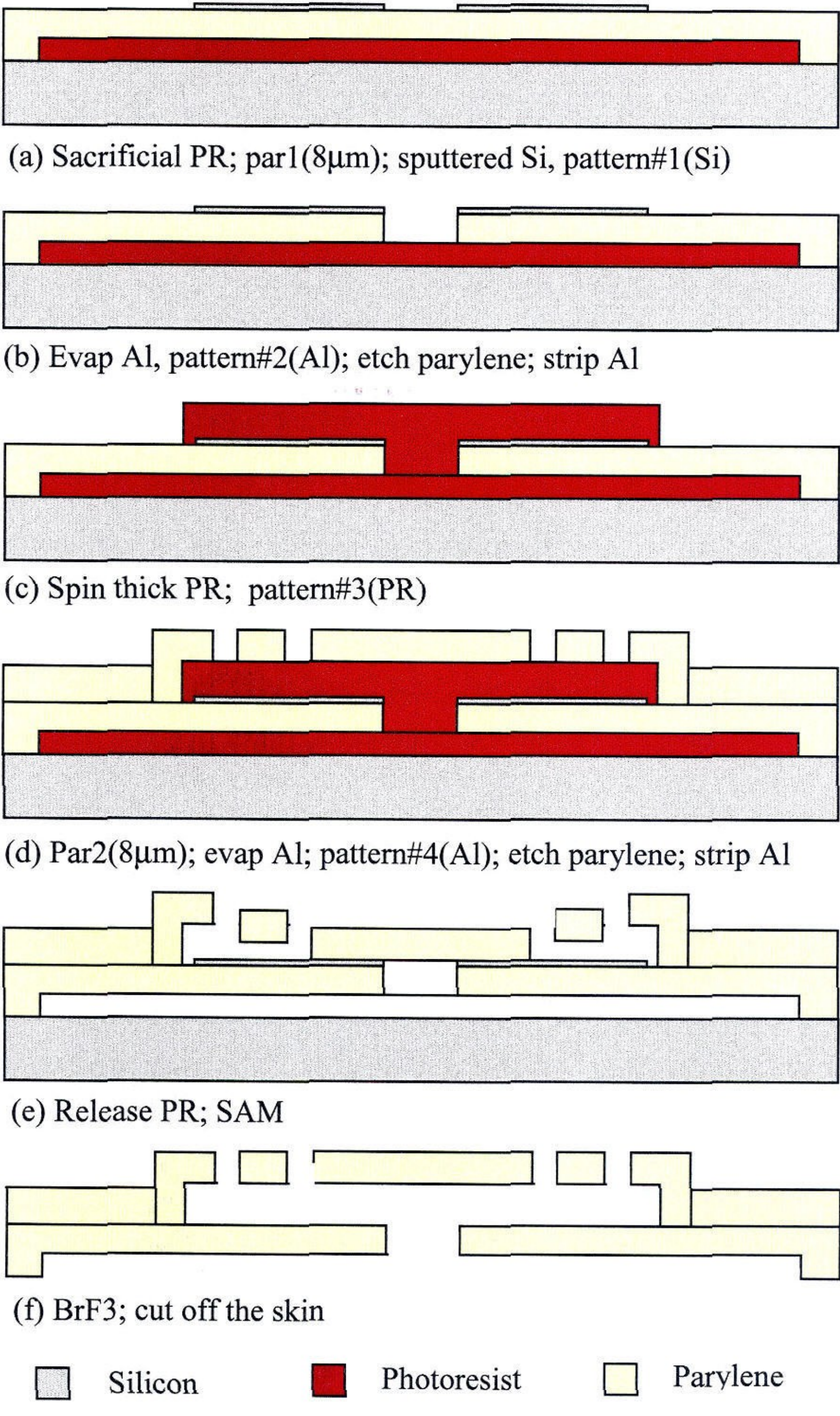

Figure 5-21: Summary of the fabrication process of the parylene MEMS passive check-valve pneumatic actuator skin

After depositing 4500 A° of amorphous silicon, the film is patterned in SF_6 gas at 300 mT with 300 watts of power for 4 minutes. Then a thin film of aluminum is evaporated as a mask to pattern parylene. After parylene patterning, the sacrificial layer of photoresist is spun on by using AZ4400 and AZ4620 positive photoresist. The first layer of AZ4400 is spun on at 3 krpm and the second layer of AZ4620 is also spun on at 3 krpm. It is important that this step must be performed carefully to prevent the failure of the device. Because the corner step of the vent hole is the thickness of the bottom parylene (8 μm), if the photoresist is not thick enough to cover the step corner of the vent hole, this will cause the top and bottom parylene films to fuse together at the corner. It will prevent the valve from opening.

After patterning the sacrificial photoresist, the top layer of parylene is deposited and patterned to form the valve caps. Then the photoresist is released in an acetone bath to free the skin and SAM layer is later coated. Finally, the amorphous silicon is etched in BrF_3 gas to complete the fabrication process. Figure 5-22 shows the released parylene check-valved actuator skin.

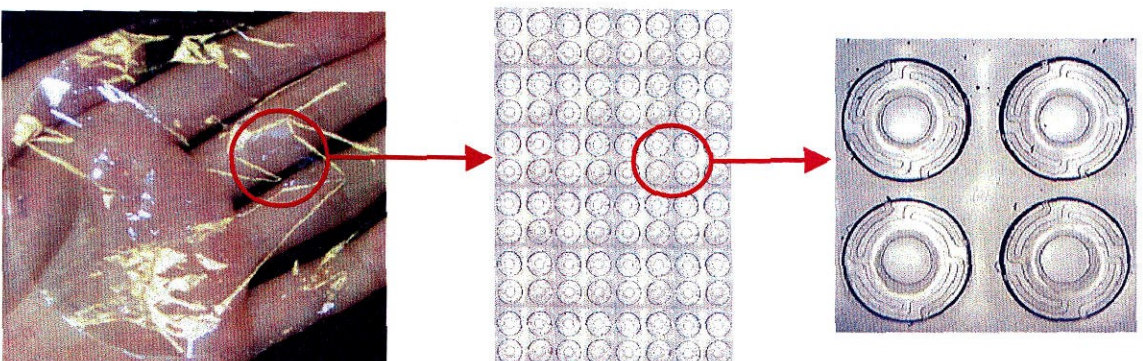

Figure 5-22: Parylene MEMS check-valve pneumatic actuator skin

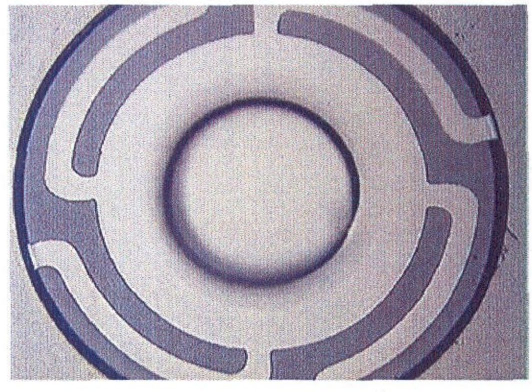

(a) Before stripping Al mask

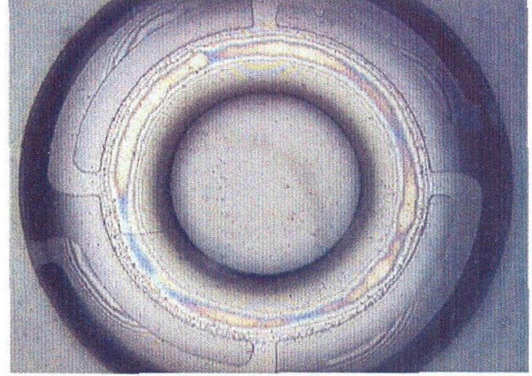

(c) After PR release; Parylene on top of amorphous Si

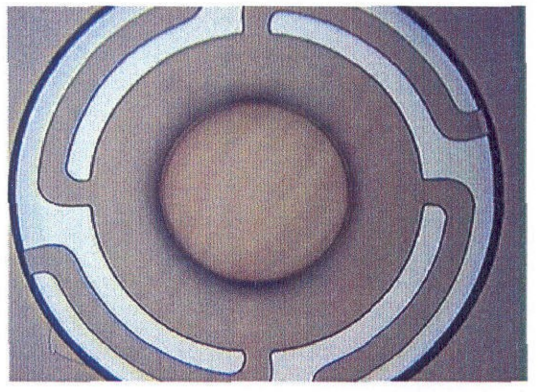

(b) After stripping Al mask; PR Sacrificial layer underneath on top of amorphous Si

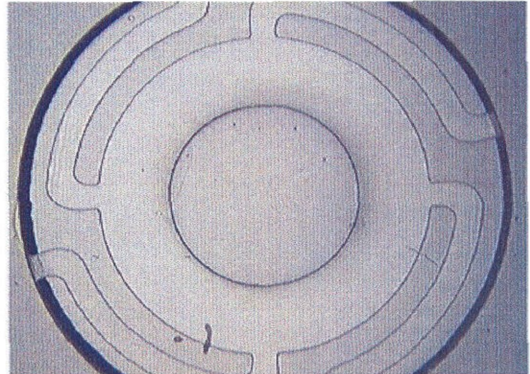

(d) After BrF3 release of amorphous Si

Figure 5-23: Snap shots of various stages of the check-valve during the fabrication

Figure 5-23 shows snapshots of various stages of the valve during the releasing steps. In Figure 5-23 (a), the top parylene layer is etched by oxygen plasma with aluminum as a mask. Once aluminum masked is stripped in aluminum etchant, sacrificial photoresist can be seen underneath the transparent parylene as shown in Figure 5-23 (b). From Figure 5-23 (c), it is noticeable that after photoresist is dissociated by acetone, the check-valve appeared to be stuck on top of the amorphous silicon (stiction ring) when the skin is dry. After BrF_3 gas etching of amorphous silicon, there is no more stiction. The

valve does not bend or twist out of the plane and appear to rest on top of the vent hole as seen in Figure 5-23 (d).

5.5.1.3 Processing Challenges

During the process of etching parylene, it is noticeable that the etching of parylene on one area is finished while on another area it is not. This is seen in Figure 5-24. The parylene in the outer area of the flexible arm is completely etched while the inner area is not. The unetched parylene appears black and rough. It takes several minutes to overetch this "black" residue in pure O_2 plasma before it is completely removed. On the other hand, if a small amount of fluorine-based gases such as SF_6 or CF_4 are added into the system, it can help get rid of the "black" residue faster. However, care must be taken because SF_6 and CF_4 can attack amorphous silicon underneath if it is exposed.

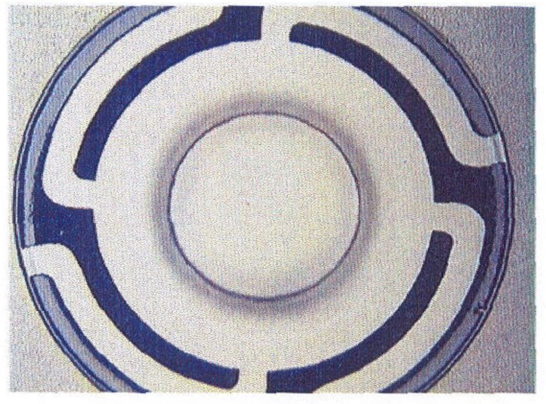

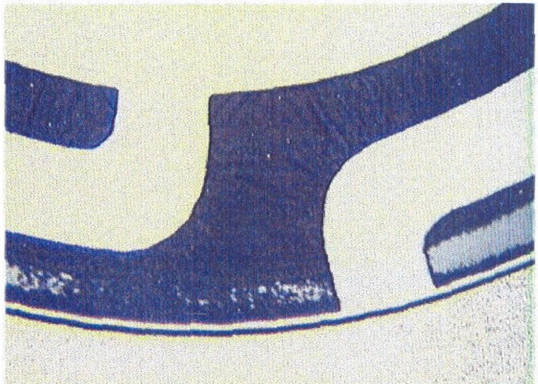

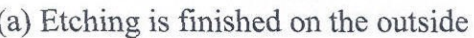

(a) Etching is finished on the outside

(b) Zoom picture of the unetched parylene

Figure 5-24: Loading effect for the parylene etching

One factor for the uneven etch rate is due to the loading effect which is commonly encountered in dry-etch process [22]. The other is perhaps due to the thickness non-uniformity of the parylene film during deposition in the chamber. These factors play an

important role to free-release the structures. If an area of the top layer of parylene is not completely removed, the device may not be able to function properly. The etch rate can be affected due to the location and the number of wafers in the etch chamber. As the number of wafers in the system is increased, it results in a high amount of etchable material exposed. Overall etch rate can be slow. Furthermore, gas flow effects, in combination with loading effects, can also cause non-uniform etch rate. The bullseye effect, in which the film at the edge of a wafer is etched more quickly than at the center, is caused by the depletion of etchant species at the wafer center. This is because more etchant species can arrive at the wafer near its edge than from just above the wafer surface.

One attempt to minimize the loading effect is to reduce the number of wafers in the etch chamber or to conduct the etching in a chamber with a large volume and high surface area [23]. In addition, utilizing large gas flows can cause the removal rate to dominate and eventually reduce the loading effect.

5.5.1.4 Aerodynamic Test Results of Passive-Valved Skin

The passive check-valved-type features vent-through holes with tethered valves on the skin to rectify the air flow in one direction. Each vent hole is covered by a tethered valve-cap and each has a diameter of 500 μm and 900 μm, respectively. In addition to the passive check-valved actuator skins, parylene skins with pin holes (500 μm in diameter) are also fabricated. The design of these skins is identical to those of the check-valved type except that there are no valve-caps. The pin-hole-integrated wings,

along with unmodified MEMS wings, are used as references to compare the effect of the check-valved actuators.

Figure 5-25 shows the phase-average plot of the lift and thrust of the reference and pin-hole-integrated wings. The MEMS wings integrated with passive check-valved pneumatic actuator are shown in Figure 5-26. The actuators are placed behind the leading-edge and trailing-edge areas where they can affect the aerodynamic performance of the wings. Figure 5-27 shows the results of MEMS wings integrated with these check-valves. The phase-average results of all types of wings are summarized in Table 5.2.

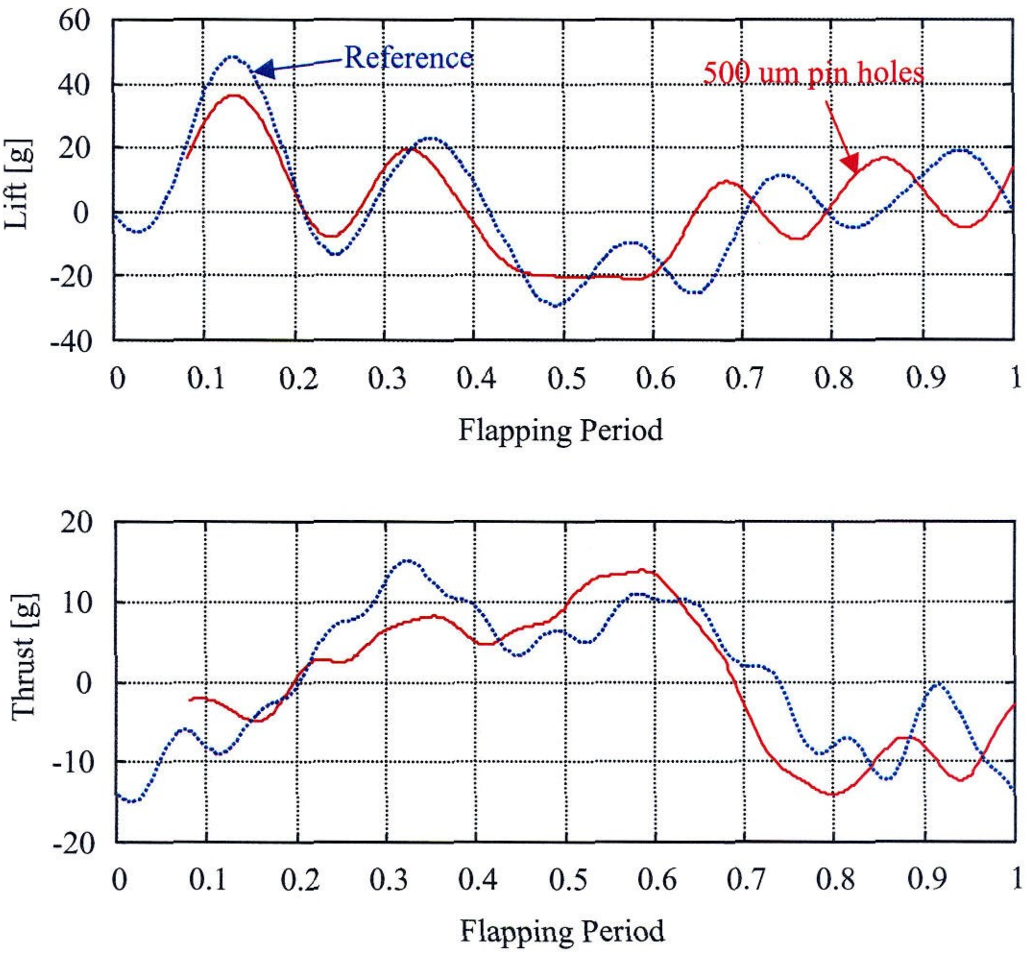

Figure 5-25: Phase-average results of the reference and hole-integrated wings

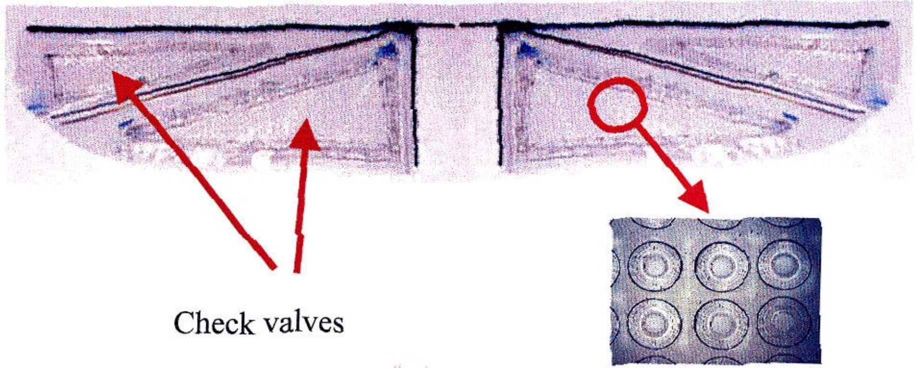

Figure 5-26: Passive Check-valved actuator-integrated MEMS wings

Figure 5-27: Phase-average results of the check-valved actuator-integrated wings

Table 5-2: Phase-average results of check-valved type wings

Actuation	Lift [g]	Thrust [g]
Reference	2.190	0.454
500-μm hole	1.376 (-37%)	0.223 (-50%)
Valves open on the downstroke	2.996 (+37%)	0.718 (+58%)
Valves close on the downstroke	3.358 (+53%)	0.663 (+46%)

The result in Figure 5-25 shows that the pin-hole-integrated wings do not perform as well compared to the reference wings. With only vent holes on the wings, the air can flow through the holes freely in both downstroke (0-0.5) and upstroke (0.5-1). The holes equalize the pressure on the upper and lower surfaces of the wings. The wing loading is reduced in both upstroke and downstroke, hence the reduction in aerodynamic performance. The phase-average of lift and thrust are 37% and 50% lower than those of the unmodified reference wings, respectively.

On the other hand, from Figure 5-27, the test results of the pneumatic check-valved type have shown a dramatic effect on the aerodynamic performance. The check-valved actuators are mounted onto the MEMS wings in two different ways. First, the valves open during downstroke and close on upstroke. Second, the valves close during downstroke and open on the upstroke. Aerodynamic test results show lift has increased significantly by 37% and 53% for the first and second ways, respectively. Similarly, the thrust has dramatically increased by almost 58% and 46%, respectively. These numbers show significant improvements. The data also shows that there is a phase delay between

opening and closing of the valves. The effect moderates the extreme lift peaks and in particular the negative lift peak that happens during the downstroke. The aerodynamic performance is highly dependent on the formation of the shedding vortices. Disturbing the leading-edge vortices will vary the pressure distribution and alter the aerodynamic performance. This delay also causes the upstroke peaks to change and phase shift relative to the unmodified reference wing.

5.5.2 Active Check-Valved Electrostatic Actuator Skin

5.5.2.1 Design

The goal for this type of skin is to investigate the effect of the active actuators between "on" and "off" states on the aerodynamic performance of the wings. It is a very difficult problem to achieve a selective optimal actively-controlled valve. Only global control will be implemented.

The design of the active check-valved electrostatic actuator skin is similar to the passive check-valved pneumatic actuator skin design except that two additional metal layers are added for ground and high-voltage contacts. A voltage can be applied to actuate the valves, controlling the valves to open or close. In addition, instead of having only two deposited layers of parylene, this design features four parylene layers. The first and forth parylene films are approximately 4.5-μm thick and the second and third are 1.5 μm. Two Cr/Au/Cr layers are sandwiched between the parylene films. Photoresist is used as a sacrificial layer to create a gap distance of 5 μm between the second and third parylene layers.

5.5.2.2 Fabrication Process

The fabrication process of the parylene MEMS active check-valved electrostatic actuator skin is a combined process of the plate-type electrostatic actuator skin and the passive check-valved pneumatic actuator processes. The fabrication process flow is shown in Figure 5-28. This process has a total of six masks. The first mask patterns the amorphous silicon. The second mask defines the shape of the bottom Cr/Au/Cr electrode. The third mask opens a contact hole to the ground electrode and the vent hole through the bottom layer of parylene while the forth mask defines the sacrificial photoresist. The fifth and sixth masks are used to pattern the top electrode and top layer parylene, respectively.

Similar to the passive check-valved pneumatic actuator process, the process begins with the spin-on sacrificial photoresist layer. Then a thin film of 1500-A° aluminum is evaporated. This layer is used as a parylene etch stop to protect the underneath photoresist. The first parylene layer (~4.5 μm) is deposited, followed by the ground Cr/Au/Cr electrode layer. Then the second parylene film is deposited to encapsulate the electrode layer. Next, the amorphous silicon is sputtered and patterned, followed by the next layer of sacrificial photoresist. Again, attention must be paid to make sure that the step corner of each vent hole is completely covered with photoresist before depositing the next parylene layer. After the deposition of the top Cr/Au/Cr, the last layer of parylene is deposited and patterned. Then the resist is released in acetone and aluminum is stripped. Finally the skin is coated with SAM and dry release the amorphous silicon with BrF_3 gas.

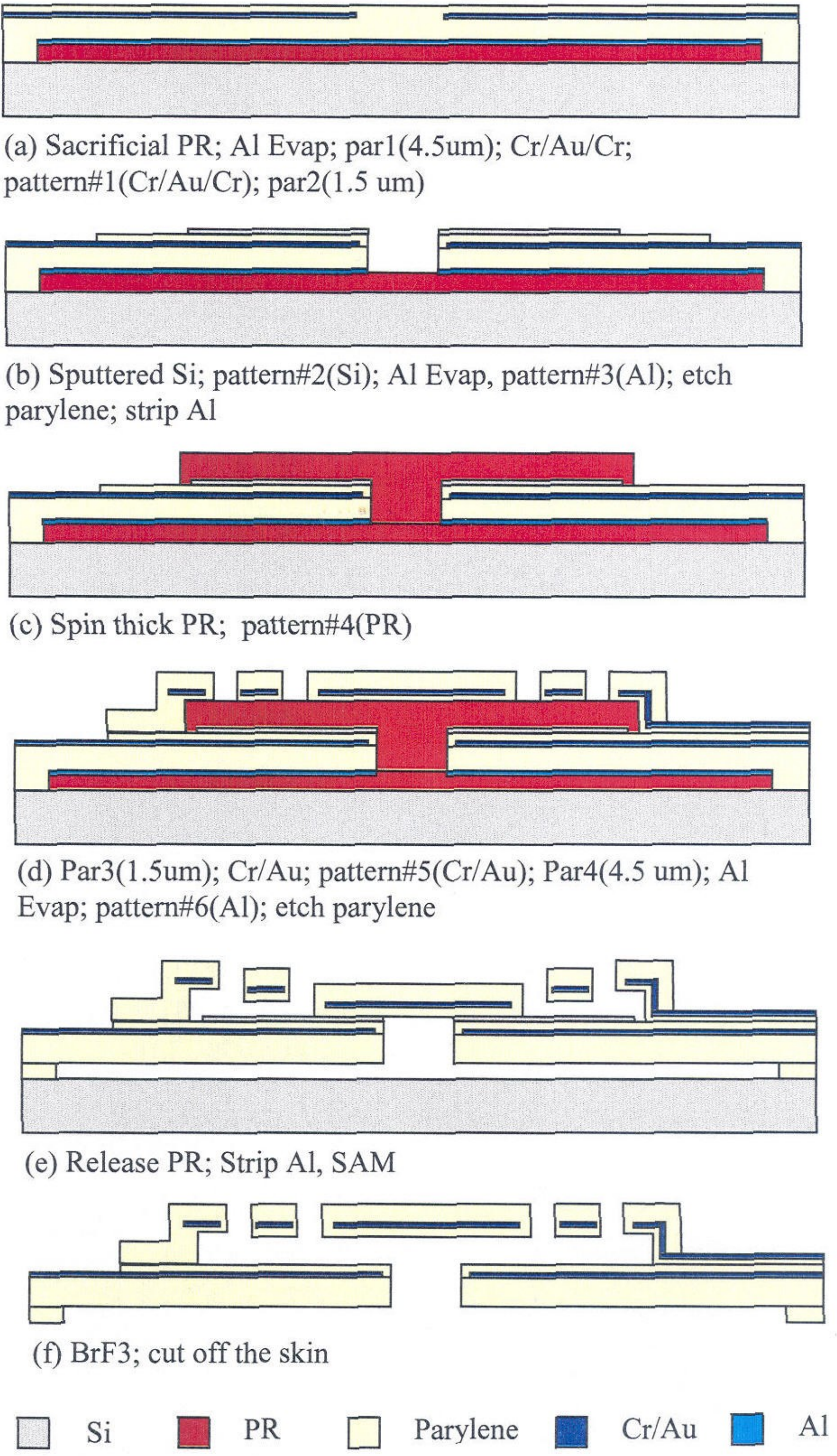

Figure 5-28: Summary of the fabrication process of the parylene MEMS active check-valved electrostatic actuator skin

There are two generations of active skins fabricated. The first has circular valve caps identical to the passive valve type. The second has square valve caps. For a given applied voltage, the latter type generated higher electrostatic force because the actuation area is larger. The fabricated check-valved skins for both types are shown in Figure 5-29.

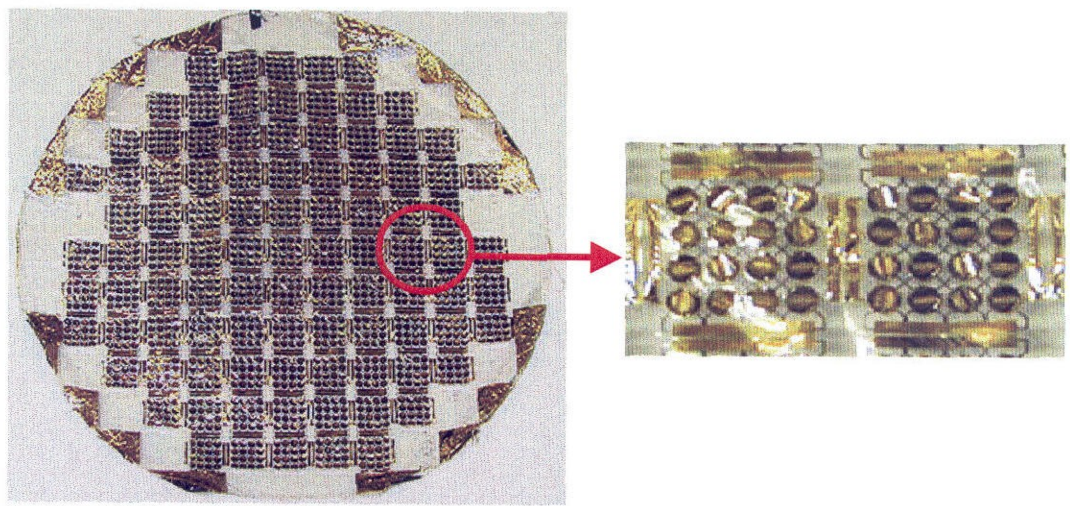

(a) First generation of the active skin with "circular" valve caps

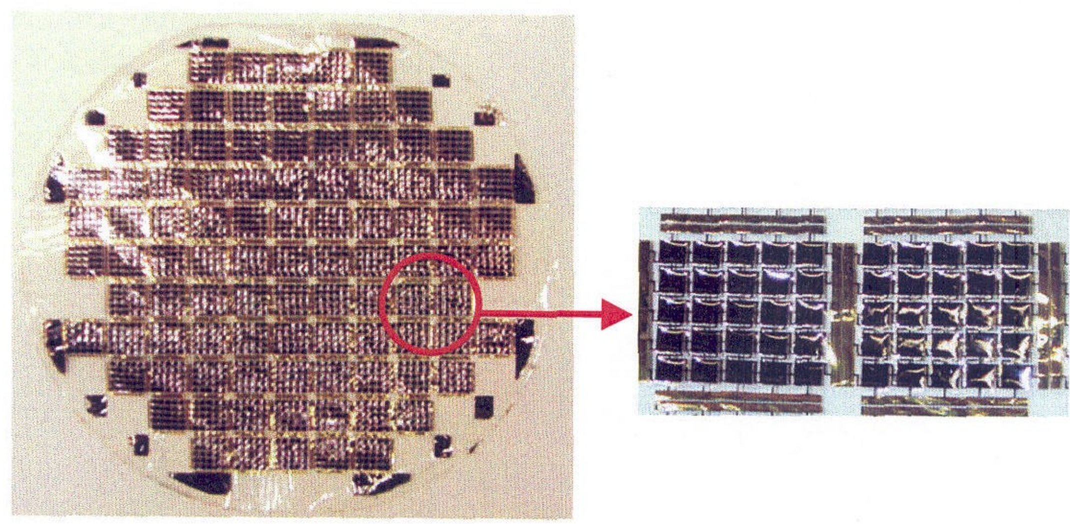

(b) Second generation of the active skin with "square" valve caps

Figure 5-29: Parylene MEMS active check-valve electrostatic actuator skins

5.5.2.3 Processing Challenges

In addition to the challenges encountered during the fabrication of plate electrostatic and passive check-valved actuator skins (resist bubbles, "black" parylene, wrinkles, etc.), we have also experienced other processing issues during fabrication. The first problem is the peeling of the last parylene film from the Au surface during thermal evaporation of aluminum. This problem is shown in Figure 5-30. The peeling is caused by the poor adhesion of the parylene to Au surface. During evaporation, the high temperature of aluminum atoms that reach the wafer's surface causes the parylene film to expand and peel off the wafer. The remedial solution is to evaporate a thin Cr layer after the Au layer and submerge the wafer in A-174 adhesion promoter before deposition of the last parylene film.

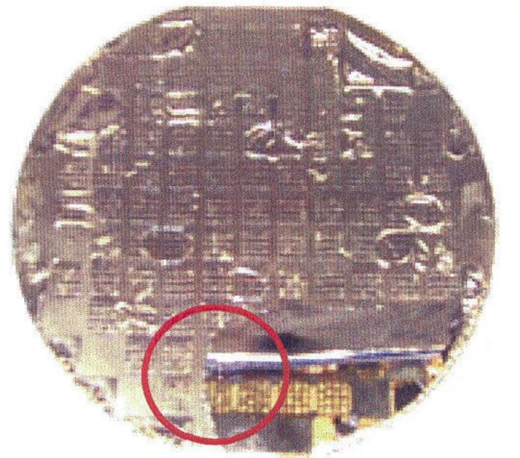

(a) Peeling of parylene on Au surface

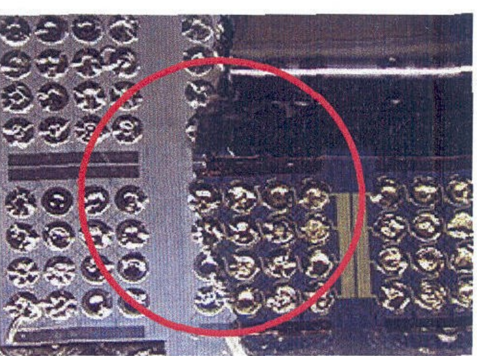

(b) Enlarged area

Figure 5-30: Poor adhesion of parylene to Au surface

The second problem is related to the disconnection of top metal electrode in the tethered arms. This is shown in Figure 5-31 where the discontinuation of the gold electrode occurs at the edge of sacrificial photoresist. There are three possible reasons.

The first reason is the poor result of lithography. Photoresist does not cover the metal layer well enough to protect it from being etched during Cr/Au etching. The second is the metal layer is too thin (~1500 A°) to cover the photoresist step (~8 μm). The third is the step of the sacrificial photoresist is perhaps too high. The solution is to spin thinner sacrificial photoresist and reflow it at 120 °C after patterning to round off the sharp edges [24]. This will make the transition smoother. Also, thicker metal film is preferred (~2500 A°) and the wafers should be continuously tilted at different angles during evaporation to ensure good step coverage. Lastly, thicker photoresist (AZ4400 instead of AZ1518) should be used during lithography to assure that the step will be covered after developing is finished.

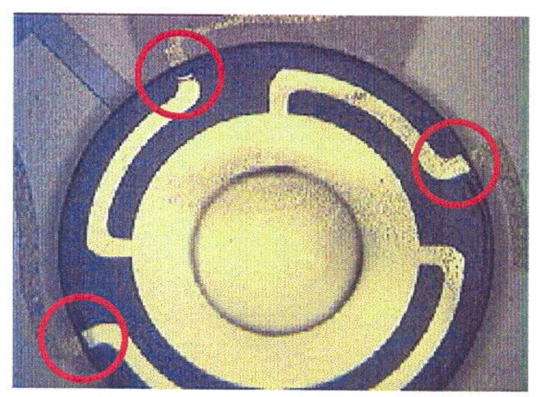

(a) Problem at the step corner

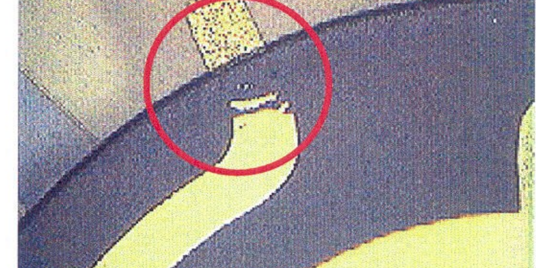

(b) Enlarged area

Figure 5-31: Disconnection of top electrode

Lastly, the stress in the top metal film causes the valve cap to curl after the photoresist underneath is released. Figure 5-32 shows the comparison of a valve with and without metal layer. The valve without metal layer appears to be flat and smooth. On the other hand, the valve with metal layer, sandwiched in between two parylene layers of 1.5 μm and 8.5 μm, curls upwards after being released due to stress. Several heat

treatments of the curled valves, with temperatures range from 60 °C to 120 °C up to 24 hours in a convection or a vacuum oven, seem to have some effect on the curling. The stress appears to be lessened. However, temperature annealing does not get rid of the stress to completely level the valve caps.

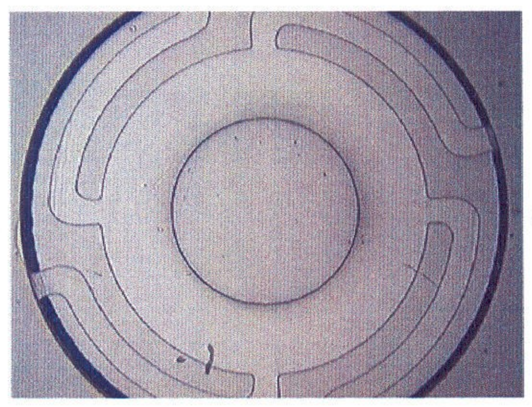

(a) No metal layer (No curling)

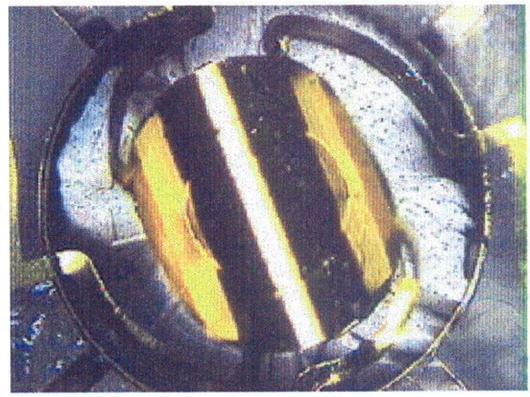

(b) With metal layer (out-of-pane curling)

Figure 5-32: Curling of valve cap

To minimize this problem, the tethered arms are redesigned to be stiffer by widening the width from 80 μm to 100 μm. This increases the stiffness of the arms to hold down the valve cap. In addition, Cr layer is evaporated before the last parylene is deposited. The Cr layer, along with A-174 adhesion promoter, helps improve the adhesion of the parylene to the metal layer. Also, the thickness of last parylene layer deposited is reduced from 8.5 μm to 4.5 μm to reduce the stress mismatch. This remedy seems to help level the valve cap after photoresist releasing. As shown in Figure 5-33, the valve cap with Cr/Au/Cr metal layers appears flat and smooth. No heat treatment is necessary.

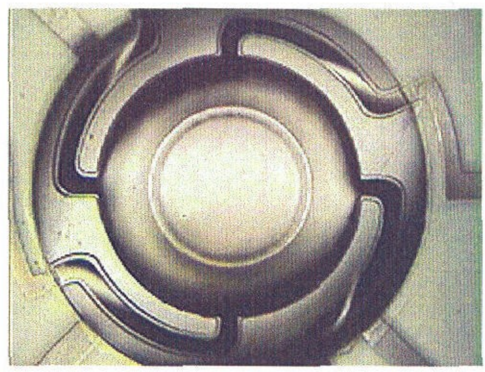

Figure 5-33: Leveled valve cap (with metal layer)

5.5.2.4 Electrostatic Actuation Test

The electrostatic actuation test is conducted by using a probe station which is connected to a high-voltage power supply and an ohmmeter. For all dice tested, there are no shortages of the top and bottom electrodes observed. The resistance measurement between the ground and high-voltage contacts is infinite. The actuators start to actuate after more than 50 volts is applied. These actuators can be continuously operated safely at 200 volts without breakdown. Breakdown is observed at voltages higher than 250 volts. During testing, some actuators can stand up to as high as 400 volts before breakdown occurs. Figure 5-34 shows the damaged actuators after breakdown.

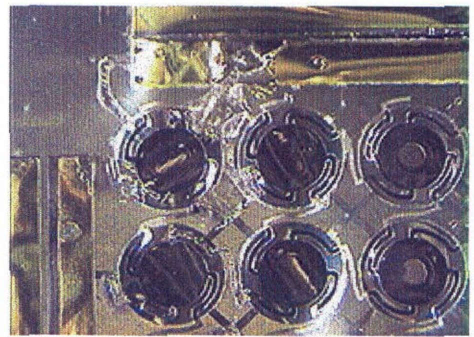

(a) Damaged actuators after breakdown

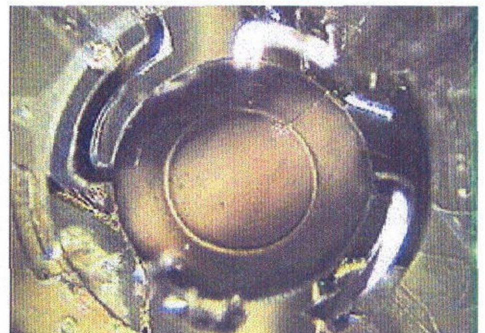

(b) Enlarged image of actuator

Figure 5-34: Breakdown of the electrostatic actuators

Actuation under high wing loading has also been performed. One die is cut from the skin and is mounted onto the load deflection setup, which has been described previously in chapter 4. Various back-pressure values, ranging from 0-2000 Pa are applied to open the valves. The valve caps are able to close the vent holes after 250 volts are applied to actuate the actuators. This pressure is much higher than the wing loading pressure which is only a few hundreds pascals.

5.5.2.5 Aerodynamic Test Results of Active-Valved Skin

We have successfully fabricated various types of parylene skins. Both plate and check-valved actuator types have been integrated onto the MEMS wings and tested in the low-speed wind tunnel at UCLA. Some examples of the fabricated active skins and integrated wings are shown in Figure 5-35.

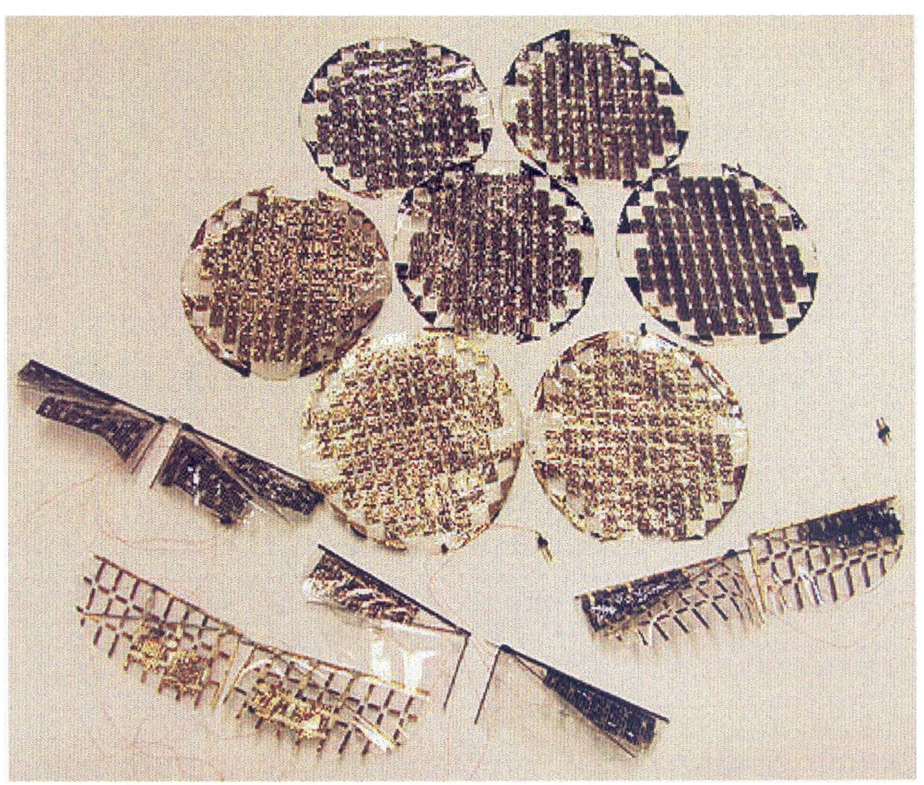

Figure 5-35: Examples of skin fabricated and integrated wings

Because the aerodynamic lift performance is highly dependent on the formation of the shedding vortices, we hope that disturbing the leading-edge vortex will also vary the pressure distribution and alter the aerodynamic performance. Moreover, aerodynamic thrust performance is coupled to the flexibility and deformation of the wings. By integrating these actuators onto the wings, the aerodynamic loading and wing deformation will be altered.

The MEMS wings integrated with active check-valved electrostatic actuator skin is shown in Figure 5-36. The skin design is similar to the pneumatic type except that two additional metal layers are added for ground and high voltage contacts. These contact pads are sandwiched in between two parylene layers. The actuators are placed behind the leading-edge where the perturbation of the air flow can lead to significant aerodynamic effect. It is believed that the location is the area where the development of the leading-edge vortex can be most affected throughout the flapping cycle. The check-valved actuators are mounted such that they are closed during the downstroke and open on the upstroke. All the actuators are wired to turn on or off in unison, effectively making them a single actuator. There are approximately five actuator die per wing, resulting in a maximum of 80 check-valves on each wing.

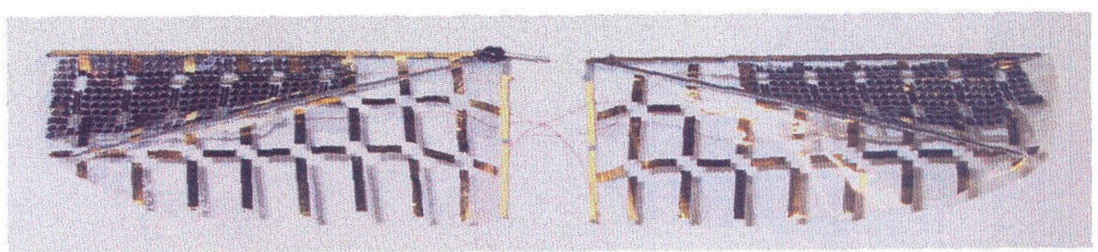

Figure 5-36: MEMS wings integrated with check-valve electrostatic actuators

The wings are place in the wind tunnel in a 30° AOA with wind speed of 3.7 m/s for dynamic test. The drive voltages applied to the electrostatic actuator range within 200-350 volts to turn on the actuators while the data is taken. The purpose is to study the effect of the valve actuators between the "on" and "off" states. The test result of the "circular" check-valved actuators in comparison to the passive-valved result is shown in Figure 5-37. Table 5-3 gives summary of the phase-average results for both "on" and "off" states of active wings in comparison to those of passive wings while Table 5-4 compares only the "on" and "off" states.

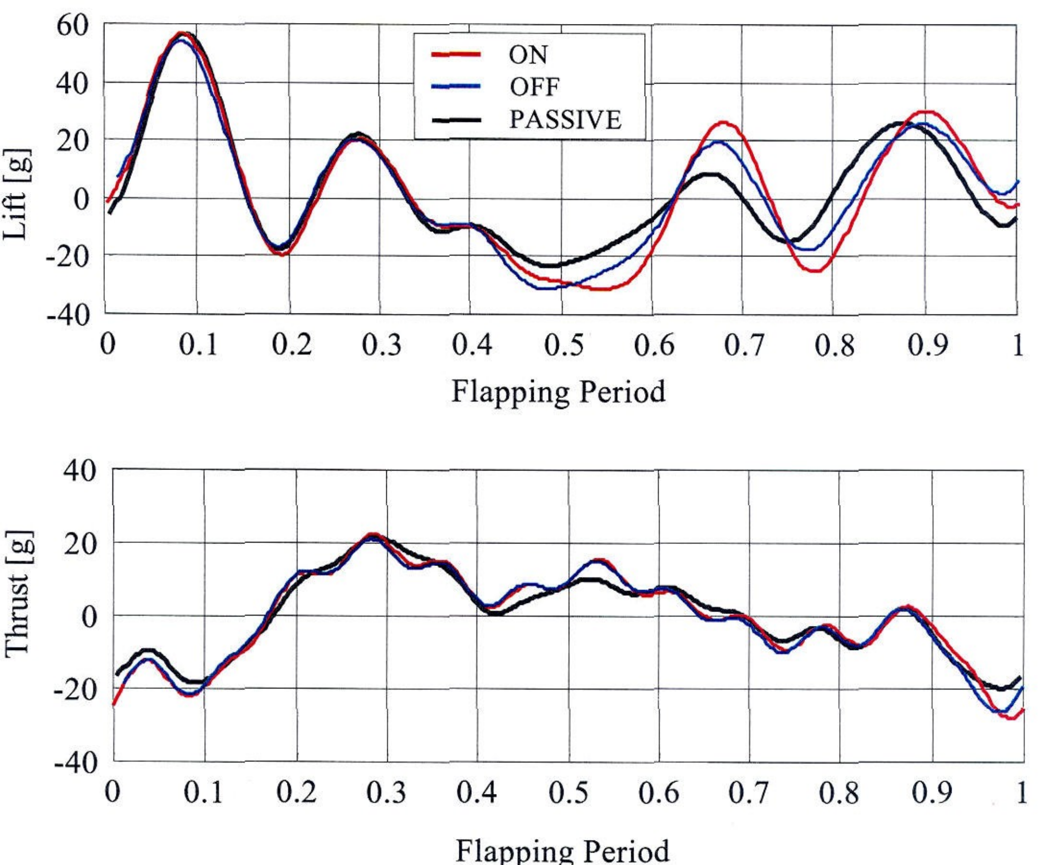

Figure 5-37: Comparison of phase-average results of the MEMS wings integrated with "circular" active and passive actuator skins

Table 5-3: Phase-average results of "circular" active-valved type wings

(Windspeed: 3.7 m/s, AOA: 30°)

Wing-Type	**Lift [g]**	**Thrust [g]**
Reference	2.190	0.454
Passive	2.610 (+19%)	0.620 (+37%)
Active "on"	2.409 (+10%)	0.712 (+57%)
Active "off"	2.388 (+9%)	0.696 (+53%)

Table 5-4: On and off states of "circular" active-valved type wings

(Windspeed: 3.7 m/s, AOA: 30°)

Wing-Type	**Lift [g]**	**Thrust [g]**
Active "off"	2.388	0.696
Active "on"	2.409 (+1%)	0.712 (+2%)

For wings integrated with the active valves, the wind tunnel test results yield small difference between "on" and "off" states as seen in Figure 5-37. During the downstroke cycle (0-0.5), the plot results show almost identical curves as expected because the valves are closed. During the upstroke cycle (0.5-1), although the difference can be observed in the lift and thrust curves, it is not as dramatic as initially expected compared to the passive-valved type. Phase-average of overall lift and thrust results shows less significant improvement between the two states. However, both states indicate positive effect compared to the reference wings.

The fact that the difference is less pronounced may be caused by several reasons. The skins are not flat and the stress of the metal layer in the valve caps prevents the complete sealing of the vent holes during testing. Because the circular valve cap has less area compared to the square valve cap with the similar dimension, the electrostatic force is not as large to hold down the valve cap to close the vent hole. If this is the case, it will affect the pressure gradient and the development of the vortex along the leading-edge. Moreover, cut-and-paste method may not have been an ideal technique to integrate the skin onto the wings. Also, previously we have stated that the advance ratio J of unsteady-state aerodynamics should be less than one. J is the ratio of the flight speed to the speed of the wingtip which is directly proportional to the flapping frequency, f, and is given by

$$J = \frac{U}{2\Phi f b} \tag{5-8}$$

where Φ, f, and b are stroke angle, flapping frequency, and wing semi-span, respectively. The given test conditions ($U = 3.7$ m/s, $\Phi = \pi/3$ radian, $f = 20$ Hz, $b = 0.07$ m) yield the J value of 1.26 which is slightly above to the unsteady-state flight regime. This may have affected the lift generation because the vortex formation, which is directly related to the amount of lift generated, is still not optimal at these test conditions. Therefore, further tests at lower J values are also investigated. This can be achieved by decreasing the wind speed or flapping the wings at higher frequency. Also, the amount of lift coefficient depends on the angle of attack of the wings and the camber. Additional tests are performed with “flat” wings and low AOA of 5°.

The numerical results of lift and thrust for both "on" and "off" states of the "square" active-valved type of the cambered wings at various J are listed in Tables 5-5 and 5-6, respectively. The plots of phase-average results at J values of 0.95, 0.61, and 0.48, are shown in Figures 5-38, 5-39, and 5-40, respectively. It can be noticed that the effect of the active valve is more pronounced, especially to the lift, at the air flow in unsteady-state regime, i.e., lower J values.

Table 5-5: Lift of "square" active-valved wings at various J values

(Wings: CIT7x3S20, AOA: 5°, f = 20 Hz)

Advance Ratio	**On [g]**	**Off [g]**
$J = 0.95$	1.43	1.42
$J = 0.61$	0.99	0.94
$J = 0.48$	0.14	-0.01

Table 5-6: Thrust of "square" active-valved wings at various J values

(Wings: CIT7x3S20, AOA: 5°, f = 20 Hz)

Advance Ratio	**On [g]**	**Off [g]**
$J = 0.95$	0.76	0.80
$J = 0.61$	1.04	0.88
$J = 0.48$	1.17	1.00

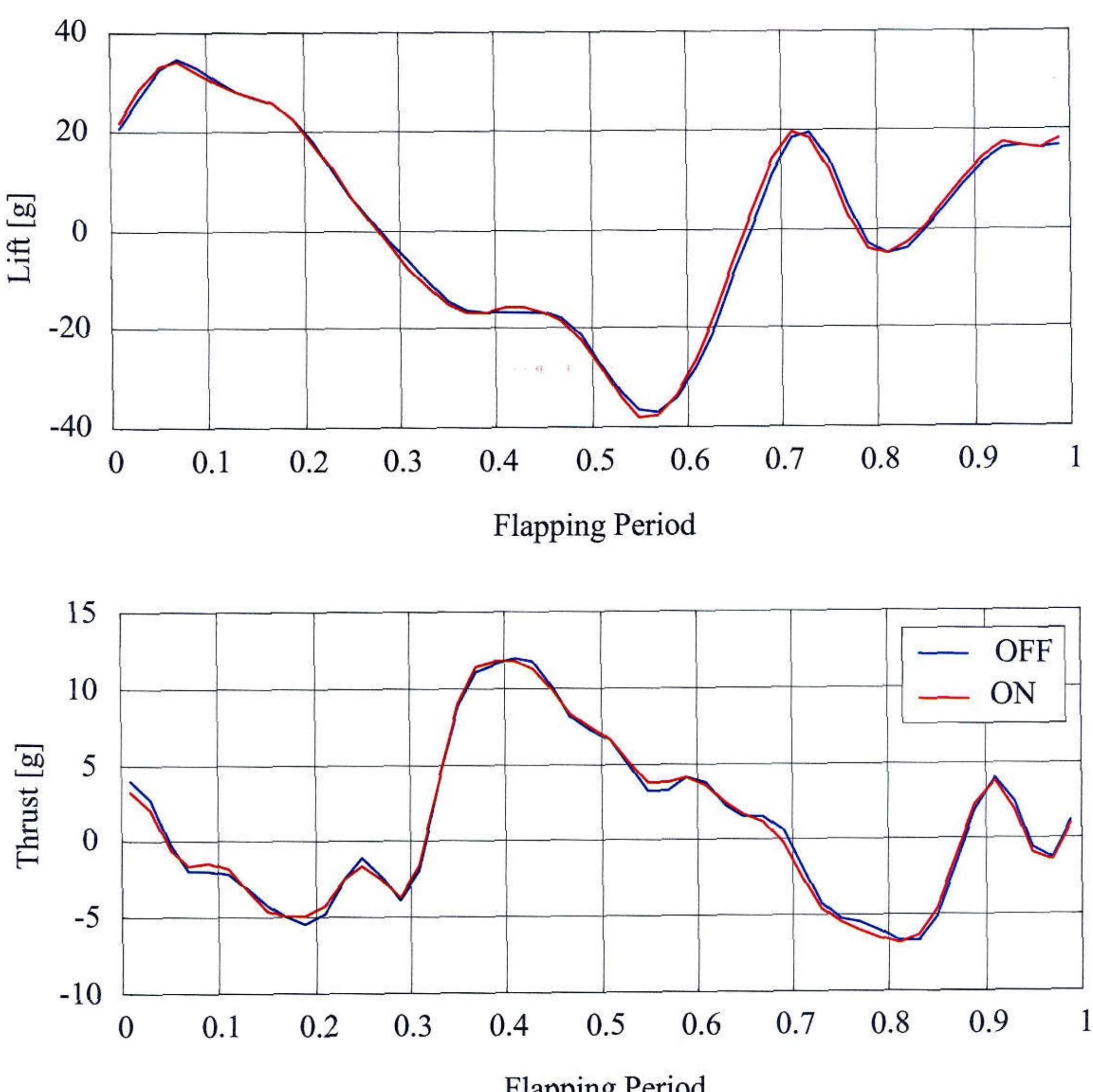

Figure 5-38: Phase-average results of the "cambered" wings integrated with "square" active-valved actuator skins at $J = 0.95$

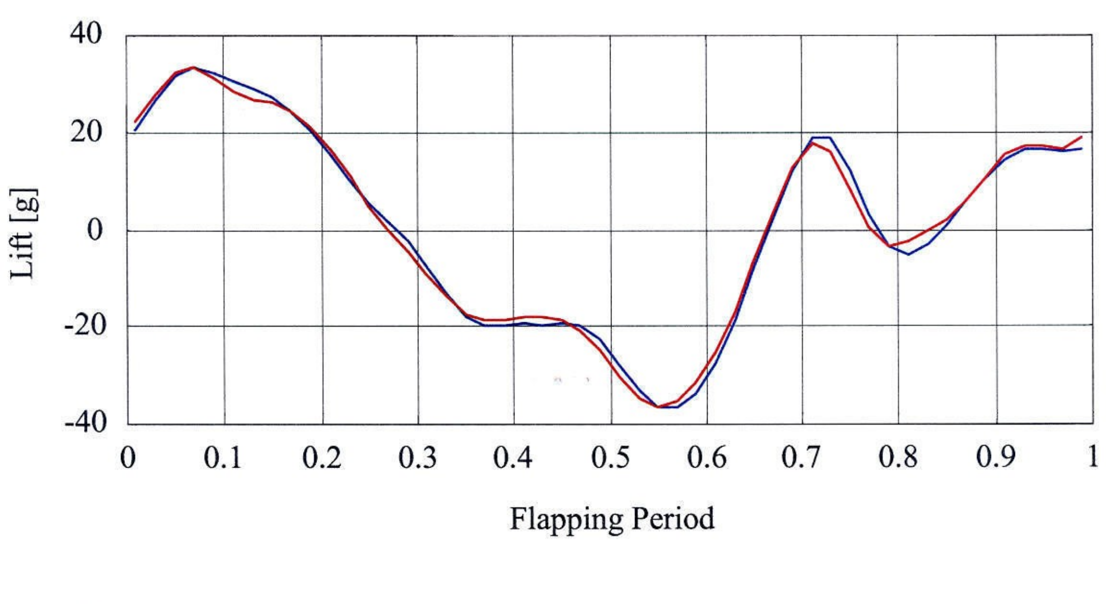

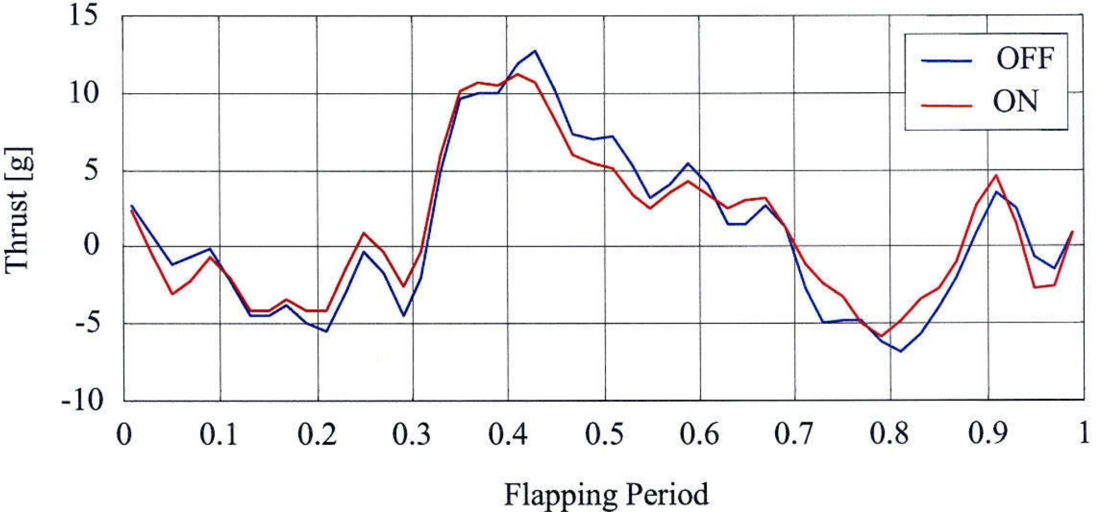

Figure 5-39: Phase-average results of the "cambered" wings integrated with "square" active-valved actuator skins at $J = 0.61$

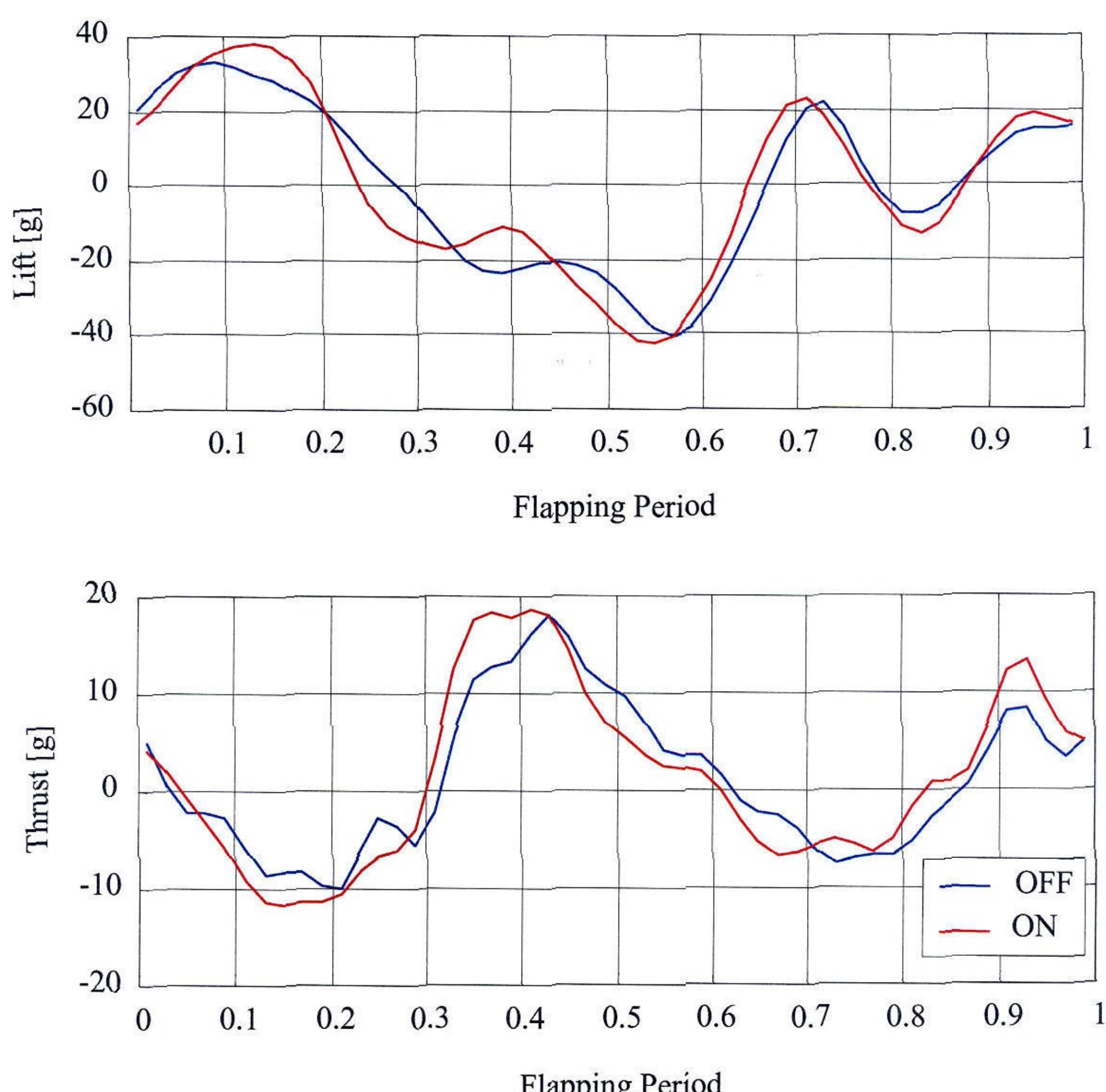

Figure 5-40: Phase-average results of the "cambered" wings integrated with "square" active-valved actuator skins at $J = 0.48$

As shown in Figures 5-38 to 5-40, the maximum lift peak occurs at the beginning of the downstroke (0-0.5) while the next lower peak is near the middle of the upstroke (0.5-1.0). The vortex that forms underneath the wing during beginning of the upstroke contributes to the negative lift portion. Similarly, the results show that the maximum thrust is not produced until almost at the end of the downstroke which is the time when the flexible trailing edge begins to snap down. It is also the time when the separation vortex is being shed. From Figure 5-40, the highest lift (~ 40 g) and thrust (~20 g) values occur during the actuators are turned on. It can also be observed that as the J value becomes lower, lift and thrust become larger due to the amount and size of the vortex formed. However, as J decreases the average of overall lift also decreases as shown in Table 5-5. This is because lift is directly proportional the wind speed. In all cases, when compared to "off" state, both lift and thrust increase when the actuators are "on" which clearly indicates the effect of the valve being closed on the aerodynamics. As seen in Figure 5-40 for $J = 0.48$, the effect is obvious from the plots of lift and thrust. The valves manipulate the unsteady leading-edge vortex and change the pressure distribution on the wings. The actuators become more effective because the strength of vortex increases as J decreases.

Additional tests are performed to observe the effect of the camber of the wings. The dynamic test of "flat" wings is conducted to compare to the results of the cambered wings at the same J value. The phase-average plot results are shown in Figure 5-41 while Table 5-7 shows the comparison of lift and thrust of both types of wings with the actuators on and off.

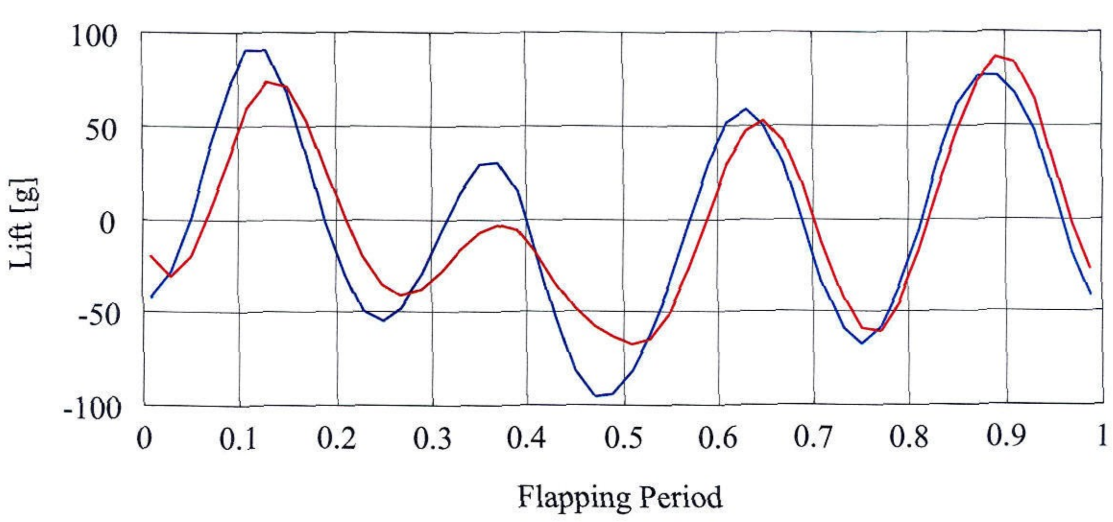

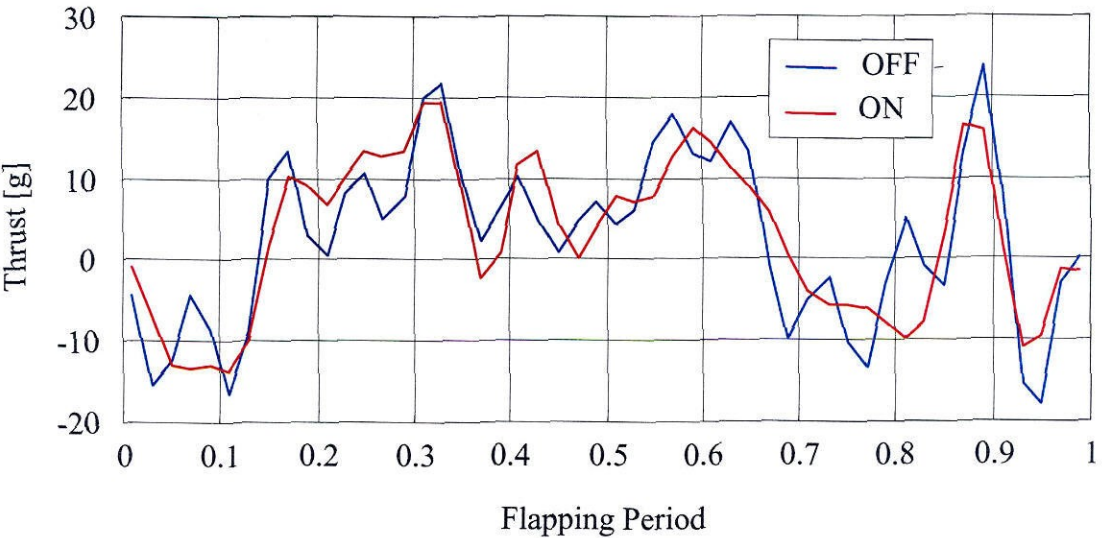

Figure 5-41: Phase-average results of "flat" wings integrated with "square" active-valved actuator skins at $J = 0.48$

Table 5-7: Comparison of lift and thrust of flat and cambered wings
(J: 0.48, AOA: 5°, 350-V actuation)

Wing-Type	**Lift [g]**	**Thrust [g]**
Flat: off	-1.42	2.54
Flat: on	-1.21	2.69
Cambered: off	-0.01	1.00
Cambered: on	0.14	1.17

The data in Table 5-7 shows that in all test cases, the average of overall lift of "flat" wings is much smaller than the "cambered" wings. This is perhaps because the flat wings are not optimized to take advantage of the vortex generation along the axial flow. Turning on the actuators helps improve the average lift and thrust of both flat and cambered wings. For the flat wings, although the lift is negative, the average lift increases by 15% while thrust increases by 6%. For the cambered wings, the average lift grows from negative to positive and the average thrust rises by 17%.

The plot results in Figure 5-41 show four distinct lift peaks during both downstroke and upstroke. This indicates the rapid generation and shedding of the vortices. These vortices result from the flow separation at the leading edge of the wings and its strength depends on the velocity gradient on top and bottom of the wings [25]. In contrast, the lift results from the cambered wings (Figure 5-40) show only two distinct peaks, one during downstroke and another during the upstroke. This is perhaps because cambered effect helps create dynamic stall that delays the separation of the flow during the downstroke and results in a smooth lift curve. The thrust diagram of the flat wings

also exhibits less smooth characteristics with several small peaks compared to that of the cambered wings. The pattern is more abrupt. Thrust is much less well-understood as it depends on the wing's flexibility and the interaction of the vortex growth and its shedding.

Clearly the aerodynamic effect of active actuator skins can be visibly seen from the phase-average diagrams of lift and thrust. The effect is obvious especially in the low J regime where the flow is more unsteady. Although the difference is not distinct in some cases, it may be perhaps due to the fact that the gradient pressure is not as significant as expected. There may be some air leakage due to the non-flatness of the skin surface. This is one of the biggest challenges because the skin is very flexible and not completely flat. Higher electrostatic force may be required to seal the vent holes. Nevertheless, we have demonstrated the effect of the active actuators to control the air flow and the results are positive and promising.

5.6 Summary

The parylene MEMS technology is successfully developed to fabricate actuator skins for adaptive flow control. The technology is an extension from the parylene actuator diaphragm on a silicon chip to fabricate and release wafer-sized actuator skins. Sacrificial photoresist is used as a skin releasing technology. Various designs of the skin, both pneumatic (passive) and electrostatic (active), are investigated. This work has presented several challenges during the fabrication and testing processes, such as stiction, wrinkles of thin films, non-uniform etching, and flatness of the released skins. Silicon wafer is only a mechanical support during the fabrication process and the final device

does not contain any silicon, making it difficult during the probing test because there is no solid support underneath the device. Sharp probes can easily puncture holes through the skin and can destroy the device.

The skins are integrated onto the MEMS wings and they are tested in the wind tunnel. The plate-type features large electrostatic actuation plates without any vent holes throughout the membrane. It is aimed to alter the effective thickness of the membrane after actuation. It is hoped that the change in stiffness would be able to impact the aerodynamic performance. The test results of this type of skin do not show significant change before and after actuation. These poor results are perhaps due to the fact that the parylene membrane is not thick enough to affect the stiffness and the location of the actuators is not optimal. Thus this type of actuators is not the best design to study this complicate problem.

The check-valved type features vent-through holes with tethered valves throughout the membrane skin. This type of skin takes an advantage of the pressure gradient difference between the top and bottom of the membrane to alter the aerodynamic performance. Several generation of both pneumatic (passive) and electrostatic (active) actuator skins are developed and fabricated. For pneumatic type, the wind-tunnel test results show that the lift and thrust of the wings integrated with passive valves increase dramatically by almost 50%, depending on the mounting direction of the valves. For wings integrated with the active valves, the wind tunnel test results yield visible effect between "on" and "off" states. Although the difference can be observed in the lift and thrust curves, it is not as dramatic as initially expected. It may be caused by several reasons. The skins are not flat and the stress of the metal layer in the valve caps prevents

the complete sealing of the vent holes during testing. This will affect the pressure gradient and the development of the vortex along the leading-edge. Moreover, cut-and-paste method may not have been an ideal technique to integrate the skin onto the wings.

In spite the fact that this problem is very complex, at least we have shown and demonstrated that the integration of MEMS devices on the wings has positive effect on altering the air flow around the wings. It may be a long time still before anyone can fully achieve and understand how to control the aerodynamics of flapping flight with distributive active actuators that can be integrated with feedback control device to optimize the overall performance.

5.7 Bibliography

[1] F. Jiang, Y. -C. Tai, Ken Walsh, T. Tsao, G. B. Lee, and C. -M. Ho, "A Flexible MEMS Technology and Its First Application to Shear Stress Sensor Skin," *Proceedings, The 10th Annual Int. IEEE Conf. on Micro Electro Mechanical Systems Workshop (MEMS '97),* Nagoya, Japan, pp. 465-470, Jan. 26-30, 1997.

[2] C. -M Ho and Y. -C. Tai, "Review: MEMS and Its Applications for Flow Control," *Journal of Fluids Engineering,* vol. 118, pp. 437-447, September, 1996.

[3] S. Wu, J. Mai, Y. Zohar, Y.-C. Tai and C.-M. Ho, "A Suspended Microchannel with Integrated Temperature Sensors for High-Pressure Flow Studies," *The 11th Annual International Workshop on Micro Electro Mechanical Systems (MEMS '98),* Heidelberg, Germany, pp. 87-92, Jan. 25-29, 1998.

[4] S. Wu, Q. Lin, Y. Yuen and Y.C. Tai, "MEMS Flow Sensor for Nano-Fluidic Applications," *Proceedings, The 13th Annual Int. IEEE Conf. on Micro Electro Mechanical Systems (MEMS 2000),* Miyazaki, Japan, pp. 745-750, Jan. 23-27, 2000.

[5] Y. -C. Tai, and R. S. Muller, "Polysilicon Bridge as a Flow Meter," *Sensors and Actuators*, vol. 15, pp. 63-75, 1988.

[6] F. Jiang, Y. -C. Tai, R. Karen, M. Gaustenauer, and C. H. Ho, "Theoretical and Experimental Studies of Micromachined Hot-Wire Anemometers," *International Electron Devices Meeting (IEDM),* San Francisco, pp. 139-142, Dec. 11-14, 1994.

[7] F. Jiang, Y. -C. Tai, C. -M. Ho, and W. J. Li, "A Micromachined Polysilicon Hot-Wire Anemometer," *Technical Digest, Solid-State Sensor and Actuator Workshop (Hilton Head '94),* Hilton Head Island, SC, pp. 264-267, June 13-26, 1994.

[8] F. Jiang, Y.-C. Tai, J.-B. Huang, and C. -M. Ho, "Polysilicon Structures for Shear Stress Sensors," *Proceedings, IEEE TENCON'95,* Hong Kong, pp. 12-15, Nov. 7-10, 1995.

[9] F. Jiang, Y. -C. Tai, B. Gupta, R. Goodman, S. Tung, and C.-M. Ho, "A Micromachined Shear Stress Imager," *Proceedings, The 9th Annual Int. IEEE Conf. on Micro Electro Mechanical Systems Workshop (MEMS '96),* San Diego, CA, pp. 110-115, Feb. 11-15, 1996.

[10] F. Jiang, Y. Xu, T. Weng, Z. Han, Y. -C. Tai, A. Huang, C. -M. Ho, and S. New Bern, "Flexible Shear Stress Sensor Skin for Aerodynamics Applications," *Proceedings, The 13th Annual Int. IEEE Conf. on Micro Electro Mechanical Systems Workshop (MEMS '00),* Miyazaki, Japan, pp. 364-369, Jan. 23-27, 2000.

[11] T. Tsao, F. Jiang, R. A. Miller, Y. -C. Tai, B. Gupta, R. Goodman, S. Tung, and C. -M. Ho, "An Integrated MEMS System for Turbulent Boundary Layer Control," *Technical Digest, 1997 International Conference on Solid-State Sensors and Actuators (Transducers '97),* Chicago, IL, vol. 1, pp. 315-318, Jun. 16-19, 1997.

[12] C. Grosjean and Y. -C. Tai. "Micro Balloon Actuators for Aerodynamic Control," *Proc. of the 11th Annual Intl. Workshop on Micro Electro Mechanical Systems (MEMS '98)*, pp. 166-171, Heidelberg, Germany, Jan. 25-29, 1998.

[13] X. Yang, *Micromachined Silicone Rubber Membrane Valves for Fluidic Applications,* Ph.D. Thesis, California Institute of Technology, 1999.

[14] Parylene Conformal Coatings Specifications and Properties, Specialty Coating Systems, Inc., 5707 West Minnesota Street, Indianapolis, IN 46241, Tel: (800) 356-8260, Fax: (317) 240-2073.

[15] X. Q. Wang, *Integrated Parylene Micro Electro Mechanical Systems (MEMS),* Ph.D. Thesis, p. 63, California Institute of Technology, 2000.

[16] H. T. G. van Lintel, F. C. M. van de Pol, and A. Bouwstra, "Piezoelectric micropump based on micromachining of silicon," *Sensors and Actuators*, vol. 15, no. 2, pp. 153-168, 1988.

[17] J. Tirén, L. Tenerz, and B. Hok, "A batch-fabricated non-reverse valve with cantilever beam manufactured by micromachining of silicon," *Sensors and Actuators*, vol. 18, pp. 389-396, 1989.

[18] M. Esashi, S. Shoji, and A. Nakano, "Normally closed microvalve and micropump fabricated on a silicon wafer," *Proc. IEEE Micro Electro Mechanical Systems (MEMS '89)*, Salt Lake City, UT, pp. 29-34, Feb. 20-22, 1989.

[19] L. Smith and B. Hok, "A silicon self-aligned non-reverse valve," *Digest of Tech. Papers, Int. Conf. on Solid-State Sensors and Actuators (Transducers 91)*, San Francisco, CA, pp. 1049-1051, June 24-27, 1991.

[20] S. Shoji, B. H. van der Schoot, N. F. de Rooij, and M. Esashi, "A study of a high-pressure micropump for integrated chemical analyzing systems," *Sensors and Actuators*, A32, pp. 335-339, 1992.

[21] X. Q. Wang, Q. Lin, and Y. -C. Tai, "A Parylene Micro Check Valve," *The 12th IEEE International Conference on Micro Electro Mechanical Systems (MEMS '99)*, Florida, U.S.A, pp. 177-182, Jan. 17-21, 1999.

[22] S. Wolf and R. N. Tauber, "Silicon Processing for the VLSI Era," Volume 1 – Process Technology, Lattice Press, Sunset Beach, CA, 1986, pp. 528-529.

[23] S. Wolf and R. N. Tauber, "Silicon Processing for the VLSI Era," Volume 1 – Process Technology, Lattice Press, Sunset Beach, CA, 1986, pp. 577-578.

[24] X. Q. Wang, *Integrated Parylene Micro Electro Mechanical Systems (MEMS)*, Ph.D. Thesis, p. 69, California Institute of Technology, 2000.

[25] H. Lui, C. P. Ellington, K. Kawachi, C. van den Berg, and A. P. Wilmott, "A Computational Fluid Dynamic Study of Hawkmoth Hovering," *Journal of Experimental Biology*, vol. 201, pp. 461-477, 1998.

Chapter 6

Conclusion

6.1 Summary of Research

The novel titanium-alloy and low-temperature parylene technologies have been developed to fabricate MEMS wings to systematically study the aerodynamic of flapping wings. Titanium-alloy (Ti-6Al-4V) is used as a substrate to fabricate light wingframe while the existing parylene technology enables the fabrication of the wing membrane. Parylene has a low young modulus; thus it is a perfect membrane material because of its flexibility. Without the assistance of MEMS technology, non-MEMS wings can be handmade using carbon fiber rods with mylar or paper as wing membrane. This method is cumbersome, time-consuming, and difficult to create a perfect matching set of wings. Using MEMS technology, wings are designed and fabricated easily with varying parameters such as chord- and spar-lengths, membrane thickness, number of spars, and

sweep angles. This indicates that MEMS technology can quickly, efficiently, and systematically accommodate these variable changes. In addition, with MEMS fabrication technology, batch fabrication of identical wings can be mass-produced without any expensive molding.

The fabricated wings are mechanically tested for their stiffness and durability at various flapping frequencies. They are also extensively tested in a low-speed wind tunnel to measure their aerodynamic lift and thrust performances in an unsteady-state environment. Among the many 7-cm wings fabricated, the wing design CIT7x3S20 shows the best results in terms of lift, thrust, and the minimal input power required. For the first time, we have also discovered that wings with stiff leading-edge can achieve higher lift coefficients compared to those with flexible leading-edge. Therefore, a novel leading-edge stiffness-enhanced titanium-alloy wingframe technology has been developed by incorporating a lightweight carbon-fiber rod to the wing's leading-edge during fabrication process prior to parylene deposition. The results are the wings that behave characteristically the same way as the natural wings, i.e., the lift coefficient C_L increases significantly as the advance ratio J decreases below unity. In addition, we have designed an experiment to gather aerodynamic test data to confirm that the inboard regions of the wings are primarily used to generate thrust while the outboard regions are used to generate lift. This is an important study to locate an ideal location to where we should integrate active devices to alter the aerodynamic performance of the wings. This idea of integrating whether passive or active devices makes sense in terms of the wing optimization aspect. The effort to fabricate passive or active actuator devices for micro

adaptive flow control for MEMS wings is a novel concept. These devices are to be integrated directly onto the MEMS wings.

The low-temperature parylene MEMS technology has been developed for this purpose to fabricate parylene actuator device for aerodynamic control. The goal is to fabricate parylene actuator "skins" that are compatible and can be integrated with the wing membrane. The device must first be realized on a silicon chip to study the release of large membrane and its actuation. Following the successful fabrication of the MEMS wings, a small actuator device is developed and fabricated. A large 2-mm x 2-mm parylene electrostatic actuator valve diaphragm on a silicon chip is designed and fabricated. The process also discusses the novel anti-stiction technologies that are crucial to release large area parylene actuator skins. The anti-stiction technologies include the combination usage of anti-stiction posts, SAM coating, surface roughening, and bromine trifluoride (BrF_3) dry etching of silicon. These technologies prove to be key factors in successful development of the parylene actuator skins which follow.

The translation of the parylene MEMS technology from a diaphragm on a single silicon chip to a "skin" on the entire wafer is carefully designed. The fabrication technology is very challenging because the final released skin contains no structural support of bulk silicon. Handling and testing must be carefully performed so that the membranes are not torn apart. Two types of skins, plate and valve, are designed and fabricated. The plate type features large electrostatic actuation plates without any vent holes throughout the membrane. It is aimed to alter the effective thickness of the membrane after actuation. It is hoped that the change in stiffness would be able to impact the aerodynamic performance. The test results of this type of skin show insignificant

change before and after actuation. These poor results are perhaps due to the fact that the parylene membrane is not thick enough to affect the stiffness and the locations of the actuators are not optimal. Thus this type of actuator may not have been the best design to study this complicate problem.

The check-valved type features vent-through holes with tethered valves throughout the membrane skin. This type of skin takes an advantage of the pressure gradient difference between the top and bottom of the membrane to alter the aerodynamic performance. There are two types of fabricated check-valved actuators: pneumatic (passive) and electrostatic (active). For pneumatic type, there are no metal layers on the skin. The actuation relies upon the wing loading during flapping cycle. For each cycle, the loading either pushes the valve caps to open or close to control air movement through the vent holes. For electrostatic type, the ground and high-voltage electrode pads are sandwiched between two parylene layers. By applying voltages to regulate the actuators, the vent holes can be opened or closed by the electrostatic force.

The skins are integrated onto the MEMS wings and tested in the wind tunnel. We have found that for the wings integrated with passive valves, the lift and thrust increase significantly by almost 50%, depending on the mount direction of the actuator valves. For wings integrated with the active valves, the aerodynamic effect between on and off states can be visibly seen from the phase-average plots of lift and thrust, especially in the low J regime. The differences in the lift and thrust curves are not as dramatic as initially expected compared to the passive type. This might be caused by the fact that the skins are not as flat and the valve caps cannot completely seal the vent holes during actuation. It would affect the pressure gradient and the development of the vortex along the leading-

edge. Moreover, cut-and-paste method may not have been an ideal solution to integrate the skin onto the wings. The skins are difficult to handle and actuators are prone to rip easily if they are not handled properly. Nevertheless, the effect of the active actuators for adaptive air flow control has been demonstrated and the results are very promising.

It is also important to note several challenges that occurred during the fabrication. The problems such as stress-induced wrinkle and curling can deteriorate the performance of the device. These are also the causes for sealing difficulties. In addition, stiction of valve caps can prevent them to open properly during flapping. These challenges are encountered and remedial solutions are applied to minimize them from occurring again.

6.2 Future Research Directions

There are still several interesting future research aspects that can be conducted. Skins can be redesigned and fabricated with larger covering area and strong holding force. The operation of our current actuator skins is comparable to digital, i.e., on or off valve. To achieve an optimal micro adaptive flow control, the active actuator may need to be analog. For example, the valves may need to be continuously controlled. Furthermore, so far the current demonstrated control is global actuator control using the output of a single force balance. Either all actuators are on or off at the same time. This scheme may not be optimal. The optimal scheme may require global and local control, or just selective control of each individual actuator. In addition, flexible sensors may need to be integrated onto the skins to achieve the optimal adaptive flow of control using both flexible sensor and actuator skins. Finally, angular speed control effect can be studied using asynchronization of the flapping cycle to vary the wing speed during downstroke

and upstroke to achieve optimal aerodynamic effect. Initial test has shown significant differences before and after the angular speed control is employed.

While we are still a long way from building ideal "bird-like" wings that can utilize unsteady-state environment effectively and efficiently, the development of this novel low-temperature parylene technology is a good indication what we are stepping in the right direction. The compatibility and suitability of parylene as a material for microfabrication, specifically integration with the existing MEMS wing process, is essential. It is beginning to look reasonable that, with properly engineered aeroelastic materials, integrated sensors, and advanced power supplies, one day it may be possible to design optimal wings that can take advantage of the development and shedding of these vortices. The device fabrication with MEMS technology has been established and it may one day become a foundation for the future direction of this type of research.

Appendix A

Development of Biomimetic Flight

A.1 Introduction

Flight has undoubtedly intrigued mankind for several hundred of years. During the late 15th century, Leonardo da Vinci made the first design of flying machines, using bird wings for models. In the late 18th century, the balloon of the Montgolfier Brothers, propelled by burning piles of moist wool and old shoes, became the first balloon in history to take off (tethered flight). Not until the early 20th century was the first successful sustained flight attempted by the Wright Brothers. It was in the morning of December 17, 1903, at Kitty Hawk, North Carolina, when the first powered, manned, heavier-than-air, controlled flight was successfully attempted. The flight lasted for only 12 seconds and covered a distance of just 121 feet (37 m), but the new history of flight was rewritten and had never been the same. Since those days, the understanding of the laws of aerodynamics, stability and control of "fixed-wing" flight has progressed tremendously. Today new technologies have been developed to build planes that can fly

faster than the speed of sound or even space shuttles that can routinely travel to outer space and return to earth in a matter of days.

Although today's advanced technologies and current engineering designs of fixed-wing aircraft may have exceeded nature with regard to size, weight, speed, and range, they are still much inferior to nature in many ways. Nature builds self-assembling systems with staggering complexity, yet these systems provide robust, autonomous, agility, and efficiency that are well-adapted to various environments. Therefore, perhaps it is time that today we revisit and reevaluate the nature once more.

A.2 Biomimetic Flight

A.2.1 Background

If we look at most living creatures closely, we find that most of them fly [1]. There are more than one million species of flying insects with perhaps as many as ten million yet undescribed worldwide [2]. In addition, there exists approximately ten thousand species of birds and bats [3]. The vast majority of these creatures, many of which are not well understood, exhibit a bewildering variety of ways to achieve flight. To present days, flapping-wing flight has undoubtedly been the most sophisticated realm of flight and still remains underexplored. The key aerodynamics is the employment of the unsteady flows to control the biologic flight systems. This is a non-trivial problem that many aerodynamicists and engineers have been trying to solve. In unsteady flows, the generation of lift force on flapping wings involves continuous shedding of vorticity into the surrounding air and generation of a complex flow field called the vortex wake. Production and manipulation of these unsteady vortex flows form the basis for extraordinary maneuverability. In contrast to the typical fixed-wing flight, most

flapping-wing creatures are capable of exceedingly rapid changes in flight speed and direction. This results in near-instantaneous turns, accelerations, directional changes, and other dynamic characteristics of which are unmatched by the current technologies.

Early attempts at flapping-wing flight relied upon designs mainly based on natural flying creatures, such as birds, bats and insects. Unmatched by any man-made systems, these biological creatures have mastered the unsteady flows and the low Reynolds number (*Re*), the dimensionless parameter that is proportional to the ratio of inertial to viscous forces acting on objects moving within fluids [4-6]. The development of flapping-wing flight can be dated back to the period around 1500 A.D. when Leonardo da Vinci designed his flapping-wing device [7]. The examples of other man-sized, human-powered aircraft designs by early inventors from mid to late 19th century can be seen in Figure A-1. These aircrafts, however, were not able to successfully stay airborne [8]. The first time that a flapping-wing aircraft, or ornithopter, had flown successfully was in 1870. Gustave Trouvé's ornithopter, powered by an internal combustion engine using gunpowder, flew 70 meters in a demonstration to the French Academy of Sciences. His ornithopter design is shown in Figure A-2.

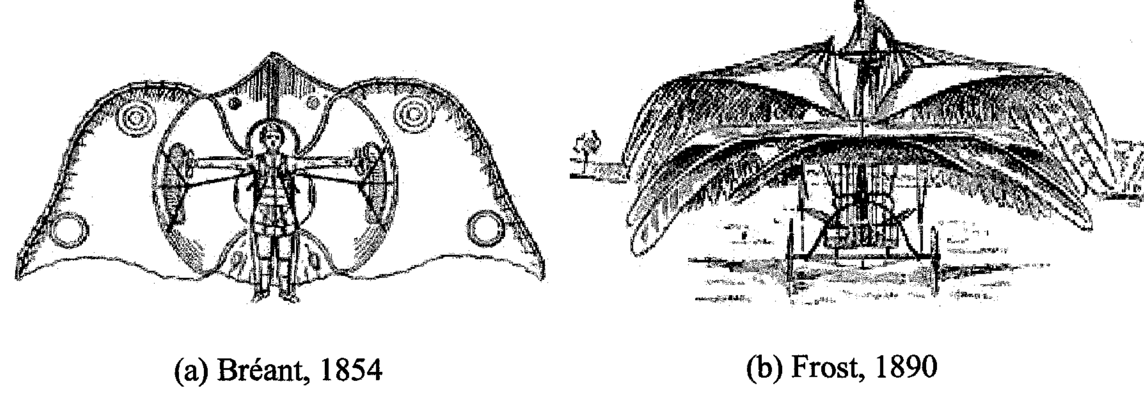

(a) Bréant, 1854 (b) Frost, 1890

Figure A-1: Examples of man-made ornithopters in 19th century [8]

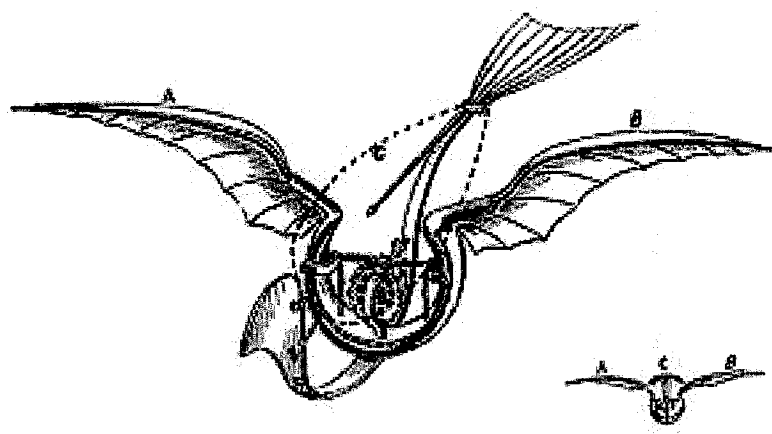

Figure A-2: Ornithopter built by George Trouvé [8]

In the meantime, other smaller and cheaper ornithopters were also developed, especially simple ornithopters powered by rubber bands. Jobert was the first to design and build his mechanical bird using rubber bands in 1871 [8]. The propulsion was obtained from the twisted rubber bands that connected to the crank arms with wings attached to them. The construction of this type of ornithopters was simple, but the flight duration did not last long.

Since the early periods of ornithopter development, today there are many competitions even for small indoor ornithopters that are as light as paper to heavy outdoor ornithopters powered by gas combustion engines. Some of these ornithopters have wingspan as large as 2 meters and can be radio-controlled. Some can stay airborne for several minutes. All are fascinating to design and build because of the endless possible variations. Although current technological advancement has allowed inventors and researchers to miniaturize the components and build smaller ornithopters, propulsion still remains a challenge because as size is reduced, so are the Reynolds numbers. This affects vehicle drag and achievable lift-to-drag ratios. Because of the relatively high drag associated with the platform size, propulsive power becomes increasingly important.

Flapping-wing flight is a highly efficient means of propulsion for low Reynolds number flight, as evidenced by the abundant examples we observe in nature.

A.2.2 Micro-Air-Vehicle (MAV)

MAV, defined by DARPA, is a small aircraft, typically less than 6" in dimension. The designs can be fixed-wing, flapping-wing, rotor, or propeller systems. It is designed to be an airborne platform to carry high-resolution imaging sensor and communication hardware needed to transmit the data over usable distance [9]. MAVs can also be used to search the local terrain to locate and monitor possible threats of enemies. Among the significant engineering challenges for a successful MAV deployment are ultra-compact, lightweight, high-power- and high-energy-density propulsion, and power sources. In addition, novel concepts for lift generation, flight stabilization and control for low Reynolds numbers aerodynamics, onboard electronic guidance, navigation, and signal processing are also important.

In 1998, DARPA launched a three-year, $35 million program to develop MAV programs [10]. The grants for research and development were awarded to a wide range of organizations, including university laboratories, aerospace firms, and small businesses. R&D of several MAV prototypes has already shown some promising results. One of the most successful flights was produced by the engineers at AeroVironment Inc. [11] in Simi Valley, California. They have flown a palm-sized disk-wing airplane called "Black Widow" for 22 minutes on lithium battery power. The Black Widow MAV prototype, which looks like a discus with a propeller, tail, and flaps, is integrated with miniaturized computer flight-control, navigation, and communications systems. As shown in Figure A-3, the Black Widow is a fixed-wing propeller aircraft and weighs about 70 grams. Its

internal subsystems include linear actuators for the elevons, piezoelectric gyros, GPS receiver, a pressure sensor, a central processor, and lithium and nickel-cadmium batteries. It also carries a miniature camera and transmitter for a real-time video downlink. The Black Widow can fly at speeds of up to 43 miles per hour.

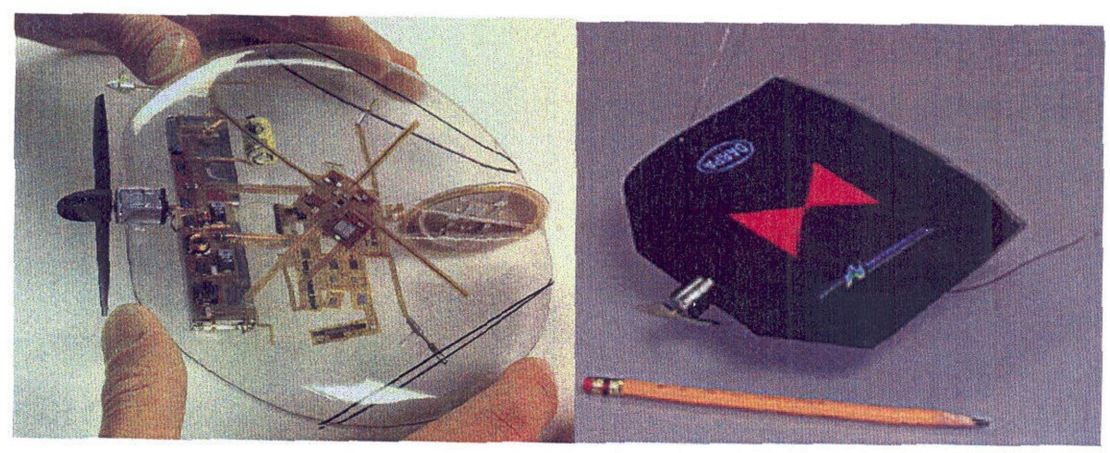

(a) Earlier design (b) Current design

Figure A-3: Black Widow MAV [11]

Although the 6-inch limitation for MAV size may appear somewhat arbitrary, the limit has taken natural physics and technology into considerations. Figure A-4 compares the size of MAVs to other birds and insects. Based upon natural data, the MAV-sized vehicles should weigh in the order of tens of grams. To fully appreciate the scale implications, we can compare this class of vehicle with other familiar systems. Figure A-5 shows a plot of vehicle gross weight vs. Reynolds numbers. The Reynolds number is a useful parameter for characterizing the flight environment. The smallest current unmanned-air-vehicle (UAV) is called the "Sender," developed and operated by the Naval Research Laboratory. The Sender has a 4-foot wingspan and weighs almost 5 kilograms. It is capable of travelling impressively up to a 100-mile range. MAVs are an

order of magnitude smaller in weight and size and can display a wide variety of configurations, depending on specific mission requirements.

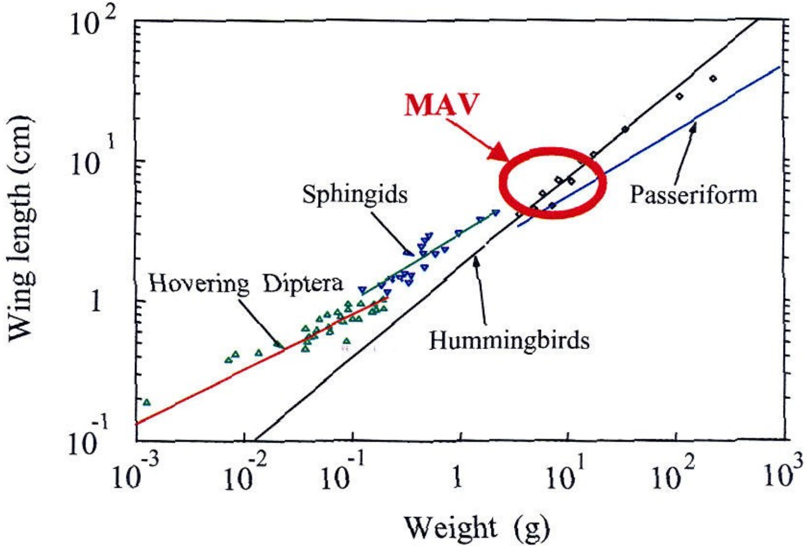

Figure A-4: Size of natural flyers

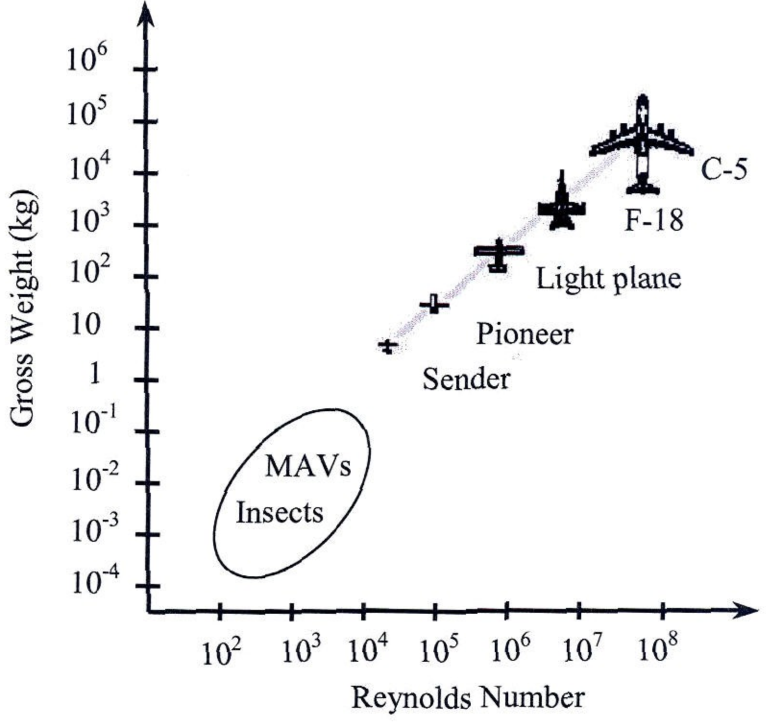

Figure A-5: MAV flight regime compared to existing flight vehicles [15]

It can be seen in Figure A-5 that the Reynolds numbers for MAVs and insects are low and in the range of 100 to 10,000. Unless flying at a high speed, airfoil performance of fixed-wing deteriorates severely for the Reynolds number at this range. Natural flight has provided unmatched maneuverability in these low-Reynolds-number regimes. It is also interesting to note that 6-inch wingspan is the border between flyers capable of two different types of flight: hovering and soaring. Most flyers smaller than this size are able to hover but cannot soar, while bigger flyers cannot hover but can soar. Thus, in nature there is a great difference in the use of wings and in the type of flight. For larger birds, the more common flight is soaring. Flapping is restricted to limited operations such as taking off, landing, or stabilization. When soaring, the wings are used as fixed-wing airfoils. For the smaller size of flyers, the less of such mechanism is employed. If we look at small birds and insects, such as hummingbirds, bees, or flies, nature indicates that flyers of small sizes use the flapping-wing mechanism to generate lift to overcome their own weights. Thus flapping is by far the most advantageous mechanism for flyers at these sizes when compared to mechanisms employing for fixed or rotating wings.

Also, when the sizes decrease flapping-wing flight is more efficient than fixed-wing flight. The main effects are: (1) lower lift coefficient, which means lower loading capability; (2) higher drag coefficient, which means high power input; and (3) flow separation on the wing, which means stall at low angles of attack, hence reduces the wing's performance and maneuverability. The conclusion is that fixed-wing mechanism is not as suitable for flight in this low-Reynolds-number regime compared to that of flapping-wing. Thus, the development of biomimetic MAVs is preferred when the Reynolds number is low.

A.2.3 Biomimetic MAVs

Many research programs have explored and developed flight technologies inspired by biological systems. Still, the challenge remains who can race to be the first to successfully design a small, lightweight, untethered, and electrically-powered ornithopter. This has proven to be more difficult because a lightweight and suitable power source that can provide a long flight duration has yet been available. In addition, the knowledge of flapping-wing aerodynamics for ornithopters of this size is still limited.

In a typical fixed-wing aircraft, the wing's camber and its angle of attack create an area of low pressure over the top of the wing which generates lift. If the fixed-wing aerodynamics and the size of the wings are considered, insects should not be able to generate enough lift to stay airborne. Yet they do. In 1994 Charles Ellington, a zoologist at the University of Cambridge in England, and his colleagues built a large, slow-motion insect model for wind-tunnel tests. Confirming the group's theory, the experiment revealed an intense micro-scale leading-edge vortex during the downstroke. The vortex spiraled out towards the wingtip with spanwise velocity comparable to the flapping velocity. The swirling produced a low-pressure regime over the wings, generating a high lift force [12].

As part of a DARPA funded MAV program, Ellington is working with a design team at the Georgia Tech Research Institute (GTRI) to develop a flapping-wing flying vehicle called the "Entomopter" (Figure A-6 (a)). The Entomopter's innovative flying ability is based on a reciprocating chemical muscle (RCM) that generates autonomic wing-beating from a chemical energy source. Through direct conversion, the RCM also provides small amounts of electricity for on-board systems for at least three minutes.

Although the team has not yet achieved sustained powered flight, a rubber band-driven ornithopter model with a 25-centimeter (10-inch) wingspan has managed to lift its 50-gram weight into the air for 15 seconds [13].

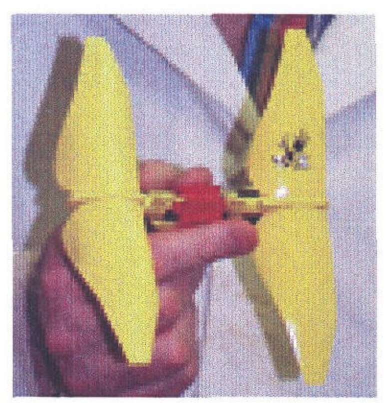

(a) GTRI's Entomopter

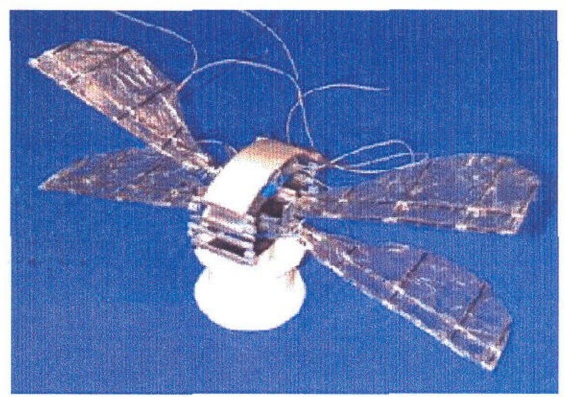

(b) Vanderbilt's Mesohawk

Figure A-6: DARPA-funded ornithopter MAV programs

Meanwhile Ephrahim Garcia and Michael Goldfarb of Center for Intelligent Mechatronics at Vanderbilt University proposed a sustained tethered flight with their 5-gram, 6-inch-wingspan artificial insect called "Mesohawk." The Mesohawk prototype is shown in Figure A-6 (b). The insect wings are attached to piezoelectric actuators. This type of ceramic material contracts when a voltage is applied to it. The flapping mechanisms developed use piezoelectric actuators integrated with solid-state flexure based mechanisms. Bar linkages are used to convert the linear unimorph output into a single degree-of-freedom rotational flapping motion. Due to their capacitive nature, piezoelectric actuators generally dissipate less power than traditional actuation methods such as electromagnetic motors. They also possess a high power density and are capable

of high force output. The Mesohawk flying robotic insect is powered by a 15-gram lithium battery. Currently, the project has not yet achieved a successful flight.

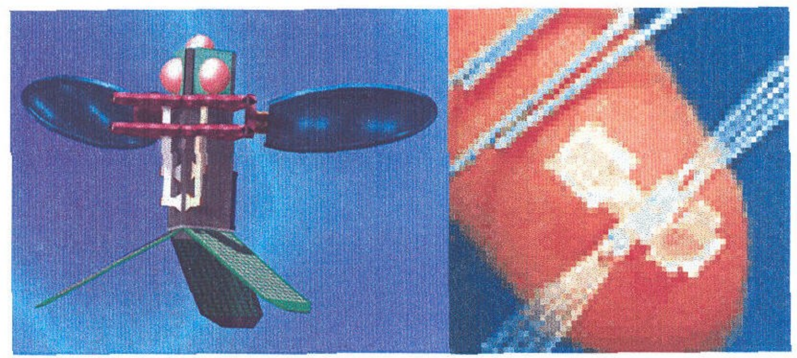

(a) Berkeley's Micromechanical Flying Insect

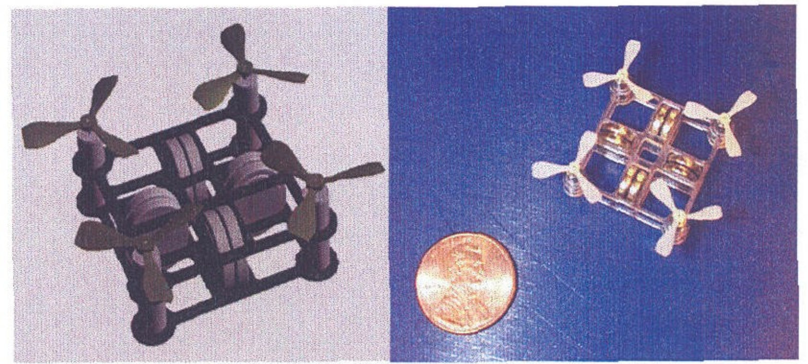

(b) Stanford's Mesocopter

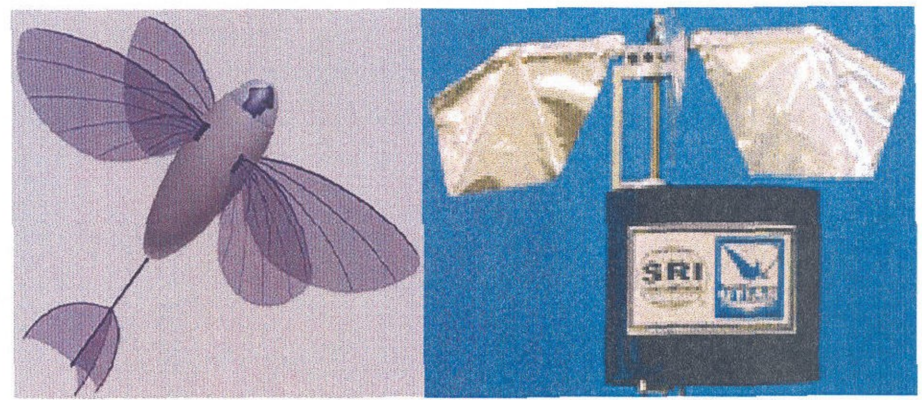

(c) UTIAS's and SRI International's Mentor MAV

Figure A-7: Other MAV concepts and prototypes

Figure A-7 shows other MAV concepts and prototype vehicles conducted by leading universities and research institutions. Researchers at the University of California at Berkeley, led by Ron Fearing and Michael Dickinson, are building a small robotic fly called Micromechanical Flying Insect (MFI), often dubbed as "Robofly." Figure A-7 (a) shows Berkeley's MFI's concept design and fabricated prototype. The goal of the MFI project is to use biomimetic principles to capture some of the exceptional flight performances achieved by true flies. They hope that one day the Robofly will eventually be able to sustain autonomous flight. The prototype is about the size of a housefly with 10-mm width and 25-mm wingtip-to-wingtip length. Its body is made of paper-thin stainless steel and its wings of mylar. The total weight is about 43 milligrams. The power will be generated by solar cells. Piezoelectric actuators are used to flap its wings up to 180 Hz. The Robofly can be used in an urban environment, clandestine surveillance and reconnaissance applications. The plan to airborne the Robofly is scheduled to be around the year 2004.

Led by Ilan Kroo and Fritz Prinz of Stanford University, another MAV effort called "Mesicopter" is designed based on the rotocraft technology. With support from industrial partners, Intel and SRI International, the proposed program combines the experience of the aircraft aerodynamics with the state-of-the-art manufacturing facilities and expertise of the Rapid Prototyping Laboratory (RPL) and Stanford Nano-fabrication Facility (SNF). SRI, a leader in advanced battery and sensor development, consults with the project on power systems, while Intel Corporation focuses on communications issues that will be important for the Mesicopter's command and control. The design concept and fabricated prototype is shown in Figure A-7 (b). The Mesicopter is a four-rotor

centimeter-scale rotorcraft. It is the size of a large insect and is slightly larger than the Berkeley's MFI. Its goal is to provide atmospheric research that includes potential applications such as windshear and turbulence monitoring, biological and chemical hazard detection, and planetary atmospheric data gathering on Mars.

Figure A-7 (c) shows another DARPA-funded MAV program called "Mentor." The work is collaboration among a team of researchers from SRI International in Menlo Park, California, and John DeLaurier of University of Toronto Institute for Aerospace Studies (UTIAS). This gives rise to the name "Mentor," after MENlo Park and TORonto. The goal is to provide a useful application for indoor and outdoor reconnaissance and surveillance missions. The Mentor MAV prototype weighs 50g and is modeled after a hummingbird. Although the current design bears little resemblance to any flying creature, it uses many of the same aerodynamic features. The prototype features four wings, flapping in a fashion that provides no unbalanced shaking forces. The wings, based on "Clap-Fling" flapping motion, make contact during the flapping cycle to provide lift. This flapping motion, identified by researchers at Cambridge University, England, can be found in insects that can hover [14]. The flapping motion of the Montor prototype is driven by "artificial muscles," which are actuators fabricated from electrostrictive polymer. The technology used is called "EPAM," for Electrostrictive Polymer Actuated Muscle, in which elastomeric actuators are contracted and relaxed by means of rapid jolts of high voltage up to 5000 volts. Most recently, brief successful tethered flights have been achieved. Current work is being directed to obtain longer duration, as well as developing a complementary theoretical model.

A.2.4 The Microbat Project

Although there are many biomimetic MAV programs that are being developed as mentioned in the previous section, none of the programs have been able to achieve a long and sustainable flight. Many programs still revise and develop their concept designs concurrently. However, the "Microbat" project [16] is one of a few of DARPA-funded MAV programs that has steadily progressed and was the first to demonstrate both tetherless free- and radio-controlled flapping-wing flights.

The Microbat project is led by Yu-Chong Tai of California Institute of Technology (Caltech) and Chih-Ming Ho of University of California at Los Angeles (UCLA). They are in collaboration with the Design and Development Center of AeroVironment, Inc., in Simi Valley, California, to develop the first lightweight (~12 grams), radio-controlled, battery-powered ornithopter. The project was started in March of 1998 and produced the first free-flight 6 months later with the super-capacitor-powered prototype which weighed merely 7.5 grams. The prototype was powered by two lightweight one-farad super-capacitor that only weighed one gram each. The free-flight only lasted 9 seconds because the capacitors were completely discharged. To obtain the longer flight time, a small nickel-cadmium (Ni-Cd) battery (3 grams) was used in conjunction with a DC-to-DC voltage converter. The function of the converter is to step up the voltage from Ni-Cd battery's 1-volt nominal output to 4-6 volts input for the electric motor that connected to the flapping transmission. In April of 1999, the first battery-powered ornithopter was successfully tested and the free-flight duration was 18 seconds. In order to gain an extra lift and thrust, the wingspan was increased from 6 inches to 8 inches, pushing the dimension slightly outside the MAV limitation. The

result was an increase in the flight time to 22 seconds. Figure A-8 shows the super-capacitor- and battery-powered Microbat prototypes.

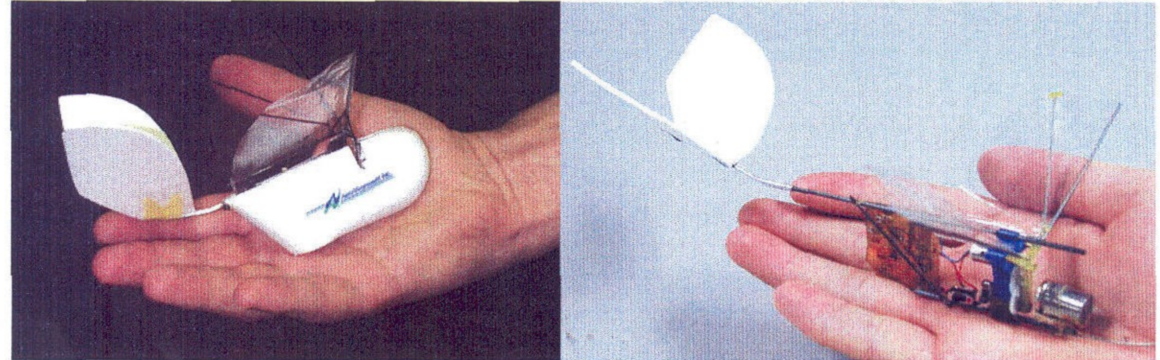

(a) Super-capacitor-powered Microbat; flight duration: 9 seconds (Oct '98)

(b) Battery-powered Microbat; flight duration: 18 seconds (Apr '99)

Figure A-8: Super-capacitor- and battery-powered Microbat prototypes

Over the year 2000, several systems had been redesigned or added on the Microbat prototype. The prototype's fuselage was reconstructed to hold battery, gearbox, and other avionics. The flexible composite airframe was composed of lightweight graphite-epoxy structural frame that provides both flexibility, durability, and stability during flight. A new gearbox transmission is also redesigned to be lighter (Figure A-9) and a radio control system was implemented to allow a pilot to control the throttle, elevator, and rudder on the Microbat prototype. The elevator and rudder are controlled using muscle-wire actuators in a pull-pull arrangement. Muscle wires are shape-memory-alloy (SMA) metal wires that have the property of shrinking in length when heated, and expanding when cooled. The wireless radio link is based on the RF Monolithics (RFM) ASH receivers and amplitude modulation transmitters. These are small multi-chip-modules which are lightweight and only require few additional components to operate.

In early December 2000 the new radio-controlled prototype was tested and it was successful. The flight duration lasted 42 seconds. For the first time, the ornithopter was able to demonstrate the turning and pitching capabilities. This new, redesigned, radio-controlled Microbat is shown in Figure A-10. Although several new components have been added, the prototype is still very light with the total weight less than 12 grams. Table A-1 summarizes the weight breakdown.

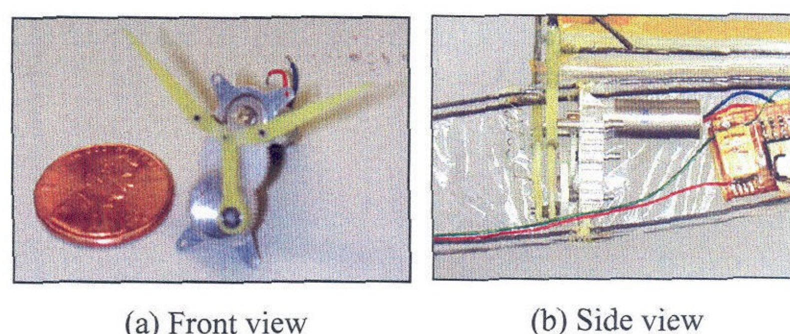

(a) Front view (b) Side view

Figure A-9: The new redesigned lightweight gearbox transmission

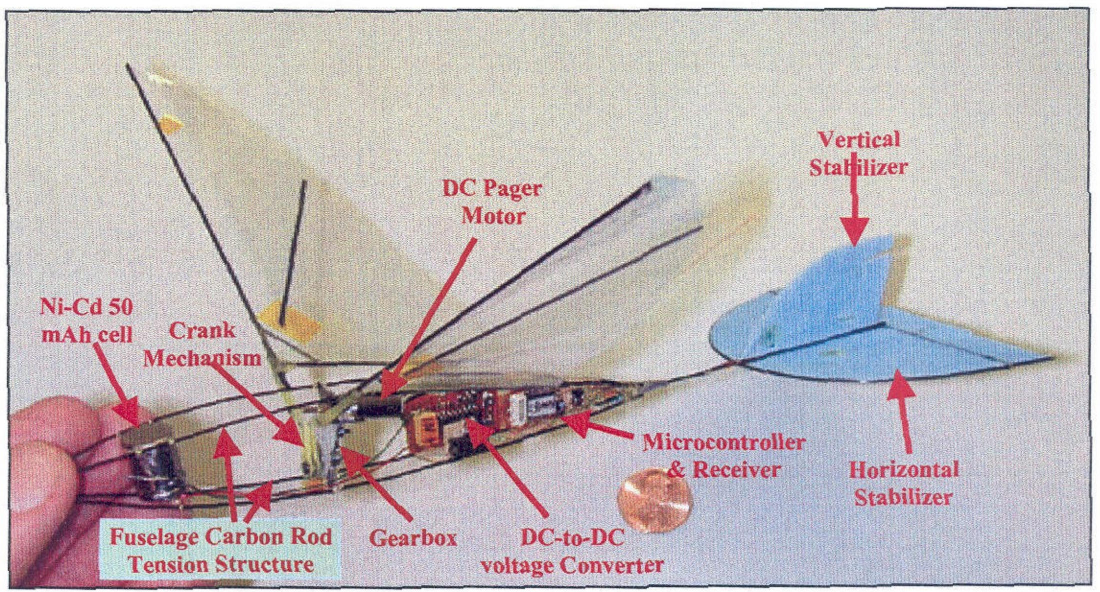

Figure A-10: Radio-Controlled Microbat prototype; duration 42 seconds (Dec '00)

Table A-1: Weight summary of the radio-controlled Microbat prototype

Components	**Weight [g]**
Battery	3.50
Power Converter	2.40
Motor	1.83
Gearbox	1.27
RC system	0.99
Fuselage & Tails	0.90
Wings	0.60
Wiring & Switches	0.20
Total	11.69

Even though the flight duration has steadily progressed for various Microbat prototypes, the main technological limitation to ensure a longer flight time remains the power from the battery. The difficulty with the Microbat ornithopter prototype is that the aircraft is small and typically less efficient than propeller-driven aircraft. There are few batteries produced that are optimized to be discharged in less than 5 minutes. All other batteries can be formulated for either high energy over long discharge times (hours) or for moderate energy over short discharge times (minutes). Discharge times of most commercial batteries, i.e., watch and photo cell batteries, are very long. Also the small batteries produced typically have very heavy cases because typically the manufacturers use the same metal case thickness for their large cells as their small cells.

Ni-Cd batteries typically can be discharged in less than 5 minutes with reasonable performance. The rechargeable Ni-Cd battery that is used on the Microbat prototype is Sanyo N-50AAA battery, which is the one of the smallest and lightest Ni-Cd batteries available commercially. However, the Ni-Cad battery has low energy density per weight compared to Lithium-ion or Lithium polymer batteries. Further, its nominal cell voltage is about 1 volt compared to a typical 3 volts for the latter types of batteries. Thus the DC-to-DC converter is needed in order to input 6 volts into the electric motor.

During the year 2001, the Microbat research team has searched a replacement battery technology and has found a new technology by Telcordia Technologies, Inc., called Plastic Lithium-ion Battery Technology™ (PLiON™) [17] to be suitable for the Microbat prototype. The battery is custom-made with each cell has approximately 3-volt nominal voltage and weighs about 2.5 grams. Two cells are utilized in series to provide a nominal 6 volts to the motor and avionics. Therefore, the need for a DC-to-DC voltage converter is no longer necessary.

The PLiON™ battery technology provides several advantages. Besides being lightweight, it can also be bent, folded, or flexed into virtually any shapes or configurations. The battery does not require a metal casing because all its components are chemically bound together. It contains no toxic materials, making it environmentally safe. In addition, the cell is very durable that it retains its voltage and will not leak even after it is cut or punctured. Some other advantages include its thinness, high capacity and energy density. Based on lithium-ion technology, the PLiON™ battery can deliver twice the power at the same weight of Ni-Cd batteries. It can also retain longer charges. Telcordia claims that it loses just 5% of its charge in a month's storage compared to 20%

for Ni-Cd and 60% for nickel metal-hydride (NiMH) [17]. Figure A-11 shows the size comparison of the PLiON™ Lithium polymer battery in comparison to the Sanyo Ni-Cd 50-AAA battery. Although the PLiON™ battery is larger than the Ni-Cd battery, it is lighter (2.5 vs. 3 grams) and has higher nominal voltage for each cell (3 vs. 1 volt).

Figure A-11: Lithium polymer battery in comparison to Sanyo N50-AAA battery

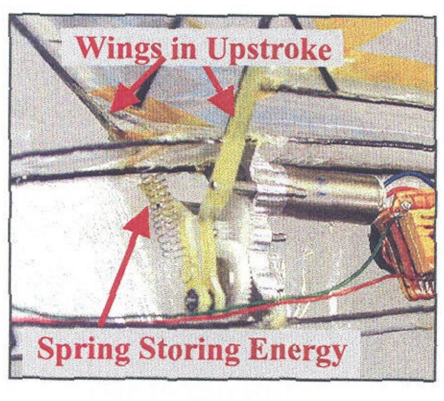

(a) Upstroke

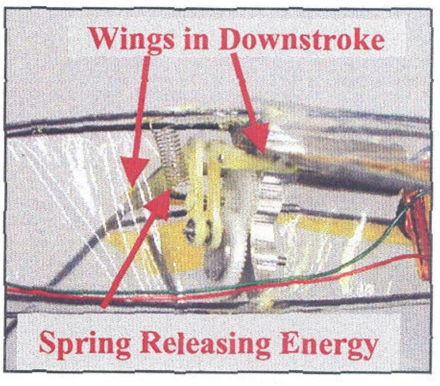

(b) Downstroke

Figure A-12: Wingbeat energy conservation spring system

Another aspect of recent research of the Microbat research team has been the energy conservation system as shown in Figure A-12. The team has developed a metal tension spring system that is used to save and release cyclic energy. The spring stores

energy in the wing upstroke, as seen in Figure A-12 (a), when the motor is under low load. Then it releases the energy during wing downstroke, as seen in Figure A-12 (b), when the motor is under high load. This allows the motor to operate more efficiently and provides a smooth loading on the motor. As a result, it yields a better battery life endurance as well.

The addition of the new PLiON™ Lithium polymer battery technology to replace the Ni-Cd and DC-to-DC voltage converter proves to be successful. For the first time, the latest version of the radio-controlled Microbat MAV prototype, shown in Figure A-13, flew over 2-minute mark on August 22, 2001 and 6-minute mark on November 17, 2001. The flight mode is shown in Figure A-14. With throttle control, the pilot was able to command left and right turns, climbing, descending, and stalling during flight. The longest flight duration obtained was 6 minutes and 17 seconds. It was a new world's record of an electric-powered MAV ornithopter ever flown for this size.

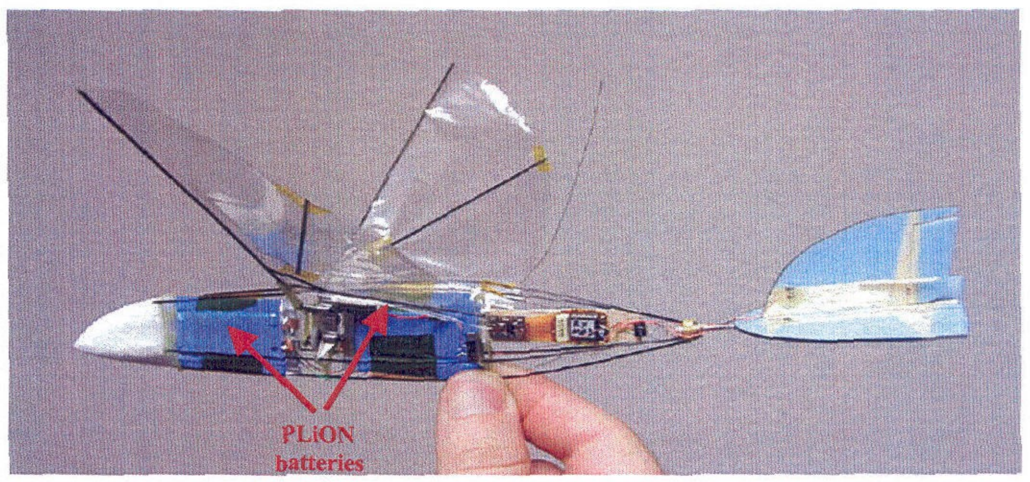

Figure A-13: The latest radio-controlled Microbat with PLiON battery;

Duration: 6 min. 17 sec. (11/01)

Figure A-14: The Microbat in flight mode

Table A-2 summarizes of the characteristics and progression of the Microbat prototype. When the project was started in 1998, the proposed flight endurance was one minute. The flight endurance of the recent prototype has already far surpassed that mark.

Table A-2: Summary of the Microbat prototypes

Microbat Prototype				
Size	6-inch	6-inch	8-inch	8-inch
Weight [g]	7.5	11.5	11.7	11.5
Power	Super capacitors	Ni-Cd battery	Ni-Cd battery	PLiON battery
Propulsion	Flapping	Flapping	Flapping	Flapping
Type of flight	Free	Free	Radio-controlled	Radio-controlled
Flight date	Oct '98	Apr '99	Dec '00	Nov '01
Endurance	9 sec.	18 sec.	42 sec.	6 min. 17 sec.

A.3 Summary

It has been several hundred years of flapping-wing flight development since the time of Leonardo da Vinci. Despite the fact that nature has been evolving for millions of years, today we have made a vast progress in our knowledge about flapping-wing flight. There are several MAV prototypes being developed with a staggering number of potential civil and military applications. The success of Microbat has indicated how far the technology has come. A task that once deemed almost impossible is now feasible. Providing the advancement in the battery technology, one day in the future these MAV vehicles may become as ubiquitous as automobiles. They may represent an emerging growth sector of the aerospace market. By drawing inspiration from insects, birds, or bats, technologies developed will enable new capabilities for MAV, such as collaborating swarms, autonomous operation, and bird-like agility. Some end-users applications are reconnaissance, remote sensing, search and rescue, and micro payloads.

A.4 Bibliography

[1] K. P. Dial, "An Inside Look at How Birds Fly: Experimental Studies of the Internal and External Processes Controlling Flight," *1994 Report to the Aerospace Profession, 38th Symposium Proceedings*, Beverly Hills, CA, Sept. 1994.

[2] R. Dudley, *The Biomechanics of Insect Flight,* Princeton University Press, Princeton, NJ, 2000.

[3] T. Weis-Fogh, "Dimensional Analysis of Hovering Flight," *Scale Effects in Animal Locomotion,* T. J. Pedley ed., Academic Press, London, 1977.

[4] M. Okamoto, K. Yasuda, and A. Azuma, "Aerodynamic Characteristics of the Wings and Body of a Dragonfly," *Journal of Experimental Biology*, vol. 199, pp. 281-294, 1996.

[5] M. Sato and A. Azuma, "The Flight Performance of a Damselfly Ceriagrion Melanuram Selys," *Journal of Experimental Biology*, vol. 200, pp. 1765-1779, 1997.

[6] M. F. M. Osborne, "Aerodynamic of Flapping Flight with Application to Insects," *Journal of Experimental Biology*, vol. 28, pp. 221-245, 1951.

[7] J. B. Anders, "Biomimetic Flow Control," *Fluids 2000,* Denver, CO, June 19-22, 2000.

[8] O. Chanute, *Progress in Flying Machines*, Dover Publications, Inc., 1894.

[9] D. C. Johnson, "Micro Air Vehicle Missions and Technology Assessment," *Project Report MAV-1*, Lexington, MA, Nov. 25, 1997.

[10] S. Ashley, "Palm-Size Spy Plane," *The American Society of Mechanical Engineers*, February, 1998.

[11] AeroVironment, Inc., Design Development Center, 4685-3H Industrial St., Simi Valley, CA 93063, (805) 581-2187, http://www.aerovironment.com.

[12] C. P. Ellington, C. van den Berg, A. P. Willmott, and A. L. R. Thomas, "Leading-Edge Vortices in Insect Flight," *Nature*, vol. 384, pp. 626-630, December, 1996.

[13] P. Scott, "A Bug's Lift," *Scientific American*, vol. 280, no. 4, April 1999.

[14] T. Weis-Fogh, "Quick Estimates of Flight Fitness in Hovering Animals, Including Novel Mechanisms for Lift Production," *Journal of Experimental Biology*, vol. 59, pp. 169-230, 1973.

[15] J. M. McMichael and M. S. Francis, "Micro Air Vehicles – Toward a New Dimension in Flight," http://www.darpa.mil/tto/mav/mav_auvsi.html, Aug. 7, 1997.

[16] T. N. Pornsin-Sirirak, S.W. Lee, H. Nassef, J. Grasmeyer, Y. -C. Tai, C. -M Ho, and M. Keennon, "MEMS Wing Technology for a Battery-Powered Ornithopter," *The 13th IEEE International Conference on Micro Electro Mechanical Systems (MEMS'00)*, Miyazaki, Japan, pp. 799-804, Jan. 23-27, 2000.

[17] Telcordia Technologies, Inc., Telcordia Applied Research, (800) 521-2673, http://www.telcordia.com

Appendix B

Description of Fabrication Processes

The detailed description of the fabrication process of each device described in the thesis is presented in this appendix. Because it is almost impossible to achieve a successful working device in the first trial without encountering any problems, these process flows are the results of numerous revisions of problematic process flows of successful devices. If these process flows are followed closely, the same working devices as tested in this thesis dissertation should be achieved.

B.1 Titanium-Alloy MEMS Wings

1. Substrate preparation
    1.1. Start with a 5"x5" titanium-alloy (Ti-6Al4V grade) with thickness of 250 μm
    1.2. Dip clean in trichloroethylene (TCE) for 20 min
    1.3. Rinse clean with de-ionized water (DI H_20)
    1.4. Roughen the surface: Dip in 5% HF solution for 15 sec
    1.5. Rinse clean with DI H_20 and air dry
2. Lamination of dry film photoresist

2.1. Bench-Top Laminator model BTL-121A from Kepro Circuit Systems, Inc.

2.2. Select dry film resist type DFR-4713

2.3. Laminator parameter settings:

- Speed setting: 3 or 4
- Temperature setting: 250 ^{o}F
- Roller height setting: Laminating 1.5 mil/36 micron

2.4. Place the titanium-alloy substrate with the frontside up on a PCB board

2.5. Laminate the frontside of the titanium-alloy substrate

2.6. Trim and get rid of excess dry film resist on the frontside

2.7. Repeat step 2.3 and 2.4 for the backside of the substrate. Do not peel off the clear plastic cover sheet

3. Photolithography

3.1. Turn on the Canon UV lamp for at least 20 min

3.2. Measure the power density:

- Sensor A (365 nm, I-line) measured = 5.8 mW/cm^2
- Sensor B (405 nm, H-line) measured = 6.3 mW/cm^2

3.3. Place the wingframe mask on top of the dry film resist

3.4. Cover and press the film firmly with a clear 5"x5" glass plate

3.5. Expose under the Canon UV lamp for 60 sec

3.6. Peel off the clear plastic film that covers the exposed dry film photoresist. Do not peel off the clear plastic film on the other side

3.7. Develop in sodium carbonate (Na_2CO_3) solution for 5 min

- DI H_20: dry film developer (DFD-12G) = 200 ml: 2 g

3.8. Hardbake at 120 °C for 20 min

4. Titanium-alloy etching

4.1. Etch titanium-alloy substrate: HF: HNO_3: DI H_2O = 5: 2: 100 in volume

- etching rate ~ 2.5 µm/min

4.2. Rinse clean with DI H_20 and dry the substrate

4.3. Peel the clear film off the backside of the substrate after etching is finished

4.4. Expose backside dry film photoresist under the UV lamp for 60 sec

4.5. Strip dry film resist in diluted potassium hydroxide (KOH) solution:

- DI H_20: dry film stripper (DFS-12G) = 200 ml: 2 g

4.6. Dip in 5% HF solution for 15 sec

5. Lamination of dry film photoresist

5.1. Place the titanium-alloy substrate on a PCB board with the backside facing up

5.2. Laminate only on the backside of the titanium-alloy substrate. Do not peel off the clear plastic film. This photoresist layer will serve as a lift-off material for the membrane

6. 1st parylene layer deposition

6.1. Deposition parameters:

- Furnace setting: 690 °C
- Gauge setting: 150 °C
- Vacuum setting: 22 mT
- Vaporizer setting: 170 °C

6.2. Weigh parylene-C dimer = 8 g

- The measurement yields ~ 5 μm thickness

6.3. After the deposition is finished, peel off the clear plastic film that protects the dry film resist

7. Strip dry film resist

7.1. Expose the dry film resist under the Canon UV lamp for 60 sec

7.2. Strip dry film photoresist on the backside in diluted potassium hydroxide (KOH) solution. The clear parylene membrane will appear

- DI H_20: dry film stripper (DFS-12G) = 200 ml: 2 g

7.3. Rinse with DI H_20 and air dry

8. 2nd parylene layer deposition

8.1. Weigh parylene-C dimer = 8 g

- The measurement yields ~ 5 μm thickness

8.2. After the deposition is finished, cut off the wings

8.3. Bend the diagonal spar to create wing camber

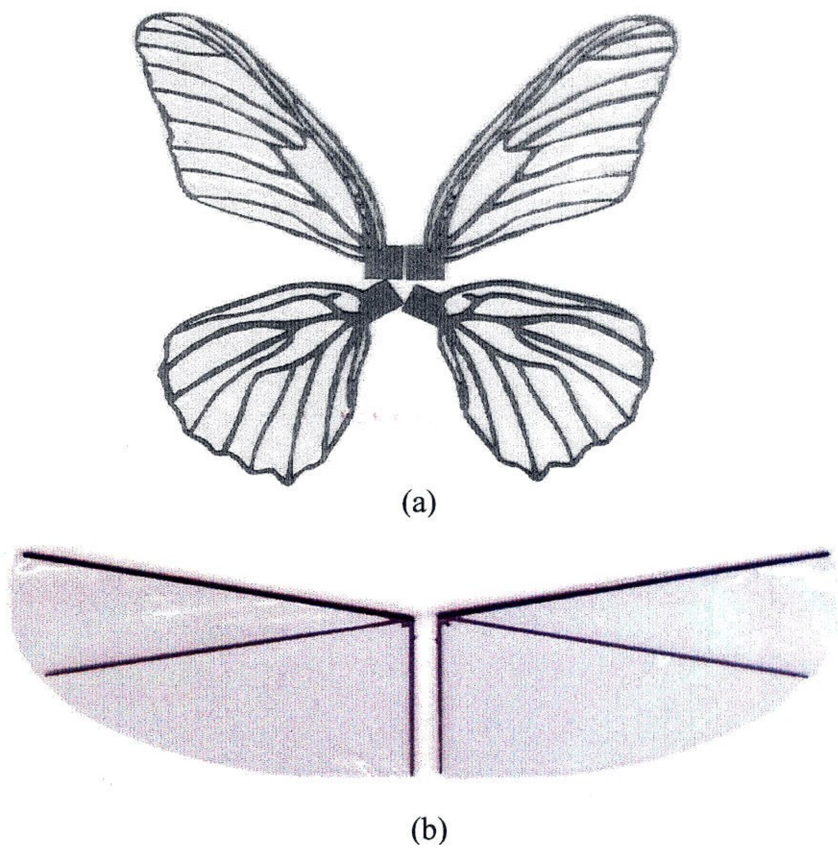

(a)

(b)

Figure B-1: Titanium-alloy MEMS wing:
(a) Butterfly; (b) Simple wing spar CIT7x3S20

B.2 Parylene MEMS Electrostatic Actuator on a Silicon Chip

1. Mask fabrication
    - 1.1. Turn on the Canon UV lamp for at least 20 min
    - 1.2. Measure the power density:
        - Sensor A (365 nm, I-line) measured = 11.6 mW/cm^2
        - Sensor B (405 nm, H-line) measured = 12.2 mW/cm^2
    - 1.3. Place the mask film with the matte side facing down on top of the photoresist and firmly press a clear glass plate on top of the film
    - 1.4. Expose with UV light: exposed time = 10 seconds
    - 1.5. Develop the mask with AZ351 developer
        - AZ351 developer: H_2O (1:4) = 1 min
    - 1.6. Rinse and blow dry. Check under microscope. If it is underdeveloped, resubmerge the mask in the developer bath longer
    - 1.7. Etch the chrome mask with Cr-7 etchant: 2 min
    - 1.8. Rinse and blow dry. Check under microscope
    - 1.9. When finish, remove PR by submerge the mask in a fresh AZ351 developer bath (no water)
2. Double-side alignment
    - 2.1. Prime the wafer with HMDS for 3 min
    - 2.2. Spin coat the frontside with AZ4400 photoresist at 4 krpm speed for 40 sec
        - Resist thickness is approximately = 4 μm
    - 2.3. Softbake at 90 °C for 20 min in a convection oven. Let cool down for 3 min
    - 2.4. Spin coat the backside with AZ4400 photoresist at 4 krpm speed for 40 sec
    - 2.5. Softbake at 90 °C for 20 min in a convection oven. Let cool down for 3 min
    - 2.6. Place the wafer in the double-side alignment jig
    - 2.7. Expose with Canon UV light for 10 sec on both sides
    - 2.8. Spot develop with AZ351 developer
        - AZ351 developer: H_2O (1:4) = 4 min
    - 2.9. Etch with plasma etching in PEII machine

- SF_6/O_2 = 300/30 mT
- Power = 300 W
- Etch time = 2 min

2.10. Strip the photoresist with acetone

2.11. Rinse with isopropanol alcohol and DI H_2O. Spin dry

3. Thermal Oxidation

3.1. Wafer cleaning

- Clean wafers using standard piranha recipe (H_2SO_4:H_2O_2 = 5:1 in volume)
- Set the temperature of the solution to 120 °C for both left and right tanks
- Submerge the wafers in the solution for 10 min in the right tank
- Rinse the wafers with the DI H_2O from the dirtiest tank to the cleanest tank for 5 min each
- Resubmerge the wafers in the solution for another 10 min in the left tank
- After rinsing in the first clean tank, dip each wafer in 5% HF solution (200 ml H_2O: 10 ml HF) for 10-15 sec/wafer until it is hydrophobic
- Rinse in the second clean tank for an additional 5 min, then transfer to the cleanest tank
- Wait until the meter read above 12 M-Ohm before removing wafers. Using the N_2 bubbler is optional.

3.2. Wet thermal oxidation

- Set temperature of wet oxidation at 1050 °C for 8 hrs
  - control setting: 330 646 540
  - H_2O drop rate: 5-8 drops/min
  - O_2 flow rate: 0.5 liter/min
- Thickness = 1.8 μm

4. Backside oxide patterning

4.1. Standard photolithography

- Prime the wafers with HMDS for 3 min
- Spin coat the frontside with AZ1518 resist at 2.5 krpm speed for 40 sec

  - Resist thickness is approximately = 2 μm
- Softbake at 90 °C for 20 min in a convection oven. Cool down for 3 min
- Spin coat the backside with AZ1518 at 2.5 krpm speed for 40 sec
- Softbake at 90 °C for 20 min in a convection oven. Cool down for 3 min
- Stepper expose for 0.4 sec using mask # 1
- Develop with AZ351 developer
  - AZ351 developer: H_2O (1:4) = 1 min
- Rinse with DI H_2O. Spin dry

4.2. Photoresist descum with PEII machine

- O_2 = 200 mT
- Power = 100 W
- Descum time = 2 min

4.3. Rotate wafers 180° and repeat step 4.2

4.4. Spot etch oxide on the backside with BHF

- Etch time is approximately 30 min

4.5. Rinse with DI H_2O. Observe hydrophilic effect for all dice. If the effect is not observed, it means that thin oxide still remains. Repeat step 4.4 until the oxide is etched away

4.6. Strip the photoresist with acetone

4.7. Rinse with isopropanol alcohol and DI H_2O. Spin dry

5. KOH etching

5.1. Heat the KOH solution to 58 °C

- Recipe: 45% KOH: DI H_2O: IPA = 1.44: 1.76: 0.05 liter in volume

5.2. Measure the thickness of the wafer without oxide

- Thickness = 550 μm

5.3. Time etch the wafers until thin membranes of 20 μm remain

- Target etch distance = 530 μm
- KOH etching rate = 23 μm/hr
- Etch time = 23 hrs

- Oxide remained = 0.6 μm (oxide etching rate ~ 500 A°/hr)

6. Frontside oxide patterning

    6.1. Photolithography

    - Prime the wafers with HMDS for 3 min
    - Spin coat the frontside with AZ1518 resist at 2.5 krpm speed for 40 sec
        - Resist thickness is approximately = 2 μm
    - Softbake at 90 °C for 20 min in a convection oven. Cool down for 3 min
    - Stepper expose for 0.4 sec using mask # 2
    - Develop with AZ351 developer
        - AZ351 developer: H_2O (1:4) = 1 min
    - Rinse with DI H_2O. Spin dry

    6.2. Photoresist descum with PEII machine (see step 4.2)

    6.3. Rotate wafers 180° and repeat step 6.2

    6.4. Brush paint the edge with thin layer of AZ1518 resist

    6.5. Bake at 90 °C for 10 min in a convection oven. Cool down for 3 min

    6.6. Cover the backside of the wafer with blue dicing tape

    6.7. Spot etch oxide on the backside with BHF

    - Etch time is approximately 10 min

    6.8. Rinse with DI H_2O. Observe hydrophilic effect for all dice. If the effect is not observed, it means that thin oxide still remain. Repeat step 6.7 until the oxide is etched away

    6.9. Rinse with DI H_2O. Spin dry

7. BrF_3 surface roughening

    7.1. Cover the backside of the wafer with blue dicing saw tape

    7.2. Roughen the surface with BrF_3 gas

    - Number of pulses: 1
    - Pressure: 5 Torrs
    - Etch time: 1 min

    7.3. Carefully peel off the blue dicing tape. Strip the photoresist with acetone

7.4. Rinse with isopropanol alcohol and DI H_2O. Spin dry

8. Parylene adhesion promoter

8.1. Prepare the A-174 organic silane adhesion promoter

- Recipe: H_2O: IPA: A-174 = 100:100:1 in volume
- Stir the solution well. Let it sit for at least 2 hrs

8.2. Immerse the wafers in the solution for 15 min

8.3. Let air dry for at least 15 min

8.4. Use IPA to rinse each wafer for 15 sec

8.5. Let air dry for 15 min

- Note: the wafers can also be dried by heat at 150 °F

9. 1st Parylene deposition

9.1. Protect backside of the wafer with blue dicing saw tape

9.2. Deposition parameters:

- Furnace setting: 690 °C
- Gauge setting: 150 °C
- Vacuum setting: 22 mT
- Vaporizer setting: 170 °C

9.3. Weigh parylene-C dimer = 2.2 g

- The measurement yields ~ 1.2 μm thickness

9.4. After deposition, carefully peel off the blue dicing tape from the backside

10. Parylene patterning

10.1. Photolithography

- Prime the wafers with HMDS for 3 min
- Spin coat the frontside with AZ4400 resist at 3 krpm speed for 40 sec
  - Resist thickness is approximately = 4 μm
- Softbake at 100 °C for 15 min in a convection oven. Cool down for 3 min
- Stepper expose for 0.8 sec using mask # 3
- Develop with AZ351 developer
  - AZ351 developer: H_2O (1:4) = 3 min

- Rinse with DI H_2O. Spin dry
- Hardbake at 120 °C for 15 min in a convection oven. Cool down for 3 min

10.2. Etch parylene with PEII machine

- O_2 = 400 mT
- Power = 400 W
- Etch time = 4 min

10.3. Rotate wafers 180° and repeat step 10.2

10.4. Strip the remained photoresist with acetone

10.5. Rinse with isopropanol alcohol and DI H_2O. Spin dry

10.6. Roughen the surface of parylene with PEII machine. This is to improve the adhesion of metal layer to the parylene surface

- O_2 = 200 mT
- Power = 200 W
- Time = 1 min

11. Ground Cr/Au/Cr evaporation

11.1. Prepare the metal sources:

- Chrome (Cr): 2 rods
- Gold (Au): 3 g

11.2. Evaporate Cr/Au/Cr

- 1st layer of Cr: 100 A°
- Au layer: 2800 A°
- 2nd layer of Cr: 100 A°

12. Ground Cr/Au/Cr patterning

12.1. Photolithography

- Prime the wafers with HMDS for 3 min
- Spin coat the frontside with AZ1518 resist at 2.5 krpm speed for 40 sec
  - Resist thickness is ~ 2 μm
- Softbake at 90 °C for 20 min in a convection oven. Cool down for 3 min
- Stepper expose for 0.4 sec using mask # 4

- Develop with AZ351 developer
  - AZ351 developer: H_2O (1:4) = 1 min
- Rinse with DI H_2O. Spin dry

12.2. Photoresist descum with PEII machine

12.3. Rotate wafers 180° and repeat step 12.2

12.4. Rinse the wafer well with H_2O to prevent bubble trap

12.5. Metal etching

- Etch the wafer in Cr-7 etchant: etch time = 10 sec
- Etch the wafer in Au etchant: etch time = 1:20 min
- Etch the wafer in Cr-7 etchant: etch time = 10 sec

12.6. Strip photoresist using PR stripper: temp setting at 50 °C

12.7. Rinse the wafer with PR stripper rinse

12.8. Rinse with DI H_2O. Spin dry

13. Parylene adhesion promoter

14. 2nd Parylene deposition

14.1. Protect backside of the wafer with blue dicing saw tape

14.2. The same deposition parameters

14.3. Weigh parylene-C dimer = 1.5 g

- The measurement yields ~ 1 μm thickness

14.4. After deposition, carefully peel off the blue dicing tape from the backside

15. Parylene patterning

15.1. Photolithography

- Prime the wafers with HMDS for 3 min
- Spin coat the frontside with AZ4400 resist at 2.5 krpm speed for 40 sec
  - Resist thickness is approximately = 4 μm
- Softbake at 100 °C for 15 min in a convection oven. Cool down for 3 min
- Stepper expose for 0.8 sec using mask # 5
- Develop with AZ351 developer
  - AZ351 developer: H_2O (1:4) = 3 min

- Rinse with DI H_2O. Spin dry
- Hardbake at 120 °C for 15 min in a convection oven. Cool down for 3 min

15.2. Etch parylene with PEII machine

- Etch time = 3 min

15.3. Rotate wafers 180° and repeat step 15.2 for 4 min

15.4. Rotate wafers 180° and repeat step 15.2 for additional 3 min

15.5. Strip the remained photoresist with acetone

15.6. Rinse with isopropanol alcohol and DI H_2O. Spin dry

15.7. Dip in 80 °C piranha solution for 1 min to get rid of remained photoresist

15.8. Rinse with DI H_2O. Spin dry

16. Photoresist sacrificial layer

16.1. Photolithography

- Prime the wafers with HMDS for 3 min
- Spin coat the frontside with AZ4400 resist at 3 krpm speed for 40 sec
  - Resist thickness is approximately = 4 μm
- Softbake at 100 °C for 15 min in a convection oven. Cool down for 3 min
- Stepper expose for 0.8 sec using mask # 6
- Develop with AZ351 developer
  - AZ351 developer: H_2O (1:4) = 3 min
- Rinse with DI H_2O. Spin dry

17. 3rd Parylene deposition

17.1. Protect backside of the wafer with blue dicing saw tape

17.2. The same deposition parameters

17.3. Weigh parylene-C dimer = 1.5 g

- The measurement yields ~ 1 μm thickness

17.4. After deposition, carefully peel off the blue dicing tape from the backside

18. Parylene patterning

18.1. Photolithography

- Prime the wafers with HMDS for 3 min

- Spin coat the frontside with AZ4400 resist at 3 krpm speed for 40 sec
  - Resist thickness is approximately = 4 μm
- Softbake at 100 °C for 15 min in a convection oven. Cool down for 3 min
- Stepper expose for 0.8 sec using mask # 7
- Develop with AZ351 developer
  - AZ351 developer: H_2O (1:4) = 3 min
- Rinse with DI H_2O. Spin dry
- Hardbake at 120 °C for 15 min in a convection oven. Cool down for 3 min

18.2. Etch parylene with PEII machine
- Etch time = 3 min

18.3. Rotate wafers 180° and repeat step 18.2

18.4. Strip the remained photoresist with acetone

18.5. Rinse with isopropanol alcohol and DI H_2O. Spin dry

18.6. Roughen the surface of parylene with PEII machine. This is to improve the adhesion of metal layer to the parylene surface
- O_2 = 200 mT
- Power = 200 W
- Time = 1 min

19. Top electrode Cr/Au/Cr evaporation

19.1. Prepare the metal sources:
- Chrome (Cr): 2 rods
- Gold (Au): 3 g

19.2. Evaporate Cr/Au/Cr
- 1st layer of Cr: 100 A°
- Au layer: 2800 A°
- 2nd layer of Cr: 100 A°

20. Top electrode Cr/Au/Cr patterning

20.1. Photolithography
- Prime the wafers with HMDS for 3 min

- Spin coat the frontside with AZ1518 resist at 2.5 krpm speed for 40 sec
  - Resist thickness is ~ 2 μm
- Softbake at 90 °C for 20 min in a convection oven. Cool down for 3 min
- Stepper expose for 0.4 sec using mask # 8
- Develop with AZ351 developer
  - AZ351 developer: H_2O (1:4) = 1 min
- Rinse with DI H_2O. Spin dry

20.2. Photoresist descum with PEII machine

20.3. Rotate wafers 180° and repeat step 20.2

20.4. Rinse the wafer well with H_2O to prevent bubble trap

20.5. Metal etching

- Etch the wafer in Cr-7 etchant: etch time = 10 sec
- Etch the wafer in Au etchant: etch time = 1:20 min
- Etch the wafer in Cr-7 etchant: etch time = 10 sec

20.6. Rinse with DI H_2O. Spin dry

20.7. Strip photoresist using PR stripper: temp setting at 50 °C

20.8. Rinse the wafer with PR stripper rinse

20.9. Rinse with DI H_2O. Spin dry

21. Parylene adhesion promoter
22. 4th Parylene deposition

22.1. Protect backside of the wafer with blue dicing saw tape

22.2. The same deposition parameters

22.3. Weigh parylene-C dimer = 2.5 g

- The measurement yields ~ 1.8 μm thickness

22.4. After deposition, carefully peel off the blue dicing tape from the backside

23. Parylene patterning

23.1. Photolithography

- Prime the wafers with HMDS for 3 min
- Spin coat the frontside with AZ4400 resist at 2 krpm speed for 40 sec

- Resist thickness is approximately = 5.5 μm
- Softbake at 100 °C for 20 min in a convection oven. Cool down for 3 min
- Stepper expose for 1.0 sec using mask # 9
- Develop with AZ351 developer
  - AZ351 developer: H_2O (1:4) = 5 min
- Rinse with DI H_2O. Spin dry
- Hardbake at 120 °C for 15 min in a convection oven. Cool down for 3 min

23.2. Etch parylene with PEII machine

- Etch time = 10 min

23.3. Rotate wafers 180° and repeat step 23.2

24. Dicing saw

24.1. Spin coat the frontside with AZ4400 resist at 2 krpm speed for 40 sec to protect the wafer during dicing

24.2. Dice the wafer from the frontside into 1 cm x 1 cm chips

25. Photoresist sacrificial layer release

25.1. Immerse sample chips in the acetone bath

25.2. Completely cover the bath with aluminum foil to prevent acetone evaporation. Release photoresist over night

25.3. Immerse the sample chips in a new acetone bath for one minute. Let the sample air dry completely

26. BrF_3 backside silicon etching

26.1. Place the sample chips in the etching chamber. Pump down the chamber until the pressure is < 100 mT

26.2. Introduce the BrF_3 gas into the chamber until the desire pressure is reached

26.3. BrF_3 etching

- Number of sample chips: 6 chips
- Number of pulses: 2 pulses
- Pressure of each pulse: 5 Torrs
- Etching time for each pulse: 5 min

26.4. When the etching cycle is finished, pump down the chamber and purge with N_2 gas until no BrF_3 residue is remained. Turn off the vacuum and purge with N_2 until the chamber reaches the atmospheric pressure.

26.5. Take out the samples to examine whether the silicon etching is finished. If not, repeat the etching step until the clear membrane can be observed.

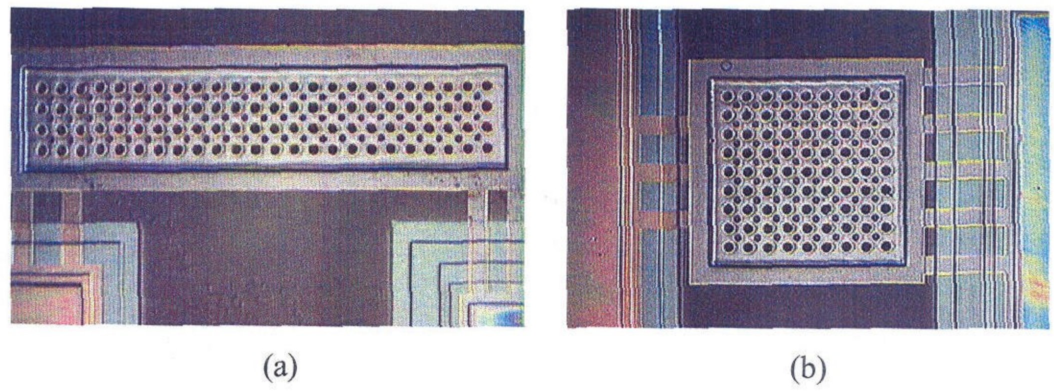

(a) (b)

Figure B-2: Parylene diaphragm actuator chip: (a) 1 mm x 5 mm rectangular

B.3 Parylene aeroMEMS Active Plate Electrostatic Actuator Skin

1. Mask fabrication
2. Double-side alignment
3. Photoresist lift-off layer and patterning
   3.1. Photolithography
   - Prime the wafers with HMDS for 3 min
   - Spin coat the frontside with AZ4400 resist at 3 krpm speed for 40 sec
     - Resist thickness is ~ 4 μm
   - Softbake at 100 °C for 15 min in a convection oven. Cool down for 3 min

   3.2. Turn on the Canon UV lamp for at least 20 min

   3.3. Place the mask film with the matte side facing down on top of the photoresist-coated wafer and firmly press a clear glass plate on top of the film

   3.4. Expose with UV light with mask # 1: exposed time = 20 seconds

   3.5. Develop the mask with AZ351 developer
   - AZ351 developer: H_2O (1:4) = 3 min

   3.6. Rinse with DI H_2O. Spin dry

   3.7. Hardbake at 120 °C for 10 min in a convection oven on a hotplate to get rid of solvent. Cool down for 3 min
4. 1st Parylene deposition
   4.1. Weigh parylene-C dimer = 6.2 g
   - The measurement yields ~ 4.4 μm thickness

   4.2. Roughen the surface of parylene with PEII machine
5. Ground Cr/Au/Cr evaporation
   5.1. Prepare the metal sources:
   - Chrome (Cr): 2 rods
   - Gold (Au): 3 g

   5.2. Evaporate Cr/Au/Cr
   - 1st layer of Cr: 100 A°
   - Au layer: 2800 A°

- 2nd layer of Cr: 100 A°

6. Ground Cr/Au/Cr patterning
   6.1. Photolithography
   - Prime the wafers with HMDS for 3 min
   - Spin coat the frontside with AZ1518 resist at 2.5 krpm speed for 40 sec
     - Resist thickness is ~ 2 μm
   - Softbake at 100 °C for 15 min in a convection oven. Cool down for 3 min
   - Stepper expose for 0.45 sec using mask # 2
   - Develop with AZ351 developer
     - AZ351 developer: H_2O (1:4) = 1.5 min
   - Rinse with DI H_2O. Spin dry

   6.2. Photoresist descum with PEII machine

   6.3. Rinse the wafer well with H_2O to prevent bubble trap

   6.4. Metal etching
   - Etch the wafer in Chrome etchant: etch time = 15 sec
   - Etch the wafer in Au etchant: etch time = 50 sec
   - Etch the wafer in Chrome etchant: etch time = 15 sec

   6.5. Strip photoresist using PR stripper: temp setting at 50 °C

   6.6. Rinse the wafer with PR stripper rinse

   6.7. Rinse with DI H_2O. Spin dry

7. 2nd Parylene deposition
   7.1. Weigh parylene-C dimer = 2 g
   - The measurement yields ~ 1.5 μm thickness

   7.2. Roughen the surface of parylene with PEII machine

8. Silicon sputtering
   8.1. Sputter thin film of silicon for anti-stiction layer (release with BrF_3)

   8.2. Parameter settings:
   - Base pressure: 7×10^{-6} Torr
   - Target number: 4 (silicon)

- Input tuning = 17
- Load tuning = 16.5
- Target bias = 7.4
- Incident power = 500 W
- Peak Voltage = 350 V
- Deposition time = 1 hr
- Thickness = 4500 A°

9. Silicon patterning

9.1. Photolithography

- Prime the wafers with HMDS for 3 min
- Spin coat the frontside with AZ1518 resist at 2.5 krpm speed for 40 sec
  - Resist thickness is approximately = 2 μm
- Softbake at 100 °C for 15 min in a convection oven. Cool down for 3 min
- Stepper expose for 0.5 sec using mask # 3
- Develop with AZ351 developer
  - AZ351 developer: H_2O (1:4) = 1.5 min
- Rinse with DI H_2O. Spin dry

9.2. Photoresist descum with PEII machine

9.3. Etch silicon with plasma etching in PEII machine

- SF_6/O_2 = 300/30 mT
- Power = 300 W
- Etch time = 2.5 min

9.4. Strip the remained photoresist with acetone

9.5. Rinse with isopropanol alcohol and DI H_2O. Spin dry

10. Photoresist sacrificial layer and patterning

10.1. Photolithography

- Prime the wafers with HMDS for 3 min
- Spin coat the frontside with AZ4400 resist at 2.5 krpm speed for 40 sec
  - Resist thickness is approximately = 5 μm

- Softbake at 80 °C for 30 min in a convection oven. Cool down for 3 min
- Stepper expose for 1.3 sec using mask # 4
- Develop with AZ351 developer
  - AZ351 developer: H_2O (1:4) = 3 min
- Rinse with DI H_2O. Spin dry

11. 3rd Parylene deposition
    - 11.1. Weigh parylene-C dimer = 2 g
      - The measurement yields ~ 1.5 μm thickness
    - 11.2. Roughen the surface of parylene with PEII machine
12. Top electrode Cr/Au evaporation
    - 12.1. Prepare the metal sources:
      - Chrome (Cr): 1 rod
      - Gold (Au): 3 g
    - 12.2. Evaporate Cr/Au/Cr
      - 1st layer of Cr: 100 A°
      - Au layer: 2900 A°
13. Top electrode Cr/Au patterning
    - 13.1. Photolithography
      - Prime the wafers with HMDS for 3 min
      - Spin coat the frontside with AZ4400 resist at 3 krpm speed for 40 sec
        - Resist thickness is ~ 4 μm
      - Softbake at 100 °C for 15 min in a convection oven. Cool down for 3 min
      - Stepper expose for 1.3 sec using mask # 5
      - Develop with AZ351 developer
        - AZ351 developer: H_2O (1:4) = 2.5 min
      - Rinse with DI H_2O. Spin dry
    - 13.2. Photoresist descum with PEII machine
    - 13.3. Rotate wafers 180° and repeat step 13.2
    - 13.4. Rinse the wafer well with H_2O to prevent bubble trap

13.5. Metal etching

- Etch the wafer in Au etchant: etch time = 1:15 min
- Etch the wafer in Chrome etchant: etch time = 15 sec

13.6. Strip photoresist using PR stripper: temp setting at 50 °C

13.7. Rinse the wafer with PR stripper rinse

13.8. Rinse with DI H_2O. Spin dry

14. Parylene adhesion promoter

15. 4th Parylene deposition

15.1. Weigh parylene-C dimer = 6.2 g

- The measurement yields ~ 4.3 μm thickness
- The total parylene thickness (3rd & 4th depositions) = 5.8 μm

16. Aluminum mask evaporation

16.1. Evaporate aluminum as mask

- Al layer: 1000 A°

16.2. Photolithography

- Prime the wafers with HMDS for 3 min
- Spin coat the frontside with AZ1518 resist at 2.5 krpm speed for 40 sec
  - Resist thickness is ~ 2 μm
- Softbake at 100 °C for 15 min in a convection oven. Cool down for 3 min
- Stepper expose for 0.45 sec using mask # 6
- Develop with AZ351 developer (attack aluminum)
  - AZ351 developer: H_2O (1:4) = 2 min
- Rinse with DI H_2O. Spin dry

16.3. Photoresist descum with PEII machine

16.4. Rotate wafers 180° and repeat step 16.3

16.5. Rinse the wafer well with H_2O to prevent bubble trap

16.6. Metal etching

- Etch aluminum in Aluminum etchant: temp setting at 50 °C
  - Etch time = 40 sec

17. Parylene patterning
    17.1. Etch parylene with PEII machine
        - Etch time = 15 min
    17.2. Rotate wafers 180° and repeat step 17.1 for 15 min
    17.3. Rotate wafers 180° and repeat step 17.1 until the parylene etching is finished. The wafers are rotated to prevent the film from cracking from excess heat and to achieve uniform etching
    17.4. Strip aluminum in aluminum etchant
18. Photoresist sacrificial layer release
    18.1. Immerse the wafer in the acetone bath
    18.2. Completely cover the bath with aluminum foil to prevent acetone evaporation. Place the acetone bath in an ultrasonic shaker. Turn off the ultrasonic bath after the membrane is completely released from the wafer
19. Self-Assembled Monolayers (SAM) anti-stiction coating
    19.1. Remove the wafer and immerse it in a new acetone bath for one min
    19.2. Immerse the wafer in an isopropanol alcohol bath for 10 min
    19.3. Move the wafer to an iso-octane bath for 10 min
    19.4. Prepare 1 mM solution of Octadecyltrichlorosilane (OTS) in iso-octane. This roughly corresponds to a drop of OTS in 50 ml of iso-octane solution
    19.5. Place the wafer in the OTS solution for 10 min
    19.6. Reverse the step by repeating step 23.3 (iso-octane) and then 23.2 (alcohol)
    19.7. Immerse the wafer in the DI water bath for 5 min. Spin Dry
    19.8. Carefully use a sharp razor to cut the skin from the edge of the wafer. Slowly peel the skin off the wafer and air dry
20. BrF_3 silicon etching
    20.1. Place the wafer in the etching chamber. Pump down the chamber until the pressure is < 100 mT
    20.2. Introduce the BrF_3 gas into the chamber until the desire pressure is reached
    20.3. BrF_3 etching

- Number of pulses: 1 pulse
- Pressure of each pulse: 4 Torrs
- Etching time for each pulse: 1 min

20.4. When the etching cycle is finished, pump down the chamber and purge with N_2 gas until no BrF_3 residue is remained. Turn off the vacuum and purge with N_2 until the chamber reaches the atmospheric pressure

20.5. Take out the wafer to examine whether the membrane is released. If not, repeat the etching cycle step 20.1 – 20.4 for an additional pulse until the membrane is completely released

20.6. Once the thin layer of sputtered silicon is etched away, the actuator plates are freed and no stiction is observed

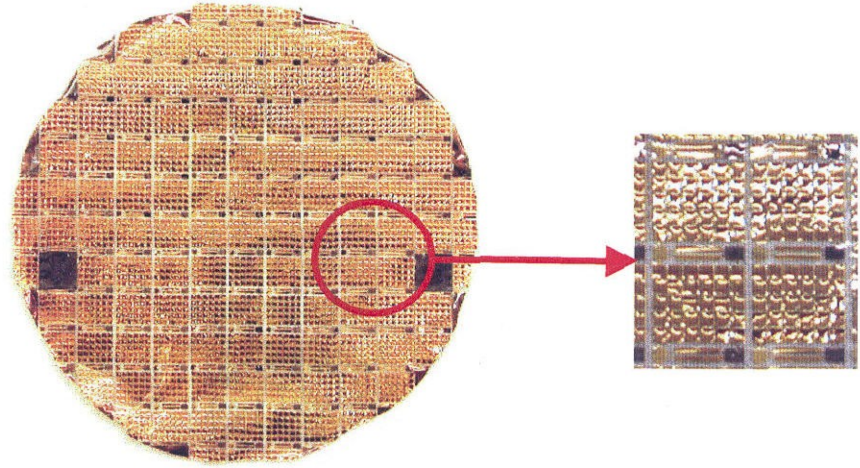

Figure B-3: Flexible parylene plate-type electrostatic actuator skin

B.4 Parylene aeroMEMS Check-Valved Pneumatic Actuator Skin

1. Mask fabrication
2. Single-side alignment
   - 2.1 Prime the wafer with HMDS for 3 min
   - 2.2 Spin coat the frontside with AZ4400 photoresist at 4 krpm speed for 40 sec
     - Resist thickness is approximately = 4 μm
   - 2.3 Softbake at 90 °C for 20 min in a convection oven. Let cool down for 3 min
   - 2.4 Place the wafer in the double-side alignment jig
   - 2.5 Expose with Canon UV light for 10 sec on the front side
   - 2.6 Spot develop with AZ351 developer
     - AZ351 developer: H_2O (1:4) = 4 min
   - 2.7 Etch with plasma etching in PEII machine
     - SF_6/O_2 = 300/30 mT
     - Power = 300 W
     - Etch time = 2 min
   - 2.8 Strip the photoresist with acetone
   - 2.9 Rinse with isopropanol alcohol and DI H_2O. Spin dry
3. Thermal Oxidation
   - 3.1 Wafer cleaning
     - Clean wafers using standard piranha recipe (H_2SO_4:H_2O_2 = 5:1 in volume)
   - 3.2 Wet thermal oxidation
     - Set temperature of wet oxidation at 1050 °C for 6 hrs
       - control setting: 330 646 540
       - H_2O drop rate: 5-8 drops/min
       - O_2 flow rate: 0.5 liter/min
     - Thickness = 1.8 μm
4. Photoresist lift-off layer
   - 4.1 Spin on photoresist

- Prime the wafers with HMDS for 3 min
- Spin coat the frontside with AZ4400 resist at 3 krpm speed for 40 sec
  - Resist thickness is ~ 4 μm
- Softbake at 100 °C for 15 min in a convection oven

4.2 Hardbake at 120 °C for 60 min in a convection oven on a hotplate to get rid of solvent. Cool down for 3 min

5. 1st Parylene deposition

5.1 Weigh parylene-C dimer = 12 g

- The measurement yields ~ 8 μm thickness

5.2 Anneal the wafers in vacuum oven at 120 °C for 20 min

5.3 Roughen the surface of parylene with PEII machine. This is to improve the adhesion of sputtered silicon layer to the parylene surface

- O_2 = 200 mT
- Power = 200 W
- Time = 1 min

6. Amorphous silicon sputtering

6.1 Sputter thin film of silicon for anti-stiction layer (release with BrF_3)

6.2 Parameter settings:

- Base pressure: 7 x 10^{-6} Torr
- Target number: 4 (silicon)
- Input tuning = 17
- Load tuning = 16.5
- Target bias = 7.4
- Incident power = 500 W
- Peak Voltage = 350 V
- Deposition time = 1 hr
- Thickness = 4500 A°

7. Silicon patterning

7.1 Photolithography

- Prime the wafers with HMDS for 3 min
- Spin coat the frontside with AZ1518 resist at 2.5 krpm speed for 40 sec
  - Resist thickness is approximately = 2 μm
- Softbake at 100 °C for 15 min in a convection oven. Cool down for 3 min
- Stepper expose for 0.5 sec using mask # 1
- Develop with AZ351 developer
  - AZ351 developer: H_2O (1:4) = 1.5 min
- Rinse with DI H_2O. Spin dry

7.2 Photoresist descum with PEII machine

7.3 Etch silicon with plasma etching in PEII machine

- SF_6/O_2 = 300/30 mT
- Power = 300 W
- Etch time = 2.5 min

7.4 Strip the remained photoresist with photoresist stripper

7.5 Rinse with stripper rinse and DI H_2O. Spin dry

8. Aluminum mask evaporation

8.1 Evaporate aluminum as mask

- Al layer: 1000 A°

8.2 Photolithography

- Prime the wafers with HMDS for 3 min
- Spin coat the frontside with AZ1518 resist at 2.5 krpm speed for 40 sec
  - Resist thickness is ~ 2 μm
- Softbake at 100 °C for 15 min in a convection oven. Cool down for 3 min
- Stepper expose for 0.7 sec using mask # 2
- Develop with AZ351 developer (attack aluminum)
  - AZ351 developer: H_2O (1:4) = 2 min
- Rinse with DI H_2O. Spin dry

8.3 Photoresist descum with PEII machine

8.4 Rotate wafers 180° and repeat step 8.3

8.5 Rinse the wafer well with H_2O to prevent bubble trap

8.6 Metal etching

- Etch aluminum in Aluminum etchant: temp setting at 50 °C
  - Etch time = 40 sec

8.7 Rinse with DI H_2O. Spin dry

9. Parylene patterning

9.1 Etch parylene with PEII machine

- Etch time = 16 min

9.2 Rotate wafers 180° and repeat step 9.1 for 16 min

9.3 Rotate wafers 180° and repeat step 9.1 until the parylene etching is finished. The wafers are rotated to prevent the film from cracking from excess heat and to achieve uniform etching

9.4 Strip aluminum in aluminum etchant

9.5 Rinse with DI H_2O. Spin dry

10. Photoresist sacrificial layer and patterning

10.1 Photolithography

- Prime the wafers with HMDS for 3 min
- Spin coat the frontside with AZ4400 resist at 3 krpm speed for 40 sec
  - Resist thickness is approximately = 4.5 μm
- Spin coat the frontside with AZ4620 resist at 3 krpm speed for 40 sec
  - Total resist thickness is approximately = 12 μm
- Hardbake at 120 °C for 20 min in a convection oven. Cool down for 3 min
- Stepper expose for 2 sec using mask # 3
- Develop with AZ351 developer
  - AZ351 developer: H_2O (1:4) = 6 min
- Rinse with DI H_2O. Spin dry

11. 2nd Parylene deposition

11.1 The same deposition parameters

11.2 Weigh parylene-C dimer = 12 g

- The measurement yields ~ 9 µm thickness
- Roughen the surface of parylene with PEII machine.

12. Aluminum mask evaporation

12.1 Evaporate aluminum as mask

- Al layer: 1000 A°

12.2 Photolithography

- Prime the wafers with HMDS for 3 min
- Spin coat the frontside with AZ1518 resist at 2.5 krpm speed for 40 sec
  - Resist thickness is ~ 2 µm
- Softbake at 100 °C for 15 min in a convection oven. Cool down for 3 min
- Stepper expose for 0.7 sec using mask # 3
- Develop with AZ351 developer (attack aluminum)
  - AZ351 developer: H_2O (1:4) = 2 min
- Rinse with DI H_2O. Spin dry

12.3 Photoresist descum with PEII machine

12.4 Rotate wafers 180° and repeat step 12.3

12.5 Rinse the wafer well with H_2O to prevent bubble trap

12.6 Metal etching

- Etch aluminum in Aluminum etchant: temp setting at 50 °C
  - Etch time = 40 sec

13. Parylene patterning

13.1 Etch parylene with PEII machine

- Etch time = 16 min

13.2 Rotate wafers 180° and repeat step 13.1 for 16 min

13.3 Rotate wafers 180° and repeat step 13.1 until the parylene etching is finished. The wafers are rotated to prevent the film from cracking from excess heat and to achieve uniform etching

13.4 Strip aluminum in aluminum etchant

13.5 Rinse with DI H_2O. Spin dry

14. Photoresist sacrificial layer release
    - 14.1 Immerse the wafer in the acetone bath
    - 14.2 Completely cover the bath with aluminum foil to prevent acetone evaporation. Place the acetone bath in an ultrasonic shaker. Turn off the ultrasonic bath after the membrane is completely released from the wafer
15. Self-Assembled Monolayers (SAM) anti-stiction coating
    - 15.1 Remove the wafer and immerse it in a new acetone bath for one min
    - 15.2 Immerse the wafer in an isopropanol alcohol bath for 10 min
    - 15.3 Move the wafer to an iso-octane bath for 10 min
    - 15.4 Prepare 1 mM solution of Octadecyltrichlorosilane (OTS) in iso-octane. This roughly corresponds to a drop of OTS in 50 ml of iso-octane solution
    - 15.5 Place the wafer in the OTS solution for 10 min
    - 15.6 Reverse the step by repeating step 15.3 (iso-octane) and then 15.2 (alcohol)
    - 15.7 Immerse the wafer in the DI water bath for 5 min. Spin Dry
    - 15.8 Carefully use a sharp razor to cut the skin from the edge of the wafer. Slowly peel the skin off the wafer and air dry
16. BrF_3 silicon etching
    - 16.1 After the skin is completely dry, cut the skin off the wafer. Tape each corner of the skin to a wafer
    - 16.2 Place the wafer in the etching chamber. Pump down the chamber until the pressure is < 100 mT
    - 16.3 Introduce the BrF_3 gas into the chamber until the desire pressure is reached
    - 16.4 BrF_3 etching
        - Number of pulses: 1 pulse
        - Pressure of each pulse: 6 Torrs
        - Etching time for each pulse: 5 min
    - 16.5 When the etching cycle is finished, pump down the chamber and purge with N_2 gas until no BrF_3 residue is remained. Turn off the vacuum and purge with N_2 until the chamber reaches the atmospheric pressure

16.6 Take out the wafer to examine whether the membrane is released. If not, repeat the etching cycle step 16.1 – 16.4 for an additional pulse until the membrane is completely released

16.7 Once the thin layer of sputtered silicon is etched away, the actuator plates are freed and no stiction is observed

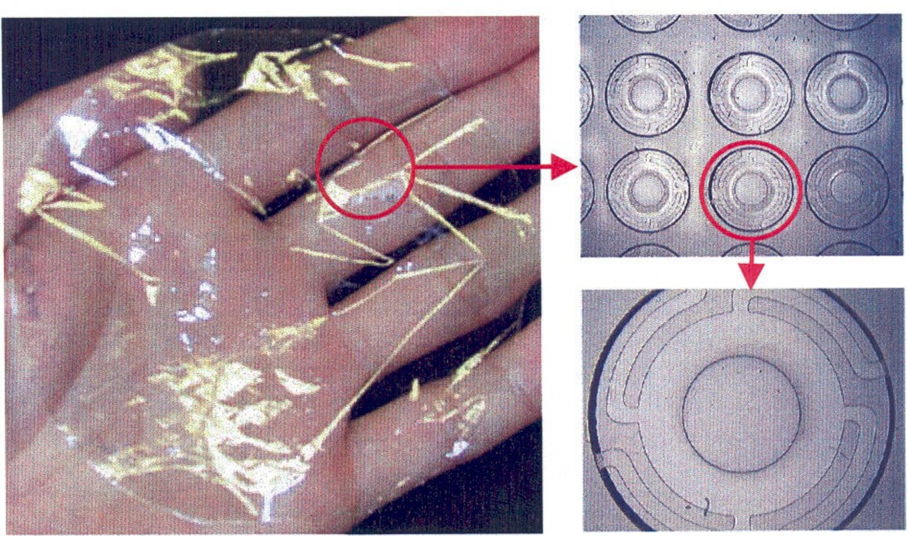

Figure B-4: Flexible parylene check-valved pneumatic actuator

B.5 Parylene aeroMEMS Check-Valved Electrostatic Actuator Skin

1. Mask fabrication
2. Single-side alignment
3. Photoresist lift-off layer
   - 3.1 Spin on photoresist
     - Prime the wafers with HMDS for 3 min
     - Spin coat the frontside with AZ4400 resist at 2.5 krpm speed for 40 sec
       - Resist thickness is ~ 4 μm
     - Softbake at 100 °C for 15 min in a convection oven
   - 3.2 Hardbake at 120 °C for 30 min in a convection oven on a hotplate to get rid of solvent. Cool down for 3 min
4. Aluminum Evaporation
   - 4.1 Evaporate thin film of aluminum to protect PR during parylene etching
   - 4.2 Aluminum film (slow rate)
     - Thickness = 1500 A°
5. 1st Parylene deposition
   - 5.1 Weigh parylene-C dimer = 6.5 g
     - The measurement yields ~ 4.5 μm thickness
     - Roughen the surface of parylene with PEII machine.
6. Ground Cr/Au/Cr evaporation
   - 6.1 Prepare the metal sources:
     - Chrome (Cr): 2 rods
     - Gold (Au): 3 g
   - 6.2 Evaporate Cr/Au/Cr
     - 1st layer of Cr: 100 A°
     - Au layer: 2300 A°
     - 2nd layer of Cr: 100 A°
7. Ground Cr/Au/Cr patterning
   - 7.1 Photolithography

- Prime the wafers with HMDS for 3 min
- Spin coat the frontside with AZ1518 resist at 2.5 krpm speed for 40 sec
  - Resist thickness is ~ 2 μm
- Softbake at 100 °C for 15 min in a convection oven. Cool down for 3 min
- Stepper expose for 0.7 sec using mask # 1 (no mask: ring3;5; with mask: ring3;4; window set at 78.5%)
- Develop with AZ351 developer
  - AZ351 developer: H_2O (1:4) = 1.5 min
- Rinse with DI H_2O. Spin dry

7.2 Photoresist descum with PEII machine

7.3 Rotate wafers 180° and repeat step 7.2

7.4 Rinse the wafer well with H_2O to prevent bubble trap

7.5 Metal etching

- Etch the wafer in Chrome etchant: etch time = 15 sec
- Etch the wafer in Au etchant: etch time = 50 sec
- Etch the wafer in Chrome etchant: etch time = 15 sec

7.6 Rinse with DI H_2O. Spin dry

7.7 Strip photoresist using PR stripper: temp setting at 50 °C

7.8 Rinse the wafer with PR stripper rinse

7.9 Rinse with DI H_2O. Spin dry

8. 2nd Parylene deposition

8.1 Weigh parylene-C dimer = 2.5 g

- The measurement yields ~ 2 μm thickness

8.2 Anneal the wafers in convection oven at 120 °C for 5 min

- Roughen the surface of parylene with PEII machine.

9. Silicon sputtering

9.1 Sputter thin film of silicon for anti-stiction layer (release with BrF_3)

10. Silicon patterning

10.1 Photolithography

- Prime the wafers with HMDS for 3 min
- Spin coat the frontside with AZ4400 resist at 3 krpm speed for 40 sec
  - Resist thickness is approximately = 4 μm
- Softbake at 90 °C for 20 min in a convection oven. Cool down for 3 min (test bake one wafer first to see if wrinkles appear)
- Stepper expose for 1 sec using mask # 2 (no mask: ring3;5; with mask: ring3;4; window set at 78.5%)
- Develop with AZ351 developer
  - AZ351 developer: H_2O (1:4) = 1.5 min
- Rinse with DI H_2O. Spin dry

10.2 Photoresist descum with PEII machine

10.3 Etch silicon with plasma etching in PEII machine

- SF_6/O_2 = 300/30 mT
- Power = 300 W
- Etch time = 2.5 min

10.4 Strip the remained photoresist with photoresist stripper

10.5 Rinse with stripper rinse and DI H_2O. Spin dry

11. Aluminum mask evaporation

11.1 Evaporate aluminum as mask

- Al layer: 1500 A°

11.2 Photolithography

- Prime the wafers with HMDS for 3 min
- Spin coat the frontside with AZ1518 resist at 2.5 krpm speed for 40 sec
  - Resist thickness is ~ 2 μm
- Softbake at 100 °C for 15 min in a convection oven. Cool down for 3 min
- Stepper expose for 0.7 sec using mask # 3
- Develop with AZ351 developer (attack aluminum)
  - AZ351 developer: H_2O (1:4) = 2 min
- Rinse with DI H_2O. Spin dry

11.3 Photoresist descum with PEII machine

11.4 Rotate wafers 180° and repeat step 11.3

11.5 Rinse the wafer well with H_2O to prevent bubble trap

11.6 Metal etching

- Etch aluminum in Aluminum etchant: temp setting at 50 °C
  - Etch time = 40 sec

11.7 Rinse with DI H_2O. Spin dry

12. Parylene patterning

12.1 Etch parylene with PEII machine

- O_2 = 400 mT
- Power = 400 W (optinal: 200 W)
- Etch time = 16 min

12.2 Rotate wafers 180° and repeat step 12.1 for 16 min

12.3 Rotate wafers 180° and repeat step 12.1 until the parylene etching is finished. The wafers are rotated to prevent the film from cracking from excess heat and to achieve uniform etching

12.4 Strip aluminum in aluminum etchant

12.5 Rinse with DI H_2O. Spin dry

13. Photoresist sacrificial layer and patterning

13.1 Photolithography

- Prime the wafers with HMDS for 3 min
- Spin coat the frontside with AZ4400 resist at 3 krpm speed for 40 sec
  - Resist thickness is approximately = 4 µm
- Spin coat the frontside with AZ4620 resist at 3 krpm speed for 40 sec
  - Total resist thickness is approximately = 12 µm
- Softbake at 100 °C for 15 min in a convection oven. Cool down for 3 min
- Stepper expose for 2 sec using mask # 4
- Develop with AZ351 developer
  - AZ351 developer: H_2O (1:4) = 6 min

- Rinse with DI H_2O. Spin dry

14. 3rd Parylene deposition

14.1 Weigh parylene-C dimer = 2.5 g

- The measurement yields ~ 2 μm thickness

14.2 Roughen the surface of parylene with PEII machine.

15. Top electrode Cr/Au/Cr evaporation

15.1 Prepare the metal sources:

- Chrome (Cr): 2 rod
- Gold (Au): 3 g

15.2 Evaporate Cr/Au/Cr

- 1st layer of Cr: 100 A°
- Au layer: 2300 A°
- 2nd layer of Cr: 100 A°

16. Top electrode Cr/Au/Cr patterning

16.1 Photolithography

- Prime the wafers with HMDS for 3 min
- Spin coat the frontside with AZ4400 resist at 3 krpm speed for 40 sec
  - Resist thickness is ~ 4 μm
- Softbake at 90 °C for 20 min in a convection oven. Cool down for 3 min
- Stepper expose for 1.3 sec using mask # 5
- Develop with AZ351 developer
  - AZ351 developer: H_2O (1:4) = 2.5 min
- Rinse with DI H_2O. Spin dry

16.2 Photoresist descum with PEII machine

16.3 Rotate wafers 180° and repeat step 16.2

16.4 Rinse the wafer well with H_2O to prevent bubble trap

16.5 Metal etching

- Etch the wafer in Chrome etchant: etch time = 15 sec
- Etch the wafer in Au etchant: etch time = 50 sec

- Etch the wafer in Chrome etchant: etch time = 15 sec

16.6 Rinse with DI H_2O. Spin dry

16.7 Strip photoresist using PR stripper: temp setting at 50 °C

16.8 Rinse the wafer with PR stripper rinse

16.9 Rinse with DI H_2O. Spin dry

17. Parylene adhesion promoter

17.1 Prepare the A-174 organic silane adhesion promoter

- Recipe: H_2O: IPA: A-174 = 100:100:1 in volume
- Stir the solution well. Let it sit for at least 2 hrs

17.2 Immerse the wafers in the solution for 15 min

17.3 Let air dry for at least 15 min

17.4 Use IPA to rinse each wafer for 15 sec

17.5 Let air dry for 15 min

18. 4th Parylene deposition

18.1 Weigh parylene-C dimer = 6.5 g

- The measurement yields ~ 4.5 μm thickness

19. Aluminum mask evaporation

19.1 Evaporate aluminum as mask

- Al layer: 1500 A°

19.2 Photolithography

- Prime the wafers with HMDS for 3 min
- Spin coat the frontside with AZ1518 resist at 2.5 krpm speed for 40 sec
  - Resist thickness is ~ 2 μm
- Softbake at 900 °C for 20 min in a convection oven. Cool down for 3 min
- Stepper expose for 0.45 sec using mask # 6
- Develop with AZ351 developer (attack aluminum)
  - AZ351 developer: H_2O (1:4) = 2 min
- Rinse with DI H_2O. Spin dry

19.3 Photoresist descum with PEII machine

19.4 Rotate wafers 180° and repeat step 19.3

19.5 Rinse the wafer well with H_2O to prevent bubble trap

19.6 Metal etching

- Etch aluminum in Aluminum etchant: temp setting at 50 °C
  - Etch time = 40 sec

19.7 Rinse with DI H_2O. Spin dry

20. Parylene patterning

20.1 Etch parylene with PEII machine

- Etch time = 15 min

20.2 Rotate wafers 180° and repeat step 20.1 for 16 min

20.3 Rotate wafers 180° and repeat step 20.1 until the parylene etching is finished. The wafers are rotated to prevent the film from cracking from excess heat and to achieve uniform etching

21. Photoresist sacrificial layer release

21.1 Immerse the wafer in the acetone bath

21.2 Completely cover the bath with aluminum foil to prevent acetone evaporation. Place the acetone bath in an ultrasonic shaker. Turn off the ultrasonic bath after the membrane is completely released from the wafer

22. Self-Assembled Monolayers (SAM) anti-stiction coating

22.1 Remove the wafer and immerse it in a new acetone bath for one min

22.2 Immerse the wafer in an isopropanol alcohol bath for 10 min

22.3 Move the wafer to an iso-octane bath for 10 min

22.4 Prepare 1 mM solution of Octadecyltrichlorosilane (OTS) in iso-octane. This roughly corresponds to a drop of OTS in 50 ml of iso-octane solution

22.5 Place the wafer in the OTS solution for 10 min

22.6 Reverse the step by repeating step 23.3 (iso-octane) and then 23.2 (alcohol)

22.7 Immerse the wafer in the DI water bath for 5 min. Spin Dry

22.8 Carefully use a sharp razor to cut the skin from the edge of the wafer. Slowly peel the skin off the wafer and air dry

23. BrF_3 silicon etching
24. Cut the skin off the wafer
25. Actuation test

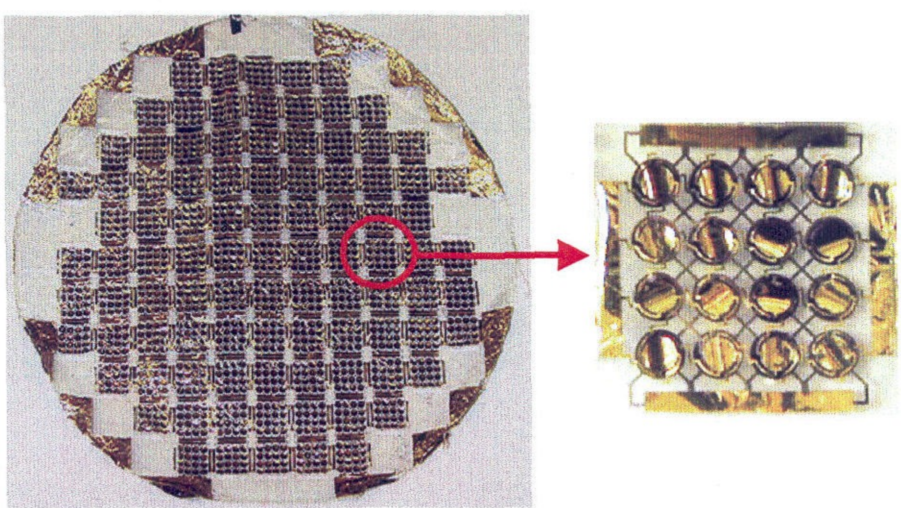

Figure B-5: Flexible parylene check-valved electrostatic actuator